

Chemistry in Block Copolymer Nanocontainers

Self - Assembly, Container Properties and Confined Enzymatic Reactions

Chemistry in Block Copolymer Nanocontainers

Qi Chen 2009

Qi Chen

ISBN: 978-90-365-2955-6

Invitation

You are cordially invited to the public defence of my PhD Thesis on December 17th, 2009 at 16:45 in Collegezaal 2, Spiegel building on the campus of the University of Twente.

At 16:30 I will give a short introduction to the contents of my Thesis.

Qi Chen
q.chen@tnw.utwente.nl

Paranimfen:

Edit Kutnyanszky
e.kutnyanszky@tnw.utwente.nl

Joost Duvigneau
j.duvigneau@tnw.utwente.nl

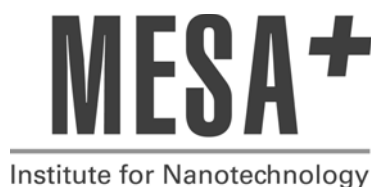
CHEMISTRY IN BLOCK COPOLYMER NANOCONTAINERS

SELF – ASSEMBLY, CONTAINER PROPERTIES

AND CONFINED ENZYMATIC REACTIONS

Qi Chen

This research was financially supported by the MESA⁺ Institute for Nanotechnology of the University of Twente (Strategic Research Orientation program Bionanotechnology).



Chemistry in Block Copolymer Nanocontainers:
Self-Assembly, Container Properties and Confined Enzymatic Reactions

Q. Chen
Ph.D Thesis
University of Twente, Enschede, The Netherlands

Cover illustration: Tapping mode atomic force microscopy image of block copolymer vesicles deposited on mica, phase signal.

© Qi Chen 2009

ISBN: 978-90-365-2955-6

No part of this work may be reproduced by print, photocopy or any other means without the permission of the publisher.

Printed by Ipskamp Drukkers B. V., Enschede, The Netherlands

CHEMISTRY IN BLOCK COPOLYMER NANOCONTAINERS

SELF – ASSEMBLY, CONTAINER PROPERTIES AND CONFINED ENZYMATIC REACTIONS

PROEFSCHRIFT

ter verkrijging van
de graad van doctor aan de Universiteit Twente,
op gezag van de rector magnificus,
prof. dr. H. Brinksma,
volgens besluit van het College voor Promoties
in het openbaar te verdedigen
op donderdag 17 december 2009 om 16.45 uur

door

Qi Chen

geboren op 27 oktober 1978
te Guangdong, China

Dit proefschrift is goedgekeurd door:

Promotor: prof. dr. G. J. Vancso

Assistent-promotor: prof. dr. H. Schönherr

Table of Contents

Chapter 1 General Introduction	1
1.1 Introduction	1
1.2 Concept of this Thesis	3
1.3 References	5
Chapter 2 Polymeric Nanocontainers for the Study of Enzymatic Reactions in Confinement	7
2.1 Introduction	7
2.2 Polymeric nanocontainers	8
2.2.1 The self-assembly approach	8
2.2.2 The template directed assembly approach	16
2.2.3 The dendrimer approach	19
2.3 Enzymatic reactions and enzyme kinetics	21
2.4 Brief overview of studies on single enzyme kinetics	23
2.4.1 Distribution of turnover times of enzymes reveals fluctuations in reactivity	23
2.4.2 Stretched exponential decay and correlations in the activity of enzymes	29
2.5 Reaction kinetics in confined geometries	31
2.5.1 Modeling a reaction inside a sphere	32
2.5.2 Collision frequencies of reagents inside a vesicle	34
2.6 References	37
Chapter 3 Preparation and Characterization of Block Copolymer Vesicles as Nanocontainers	43
3.1 Introduction	43
3.2 Controlling the size and morphology of PS- <i>b</i> -PAA aggregates via solution composition	45
3.2.1 Influence of water content	47
3.2.2 Influence of initial polymer concentration	48
3.2.3 Influence of the addition of ions	49
3.2.4 Influence of nature and composition of the common solvent	50

3.3 PS- <i>b</i> -PAA vesicles with different wall thicknesses	52
3.4 Preparing PS- <i>b</i> -PAA vesicles at different temperatures	53
3.5 Thermal stability of PS- <i>b</i> -PAA vesicles	55
3.6 Encapsulation of fluorescent molecules in PS- <i>b</i> -PAA vesicles	56
3.7 Conclusion	58
3.8 Experimental	58
3.9 References	59

Chapter 4 Mechanical Properties of Block Copolymer Vesicles by Atomic Force Microscopy

	61
4.1 Introduction	61
4.2 PS- <i>b</i> -PAA vesicles with different wall thicknesses	63
4.3 AFM force measurement on PS- <i>b</i> -PAA vesicles	65
4.4 Determination of the apparent Young's modulus of the membrane with different thicknesses	69
4.5 Conclusion	72
4.6 Experimental	73
4.7 References and notes	74

Chapter 5 Block Copolymer Vesicles as Nanosized Reactors for Trypsin Catalysis

	75
5.1 Introduction	75
5.2 Preparation of PS- <i>b</i> -PAA vesicles using different conditions	78
5.3 Encapsulation of enzyme and substrate in PS- <i>b</i> -PAA vesicles	80
5.4 Study of kinetics of trypsin catalysis	83
5.5 Conclusion	89
5.6 Experimental	90
5.7 References and notes	91

Chapter 6 Study of α -Chymotrypsin Catalysis under Confinement using Block Copolymer Vesicles

	93
6.1 Introduction	93
6.2 Results and discussion	95
6.2.1 Preparation of PS- <i>b</i> -PAA vesicles with different sizes	95
6.2.2 α -Chymotrypsin catalysis in solution	96

6.2.3	Encapsulation efficiency of enzymes and substrates inside PS- <i>b</i> -PAA vesicles	98
6.2.4	α -Chymotrypsin catalysis in PS- <i>b</i> -PAA vesicles	100
6.3	Conclusion	105
6.4	Experimental	105
6.5	References	107
Chapter 7 Temperature Induced Vesicle-to-Micelle Transition of Block Copolymer Aggregates in Solution and Encapsulation / Release of Molecular Cargos		109
7.1	Introduction	109
7.2	Observation of temperature induced morphological changes of PS- <i>b</i> -PAA aggregates	112
7.3	Turbidity change with temperature for PS- <i>b</i> -PAA aggregates	115
7.4	The influence of solution composition on the transition temperature	118
7.4.1	The effect of initial polymer concentration	118
7.4.2	The effect of solvent composition	119
7.5	Release and encapsulation of molecular cargos employing the temperature induced vesicle-to-micelle transition	121
7.6	Conclusion	126
7.7	Experimental	126
7.8	References	127
Chapter 8 Immobilization and Patterning of Block Copolymer Vesicles onto Surfaces		129
8.1	Introduction	129
8.2	Investigation on the electrostatic immobilization of PS- <i>b</i> -PAA vesicles on NH ₂ -terminated surfaces	131
8.3	Influence of pH and ionic strength on the electrostatic immobilization	135
8.3.1	Influence of pH	135
8.3.2	Influence of ionic strength	137
8.4	Patterning of PS- <i>b</i> -PAA vesicles on surfaces using MIMIC	139
8.5	Conclusion	141
8.6	Experimental	142
8.7	References and notes	143

Summary	145
Samenvatting	149
Acknowledgements	153
Curriculum Vitae	155

Chapter 1

General Introduction

1.1 Introduction

Biological systems have provided a continuous inspiration for scientists due to their natural diversity, complexity and efficiency.¹ For instance, a living cell possesses complex and intricate functions, such as maintaining a membrane boundary, transporting selective substances across this membrane and performing synthesis inside its small volume,² something that no synthetic analogues at present can do.

The developments in micro- and nanoscale fabrication, assembly and characterization in recent years, however, enable us to begin tackling the necessary methodologies and materials for mimicking and understanding some important properties and features of biological systems with control down to nanometer length scales. In the process of exploiting this nanoscale control, it is envisioned that unexpected observations will be made and new insights will emerge, which so far have been obscured in “ensemble” measurements with conventional techniques that are unable to probe individual molecular events down to such small length scales.³ One illustrative and relevant example is the study of single enzyme kinetics using optical microscopy and spectroscopy, which can detect fluorescent signals down to the single molecule level. Dynamic disorder, as an intrinsic property of enzymes, referring to fluctuations in the reaction rates of individual enzyme molecules over different turnover cycles, was first observed by Xie *et al.* just ten years ago.⁴ With the better understanding of the smallest scale features of biology, some initial efforts have been made regarding the practical developments of nanoscale technologies, which aim at the realizations of synthetic systems possessing the complexity and functionality of the biological systems.

The most widely studied biomimetic containment systems are based on vesicles prepared from amphiphilic molecules. These self-assembling structures can be formed from lipids, creating liposomes, or from synthetic molecules such as block copolymers, which are often referred to as polymersomes.⁵ They are considered to be ideal biomimetic nanoscale reaction containers.⁶ Liposomes have long been used to encapsulate enzymes and can be prepared using a variety of techniques.⁷ Their potential application as delivery vehicles for therapeutics has received much attention.

Liposomes can protect enzymes from degradation, induce slow release of a reagent, or contain chemical reactions. For example, enzymes entrapped in the interior of the liposome can be used for diagnostic applications,⁸ for metabolizing toxic reagents,⁹ or as catalysts.¹⁰

Studies of kinetics of chemical reactions confined inside these vesicles have received relatively little attention. This is in part due to the instability and fluidity of the liposome membranes.¹¹ Phospholipid membranes rupture easily as their small thickness makes them susceptible to fluctuations and defects.⁵ Due to this problem most of the kinetics studies reported in the literature regarding enzyme-encapsulated liposomes were related to diffusion limited reaction kinetics, *i.e.* the substrate molecules diffused through the vesicle membrane to react with the entrapped enzyme.⁷ Block copolymer vesicles (polymersomes), however, have better mechanical stability and impermeability towards small molecules, as a result of the thicker membrane formed from the macromolecules with a higher molar mass compared to that of phospholipid molecules.⁵ Retention of encapsulants (*e.g.*, dextrans, sucrose, physiological saline) over periods of months has been observed using polymersomes with a diameter of ~ 100 nm prepared by liposome-type extrusion techniques.¹² Recently, polymersomes that combine biological molecules with synthetic macromolecules are developed, as the synthetic components render the shape and stability of the container. Furthermore, the biological molecules (membrane channel proteins) provide the functionality that is similar to cell membranes.¹³ It should be mentioned that nanocontainers made of virus capsids emerged in recent years and can be utilized as reaction vessels for confined chemical reactions, as well.¹⁴ Living systems usually carry out biochemical reactions within cellular compartments confined by a membrane boundary. At such small volumes (in the atto-liter (10^{-18} L) and zepto-liter (10^{-21} L) range) the surface to volume ratio is very high and the encapsulated molecules collide with each other more frequently as opposed to “open space” with dimensions in the range of multiples of the collision mean free path.¹⁵ Simulation based on Brownian diffusion models including a single enzyme and substrate molecule confined in a vesicle shows that the collision frequencies between the molecules, as well as the collision frequency between the molecule and the wall depend strongly on the size of the vesicle.¹⁶ Therefore, the biochemical reactivity of the encapsulated molecules may be affected by interactions with the container surface and confinement of the containers. A study of the kinetic peculiarities of chemical processes in such restricted systems may thus provide important information on their

structures and dynamics.¹⁷ Surprisingly, such experimental studies are virtually absent in the literature. Finally, from an application point of view, studies of the reaction kinetics in restricted or confined spaces can help in designing new nanosystems to carry out efficient catalytic processes.¹⁸⁻²⁰

1.2 Concept of this Thesis

The research described in this Thesis is centered around the utilization of block copolymer (BCP) vesicles formed by the self-organization of amphiphilic block copolymers in solvents as nanocontainers to encapsulate enzymes and substrates, and the investigation of the influence of the container's dimensions on the catalytic activity of the enzymes. Parameters that are important in the self organization of the block copolymers in solution are varied and studied in detail. Enzymes and substrates are directly encapsulated into the vesicle interior during the formation of the vesicles and the progress of the enzymatic reaction is monitored using fluorescence-generating (fluorogenic) substrates.

In *Chapter 2* a literature overview on different types of nanocontainers is given along with the methodologies that are used to fabricate the containers, emphasizing their use for the encapsulation of functional molecules. Subsequently, the traditional theory of enzyme kinetics, as well as the exciting field of single enzyme kinetics revealed by single molecule optical detection is introduced. Finally some theoretical studies focusing on reactions occurring in the finite space inside the nanocontainers are presented.

In *Chapter 3*, the phase behavior of PS-*b*-PAA in solution is described. Vesicles formed as a result of the self organization of PS-*b*-PAA were prepared using the selective solvent method and characterized using microscopy methods and light scattering. The effect of different preparation conditions on the size and morphology of the BCP aggregates is addressed in detail. This work forms the basis for the study on the encapsulation/release of functional molecules utilizing BCP aggregates as nanocontainers and the investigation of spatial confinement effects of the container on the reactivity of the encapsulated species.

The assessment of mechanical properties of PS-*b*-PAA vesicles is crucial as they will be used later on as nanocontainers for the study of enzymatic reactions. The stability and robustness of the vesicles ensure enzymes and substrates are encapsulated inside

the containers. Therefore in **Chapter 4** the stiffness of the membranes of PS-*b*-PAA vesicles with different BCP chain lengths assessed using an AFM based nano-indentation method is discussed. The values of the elastic constants and apparent Young's moduli of membranes with systematically varied thicknesses were estimated and the relation between the rigidity and the thickness of the membranes was elucidated.

The enzymatic reactions in nanocontainers and the confinement effect on the catalytic activity of different enzymes were subsequently investigated using two different enzyme-substrate systems. In **Chapter 5** the utilization of PS₁₃₉-*b*-PAA₁₇ vesicles as size-tunable atto-liter reactors for the study of enzymatic reactions of encapsulated *trypsin* are discussed. Using fluorogenic substrate *rhodamine 110 bisamide*, the relation of vesicle diameter (internal volume) and enzyme reactivity was unraveled. The effect of confinement is further elucidated in **Chapter 6**, using PS₄₀₃-*b*-PAA₆₂ vesicles as small volume containers to investigate the catalytic reactivity of encapsulated *α-chymotrypsin*. The kinetic parameters for the hydrolysis reaction of fluorogenic substrate *N-succinyl-Ala-Ala-Phe-7-amido-4-methylcoumarin* hydrolysis were obtained for the unrestricted reaction in solution as well as for the reaction confined to the interior of polymeric vesicles with different sizes, and the dependence of the rate constants of the reaction on the size of the containers was studied.

In **Chapter 7**, the morphology and size of PS₁₃₉-*b*-PAA₁₇ aggregates prepared at different temperatures with a mixed water/THF solvent are displayed. The existence of a phase transition from vesicles to micelles as a result of temperature change was confirmed by experimental techniques including electron microscopy, light scattering, and ultraviolet-visible light spectroscopy. A change in temperature was then utilized as an external stimulus to trigger the release and encapsulation of enzyme and substrates, initiating their reaction.

A simple approach to immobilize PS₁₃₉-*b*-PAA₁₇ vesicles onto amino-terminated silicon/silicon oxide surfaces based on electrostatic interaction was explored in **Chapter 8**. Combining electrostatic interactions and soft lithography, line patterns containing the vesicles were created, which serve as a pre-requisite for preparing future microarray systems utilizing these vesicles as functional elements and a potential way to retain these vesicles on surfaces for real-time observation of the reaction kinetics and dynamic behavior of biomolecules of interest inside the vesicles.

1.3 References

- 1 M. J. Doktycz, M. L. Simpson, *Mol. Syst. Biol.* 2007, **3**, 125.
- 2 A. Pohorille, D. Deamer, *TRENDS in Biotech.* 2002, **20**, 123.
- 3 M. C. Roco, *Curr. Opin. Biotechnol.* 2003, **14**, 337.
- 4 H. P. Lu, L. Y. Xun, X. S. Xie, *Science* 1998, **282**, 1877.
- 5 D. E. Discher, A. Eisenberg, *Science* 2002, **297**, 967.
- 6 M. Karlsson, M. Davidson, R. Karlsson, A. Karlsson, J. Bergenholtz, Z. Konkoli, A. Jesorka, T. Lobovkina, J. Hurtig, M. Voinova, O. Orwar, *Annu. Rev. Phys. Chem.* 2004, **55**, 613.
- 7 P. Walde, S. Ichikawa, *Biomol. Engin.* 2001, **18**, 143.
- 8 R. J. Y. Ho, B. T. Rouse, L. Huang, *J. Biol. Chem.* 1987, **262**, 13979.
- 9 I. Petrikovics, K. Hong, G. Omburo, Q. Z. Hu, L. Pei, W. D. McGuinn, D. Sylvester, C. Tamulinas, D. Papahadjopoulos, J. C. Jaszberenyi, J. L. Way, *Toxicol. Appl. Pharmacol.* 1999, **156**, 56.
- 10 M. Yoshimoto, S. Q. Wang, K. Fukunaga, P. Walde, R. Kuboi, K. Nakao, *Biotechnol. Bioeng.* 2003, **81**, 695.
- 11 I. W. Hamley, *Soft Matter* 2005, **1**, 36.
- 12 J. C. -M. Lee, H. Bermudez, B. M. Discher, M. A. Sheehan, Y. Y. Won, F. S. Batters, D. E. Discher, *Biotech. Bioeng.* 2001, **43**, 135.
- 13 A. Taubert, A. Napoli, W. Meier, *Curr. Opin. Chem. Biol.* 2004, **8**, 598.
- 14 M. C. Aragonés, H. Engelkamp, V. I. Classen, N. A. J. M. Sommerdijk, A. E. Rowan, P. C. M. Christianen, J. C. Maan, B. J. M. Verduin, J. J. L. M. Cornelissen, R. J. M. Nolte, *Nature Nanotech.* 2007, **2**, 635.
- 15 D. T. Chiu, C. F. Wilson, F. Ryttsén, A. Strömberg, C. Farre, A. Karlsson, S. Nordholm, A. Gaggari, B. P. Modi, A. Moscho, R. A. Garza-López, O. Orwar, R. N. Zare, *Science* 1999, **283**, 1892.
- 16 D. T. Chiu, C. F. Wilson, A. Karlsson, A. Danielsson, A. Lundqvist, A. Strömberg, F. Ryttsén, M. Davidson, S. Nordholm, O. Orwar, R. N. Zare, *Chem. Phys.* 1999, **247**, 133.
- 17 R. F. Khairutdinov, *Prog. Reaction Kinetics*, 1996, **21**, 1.
- 18 J. Wolcke, D. Ullmann, *Drug Discov. Today* 2001, **6**, 637.
- 19 M. J. Heller, *Annu. Rev. Biomed. Eng.* 2002, **4**, 129.
- 20 J. Khandurina, A. Guttman, *Curr. Opin. Chem. Biol.* 2002, **6**, 359.

Chapter 2

Polymeric Nanocontainers for the Study of Enzymatic Reactions in Confinement

2.1 Introduction

The term nanocontainer usually refers to hollow structures with dimensions in the nanometer to submicrometer range. Among such structures, nanocapsules are of distinctive interest due to their potential for encapsulation of guest molecules within their “empty” core. For nanocontainers, a variety of different applications have already been proposed, such as reaction vessels, drug carriers, protective shells for cells or enzymes, transfection vectors in gene therapy, carrier systems in heterogeneous catalysis, dye dispersants or as materials for the removal of contaminated waste.¹⁻²²

Particularly important among these applications is the use of the nanocontainers as confined reaction vessels.²³ As well known, many biochemical reactions in nature occur in a confined space, typically on the order of tens and hundreds of nanometers, *i.e.* in atto-liter and zepto-liter volume, with concentrations of substances down to the single molecule level.

Previous studies on single enzyme reactions already led to unexpected results, as concentration, the conventional concept in reaction kinetics is obsolete when single molecules are concerned.²⁴ A time perspective, instead of a rate perspective was applied to reformulate the traditional bulk level kinetics theory.^{25, 26} On the other hand, confining bio-molecules such as enzymes into nanocontainers may provide additional insights into the kinetics of the process, as the finite space in which the molecules resided may have an impact on the kinetic behavior of the molecules.²⁷

The advancement to a new (non-) covalent complexity level generally produces entirely new structures (architectures) with properties that follow strange new rules and require unprecedented explanations, concepts, and generalizations.²⁸ In our study, amphiphilic block copolymers were used as the building blocks for the creation of nanocontainers. In aqueous solution well-defined block copolymers undergo

** Parts of this chapter were published in the following article: Q. Chen, R. Groote, H. Schönherr; G. J. Vancso, “Probing Single Enzyme Kinetics in Real-time”, Chemical Society Reviews 2009, 38, 2671-2683.*

self-organization to form ordered structures such as vesicles and micelles that resemble natural nanocontainers existing in living organisms. Biomolecules, to be more specific, enzymes were loaded into these synthetic nanocontainers with dilution down to the single molecule level. As a result of their appropriate size and functions these enzyme-container systems were utilized as a model system towards the study of single molecule chemistry in confinement.

In this chapter examples of different types of nanocontainers will be reviewed according to the approaches that are used to obtain the structures, with an emphasis on the application to utilize these nanocontainers for the encapsulation of functional molecules, such as enzymes and their reactions. The subsequent discussion starts by introducing the basics of enzymatic reaction and enzyme kinetics, followed by a brief overview of literature findings on single enzyme kinetics. Finally some theoretical studies focusing on reactions occurring in the finite space inside the nanocontainers are also presented.

2.2 Polymeric nanocontainers

2.2.1 The self-assembly approach

Owing to their amphiphilic nature and molecular geometry, lipid molecules can aggregate in dilute aqueous solution into spherically enclosed bilayer structures, so-called vesicles or liposomes.²⁹⁻³¹ The hollow sphere morphology of these aggregates makes them suitable as precursors for the preparation of more stable nanocapsules. This can be realized using different concepts. Figure 2.1 gives an overview of the various methods available to stabilize lipid membrane.³² For example, lipids that are functionalized with polymerizable groups can be polymerized within such vesicular structures.^{32,33} As a result of the polymerization reaction the individual lipid molecules are interconnected via covalent bonds which stabilize the shell-forming membrane considerably. Since the pioneering studies on polymerized vesicles derived from reactive lipids in the late 1970's and early 1980's this area has developed into a broad and active field of research.¹

In an analogous fashion to aggregation of the lipids, amphiphilic block copolymers can also aggregate in aqueous solution to form vesicular structures,³⁴⁻⁴⁵ as well as to a few other interesting structures, as shown in Figure 2.2.⁴⁶

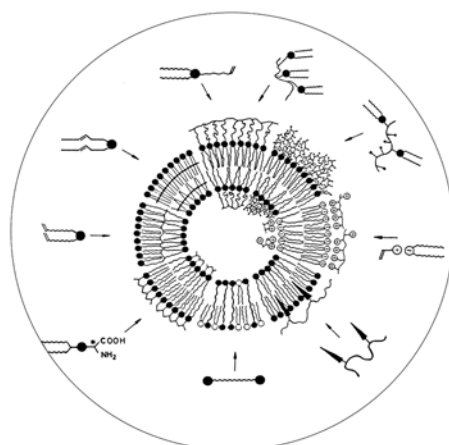


Figure 2.1 Schematic representation of the different possibilities to stabilize lipid vesicles. Adapted from reference.³²

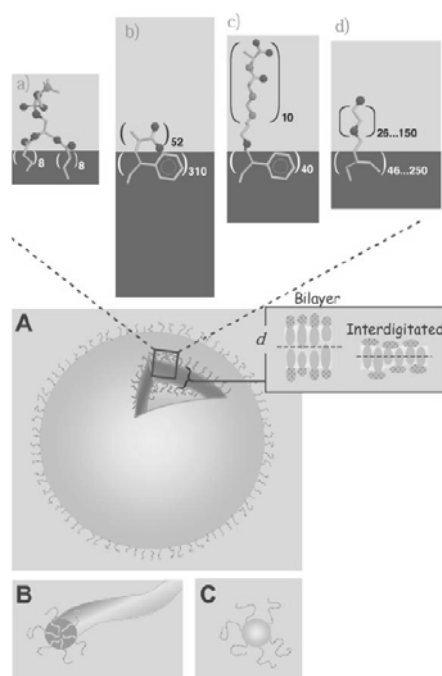


Figure 2.2 Schematic of a vesicle and related micellar aggregates plus vesicle forming molecules. (A) Vesicle with a section removed to reveal the membrane thickness d , represented by the dark gray regions for (a) a phosphatidylcholine lipid as a typical, natural liposome former; (b) a diblock copolymer of polyacrylic acid -block- polystyrene (PAA-*b*-PS), which precipitates as vesicles when water is added into the solvent; (c) PS-poly(isocyano-L-alanine-L-alanine), which makes vesicles in coexistence with rods under acidic conditions; and (d) a molecular weight series of nonionic polyethylene oxide-*b*-polybutadiene (PEO-*b*-PBD), which makes robust vesicles in pure aqueous solutions. As sketched in cross section, a vesicle membrane can be a bilayer with a well defined midplane, as is typical of a phospholipid membrane, or it can be a more interdigitated structure. Polydispersity in molecular size that is intrinsic to polymer amphiphiles would tend to give a more intermediate membrane structure. (B and C) A worm or rod like micelle and a spherical micelle, respectively, formed from block copolymers and related amphiphiles. Adapted from reference.⁴⁶

Although in some release applications such structures were rendered instable and degradable on purpose,⁴⁷ block copolymer vesicles are significantly more stable than those formed from conventional lipids due to the higher molecular weight and the slower dynamics of the constituent polymer molecules.⁴⁶

Even though block copolymer vesicles are stable enough by the weak non-covalent interactions that hold them together, the vesicles could also be modified with polymerizable groups similar to approaches to stabilize lipid vesicles. A subsequent polymerization of the resulting ‘macromonomers’ interconnects them via covalent bonds thus stabilizing the whole particle.¹ Such block copolymer based nanocapsules can be expected to possess great potential for encapsulation and controlled release from their interior. This is especially so, since the physical properties of their polymer shells can be controlled to a large extent by the block lengths, the block length ratio or the chemical constitution of the constituent polymer molecules.

A simple one-step procedure has been developed by Meier *et al.* to prepare vesicular structures from poly(2-methyloxazoline)-*block*-poly(dimethylsiloxane)-*block*-poly(2-methyloxazoline) (PMOXA-PDMS-PMOXA) triblock copolymers directly in aqueous solution.⁴⁸ The size of the resulting vesicles could be controlled in the range of 50 to 500 nm. The triblock copolymers used were modified with polymerizable methacrylate end-groups without changing their aggregation behavior in water. These ‘macromonomers’ were polymerized within the vesicles using a UV-induced free radical polymerization as shown in Figure 2.3.⁴⁸

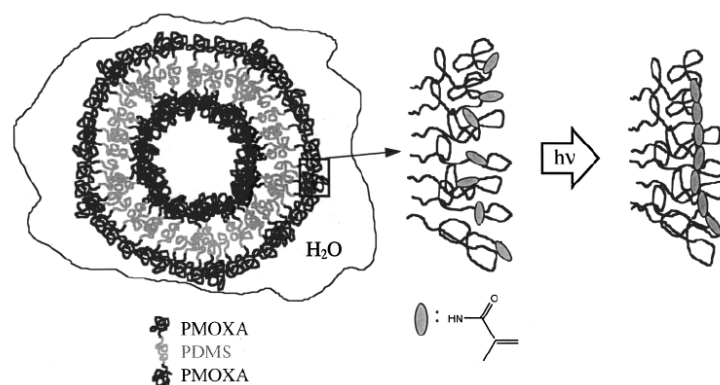


Figure 2.3 Schematic representation of a PMOXA-PDMS-PMOXA triblock copolymer vesicle in water and of the intravesicular cross-linking of the individual polymer molecules to a nanocapsule through UV irradiation of the polymerizable end groups of the triblock copolymers. Adapted from reference.⁴⁸

The polymerization did not lead to any measurable changes in the size, size

distribution or even mass of the particles. Obviously the polymer chain reaction occurs mainly intravesicularly. Intervesicle reactions like intervesicular exchange of individual triblock copolymer molecules or a chain propagation reaction involving more than one vesicular aggregate play only a minor role during the time scale of the experiment.⁴⁸

A similar concept uses just the “skeleton” of the vesicular aggregates as a template.^{49–56} (Figure 2.4a)

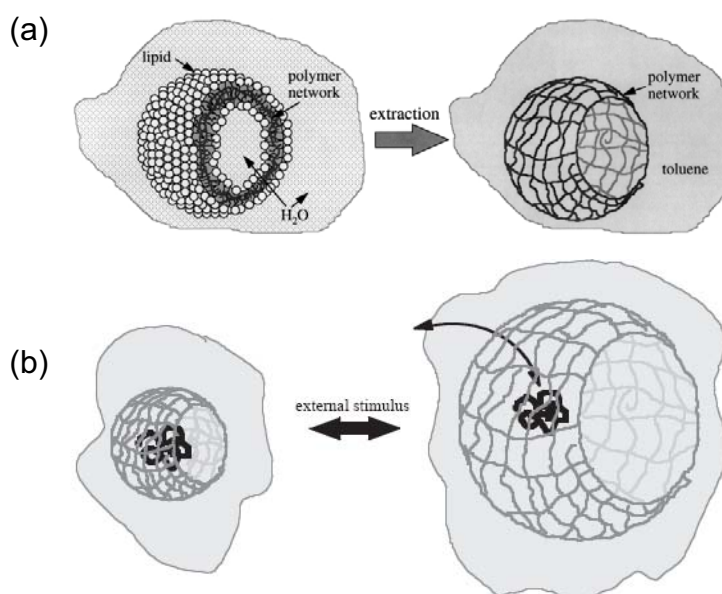


Figure 2.4 (a) Isolation of hydrophobic polymer hollow spheres formed by polymerization within monomer swollen lipid bilayers of vesicles. (b) Reversible swelling of polyelectrolyte nanocapsules fabricated using the method in (a) and release of encapsulated material. Adapted from reference.^{55, 57}

In this case the amphiphilic molecules just provide a geometrically restricted environment for dissolving and polymerizing conventional monomers. It is well known that vesicles or liposomes are able to solubilize hydrophobic substances to a certain degree. Such compounds are usually dissolved in the hydrophobic part of the lipid bilayer. If such substances also carry polymerizable groups, their subsequent polymerization should lead to the formation of polymer chains entrapped in the interior of the membrane. In contrast to polymerizable lipids, the polymer chains are now simply dissolved within the alkane part of the bilayer forming lipids (Figure 2.4a). Hence, they are of minor influence on the overall physical properties of the membranes. Using this approach, a polymer network consisting of polyelectrolytes that respond to an external stimulus, *e.g.* pH, was formed and substances were

encapsulated into and released from the interior of the network based on the change in pH (Figure 2.4b).⁵⁷

It is well-known that block copolymers may assemble to polymeric micelles with diameters in the 10 to 100 nm range. These block copolymers can be modified such that either the interior or the exterior blocks within the micelles contain polymerizable groups. For example poly(isoprene)-*block*-poly(acrylic acid) (PI-PAA) diblock copolymers form micelles in aqueous solution with a PI core and a PAA shell. It has been shown that the PAA shell can be crosslinked with α, ω -diamino-poly(ethylene glycol) (Figure 2.5).⁵⁸

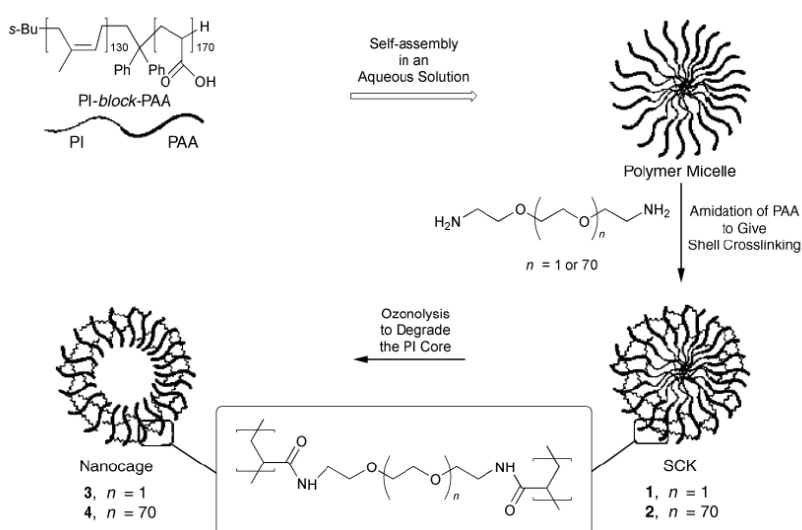


Figure 2.5 Procedure for the preparation of nanocapsules from amphiphilic diblock copolymers. The shell of the final nanocapsules consists of crosslinked poly(acrylamide). Adapted from reference.⁵⁸

Similarly, a poly(isoprene)-*block*-poly(2-cinnamoyl ethyl methacrylate)-*block*-poly(*tert*-butyl acrylate) (PI-PCEMA-PTBA) triblock copolymer forms micelles with a PTBA corona, PCEMA shell and a PI core in THF and methanol mixtures.⁵⁹ In this case the micellar structure could be locked in by UV crosslinking of the PCEMA within the micelles. Subsequently the PI cores of both the crosslinked PI-PAA and the PI-PCEMA-PTBA micelles could be degraded by ozonolysis into small fragments that diffuse into the surrounding solution and nanospheres with a central cavity are left behind as produced. A schematic representation of the whole process is given in Figure 2.5.⁵⁸ The potential of such systems for encapsulation of small molecules has been demonstrated by loading the crosslinked PCEMA-PTBA capsules with rhodamine B.⁵⁹ The incorporation of the dye into the central cavity of the particles

could directly be visualized by TEM. The degradation of the shell crosslinked PI-PAA micelles leads to water-soluble crosslinked poly(acrylamide) hollow spheres, which possess considerably larger hydrodynamic diameter of their shells after removal of the core.⁵⁸ The increase of the diameter from 27 to 133 nm was explained by the fact that the crosslinked poly(acrylamide) shells can be regarded as a hydrogel that swells when the core domain fills with water after removal of the PI. The diameter of the hollow sphere products depends sensitively on both the degree of polymerization of the block copolymers originally used to form the micelles and the nature of the crosslinking diamine used to prepare the shell crosslinked micelles.

In a number of applications, loading of vesicles was approached using a concept from nature, where cell membrane proteins allow for transport of various species to the inside of a cell, and for removal of compounds to the outside medium. Following this idea, incorporation of (cell) membrane channel proteins in the polymer vesicles' wall was performed by Meier *et al.* (Figure 2.6).⁶⁰⁻⁶⁶

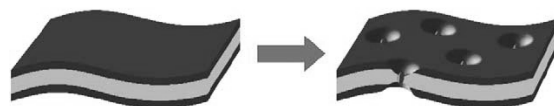


Figure 2.6 Channel protein incorporation into a block copolymer membrane. Adapted from reference.⁶⁰

Membrane proteins provide channels for transporting small molecules and ions, either specifically or non-specifically in natural cells. The transport may be directed or the substances can move freely in both directions via the channel.⁶⁷ Insertion of membrane proteins in polymer stabilized lipid membranes has been successful.⁶⁸ Recently, it has been shown experimentally that the incorporation of functional membrane proteins into block copolymer membranes is feasible, yet the question concerning the mechanism of such an insertion remains unanswered.⁶⁷ Several well-characterized channel proteins, *e.g.* OmpF⁶⁵ and LamB⁶¹, naturally found in Gram-negative bacteria were subject to those studies, which focused not only on the insertion of proteins themselves, but also on their functionality within the polymer membranes. A fully functional incorporation of porins into the artificial (non-physiological) environment of a polymer membrane was achieved.⁶⁷ Extending the idea, a pH sensitive enzyme acid phosphatase was chosen for encapsulation into the nanoreactor made from triblock copolymer membrane functionalized with bacterial OmpF pore proteins.⁶⁶ The resulting pores in the amphiphilic polymer membranes are known to remain fully functional and allow the passive diffusion of

polar molecules smaller than 600 Da through the channels of this trans-membrane protein.⁶⁹ A non-fluorescent water soluble substrate was then used to monitor the activity of the encapsulated enzyme at different pH environment (Figure 2.7).

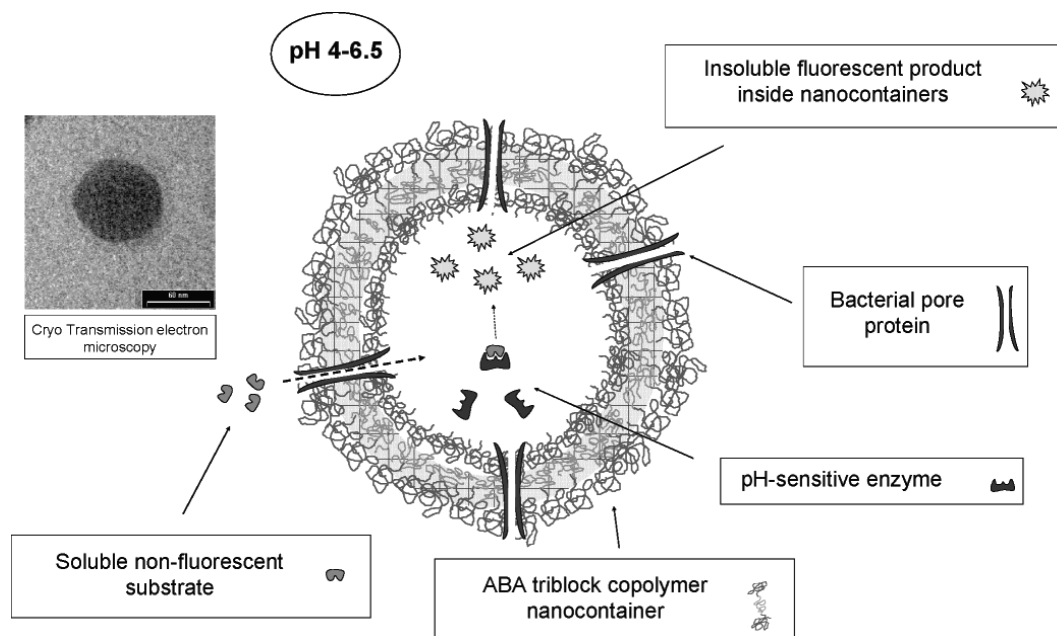


Figure 2.7 Two dimensional outline and visualization of the nanoreactor system: The nanoreactors are based on a synthetic triblock copolymer membrane functionalized with bacterial OmpF pore proteins that make intact, size-selective channels for passive diffusion across the membrane. Encapsulated acid phosphatase enzyme processes a non-fluorescent substrate into an insoluble fluorescent product at pH 4-6.5. Visualization of the final “nanoreactor” was done by cryogenic transmission electron microscopy, where a distinct core is surrounded by a fine halo, corresponding to the polymer membrane. Adapted from reference.⁶⁶

Experiments with the pH controlled nanoreactors showed a strong fluorescent signal when the nanocontainers with the integrated OmpF were tested near the optimum pH of the enzyme, while a series of experiments using containers lacking of such transporting properties or experiments under an unfavorable pH to the enzyme do not exhibit any fluorescent signal, as shown in Figure 2.8. This proof of concept of an externally triggerable nanoreactor is a step forward in equipping artificial nanosystems with an increasingly complex range of biological functionalities from plant and bacterial origin and has the potential for technical as well as biomedical applications.⁶⁶

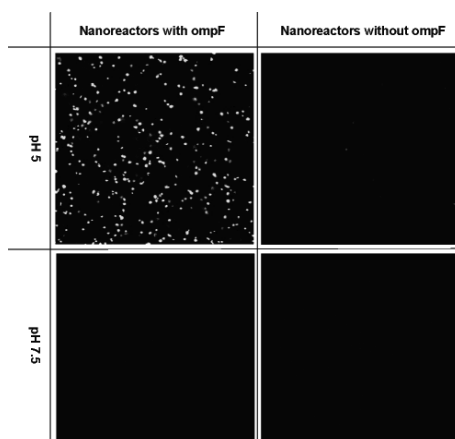


Figure 2.8 Channel- and pH-dependent nanoreactor activity: Active nanoreactors with *ompF* pores in the upper left panel show strong fluorescent activity at pH 5, whereas controls at pH 7.5 and without the *ompF* pores show no significant fluorescent activity in confocal microscopy after 3 h. The substrate concentration in this experiment was 75 μ M. Adapted from reference.⁶⁶

A new type of nanocontainers, made from the protein shell of a virus, also known as a capsid, was developed in the recent years.⁷⁰⁻⁷⁶ The virus capsid, which consists of several oligomeric structural subunits made of proteins, is used to enclose the generic material of the virus, and has been studied as a container.^{70-73, 77} The cowpea chlorotic mottle virus (CCMV) capsid, whose structure was well defined with a size of 20 nm and extensively studied,⁷⁸ was used to encapsulate enzyme horseradish peroxidase (HRP) as a model system to investigate single enzyme processes inside the container by Cornelissen *et al.*⁷⁷ CCMV capsids possess an interesting pH dependent assembly/disassembly property, as they dissociate into protein dimers at neutral pH (7.5) and re-assemble at low pH (5), shown in Figure 2.9.

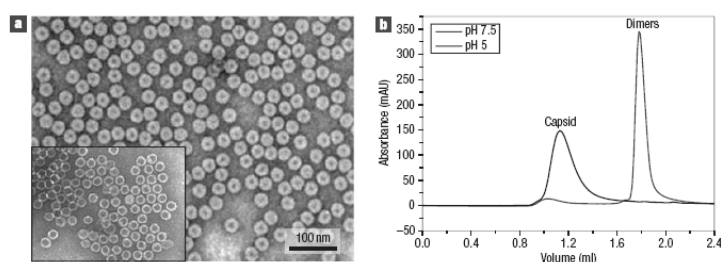


Figure 2.9 Characterization of CCMV and the empty CCMV capsid. (a) TEM (negative staining) of the CCMV virus and the empty capsid (inset). (b) Size-exclusion fast protein liquid chromatography (FPLC) of the CCMV protein at pH 5 (black curve) and at pH 7.5 (grey curve), illustrating the difference in the assembly behavior depending on the acidity of the solution. The protein forms capsids at pH 5, which fall apart into protein dimers when the pH is raised to 7.5. Adapted from reference.⁷⁷

Utilizing this property HRP was mixed with protein dimers at pH 7.5 and assembled into the interior of the capsid at pH 5 (Figure 2.10a).

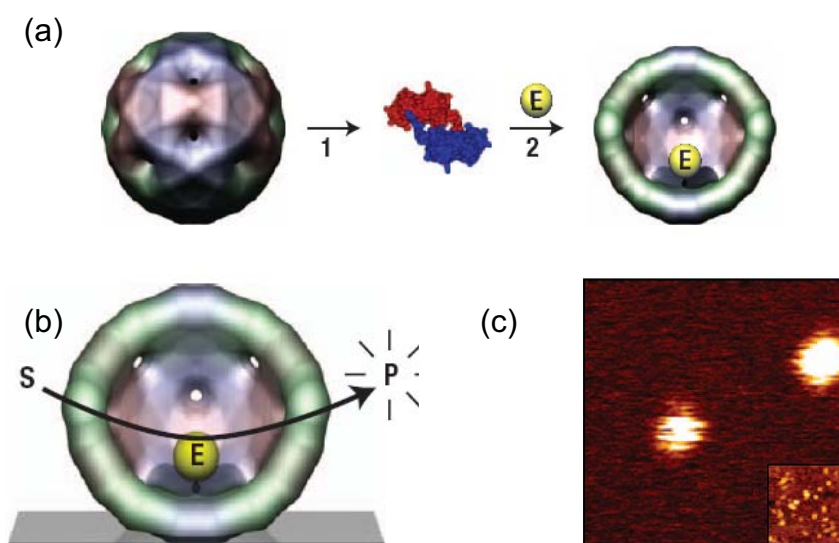


Figure 2.10 (a) Schematic pathway for inclusion of a protein or an enzyme in the CCMV capsid. After disassembling the CCMV capsid into dimers (step 1, pH 7.5), the guest protein (E) is added and the CCMV capsid assembled again by decreasing the pH (step 2, pH 5). (b) When HRP is encapsulated inside a capsid, substrate molecules (S) diffuse into the capsid and are subsequently converted to product molecules (P), which then accumulate before diffusing out through the capsid pores. (c) A typical confocal fluorescence image ($1.68 \mu\text{m} \times 1.68 \mu\text{m}$) showing the formation of a fluorescent product (rhodamine 6G) from a non-fluorescent substrate (dihydrorhodamine 6G) by HRP encapsulated inside a capsid. Inset: AFM image (to scale) at the same sample location, showing that only a small fraction of the capsids contain an active enzyme molecule. One in every 130 capsids is estimated to contain HRP. Adapted from reference.⁷⁷

The activity of HRP was monitored using a fluorogenic substrate. Substrates diffused through the pores of the capsid and reacted with HRP to form the highly fluorescent product. (Figure 2.10b) The reaction was then probed with confocal fluorescence microscopy. (Figure 2.10c) Further analysis of the fluorescence intensity fluctuation proved that the enzymatic reaction indeed occurred inside the capsid. The inclusion of enzyme molecules into the capsid is a potential pathway to study enzyme behavior at a single molecule level inside a nanocontainer.⁷⁷

2.2.2 The template directed assembly approach

Another possibility for generating polymeric nanocontainers is to form a polymer shell around a pre-formed template particle that can subsequently be removed, thus

leaving an empty polymeric shell. Several methods of realizing such a template synthesis of hollow polymer particles have been developed.⁷⁹⁻⁸⁹

A convenient way is to exploit the well-known polyelectrolyte self-assembly at template surfaces. This method utilizes a series of layer-by-layer deposition steps of oppositely charged polyelectrolytes.⁷⁹ Typically one starts with colloidal particles carrying surface charges (*e.g.*, a negative surface charge). Polyelectrolyte molecules having the opposite charge (*i.e.*, polycations) are readily adsorbed to such a surface due to electrostatic interactions. Not all of the ionic groups of the adsorbed polyelectrolyte participate in the electrostatic interactions with the surface. As a result the original surface charge is usually overcompensated by the adsorbed polymer. Hence, the surface charge of the coated particle changes its sign and is now available for the adsorption of a polyelectrolyte of the opposite charge (*i.e.*, a polyanion). As shown in Figure 2.11 such sequential deposition produces alternating polyelectrolyte multilayers,⁹⁰ the thickness of which can be exactly controlled by the number of deposition steps, *i.e.* the number of layers deposited onto the template.⁷⁹

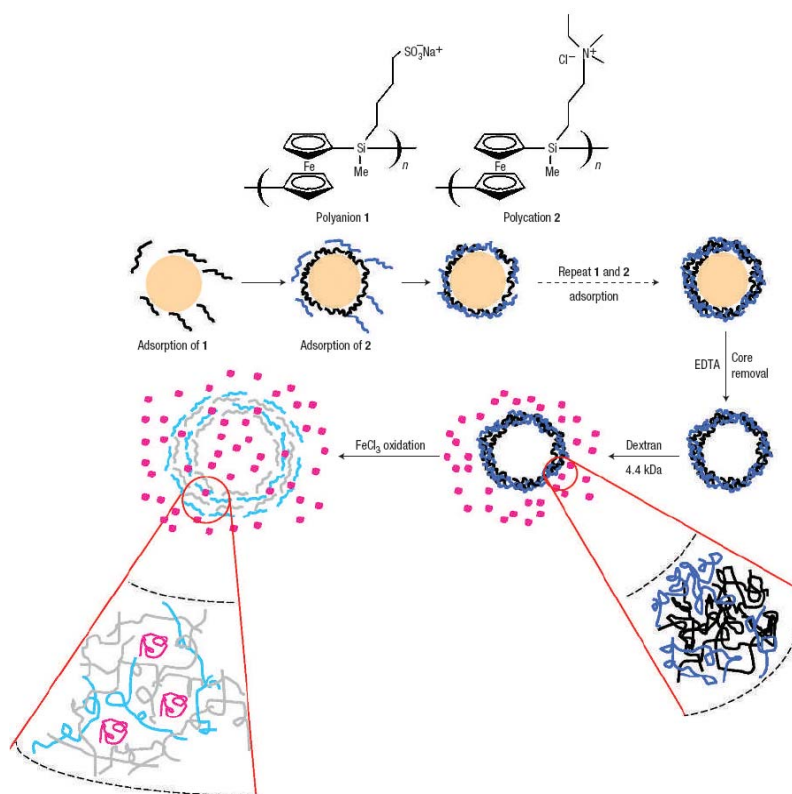


Figure 2.11 Schematic diagram of the formation of an organometallic multilayer capsule and the change in permeability of the capsules. Polyanion 1 (black lines) and polycation 2 (blue lines) were used in the electrostatic self assembly onto particle templates followed by core removal. The permeability of the capsules could be tuned via chemical oxidation (*e.g.* FeCl₃). Red bundles represent dextran. The varying colours of the polymer chains in the bottom left represent their different oxidational/conformational states. Adapted from reference.⁹⁰

It has been shown that capsules made by this approach allowed the storage and release of encapsulated molecules by an external stimulus, which is of key interest in bioengineering, nanotechnology and medicine. In a study carried out by Vancso *et al.*, water soluble polyferrocenylsilane (PFS) anions and cations were assembled via electrostatic interactions to form multilayer capsules onto manganese carbonate templates.⁹⁰ Hollow spheres were obtained after core removal (Figure 2.11).

The redox-control of the permeability of composite-wall capsules with five PFS⁻/PFS⁺ polyion pairs as inner layers and redox-insensitive polyelectrolyte pairs (PSS⁻/PAH⁺) in the outer layers was demonstrated using Confocal Scanning Laser Microscopy (CSLM) experiments (Figure 2.12). These capsules were robust and essentially impermeable to fluorescent dye-labeled 4.4-kdalton dextran molecules in the neutral state (Figure 2.12a, image 1). On oxidation (with FeCl₃ solution), the capsules started to become permeable, as indicated by the strong increase in the fluorescence intensity in the capsule interior (Figure 2.12a, image 2). During the course of the oxidation process of the PFS, an almost complete permeability of all capsules was observed (Figure 2.12a, image 3). The capsule integrity was preserved, as shown in Figure 2.12b by AFM.⁹⁰

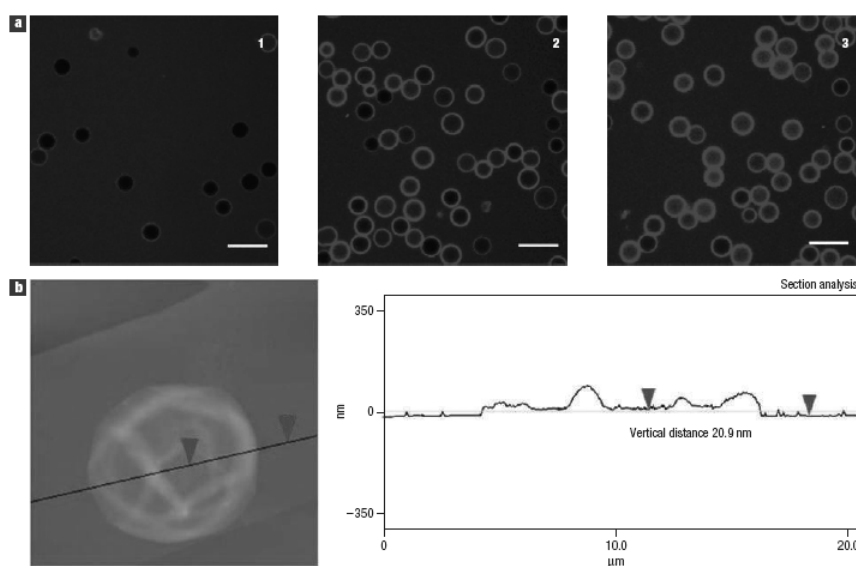


Figure 2.12 Redox-responsive permeability of multilayer capsules with organometallic–organic composite-wall structures. (a) Local oxidation of (PFS⁻/PFS⁺)₅ (PSS⁻/PAH⁺)₁ microcapsules by FeCl₃ (1 mM, pH = 4) monitored by CSLM. Capsules that are originally impermeable (1) to 4.4-kDa dextran molecules show partial permeability (2) in the early stage of oxidation (10 min) and almost complete permeability (3) after oxidation for more than 1 h. Scale bar = 20 μm. (b) Tapping-mode AFM height image of a (PFS⁻/PFS⁺)₅ (PSS⁻/PAH⁺)₁ capsule after oxidation for over 2 h by FeCl₃ (1 mM, pH = 4). The integrity of the capsules has been preserved. Adapted from reference.⁹⁰

2.2.3 The dendrimer approach

Dendrimers are highly branched cascade molecules that emanate from a central core through a step-wise repetitive reaction sequence. By design such a molecule consists of three topologically different regions: a small initiator core of low density and multiple branching units, the density of which increases with increasing separation from the core, thus eventually leading to a rather densely packed shell. Hence, at some stage in the synthesis of such a dendrimer the space available for construction of the next generation is not sufficient to accommodate all of the atoms required for complete conversion. Extending this principle in a more general fashion, dendrimers that have internal ‘cavities’ with a dense outer shell may be synthesized by controlling the chemistry of the last step, which terminates the stepwise growth. This has been demonstrated by the preparation of the fifth generation poly(propylene imine) dendrimer shown in Figure 2.13.⁹¹

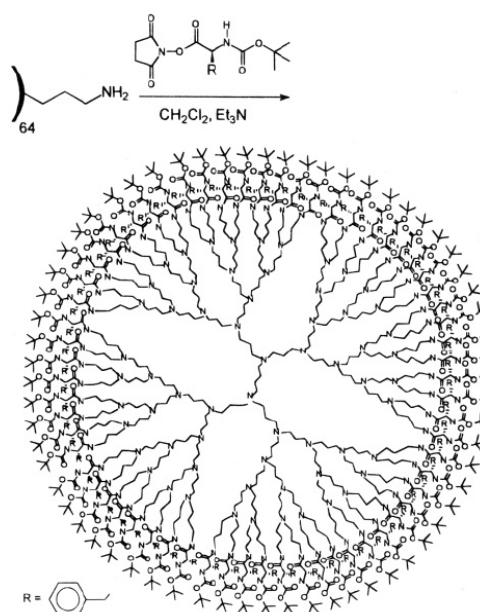


Figure 2.13 Schematic representation of a dendritic box which can encapsulate small guest molecules during the preparation. Adapted from reference.⁹¹

Due to their dense outer shell these molecules can be regarded as dendritic “boxes” that are capable of retaining guest molecules trapped during synthesis. Subsequent guest diffusion out of the box is slow since the dendrimer shell is close packed due to the bulky H-bonded surface groups. If the tertiary butyl groups were removed guest molecules could diffuse out of the boxes, but only if they were sufficiently small. For example Rose Bengal remained in the containers while *p*-nitrobenzoic acid leaked

out.⁹¹

Closely related to such dendritic boxes are amphiphilic dendrimers⁹² or hyper-branched polymers⁹³ consisting of a hydrophobic (hydrophilic) core and a hydrophilic (hydrophobic) shell. Due to their amphiphilic nature these systems are also selectively able to solubilize guest molecules within their core domain. The permeability of the outer shell to small molecules and ions could, for example, be exploited for a controlled synthesis of inorganic nanoparticles in the core region of a poly(amidoamine) starburst dendrimer.⁹⁴ While small Cu^{2+} ions could diffuse into the interior of the dendritic boxes the *ca.* 2 nm diameter Cu nanoparticles formed upon reduction were too bulky to leak out.

Dendrimers are, however, generally not real hollow polymer particle systems due to the fact that their core covalently links the ‘dendritic wedges’ of the molecule. It is obvious that this core part is of crucial importance for the integrity of the whole molecule. Hence, removing the core requires another connection between the outer zones of the molecule. Indeed, applying similar concepts as reported by Wooley⁹⁵ and Liu⁹⁶, it is also possible to produce real hollow structures from dendrimers. This has recently been demonstrated using a polyether dendrimer with a trimesic acid ester core.⁹⁷ This polymer contains three cleavable ester bonds at its core and robust ether bonds throughout the rest of the molecule. As shown schematically in Figure 2.14 hollow particles were formed by selective crosslinking of homoallyl ether groups at their periphery and subsequent degradation of the core region by hydrolysis.

An interesting possibility offered by this method is that the remaining functional groups in the interior of the container system could serve as ‘endo-receptors’ available for molecular recognition. This approach allows a high control over the size and geometry of the formed nanocapsules. However, the preparation of these particles requires a rather costly and tedious procedure which clearly presents a limiting factor for possible applications.

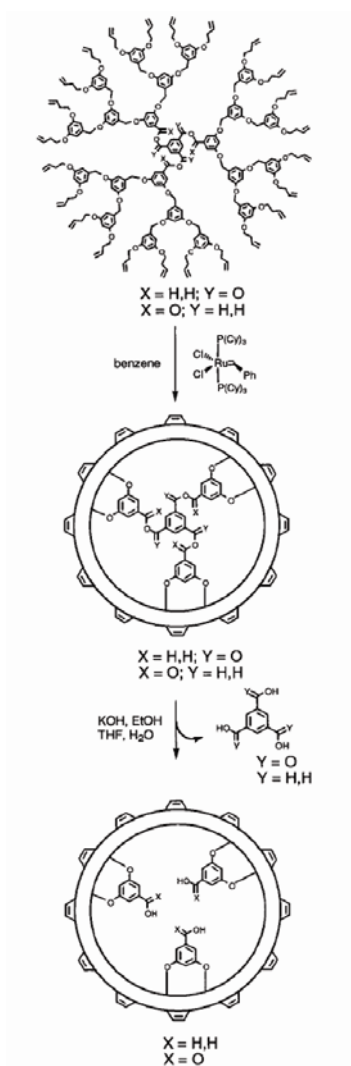


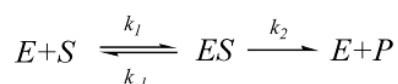
Figure 2.14 A schematic showing the preparation of a cored dendrimer. Adapted from reference.⁹⁷

2.3 Enzymatic reactions and enzyme kinetics

Chemical transformations carried out in living systems are usually accelerated by enzymes. Enzymes are biological macromolecules that catalyze the conversion of one or more compounds (substrates) into one or more different compounds (products).⁹⁸ Enzyme catalysis can produce rate enhancement by as high as a factor of 10^{19} ,⁹⁹ while involving molecular recognition at the highest level of development.¹⁰⁰ The reason that enzymes enhance reaction rates was originally proposed to be a decrease of the activation energy towards the transition state of the substrate.¹⁰¹ Now this concept in enzyme catalysis is expanded based on the advancement in transition state theory, due to the development of new

experimental tools for studying the structure and kinetics of enzymes, as well as computer simulations. Kinetic analyses become more and more important since they allow one to reconstruct the number and order of the individual steps in the reaction mechanism. The study of enzyme kinetics also represents a principal way to identify potential therapeutic agents that can selectively enhance or inhibit the rates of specific enzyme catalyzed processes.⁹⁸

The Michaelis-Menten theory is widely used to describe and quantify enzymatic reactions.¹⁰² In this theory, the enzymatic reaction cycle is divided into two elementary reaction steps: a reversible substrate binding step (k_1 , k_{-1}) between the enzyme (E) and the substrate (S) to form an intermediate enzyme-substrate complex (ES) and the catalytic step (k_2) to generate the product (P) and to release the enzyme.



The rate of consumption and formation of the ES complex can be expressed by the following equation:

$$\frac{d[ES]}{dt} = k_1[E][S] - k_{-1}[ES] - k_2[ES] \quad (2.1)$$

The square brackets refer to concentrations. Using the steady state approximation and rearranging (2.1) one obtains

$$\frac{[E][S]}{K_M + [S]} = [ES] \quad (2.2)$$

where K_M is the Michaelis-Menten constant defined as

$$K_M = \frac{k_{-1} + k_2}{k_1} \quad (2.3)$$

The initial rate of the reaction V_i can be obtained by the Michaelis-Menten equation (in the absence of inhibitor):

$$V_i = \frac{V_{\max}[S]}{K_M + [S]} \quad (2.4)$$

The initial rate of the reaction is zero for $[S] = 0$ and reaches a maximum value, V_{\max} , at high $[S]$ values. If $[S] = K_M$ then the value of the reaction rate becomes $1/2 V_{\max}$. As the reaction rate changes with the substrate concentration, usually the initial rate of the reaction is used to characterize enzyme kinetics. The Michaelis-Menten equation can provide a faithful description for most enzyme kinetics without inhibition on an ensemble level. However, in a time-dependent

process, the actions of different enzyme molecules are not synchronized. Any uncommon effects or phenomena will be averaged out during measurements on the ensemble.

Owing to the development of single molecule detection (SMD) techniques,¹⁰³⁻¹⁰⁵ single enzyme kinetics were probed and unusual phenomena of reaction kinetics were observed in a few studies.¹⁰⁶⁻¹¹³ In these studies, fluctuations of the rate constants of single enzyme molecules over orders of magnitude were revealed for various enzymes.¹⁰⁶⁻¹¹³ The correlation between single enzyme turnover times, which is the time needed for a single enzyme to complete one catalysis cycle, shows that a much longer characteristic correlation time is present, which is orders of magnitude longer than the typical cycle time.¹⁰⁶⁻¹¹³ This correlation suggests a coupling between the catalytic reaction and other process(es) that is characterized by longer time scales.

Conformational changes of enzymes are sensitively linked to the catalytic activity of enzyme molecules¹¹⁴ and take place over longer time scales compared to the enzymatic reaction.^{115, 116} The observation of rate fluctuations was attributed to a combination between the mentioned slow conformational changes and the fast transition kinetics which is explained in Kramers' model.¹¹⁷ In this model the reactant is taken to be trapped in a one-dimension potential well that is separated by an energy barrier with a certain height from another deeper well representing the product state. The model allows the calculation of the distribution of waiting times (time between reaction cycles), which follows a single exponential decay.

In the next section, a few examples of experimental findings on rate fluctuations in single enzyme kinetics will be discussed, emphasizing the correlation between single enzyme turnover times, the observation of dynamic disorder, which refers to the fluctuation in turnover rates of an individual enzyme, and how this is attributed to slow conformational changes of the enzyme.

2.4 Brief overview of studies on single enzyme kinetics

2.4.1 Distribution of turnover times of enzymes reveals fluctuations in reactivity

In a comprehensive review on single molecule approaches to enzymology,¹¹⁸ Xie emphasizes that single molecule detection (SMD) experiments yield new information on biochemical systems that cannot be obtained by conventional

ensemble experiments, a statement that is supported by other reports in the literature:¹⁰⁶⁻¹¹³

1. Direct measurements of distributions of various molecular properties can be obtained, in contrast to the ensemble-averaged values of the respective property. The obtained distributions can either arise from heterogeneity in the system or from dynamic fluctuations on sub-measurement timescales;
2. Enzymatic processes can be followed in real-time and one can also distinguish among different intermediate states in the overall process;
3. Statistical analyses of the obtained experimental signals provide detailed information about the systems' molecular dynamics that can not be obtained in any other way.

However, the corresponding chemical reactions occur on very short timescales (picoseconds or faster) and cannot be directly detected because no analytical technique developed to date has sufficient time resolution to do so.¹¹⁸ On the other hand, the time interval between the events of interest (the so-called waiting time) is longer and can hence be detected using conventional analytical techniques, such as fluorescence spectroscopy. Statistical analyses of these waiting time trajectories yield valuable information about the system, including information about system dynamics and reaction kinetics.¹¹⁸ In this section, the work of Xie and co-workers¹⁶ on the oxidation of cholesterol using cholesterol oxidase (COx) will be discussed to establish a link between single molecule observations and results for the conventional ensemble experiments on enzyme kinetics.

In the case of the cholesterol oxidase,¹¹³ the intrinsic fluorescence properties of the flavin adenine dinucleotide (FAD), which is part of the active catalytic site of COx, is used to study the enzymatic process on the single molecule level. The reaction scheme for the oxidation of cholesterol using COx is shown in Figure 2.15.

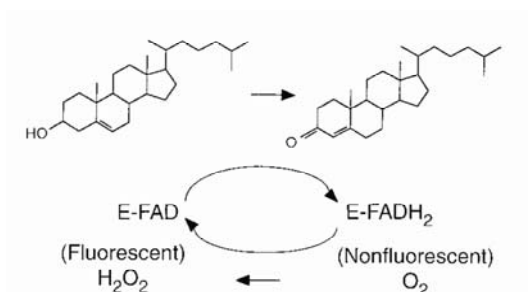


Figure 2.15 Reaction scheme for the oxidation of cholesterol to cholesterolone catalyzed by cholesterol oxidase (COx). Adapted from reference.¹¹³

It is known that the oxidation reaction obeys the Michaelis-Menten mechanism. During the reaction, the active site of COx switches between its oxidized (E-FAD, fluorescent) and reduced (E-FADH₂, non-fluorescent) state. The fluorescent state is referred to as the “on” state and the non-fluorescent state as the “off” state of the enzymatic turnover cycle (TOC), respectively. The FAD structural unit itself is non-covalently and tightly bound to the centre of the COx and the active site is surrounded by hydrophobic pockets for binding cholesterol molecules.¹¹³ On a single (enzyme) molecule scale it is meaningless to define the enzyme concentration required for evaluation of the Michaelis-Menten mechanism; instead, it is more appropriate to consider the probability $P_E(t)$ of finding the single enzyme molecule in an catalytically active state at any time t during the process. The same holds for the enzyme-substrate complex ES and any other (intermediate) states involving the enzyme.¹¹⁸ Equation (2.1) for ensemble reaction kinetics is then re-written in terms of probabilities:

$$\frac{dP_{E-FAD\bullet S}(t)}{dt} = k_1' P_{E-FAD}(t) - k_{-1} P_{E-FAD\bullet S}(t) - k_2 P_{E-FAD\bullet S}(t) \quad (2.5)$$

where $k_1' = k_1[S]$ represents the combined reaction rate constant. In contrast to ensemble kinetics, this relation holds for both high and low values of $[S]$ (*i.e.* the pseudo first order approximation is always valid in single molecule kinetics).¹¹⁸ An analogous expression is obtained for the probability function of the enzyme:

$$\frac{dP_{E-FADH_2}(t)}{dt} = k_2 P_{E-FAD\bullet S}(t) \quad (2.6)$$

The probability distribution of on-times, $p_{on}(\tau)$, considers the probability that the reaction occurs within the time interval between $t = \tau$ and $t = \tau + \Delta t$.

$$p_{on}(\tau) = \left. \frac{dP_{E-FADH_2}(t)}{dt} \right|_{t=\tau} = k_2 P_{E-FAD\bullet S}(\tau) \quad (2.7)$$

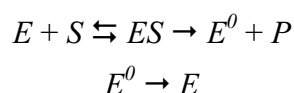
which is solved for $P_{ES}(t)$ by Laplace transformation and using initial conditions $P_E(0) = 1$ and $P_{ES}(0) = 0$:

$$p_{on}(\tau) = \frac{k_1' k_2}{k_2 - k_1'} (e^{-k_1' \tau} - e^{-k_2 \tau}) \quad (2.8)$$

From equation (2.8) it is seen that $p_{on}(\tau)$ has an exponential rise followed by an exponential decay.

In the example of cholesterol oxidation, the COx switches between the oxidized and reduced state via an intermediate state (denoted with E^0) according to the “ping-pong” mechanism.⁹⁸ For a proper description of the overall reaction, the reaction equation is hence expanded with an additional step taking into account the

intermediate state:



In the actual experiments, a He-Cd laser was used to excite the FAD units in COx (immobilized in agarose gel) at a wavelength of 442 nm. The fluorescence emission of FAD was recorded with high efficiency at 520 nm (Figure 2.16).^{113, 118} A solution of the substrate cholesterol ($[S] = 0.2$ mM) and saturated oxygen ($[O_2] = 0.25$ mM) were fed to the gel. An on/off behaviour in the fluorescence emission of FAD was observed, indicating the switching between the oxidized and reduced states of FAD and, hence, the occurrence of cholesterol oxidation.¹¹³ Trajectories of more than 500 TOCs and 2×10^7 emitted photons (detection efficiency 10 %) were recorded.

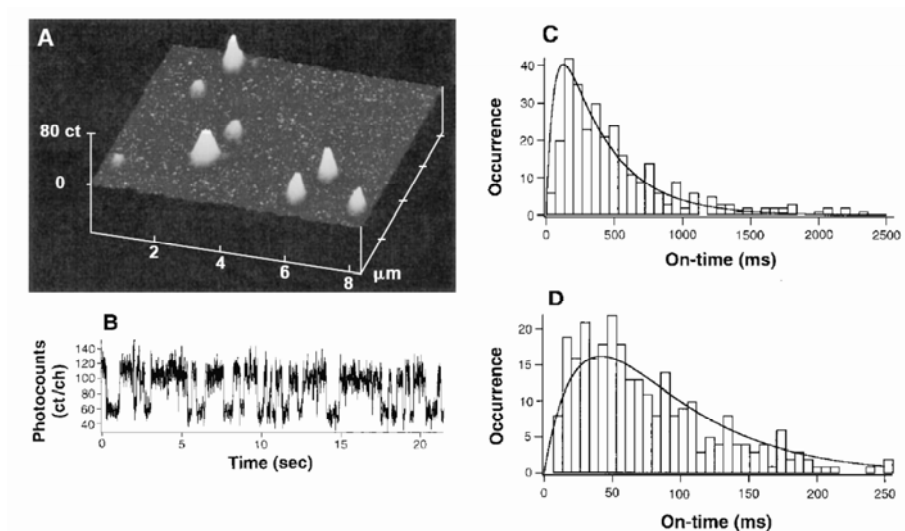


Figure 2.16 (A) Fluorescence microscopy image ($8 \mu\text{m} \times 8 \mu\text{m}$) of single COx molecules immobilized in a $10\text{-}\mu\text{m}$ -thick film of agarose gel of 99% buffer solution (pH 7.4). The emission originates from the fluorescent active site, FAD, which is tightly bound to the centre of COx. (B) Real-time record of TOCs for a single COx molecule with a cholesterol concentration of 0.2 mM. (C) On-time distribution diagram derived from (B) and (D) on-time distribution diagram of another COx molecule recorded at 2 mM cholesterol. The fit is based on eq. (2.8). Adapted from reference.¹¹³

A part of the resulting (real-time) data is shown in Figure 2.16B which displays the number of photons that was recorded during a certain time interval. A more detailed discussion of this type of recordings will be provided in the next section. The average TOC did not decrease with time because substrate (cholesterol) and oxygen were present in large excess compared to the enzyme.

From this real-time recording of fluorescence emission events, on-time distribution diagrams can be derived for each individual single COx molecule (Figure 2.16C, D). Figure 2.16D shows a non-exponential distribution. This does not obey Poisson statistics, which expresses the probability of a number of events occurring in a fixed period of time if these events occur with a known average rate and independent of the time since the last event. Generally, such a non-exponential behaviour of the waiting time distribution implies the existence of more complex underlying reaction mechanisms. As already mentioned before, for COx (and, in fact, many other enzymes) this is indeed the case: during the course of the reaction the enzyme passes through an intermediate stage.¹¹³ Hence, from the shape of the on-time probability distribution, details about the mechanism of and the number of intermediate steps in an enzyme-catalyzed reaction can be derived. In general, when the enzymatic reaction occurs via one or more intermediates $E^0, E^1, E^2, \dots, E^n$, and when the interconversion rate constants for the different conformations are approximately the same in magnitude (say, $\langle \gamma \rangle$ on average), the probability distribution becomes

$$p(\tau) = \frac{\langle \gamma \rangle^n \tau^{n-1} e^{-k\tau}}{(n-1)!} \quad (2.9)$$

This distribution converges to a Gaussian distribution of on-times for large values of n .¹¹³ For the oxidation of cholesterol by COx, it is assumed that $k_{-1} = 0$ in equation (2.5). The other parameters in the probability distribution equation (2.9) are estimated by regression analysis of each individual waiting time distribution diagram.¹¹³

Static disorder refers to heterogeneity in the system which leads to different reaction rates for different enzyme molecules. Dynamic disorder, on the other hand, refers to differences in the reaction rates of individual enzyme molecules observed over different TOCs. Dynamic disorder is an intrinsic property of enzymes which can be observed experimentally through the so-called memory effect (meaning that the properties of the enzyme in a certain cycle are still affected by the previous cycle(s) of that enzyme) which leads to non-Markovian behaviour of the system.^{113,}

¹¹⁸ In a typical Markovian system the probability of crossing the energy barrier from one state to the other depends only on reactant state and barrier height according to Kramers' model, *i.e.* no correlation between consecutive turnover times is expected. The memory effect is taken into account in statistical analyses by applying the autocorrelation function on the experimental data. In a subsequent

work, published by Xie *et al.*, it was demonstrated that the mean waiting time $\langle \tau \rangle$, which is found in single molecule experiments, in fact, obeys a Michaelis-Menten type behaviour, even in the presence of dynamic disorder:¹¹²

$$\frac{1}{\langle \tau \rangle} = \frac{\langle k_2 \rangle [S]}{[S] + C_M} \quad (2.10)$$

where $\langle k_2 \rangle$ denotes the weighed mean value of the k_2 values for all catalytically active conformations. $C_M = (\langle k_2 \rangle + k_{-1})/k_1$. In the absence of dynamic disorder, $\langle k_2 \rangle = k_2$ and $C_M = K_M$.

The existence of dynamic disorder was proven by Xie and co-workers using SMD.¹¹³ 2-D histogram plots were composed in which the probability distribution for pairs of on-time states from 33 COx molecules was visualized (Figure 2.17).

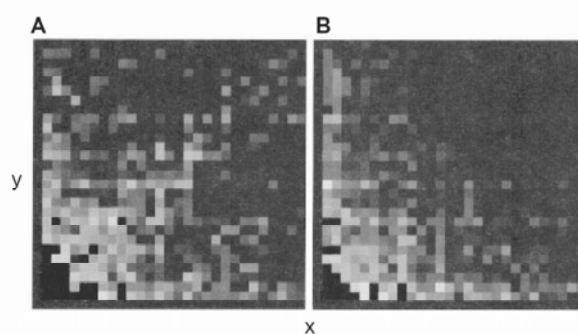


Figure 2.17 2-D histograms displaying the probability distribution for pairs of on-time states of COx molecules, for (A) pairs of adjacent on-time states and for (B) pairs of on-time states separated by 10 TOCs. The scale of x and y axes are from 0 to 1s. Adapted from reference.¹¹³

Two situations were compared: 1. the pairs consisting of on-time states adjacent to each other (Figure 2.17A), and 2. the pairs consisting of on-time states that were separated by 10 TOCs (Figure 2.17B). In case of Markovian behaviour, the two distributions would be identical, since one particular on-time event does not depend on a second one. However, the histograms in Figure 2.17 are clearly different, indicating a correlation between two successive on-time states for COx-catalyzed oxidation of cholesterol. This feature evidences the existence of a memory effect and, hence, dynamic disorder within this system. The dynamic disorder was attributed to structural fluctuations around the FAD active site in COx, which was evidenced by fluctuations in the fluorescence emission spectra of COx in the absence of cholesterol.¹¹³ Note that this is in full agreement with the existence of an intermediate state of the enzyme, which was found experimentally.

2.4.2 Stretched exponential decay and correlations in the activity of enzymes

The evaluation of experimental results to obtain information on enzyme kinetics on a single molecule level is nicely illustrated in a series of papers by Flomenbom *et al.*^{119, 120} These authors have studied the catalytic activity of the lipase B from *Candida Antarctica* (CALB) in the hydrolysis of the acetoxymethyl ester of 2',7'-bis-(2-carboxyethyl)-5(/6)-carboxyfluorescein. Upon hydrolysis, this non-fluorescent ester yields a highly fluorescent carboxylic acid as reaction product. The formation of this product was followed by confocal microscopy. The presence of fluorescent product in the confocal beam was designated the “on” state and the absence of it designated the “off” state, respectively. Long photon count trajectories could be measured because only the depletion of the substrate was a limiting factor in these experiments.¹²⁰

From the recorded diagrams of photon counts versus elapsed time, probability density functions for both the on and off states were composed. The difference between the on and off states in the continuous photon count signal (assigned with $a(t)$) that was obtained was made by assigning a threshold value a^* . The on state was characterized by a value $a(t) \geq a^*$ and the off state by $a(t) < a^*$, respectively. The threshold value a^* was estimated from the statistical analysis of the probability density function, which allowed for distinguishing between photon emission originating from product molecules and background signals (Figure 2.18).¹¹⁹

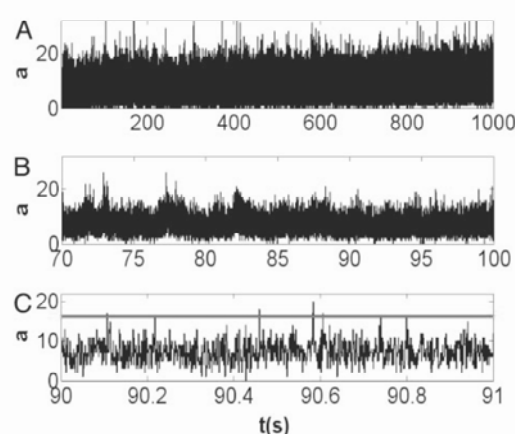


Figure 2.18 Photon count trajectory and its analysis. (A) A photon count trajectory as a function of time ($\Delta t = 1$ ms) of a single CALB during catalysis. (B and C) Zooming into segments of the trajectory in A. A local threshold value is shown in C. Adapted from reference.¹¹⁹

The probability density function for the off state, as resulting from the above photon count trajectories, was reported to be best fitted by a stretched exponential function:

$$\phi_{off}(t) = \phi_0 e^{-(t/\tau)^\alpha}; \phi_0 = 1 / \int_0^\infty e^{-(t/\tau)^\alpha} dt = \frac{\alpha/\tau}{\Gamma(1/\alpha)} \quad (2.11)$$

In this equation, $\Gamma(x)$ represents the gamma function and the value of the normalization factor ϕ_0 is valid when assuming the stretched exponential behaviour can characterize the process for all times ($t \rightarrow \infty$). The stretched exponent α and decay time τ are independent of the substrate concentration within the investigated range. It should be noted that the pair α and τ , rather than each of the parameters alone, is the relevant quantity when describing the stretched exponential behaviour.^{119, 120} It was concluded that the stretched exponential behaviour that was observed does not originate from any anomalous diffusion of the substrate to the CALB, because all experiments were run at saturation levels of the substrate concentration (as shown in reference¹¹⁹, $[S] > 0.6 \mu\text{M}$). It was reported that in this case, $\alpha = 0.15$ and $\tau = 1.15 \mu\text{s}$. Further analysis shows that the stretched exponential behaviour is, in fact, a cumulative effect of simple exponential events that occur, each of them contributing to the ensemble.¹¹⁹ Based on this observation and autocorrelation analysis, it was concluded that several catalytically active conformations of the CALB exist, analogous to the observations of Xie and co-workers in their study of COx (Figure 2.19).¹¹³ This observation, in fact, is a common feature in enzyme catalysis, being unravelled only by SMD.

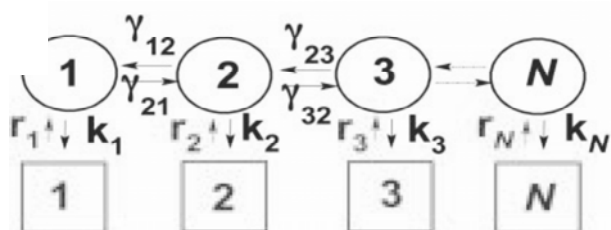


Figure 2.19 A schematic model of the enzymatic process. The off state consists of a spectrum of N -coupled substrates. Also indicated are the coupling rates between the conformations and the enzymatic reaction rates. Adapted from reference.¹¹⁹

In conclusion, single molecule optical experiments were shown to comprise powerful methods to unravel the mechanism and dynamics in enzymatic reactions. Experimental results, together with theoretical and computational studies have provided new insight into how the fluctuations of enzyme conformations modulate the catalytic behaviour of enzymes, which cannot be obtained otherwise from conventional ensemble studies. The existence of dynamic disorder of single enzymes does not affect the dependence of the enzymatic rates of substrate

concentration as predicted by the Michaelis-Menten theory. The single molecule Michaelis-Menten equation, which is reformulated in terms of a time perspective instead of a rate perspective, reconciles single molecule and ensemble average kinetics.^{25, 26}

Although the exploration of the field has only recently started, the experiments described here can already provide a good understanding of the processes leading to non-Markovian fluctuations. This also includes the dynamic disorder in single enzyme reactions and even the correlation between the single molecule kinetics and infinite-time limit as expressed by the Michaelis-Menten kinetics. We believe that future research will in part focus on the study of single enzyme reactions in *confined geometry*. It is well known that there are a variety of situations in which a reaction occurs when the reaction volume is too small to permit the use of infinite-space theories of chemical kinetics.²⁷ Recently, single enzymes were successfully encapsulated into enclosed volumes on the order of atto-litres created either by liposomes¹¹, block copolymer vesicles (see Chapter 5 and Chapter 6)¹²¹ or virus capsid particles.⁷⁷ By systematically altering the physics of the confined environment, additional insight into single enzyme dynamics may be obtained.

2.5 Reaction kinetics in confined geometries

There are a handful of experimental conditions in which a reaction takes place when the volume of the system is too small to allow the use of conventional infinite space theories of chemical kinetics.¹²²⁻¹²⁵ In such cases, a reaction cannot be modeled by an infinite volume with a constant density, *i.e.* constant concentration of molecules inside it. Examples are micellar and vesicular systems,¹²⁶⁻¹²⁸ polymer coils in solution,¹²⁹ zeolite structures,¹³⁰ porous materials,¹³¹ silica gels¹³² and nanoparticles.^{133, 134} Common to these systems is that reactant molecules occupy space in restricted geometries. The reaction kinetics in such systems differs from the kinetic behavior in infinite space. The mathematical approach of “classical” deterministic modeling does not account for the fluctuation of the concentration of reactant species. However, in systems containing a small number of interacting species a relatively large fluctuation in the number of reactants is inherent. Therefore, the partitioning of the reagent species in small volume and the small number of the species present in each individual volume make it difficult to apply classical chemical kinetics to describe the

temporal course of individual reactions in restricted geometries. A study of the kinetic peculiarities of chemical processes in restricted systems may thus provide important information on their structures and dynamics.²⁷

2.5.1 Modeling a reaction inside a sphere

A diffusion-controlled bimolecular reaction inside a restricted sphere volume was first considered by Khairutdinov *et al.*²⁷ This model system can be viewed as a good approximation to the reactions taking place inside block copolymer vesicles. For a bimolecular reaction between the reactant molecules A and B , the survival probability $p(r, t)$ at time t for the $(A...B)$ pair, whose initial separation is r , satisfies the following differential equation and boundary conditions:

$$\frac{\partial p(r, t)}{\partial t} = D\nabla^2 p(r, t) \quad (2.12)$$

$$p(r, 0) = 1 \quad (2.13)$$

$$p(d, t) = 0 \quad (2.14)$$

$$\left[\frac{\partial p(r, t)}{\partial r} \right]_{r=R} = 0 \quad (2.15)$$

For the sake of simplicity, molecule B is assumed to be fixed at the center of the sphere and the other can diffuse with diffusion coefficient D equal to the sum of the coefficients of the two reactants. A schematic of the reaction is shown in Figure 2.20.

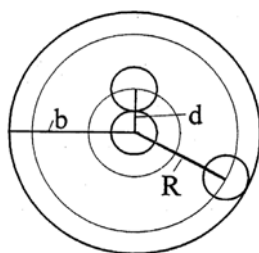


Figure 2.20 Schematic representation of the reaction between a pair of reactants inside a sphere. Small circles of radius $d/2$ and the large circle of radius b represent the volume of reactant and sphere, respectively. Adapted from reference.²⁷

The term on the right hand side of equation (2.12) describes the random motion of A with respect to B . The next equation (2.13) is the initial condition. Equation (2.14) states that A and B react instantaneously on approaching each other to a distance d .

The last equation (2.15) takes into account the reflection of A when it reaches the periphery of the sphere.

The problem of bimolecular reaction kinetics inside the sphere volume in the above formulation was then solved by Khairutdinov *et al.*²⁷ using the solution of a similar problem, 3D heat flow survival probability, obtained by Carslaw and Jaeger.¹³⁵ $p(r, t)$ can be calculated using equation (2.16):

$$p(r, t) = \sum_{i=1}^{\infty} G_i(r) \exp(-\alpha_i^2 \frac{Dt}{R^2}) \quad (2.16)$$

where

$$G_i(r) = \frac{2d \sin\left[\alpha_i \frac{r-d}{R}\right]}{\alpha_i r \left(\frac{\alpha_i^2}{1 + \alpha_i^2} - \frac{d}{R}\right)} \quad (2.17)$$

and α_i are the positive roots of the equation:

$$\tan\left(1 - \frac{d}{R}\right)\alpha = \alpha \quad (2.18)$$

In a general case where a sphere contains one B molecule and a number N of A molecules that move mutually independently, the survival probability $P(t)$ can be written as a product of the survival probabilities of all ($A...B$) pairs:

$$P(t) = \prod_{i=1}^N p(r_i, t) \quad (2.19)$$

where r_i is the initial position of the i^{th} A molecule. Averaging equation (2.19) over the random initial distribution of A molecules inside the sphere results in:¹³⁶

$$P(t) = \left\{ \sum_{i=1}^{\infty} H_i \exp(-\alpha_i^2 \frac{Dt}{R^2}) \right\}^N \quad (2.20)$$

where

$$H_i = \frac{6\left(\frac{d}{R}\right)^2}{\alpha_i^2 \left[1 - \left(\frac{d}{R}\right)^3\right] \left(\frac{\alpha_i^2}{1 + \alpha_i^2} - \frac{d}{R}\right)} \quad (2.21)$$

When t is sufficiently large $P(t)$ approaches

$$P(t) \approx H_i^N \exp(-\alpha_i^2 \frac{NDt}{R^2}) \quad (2.22)$$

Thus, $P(t)$ decays exponentially at long times with rate constant $k_q = \alpha_i^2 \frac{ND}{R^2}$, indicating that the reaction inside the restricted sphere obeys first order kinetics. In infinite space, the appropriate survival probability at long time t is given by the following equation:

$$P(t) = \exp(-4\pi cdDt) \quad (2.23)$$

where c is the concentration of A molecules. The rate constant in infinite space is $k_\infty = 4\pi cdD$. Assuming a very large R , $d/R \ll 1$, the root of equation (2.18) is $\alpha_1 = (3d/R)^{0.5}$, and the rate constant in restricted space $k_q = 3dND/R^3$ coincides with the rate constant in infinite space k_∞ , as $c = 3N/(4\pi R^3)$. The authors solved equation (2.18) numerically to find the k_q dependence on the relative size of the reactant molecules and of the sphere. This dependence is illustrated in Figure 2.21 which presents k_q/k_∞ as a function of d/R . It is seen that an increase of d/R results in an increase of k_q/k_∞ . In other words, confinement of reactant molecules inside a spherical volume results in a reaction that at large times is faster than a similar reaction in infinite space.²⁷

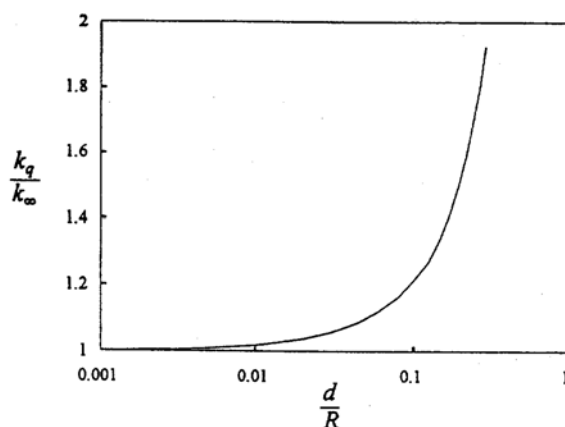


Figure 2.21 The relative value of the reaction rate constant as a function of the relative size of the reactant molecules. Adapted from reference.²⁷

2.5.2 Collision frequencies of reagents inside a vesicle

To further understand the reaction kinetics inside a confined container, Chiu *et al.* used Monte-Carlo simulation to estimate the collision frequencies between the substrate (S) and enzyme (E) as well as between the reagents and the vesicle wall.¹³⁷ One single enzyme and one substrate molecule were treated as hard spheres with specific radius r_S and r_E , respectively. The vesicle was simplified as a spherical container with hard walls and radius of r_V . Collision takes place when the molecules

are separated by a minimal distance R_{SE} and $R_{SE} = r_S + r_E$. This condition creates an excluded volume around each molecule with respect to the other. The collision frequency between S and E ω_{SE} was estimated without explicitly accounting for the solvent by calculating the influx of particles into the excluded volume as the following equation:

$$\omega_{SE} = (R_{SE}^2 / V)(8\pi k_B T / \mu)^{1/2} \quad (2.24)$$

where V is the vesicle volume, k_B is the Boltzmann constant, T is temperature in Kelvin and μ is the reduced mass. Similarly the substrate-wall and enzyme-wall collision frequencies (ω_{SW} and ω_{EW} , respectively) were obtained:

$$\omega_{SW} = (3 / r_V)(k_B T / 2\pi m_s)^{1/2} \quad (2.25)$$

$$\omega_{EW} = (3 / r_V)(k_B T / 2\pi m_E)^{1/2} \quad (2.26)$$

From the Brownian dynamics Monte-Carlo simulations,¹³⁸⁻¹⁴⁰ the authors calculated the number of collisions between enzyme and substrate and between the contained molecules and the vesicle wall. Figure 2.22A and B showed the diffusive paths of the vesicle-confined substrate and the enzyme, respectively. The smaller size and faster diffusive movement of the substrate allowed more space inside the vesicle to be sampled, as reflected in the dense, more crowded trajectories. Figure 2.22C traced the substrate-wall collisions during a 60 ms simulation.¹³⁷

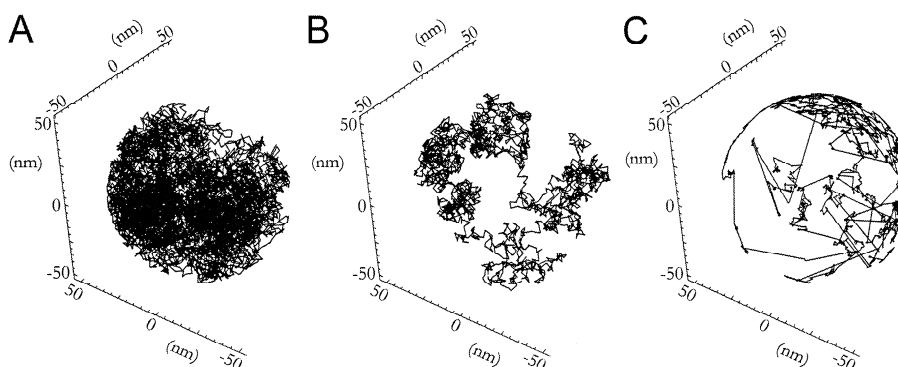


Figure 2.22 Trajectories of a single substrate (A) and enzyme (B) inside a 104-nm diameter sphere modeled using a Brownian dynamics Monte-Carlo simulation. The substrate was followed for 10^4 steps with each step at 10 ns, and the enzyme was followed for 2.5×10^3 steps with each step at 40 ns. (C) A trace showing collisions between a single substrate and the spherical wall (same simulation conditions as in (A) and (B), substrate was followed for 40×10^6 steps, each step at 1.5 ps). Adapted from reference.¹³⁷

Subsequently the collision frequency was plotted as a function of vesicle size, shown in Figure 2.23.¹³⁷ Inside a 170 nm diameter vesicle, a single enzyme and a single

substrate collide at a rate of 300 kHz. The enzyme–wall collision frequency for this vesicle is above 50 MHz, over 150 times more frequent than the enzyme–substrate interactions; the substrate–wall collision rate is 200 MHz, almost 1000 times the enzyme–substrate collision frequency. This fact implies that surface interactions can have significant or even dominant effects on the rate and mechanism of biochemical reactions.

This simulated collision environment inside a vesicle assumed a perfect spherical reflective boundary for the wall (zero residence time) and did not account for any charge or hydrophobic interactions between the wall and the contained molecules. If these effects were included, molecules inside bio-compartments can be significantly biased to reside near (or away from) the wall of the bio-compartment. Still, if both molecules spend sufficient time near the wall, most reactions might occur at or near the wall because collisions between two-dimensionally diffusing molecules are more likely than from three-dimensional diffusion. Later on the authors developed an approach based on electroporation or electrofusion of lipid vesicles to monitor chemical transformations occurring inside the vesicles.¹⁴¹ By manipulating two vesicles with cargos of different molecules, *e.g.* enzyme and substrates using pipette tips, they were able to fuse the vesicles into a giant vesicle (over 10 μm) and mix the contents, which allowed for investigation with optical microscopy.¹⁴²⁻¹⁴³

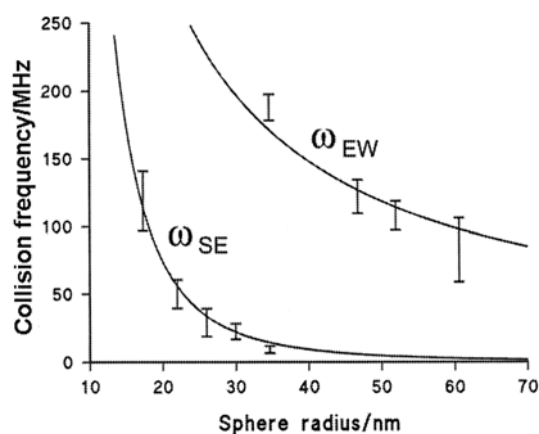


Figure 2.23 A plot showing collision frequency vs. vesicle radius. ω_{SE} is the substrate–enzyme collision frequency (40×10^6 steps, each at 1.5 ps), and ω_{EW} is the enzyme–wall collision frequency (10×10^6 steps, each at 6 ps). The functions were fitted to $y = kx^r$, where $r = -3$ for ω_{SE} (correlation coefficients = 0.997) and -1 for ω_{EW} (correlation coefficients = 0.999) to demonstrate the volume and radius dependence, respectively. Adapted from reference.¹³⁷

Experiments on single-enzyme kinetics have provided exciting results as discussed in the previous section. But are these differences caused by variations in local

nano-environments or by the different ways in which these enzymes were attached? Do they represent true biological variations? Such questions can only be addressed by studying the reaction under conditions that approximate the intimate presence of a membrane wall. Even traditional measurements of enzymatic activities in bulk solutions might not truly represent the reaction conditions inside the highly compartmentalized cell, where strong interactions with bilayer membranes exist. Therefore, studies of enzymatic reactions inside small volumes *i.e.* nanocontainers on a single molecular level, represent true challenges for scientists to reveal the nature of (bio-) chemical reactions that take place in living organisms.

2.6 References

- 1 W. Meier, *Chem. Soc. Rev.* 2000, **29**, 295.
- 2 R. Djatali, J. Samsom, H. Matsui, *J. Am. Chem. Soc.* 2004, **126**, 7935.
- 3 L. Kaanumalle, J. Nithyanandhan, M. Pattabiraman, N. Jayaraman, V. Ramamurthy, *J. Am. Chem. Soc.* 2004, **126**, 8999.
- 4 S. Liu, J. Weaver, M. Save, P. Armes, *Langmuir* 2002, **18**, 8350.
- 5 D. Shchukin, G. Sukhorukov, *Adv. Mater.* 2004, **16**, 671.
- 6 J. Meyer, L. Whitcomb, D. Collins, *Biochem. Biophys. Res. Commun.* 1994, **199**, 433.
- 7 S. V. Balasubramanian, J. Bruenn, R. M. Straubinger, *Pharm. Res.* 2000, **17**, 344.
- 8 S. Zheng, Y. Zheng, R. L. Beissinger, R. Fresco, *Biochim. Biophys. Acta* 1994, **1196**, 123.
- 9 G. Adrian, L. Huang, *Biochemistry* 1979, **18**, 5610.
- 10 P. Walde, S. Ichikawa, *Biomol. Engin.* 2001, **18**, 143.
- 11 T.-M. Hsin, E. S. Yeung, *Angew. Chem. Int. Ed.* 2007, **46**, 8032.
- 12 M. Gradzielski, *J. Phys.: Condens. Matter* 2003, **15**, R655.
- 13 I. W. Hamley, *Soft Matter* 2005, **1**, 36.
- 14 T. S. Koblenz, J. Wassenaar, J. N. H. Reek, *Chem. Soc. Rev.* 2008, **37**, 247.
- 15 B. Adhikari, S. Majumdar, *Prog. Polym. Sci.* 2004, **29**, 699.
- 16 P. P. Ghoroghchian, J. J. Lin, A. K. Brannan, P. R. Frail, F. S. Bates, M. J. Therien, D. A. Hammer, *Soft Matter* 2006, **2**, 973.
- 17 M. Lee, C.-J. Jang, J.-H. Ryu, *J. Am. Chem. Soc.* 2004, **126**, 8082.
- 18 B. Okums, T. J. Wilson, D. M. J. Lilley, T. Ha, *Biophys. J.* 2004, **87**, 2798.
- 19 P. P. Ghoroghchian, P. R. Frail, K. Susumu, D. Blessington, A. K. Brannan, F. S. Bates, B. Chance, D. A. Hammer, M. J. Therien, *Proc. Natl. Acad. Sci. USA* 2005, **102**, 2922.
- 20 T. Cai, Z. Hu, B. Ponder, J. John, D. Moro, *Macromolecules* 2003, **36**, 6559.
- 21 R. Haag, *Angew. Chem. Int. Ed.* 2004, **43**, 278.
- 22 L. Twyman, A. King, I. Martin, *Chem. Soc. Rev.* 2002, **31**, 69.
- 23 J. L. Chávez, J. L. Wong, A. V. Jovanovic, E. K. Sinner, R. S. Duran, *IEE Proc. – nanobiotechnol.* 2005, **152**, 73.
- 24 Q. Chen, R. Groote, H. Schönherr, G. J. Vancso, *Chem. Soc. Rev.* 2009, **38**, 2671.

- 25 S. C. Kou, B. J. Cherayil, W. Min, B. P. English, X. S. Xie, *J. Phys. Chem. B* 2005, **109**, 19068.
- 26 W. Min, I. V. Gopich, B. P. English, S. C. Kou, X. S. Xie, A. Szabo, *J. Phys. Chem. B* 2006, **110**, 20093.
- 27 R. F. Khairutdinov, *Prog. Reaction Kinetics* 1996, **21**, 1.
- 28 D. A. Tomalia, *Prog. Polym. Sci.* 2005, **30**, 294.
- 29 H. Hauser, *Phospholipids handbook*, Marcel Dekker, New York, 1993.
- 30 A. D. Bangham, R. W. Horne, *J. Mol. Biol.* 1964, **8**, 660.
- 31 A. D. Bangham, M. M. Standish, J. C. Watkins, *J. Mol. Biol.* 1965, **13**, 238.
- 32 H. Ringsdorf, B. Schlarb, J. Venzmer, *Angew. Chem.* 1988, **100**, 117.
- 33 D. F. o'Brien, B. Armitage, A. Benedicto, D. E. Bennett, H. G. Lamparski, Y.-S. Lee, W. Srisiri, T. H. Sisson, *Acc. Chem. Res.* 1998, **31**, 861.
- 34 J. C. M. van Hest, D. A. P. Delnoye, M. W. P. L. Baars, M. H. P. van Genderen, E. W. Meijer, *Science* 1995, **268**, 1592.
- 35 V. Percec, C. H. Ahn, G. Ungar, D. J. P. Yearley, M. Moller, S. S. Sheiko, *Nature* 1998, **391**, 161.
- 36 J. J. L. M. Cornelissen, M. Fischer, N. A. J. M. Sommerdijk, R. J. M. Nolte, *Science* 1998, **280**, 1427.
- 37 A. Harada, K. Kataoka, *Science* 1999, **283**, 65.
- 38 D. E. Discher, A. Eisenberg, *Science* 2002, **297**, 967.
- 39 S. Jain, F. S. Bates, *Science* 2003, **300**, 460.
- 40 L. Zhang, A. Eisenberg, *Science* 1995, **268**, 1728.
- 41 S. A. Jenekhe, X. L. Chen, *Science* 1998, **279**, 1903.
- 42 B. M. Discher, Y.-Y. Won, D. S. Ege, J. C.-M. Lee, F. S. Bates, D. E. Discher, D. A. Hammer, *Science* 1999, **284**, 1143.
- 43 M.-H. Li, P. Keller, *Soft Matter* 2009, **5**, 927.
- 44 J.-F. Gohy, *Adv. Polym. Sci.* 2005, **190**, 65.
- 45 A. Blanz, S. P. Armes, A. J. Ryan, *Macromol. Rapid Commun.* 2009, **30**, 267.
- 46 D. E. Discher, A. Eisenberg, *Science* 2002, **297**, 967.
- 47 F. Meng, G. H. M. Engbers, J. Feijen, *J. Controlled Release* 2005, **101**, 187.
- 48 C. Nardin, T. Hirt, J. Leukel, W. Meier, *Langmuir* 2000, **16**, 1035.
- 49 J. Murtagh, J. K. Thomas, *Faraday Discuss. Chem. Soc.* 1986, **81**, 127.
- 50 J. Kurja, R. J. M. Noelte, I. A. Maxwell, A. L. German, *Polymer* 1993, **34**, 2045.
- 51 N. Poulain, E. Natache, A. Pina, G. Levesque, *J. Polym. Sci., Part A: Polym. Chem.* 1996, **34**, 729.
- 52 J. D. Morgan, C. A. Johnson, E. W. Kaler, *Langmuir* 1997, **13**, 6447.
- 53 M. Jung, D. H. W. Huber, P. H. H. Bomans, P. M. Frederic, J. Meuldijk, A. M. van Herk, H. Fischer, A. L. German, *Langmuir* 1997, **13**, 6877.
- 54 J. Hotz, W. Meier, *Langmuir* 1998, **14**, 1031.
- 55 J. Hotz, W. Meier, *Adv. Mater.* 1998, **10**, 1387.
- 56 M. Hetzer, H. Clausen-Schaumann, S. Bayerl, T. M. Bayerl, X. Camps, O. Vostrowsky, A. Hirsch, *Angew. Chem. Int. Ed.* 1999, **38**, 1962.
- 57 M. Sauer, D. Streich, W. Meier, *Adv. Mater.* 2001, **13**, 1649.
- 58 H. Huang, E. E. Remsen, T. Kowalewski, K. L. Wooley, *J. Am. Chem. Soc.* 1999, **121**,

- 3805.
- 59 S. Stewart, G. J. Liu, *Chem. Mater.* 1999, **11**, 1048.
- 60 A. Taubert, A. Napoli, W. Meier, *Curr. Opin. Chem. Biol.* 2004, **8**, 598.
- 61 A. Graff, M. Sauer, P. van Gelder, W. Meier, *Proc. Natl. Acad. Sci. USA* 2002, **99**, 5064.
- 62 M. Sauer, T. Haefele, A. Graff, C. Nardin, W. Meier, *Chem. Comm.* 2001, 2452.
- 63 M. Meier, C. Nardin, M. Winterhalter, *Angew. Chem. Int. Ed.* 2000, **39**, 4599.
- 64 C. Nardin, J. Widmer, M. Winterhalter, W. Meier, *Eur. Phys. J. E* 2001, **4**, 403.
- 65 A. Ranquin, W. Versées, W. Meier, J. Steyaert, P. van Gelder, *Nano Lett.* 2005, **5**, 2220.
- 66 P. Broz, S. Driamov, J. Ziegler, N. Ben-Haim, S. Marsch, W. Meier, P. Hunziker, *Nano Lett.* 2006, **6**, 2349.
- 67 K. Kita-Tokarczyk, J. Grumelard, T. Haefele, W. Meier, *Polymer* 2005, **46**, 3540.
- 68 A. Graff, M. Winterhalter, W. Meier, *Langmuir* 2002, **17**, 919.
- 69 R. Koebnik, K. P. Locher, P. van Gelder, *Mol. Microbiol.* 2000, **37**, 239.
- 70 D. M. Vriezema, M. C. Aragonés, J. A. A. W. Elemans, J. J. L. M. Cornelissen, A. E. Rowan, R. J. M. Nolte, *Chem. Rev.* 2005, **105**, 1445.
- 71 T. Douglas, D. P. E. Dickson, S. Betteridge, J. Charnock, C. D. Garner, S. Mann, *Science* 1995, **269**, 54.
- 72 F. C. Meldrum, B. R. Heywood, S. Mann, *Science* 1992, **257**, 522.
- 73 T. Ueno, M. Suzuki, T. Goto, T. Matsumoto, K. Nagayama, Y. Watanabe, *Angew. Chem. Int. Ed.* 2004, **43**, 2527.
- 74 T. Douglas, M. Young, *Nature* 1998, **393**, 152.
- 75 T. Douglas, M. Young, *Science* 2006, **312**, 873.
- 76 P. S. Arora, K. Kirshenbaum, *Chem. Biol.* 2004, **11**, 418.
- 77 M. C. Aragonés, H. Engelkamp, V. I. Classen, N. A. J. M. Sommerdijk, A. E. Rowan, P. C. M. Christianen, J. C. Maan, B. J. M. Verduin, J. J. L. M. Cornelissen, R. J. M. Nolte, *Nature Nanotech.* 2007, **2**, 635.
- 78 J. A. Speir, S. Munshi, G. J. Wang, T. S. Baker, J. E. Johnson, *Structure* 1995, **3**, 63.
- 79 E. Donath, G. B. Sukhorukov, F. Caruso, S. A. Davis, H. Möhwald, *Angew. Chem. Int. Ed.* 1998, **37**, 2201.
- 80 C. S. Peyratout, L. Dähne, *Angew. Chem. Int. Ed.* 2004, **43**, 3762.
- 81 C. Gao, S. Moya, E. Donath, H. Möhwald, *Macromol. Chem. Phys.* 2002, **203**, 953.
- 82 F. Caruso, H. Lichtenfeld, M. Giersig, H. Möhwald, *J. Am. Chem. Soc.* 1998, **120**, 8523.
- 83 F. Caruso, R. A. Caruso, H. Möhwald, *Chem. Mater.* 1999, **11**, 3309.
- 84 I. Pastoriza-Santos, B. Schöler, F. Caruso, *Adv. Funct. Mater.* 2001, **11**, 122.
- 85 A. A. Antipov, D. Shchukin, Y. Fedutik, A. I. Petrov, G. B. Sukhorukov, H. Möhwald, *Colloid Surf. A-Physicochem. Eng. Asp.* 2003, **224**, 175.
- 86 G. B. Sukhorukov, D. V. Volodkin, A. M. Günther, A. I. Petrov, D. B. Shenoy, H. Möhwald, *J. Mater. Chem.* 2004, **14**, 2073.
- 87 H. Zhu, E. W. Stein, Z. Lu, Y. M. Lvov, M. J. McShane, *Chem. Mater.* 2005, **17**, 2323.
- 88 G. K. Such, E. Tjipto, A. Postma, A. P. R. Johnston, F. Caruso, *Nano Lett.* 2007, **7**, 1706.
- 89 G. Schneider, G. Decher, *Nano Lett.* 2004, **4**, 1833.
- 90 Y. Ma, W.-F. Dong, M. A. Hempenius, H. Möhwald, G. J. Vancso, *Nature Mater.* 2006, **5**, 724.
- 91 J. F. G. A. Jansen, D. A. F. J. van Boxtel, E. M. M. de Brabander-van den Berg, E. W.

- Meijer, *J. Am. Chem. Soc.* 1995, **117**, 4417.
- 92 C. R. Newkome, C. N. Moorefield, G. R. Baker, M. J. Saunders, S. H. Grossman, *Angew. Chem. Int. Ed.* 1991, **30**, 1178.
- 93 A. Sunder, M. Krämer, R. Hanselmann, R. Mühlhaupt, H. Frey, *Angew. Chem. Int. Ed.* 1999, **38**, 3552.
- 94 M. Zhao, L. Sun, R. M. Crooks, *J. Am. Chem. Soc.* 1998, **120**, 4877.
- 95 H. Huang, E. E. Remsen, T. Kowalewski, K. L. Wooley, *J. Am. Chem. Soc.* 1999, **121**, 3805.
- 96 S. Stewart, G. J. Liu, *Chem. Mater.* 1999, **11**, 1048.
- 97 M. S. Wendland, S. C. Zimmerman, *J. Am. Chem. Soc.* 1999, **121**, 1389.
- 98 R. K. Murray, D. K. Granner, P. A. Mayes, V. W. Rodwell, *Harper's Illustrated Biochemistry 26th ed*, Lange Medical Books / McGraw-Hill, New York, 2003.
- 99 R. Wolfenden, M. J. Snyder, *Acc. Chem. Res.* 2001, **34**, 938.
- 100 M. Garcia-Viloca, J. Gao, M. Karplus, D. G. Truhlar, *Science* 2004, **303**, 186.
- 101 L. Pauling, *Chem. Eng. News* 1946, **24**, 1375.
- 102 L. Michaelis, M. Menten, *Biochem. Z.* 1913, **49**, 333.
- 103 X. S. Xie, J. K. Trautman, *Annu. Rev. Phys. Chem.* 1998, **49**, 441.
- 104 W. E. Moerner, M. Orrit, *Science* 1999, **283**, 1670.
- 105 S. Weiss, *Science* 1999, **283**, 1676.
- 106 R. D. Smiley, G. G. Hammes, *Chem. Rev.* 2006, **106**, 3080.
- 107 A. M. van Oijen, P. C. Blainey, D. J. Crampton, C. C. Richardson, T. Ellenberger, X. S. Xie, *Science* 2003, **301**, 1235.
- 108 X. S. Xie, H. P. Lu, *J. Biol. Chem.* 1999, **274**, 15967.
- 109 L. Edman, R. Rigler, *Proc. Natl. Acad. Sci. USA* 2000, **97**, 8266.
- 110 K. Hassler, P. Rigler, H. Blom, R. Rigler, J. Widengren, T. Lasser, *Optic. Ex.* 2007, **15**, 5366.
- 111 B. P. English, W. Min, A. M. van Oijen, K. T. Lee, G. B. Luo, H. Y. Sun, B. J. Cherayil, S. C. Kou, X. S. Xie, *Nature Chem. Bio.* 2006, **2**, 87.
- 112 W. Min, B. P. English, G. Luo, B. J. Cherayil, S. C. Kou, X. S. Xie, *Acc. Chem. Res.* 2005, **38**, 923.
- 113 H. P. Lu, L. Y. Xun, X. S. Xie, *Science* 1998, **282**, 1877.
- 114 S. Hammes-Schiffer, B. J. Benkovic, *Ann. Rev. Biochem.* 2006, **75**, 519.
- 115 W. Min, G. Luo, B. J. Cherayil, S. C. Kou, X. S. Xie, *Phys. Rev. Lett.* 2005, **94**, 198302-1.
- 116 T. J. Ha, A. Y. Ting, J. Liang, W. B. Caldwell, A. A. Deniz, D. S. Chemla, P. G. Schultz, S. Weiss, *Proc. Natl. Acad. Sci. USA* 1999, **96**, 893.
- 117 H. A. Kramers, *Physica* 1940, **7**, 284.
- 118 X. S. Xie, *Single Mol.* 2001, **2**, 229.
- 119 O. Flomenbom, K. Velonia, D. Loos, S. Masuo, M. Cotlet, Y. Engelborghs, J. Hofkens, A. E. Rowan, R. J. M. Nolte, M. van der Auweraer, F. C. de Schryver, J. Klafter, *Proc. Natl. Acad. Sci. USA* 2005, **102**, 2368.
- 120 K. Velonia, O. Flomenbom, D. Loos, S. Masuo, M. Cotlet, Y. Engelborghs, J. Hofkens, A. E. Rowan, J. Klafter, R. J. M. Nolte, F. C. de Schryver, *Angew. Chem. Int. Ed.* 2005, **44**, 560.
- 121 Q. Chen, H. Schönherr, G. J. Vancso, *Small* 2009, **5**, 1436.

- 122 T. Nomura, J. R. Escabi-Perez, J. Sunamoto, J. H. Fendler, *J. Am. Chem. Soc.* 1980, **102**, 1484.
- 123 K. Kano, H. Kawazumi, T. Ogawa, *J. Phys. Chem.* 1981, **85**, 2998.
- 124 D. J. Barbar, D. A. Morris, J. K. Thomas, *Chem. Phys. Lett.* 1976, **37**, 481.
- 125 P. Herve, F. Nome, J. H. Fendler, *J. Am. Chem. Soc.* 1984, **106**, 8291.
- 126 V. Ramamurthy, *Photochemistry in organized and constrained media*, VCH Publishers, Inc. New York, 1991.
- 127 M. Almgren, *Kinetics and catalysis in microheterogeneous systems*, Marcel Dekker, New York, 1991.
- 128 M. Tachiya, *Kinetics of non homogeneous processes*, Wiley, New York, 1987.
- 129 M. D. Ediger, M. D. Fayer, *Macromolecules* 1983, **68**, 13.
- 130 D. Mobius, *Kinetics of non homogeneous processes*, Wiley, New York, 1987.
- 131 J. Klafter, J. M. Drake, *Molecular dynamics in restricted geometries*, Wiley, New York, 1989.
- 132 J. M. Drake, P. Levitz, N. J. Turro, K. S. Nitsche, K. F. Cassidy, *J. Phys. Chem.* 1988, **92**, 4680.
- 133 R. F. Khairutdinov, P. P. Levin, S. M. B. Costa, *Langmuir* 1996, **12**, 714.
- 134 R. F. Khairutdinov, N. A. Rubtsova, S. M. B. Costa, *J. Lumin.* 1996, **68**, 299.
- 135 H. S. Carslaw, J. C. Jaeger, *Proc. London Math. Soc.* 1940, **46**, 36.
- 136 M. Tachiya, *Chem. Phys. Lett.* 1980, **69**, 605.
- 137 D. T. Chiu, C. F. Wilson, A. Karlsson, A. Danielsson, A. Lundqvist, A. Strömberg, F. Ryttsén, M. Davidson, S. Nordholm, O. Orwar, R. N. Zare, *Chem. Phys.* 1999, **247**, 133.
- 138 M.P. Allen, *Mol. Phys.* 1980, **40**, 1073.
- 139 M.P. Allen, *Mol. Phys.* 1982, **45**, 599.
- 140 W. F. van Gunsteren, H. J. C. Berendsen, *Mol. Phys.* 1982, **45**, 637.
- 141 D. T. Chiu, C. F. Wilson, F. Ryttsén, A. Strömberg, C. Farre, A. Karlsson, S. Nordholm, A. Gaggari, B. P. Modi, A. Moscho, R. A. Garza-López, O. Orwar, R. N. Zare, *Science* 1999, **283**, 1892.
- 142 A. Karlsson, K. Sott, M. Markström, M. Davidson, Z. Konkoli, O. Orwar, *J. Phys. Chem. B* 2005, **109**, 1609.
- 143 M. Karlsson, M. Davidson, R. Karlsson, A. Karlsson, J. Bergenholtz, Z. Konkoli, A. Jesorka, T. Lobovkina, J. Hurtig, M. Voinova, O. Orwar, *Annu. Rev. Phys. Chem.* 2004, **55**, 613.

Chapter 3

Preparation and Characterization of Block Copolymer

Vesicles as Nanocontainers

In this chapter the formation of vesicles utilizing amphiphilic block copolymers in a mixed solvent system was explored. Polystyrene-*block*-poly(acrylic acid) (PS-*b*-PAA), a classical amphiphilic macromolecule, was selected as a model system to prepare vesicles in the nanometer size range. By varying the preparation parameters, such as the initial concentration of the polymer, the water content in the solvent mixture, the nature and composition of the solvent, the presence of ions, etc., vesicles with outer diameters in the size range from ~80 nm to ~300 nm were obtained. The membrane thickness of the vesicles was tuned from 20 nm to 40 nm via the chain length of the block copolymers. Size and morphology of the vesicles produced at different temperatures were studied. The vesicle-to-micelle phase transition at elevated temperatures received particular attention. The morphology of the vesicles on solid substrates at high temperatures was studied using atomic force microscopy (AFM). Finally, fluorescent probes with different hydrophobicities were encapsulated either in the membrane or in the interior of the vesicles during the vesicle formation process. This encapsulation strategy, in combination with the established control over the size of the vesicles, forms the basis for the study of enzymatic reactions in confinement, which will be described in Chapter 5 and Chapter 6.

3.1 Introduction

Block copolymer (BCP) aggregates with different morphologies represent an interesting research area and hence raised considerable attention over the past decades.¹⁻¹⁰ Apart from fundamental interest, research on these structures received attention also due to their potential use in cosmetics, drug delivery, electronics, pollution control and separation, among other application areas. BCP vesicles, the so-called “polymersomes” (analogous to “liposomes” as lipid vesicle counterparts), are of particular importance due to their high level of relevance in for example biomedicine and drug delivery.¹¹ To successfully utilize BCP vesicles in these applications, it is essential to understand the mechanism of their formation, with

special emphasis on the factors that control their size, their stability and the nature of their interfaces.

Different aggregate morphologies were observed in various small molecule amphiphiles. These morphologies include, among others, spheres, rods, lamellae and vesicles.¹² Control over these different morphologies is based on the ability to manipulate the factors that contribute to the excess Gibbs free energy of the system, such as the nature of the polar head group, the number and length of the hydrophobic tails, the type and concentration of ions, and the temperature. It is primarily the value of the critical packing parameter (CPP) v/a_0l_c that determines the morphology of the aggregates, where v is the volume of the hydrophobic chains, a_0 is the optimal area of the hydrophilic head group, and l_c is the critical chain length of the hydrophobic chain.¹² It is generally accepted that if the CPP is less than 1/3, then spheres are formed. As the value of CPP falls to between 1/3 and 1/2, cylinders are formed. Vesicles are the primary morphology if CPP is between 1/2 and 1. If CPP is approximately equal to 1, lamellae are formed. Inverted structures will be obtained if the value of the parameter is greater than 1.^{13, 14}

Various morphologies are also observed in BCPs in the melt state. The formation of these morphologies is a result of the inherent immiscibility of the different blocks, which, because of the covalent attachment of the blocks, leads to micro-phase separation.¹⁵ The basic equilibrium morphologies that were obtained in BCP systems in the bulk include spheres, hexagonal-packed cylinders, gyroid structures and lamellae.¹⁶ The dominating factors controlling the phase behavior of BCPs in bulk are the degree of polymerization (polymer chain length and chain length ratio between the blocks), the Flory-Huggins interaction parameter and the volume fraction of the components.¹⁷

Similarly, BCP aggregates of different morphologies can be produced in solution. Asymmetric amphiphilic BCPs, which possess in most cases a much longer hydrophobic block, may form spherical or cylindrical micelles, or vesicles in solution. Usually the cores of the micelles and the walls of the vesicles are hydrophobic, the coronas of the micelles and the vesicle walls are hydrophilic.¹⁸ A simple method to prepare the aggregates is to first dissolve the amphiphilic BCPs in a *common solvent* for both blocks. Subsequently this is followed by the addition of water (a *selective solvent* for the hydrophilic block) as *precipitant* for the hydrophobic block. Self-organization takes place above a certain critical water content, which depends on the nature of the blocks. The addition of water is continued until a desirable water

content is reached, depending on the targeted morphology, *i.e.* micelles or vesicles. The formation of the BCP aggregates is primarily controlled by a force balance between three different factors: the degree of stretching of the core-forming blocks, the interaction between the core and the surrounding solvent, and the repulsion between the corona forming chains.¹⁹

In this chapter, the phase behavior of PS-*b*-PAA in solution was studied. In our experiments the influence of different preparation conditions on the size and morphology of the BCP aggregates was addressed in detail. This work forms the basis for the study on the encapsulation/release of functional molecules utilizing BCP aggregates as nanocontainers and the investigation of spatial confinement effects of the container on the reactivity of the encapsulated species (see Chapter 5 and Chapter 6).

3.2 Controlling the size and morphology of PS-*b*-PAA aggregates via solution composition

Vesicles made from PS-*b*-PAA were investigated here as a model system for the study of enzymatic reactions under spatial confinement. Polystyrene-*block*-poly(*tert*-butyl acrylate) (PS-*b*-PtBA) was synthesized using the atom transfer radical polymerization (ATRP) technique,²⁰ as depicted in Figure 3.1. Subsequent hydrolysis of PS-*b*-PtBA using trifluoroacetic acid yields the amphiphilic PS-*b*-PAA ($M_n = 1.2$ kg/mol, $PDI = 1.02$, $Dp-PS = 92$, $Dp-PAA = 12$).

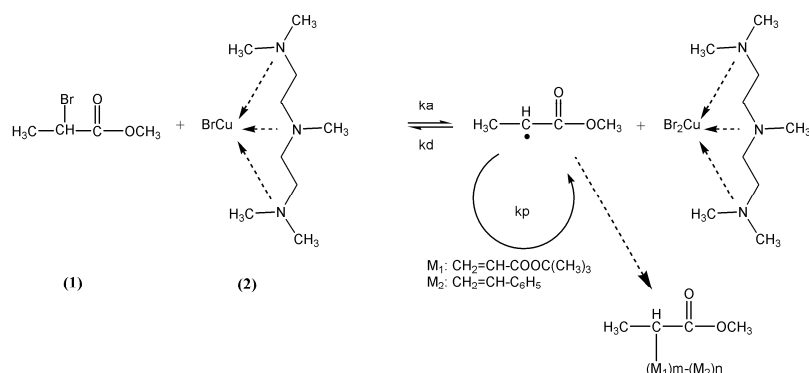


Figure 3.1 Synthesis of PS-*b*-PtBA using ATRP. In the synthesis a reversible Br atom abstraction step between the initiator methyl 2-bromopropionate (1) and the complex formed by Cu(I)Br and pentamethyl diethylene triamine (2) was utilized to generate a radical and a Cu(II) complex (k_a). The radical then attached monomers to generate the polymer chain (k_p). The polymerization can be deactivated by the Cu(II) to generate a dormant chain and Cu(I) complex (k_d).

BCP vesicles were then prepared by mixing a solution of PS-*b*-PAA in tetrahydrofuran (THF) with water. Compounds dissolved in water can be encapsulated in this formation step. After a specific water content was reached, an excess amount of water was added into the solution to quench or “freeze” the morphology of the aggregates. Subsequent dialysis of the vesicle mixture against water allowed the removal of THF, as well as non-encapsulated compounds.

A typical scanning electron microscopy (SEM) image of the BCP vesicles prepared using this approach is shown in Figure 3.2a. As can be seen in the image, PS-*b*-PAA vesicles are spherical objects with a size on the order of a few hundreds of nanometers. They are poly-disperse in nature as can be seen from the size distribution (Figure 3.2b). The width of the distribution ($\frac{D}{0.5w} = 5$ according to the Gaussian fit) may be attributed to the variation of the chemical potential of a molecule in an aggregate of N molecules.¹² The inset shows the vesicular structure of the particle revealed by transmission electron microscopy (TEM).

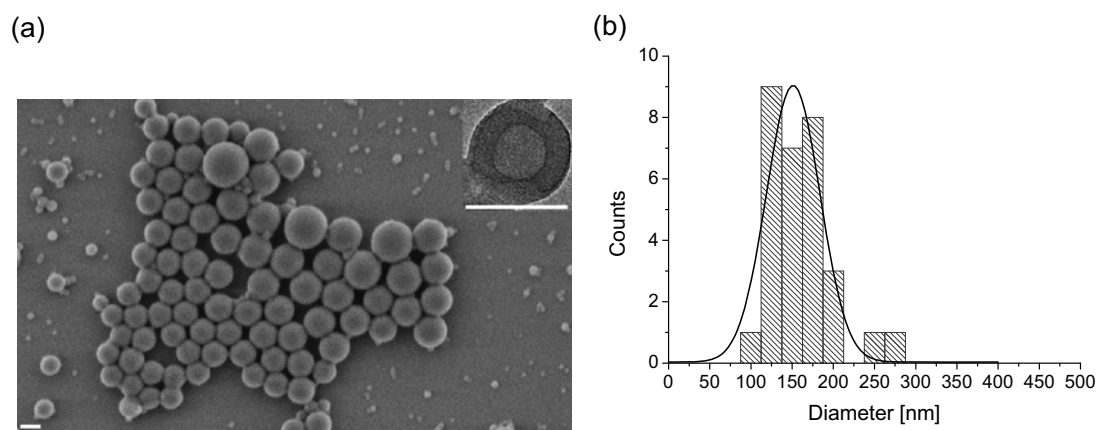


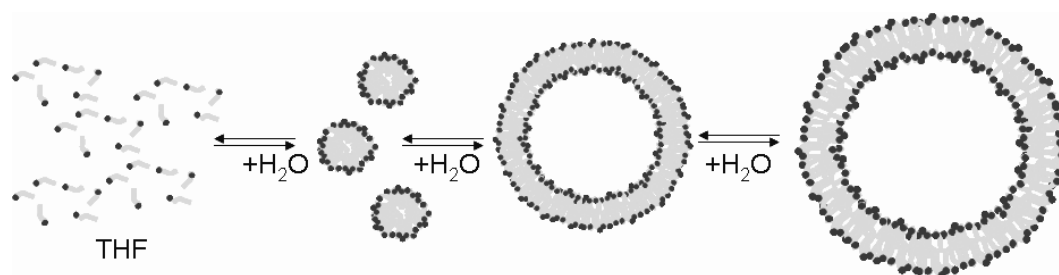
Figure 3.2 (a) SEM image of PS₁₃₉-*b*-PAA₁₇ vesicles prepared by adding water to a polymer solution in THF. The inset shows a TEM image of an individual vesicle. The scale bar is 100 nm in both images. (b) Size distribution of the vesicles determined from (a). The black curve is the Gaussian fit to the data. The obtained average diameter $D = 150$ nm and the width of the peak $w = 65 \pm 4$ nm.

According to the literature, vesicles form spontaneously in the mixture when the concentration of water exceeds the critical value of the micelle-to-vesicle transition point. Thereby an internal aqueous environment is created in which active compounds, such as enzymes and substrates, can be encapsulated.² The control over the size and morphology of the vesicles is crucial for further exploration of the vesicles as size-tunable nanocontainers. Therefore the influence of composition of the solution

mixture on the formation of the vesicles was studied in detail to allow us to establish control over the size of the vesicles via variation of the preparation conditions.

3.2.1 Influence of water content

The addition of water to a solution of PS₁₃₉-*b*-PAA₁₇ in THF results in an increase of the free energy of the system owing to unfavorable interactions of water and PS, since PS, as the major block of the BCP, is insoluble in water. To counteract this free energy increase, phase separation takes place, if the water content is further increased.²¹ At low water content micelles are formed. Here the PS blocks aggregate to form the core of the micelles. For higher water contents a micelle-to-vesicle transition occurs to further minimize the total interfacial area, as the total interfacial area decreases with increasing size of the vesicles (Scheme 3.1).



Scheme 3.1 Schematic representation of the formation of BCP aggregates by the addition of a selective solvent (H_2O) into the polymer solution in a common solvent (THF).

The total interfacial area of vesicles with different sizes was calculated and plotted as a function of vesicle radius in Figure 3.3a. The diameter of the vesicles determined from dynamic light scattering (DLS) was found to increase approximately linearly with an increasing percentage of water in the system when the water content is lower than 70% (Figure 3.3b, triangles). This trend is in agreement with reports in the literature.²¹ However, the decrease in total interfacial area becomes less prominent at high water content as can be seen in Figure 3.3a. This explains that at high water content vesicles do not increase their size as linearly as at low water content. Further increasing the amount of water to a substantial content (a five-fold excess of water) will “freeze” the BCP vesicles as PS is below its glass transition temperature (T_g) in water. If the water percentage was decreased by adding THF into the system, the size of the vesicles decreased, indicating the reversibility of the process (Figure 3.3b, circles).

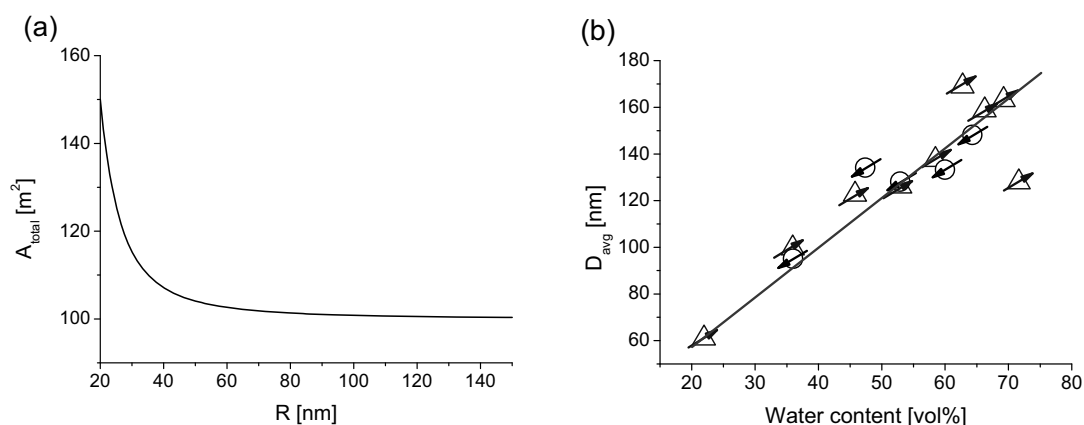


Figure 3.3 (a) Calculated total interfacial area of $\text{PS}_{139}\text{-}b\text{-PAA}_{17}$ vesicles as a function of the size of the vesicle. A total volume of 1 mL PS is assumed with a constant vesicle wall of 20 nm. (b) The average $\text{PS}_{139}\text{-}b\text{-PAA}_{17}$ vesicle diameter determined by DLS (triangles, polymer concentration 2 wt%) vs. water content in the polymer/THF/water mixture. The decrease of vesicle diameter (circles) with decreasing water content indicates that the process of vesicle formation is reversible. The solid red line represents the linear fit to the data.

3.2.2 Influence of initial polymer concentration

Figure 3.4a shows the influence of the initial polymer concentration in THF on the size of $\text{PS}_{139}\text{-}b\text{-PAA}_{17}$ vesicles. For increasing polymer concentrations in the original THF stock solution the vesicles grew larger for the same water content. The slopes of the linear fits to the data points below 60% water content in Figure 3.4a were defined as the growth increment of the vesicles as a function of water content. The plot of the growth increment against the initial polymer concentration is shown in Figure 3.4b. Clearly a more prominent increase of the size of the vesicles was observed for an initial polymer concentration range in THF between 1 wt% to 5 wt%.

The observation of an increase in vesicle diameter with higher initial polymer concentration is attributed to the change of the thermodynamic parameters. The aggregation of more PS blocks for higher initial polymer concentrations results in an increased loss of entropy of the aggregates compared to the entropy loss of a system with lower polymer concentration in THF with the same water content. The size of the vesicles increases, to further decrease the interfacial energy which contributes to the free energy and the enthalpy of the system, keeping them minimized. At even higher polymer concentrations (10 wt%), the formation of larger vesicles is expected to contribute less to a decrease in interfacial area as discussed in the previous section, and indeed a similar growth increment was observed between initial polymer concentration of 5 wt% and 10 wt% as well as a similar size of the vesicles at higher

water content (Figure 3.4a). Due to this less pronounced size dependence on thermodynamic parameters for larger vesicles, the size distribution of the vesicles broadened, as can also be seen in Figure 3.4c. PS₁₃₉-*b*-PAA₁₇ vesicles prepared using an initial concentration of 2 wt% BCP in THF with a water content of 60 vol% possessed an average size of 170 ± 30 nm, while vesicles prepared with 5 wt% in THF and the same water content showed an average size of 280 ± 100 nm. (The error is the width of the distribution).

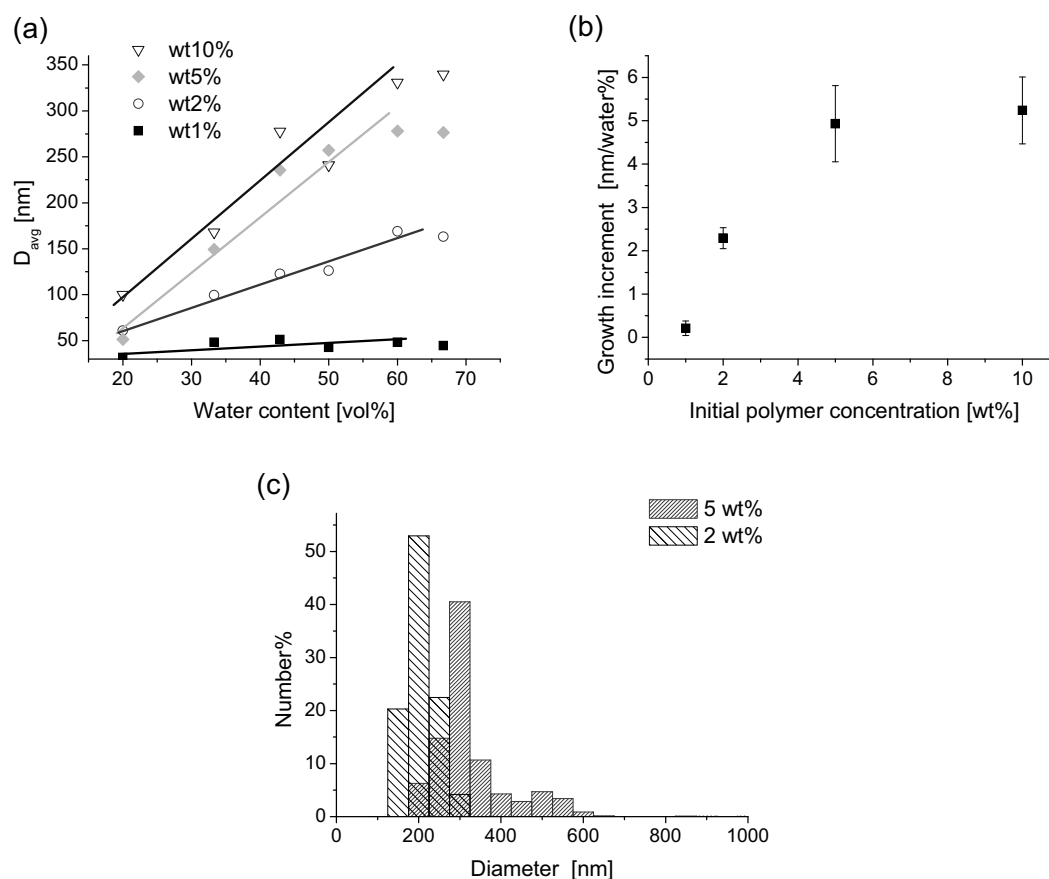


Figure 3.4 (a) Average PS₁₃₉-*b*-PAA₁₇ vesicle diameter determined by DLS vs. water content in the polymer/THF/water mixture for different initial polymer concentrations: squares: 1 wt%; circles: 2 wt%; diamonds: 5 wt% and triangles: 10 wt%. The solid lines represent the linear fits to the data below 60 vol%. (b) The growth increment of PS₁₃₉-*b*-PAA₁₇ vesicles plotted vs. the initial polymer concentration in THF. (c) Size distribution of PS₁₃₉-*b*-PAA₁₇ vesicles, prepared using initial concentrations in THF of 2 wt% and 5 wt% with a water percentage of 60 vol%, determined by DLS.

3.2.3 Influence of the addition of ions

The addition of ions or acids to BCP solutions has been used to control morphology of the aggregates.^{22,23} To investigate the influence of these additives, PS₁₃₉-*b*-PAA₁₇

was first dissolved in THF, then sodium chloride (NaCl) or hydrochloric acid (HCl) with a known concentration was added into the polymer solution, finally water was used to induce self-assembly of the BCPs to form vesicles. The size of the vesicles was then determined using DLS, and plotted against the concentration of additives in Figure 3.5.

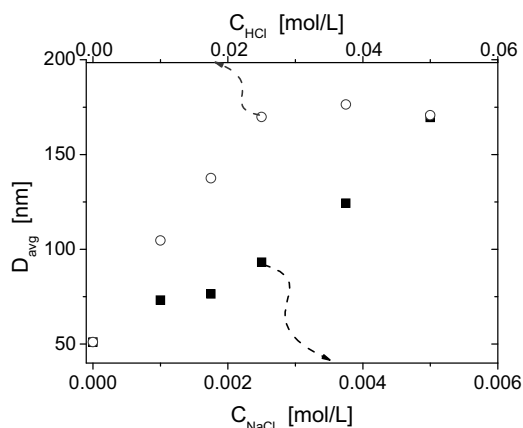


Figure 3.5 Average size of PS_{139} - b - PAA_{17} (1 wt%) vesicles prepared in NaCl (squares) or HCl (circles) containing solutions, determined by DLS.

The size of the vesicles was affected by the presence of ionic additives. As shown in Figure 3.5 a higher salt or acid concentration results in a larger size of the vesicles. The effect is primarily related to the influence of the ions on the strength of corona-chain repulsion. The addition of NaCl causes shielding of charges along the partially ionized PAA chains, subsequently reduces the electrostatic repulsion. In the case of HCl, PAA, as a weaker acid ($pK_A = 4.25$) compared to HCl, will be protonated when HCl is added into the solution, which lowers the charge density along the PAA chains. The reduction in corona-chain repulsion allows more molecules to aggregate, and therefore increases the size of the aggregates. It should be noted that at high salt or acid concentration (~ 1 M) precipitation of the aggregates takes place as a result of aggregation between different particles. The influence of ion additives on the size of the vesicles in our study is in good agreement with the results from the literature.¹⁹

3.2.4 Influence of nature and composition of the common solvent

The nature and composition of the common solvent define the type of polymer-solvent interactions, and therefore determine the coil dimensions, as well as the degree of ionization of polyelectrolytes like PAA.^{24, 25} These factors will, in turn,

affect the degree of stretching of hydrophobic chains and alter the repulsive interactions of hydrophilic chains.²⁶ To study the influence of solvents, a mixed solvent system composed of THF and dimethylformamide (DMF) with different volume ratio was used to dissolve PS₁₃₉-*b*-PAA₁₇, and then an equal amount of water was added to the solution to form the aggregates. Aggregate size as a function of DMF content (vol%) in the solvent system is shown in Figure 3.6.

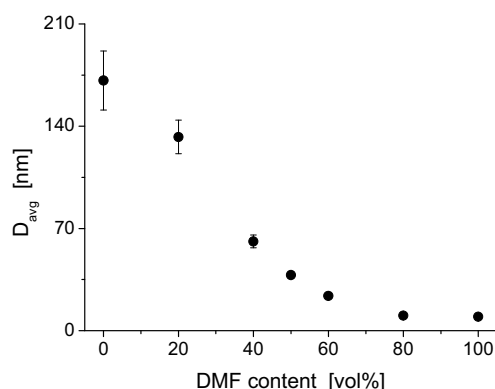


Figure 3.6 Average sizes of PS₁₃₉-*b*-PAA₁₇ aggregates (determined by DLS) prepared in THF/DMF/H₂O mixture as a function of DMF content in the THF/DMF co-solvent system.

As can be seen in Figure 3.6, PS₁₃₉-*b*-PAA₁₇ aggregates prepared in a low DMF content generally have a larger size than those prepared in a high DMF content. Aggregates prepared in pure THF have a size of 170 ± 20 nm as determined from DLS, while aggregates prepared in pure DMF have a size of 15 ± 2 nm, which corresponds to the size of micelles. It was reported before that PS-*b*-PAA self-organized into micelles in DMF at low polymer concentration range.¹⁹ The degree of swelling of the micelle core or the vesicle wall, *i.e.* the degree of core-forming chain stretching is closely related to the solubility of the chains in the solvent. In the particular case of the PS-*b*-PAA/THF/DMF mixture, the solubility parameter of THF ($\delta = 18.6 \text{ MPa}^{0.5}$) is closer to that of styrene ($\delta = 19.0 \text{ MPa}^{0.5}$) than the solubility parameter of DMF ($\delta = 24.8 \text{ MPa}^{0.5}$),²⁷ therefore the degree of stretching for PS chains increases when the content of THF increases in the co-solvent. Moreover, in a solvent with a high dielectric constant such as DMF ($\epsilon = 38.2$), the degree of ionization of the PAA chain is expected to be higher than in the case of THF ($\epsilon = 7.5$).²⁸ Consequently, the repulsion between PAA chains increases when the content of DMF increases in the THF/DMF mixture. Therefore, aggregates prepared in the co-solvent with a high THF content will experience a higher degree of PS stretching and a lower repulsion between PAA, resulting in a stronger driving force to

form aggregates with a larger number of molecules, which corresponds to the larger sizes as displayed in Figure 3.6. This qualitative analysis proves that the size and morphology of BCP vesicles can be effectively controlled by changing the composition of the common solvent(s), which confirms previous results from the literature.²⁶

3.3 PS-*b*-PAA vesicles with different wall thicknesses

The PS-*b*-PAA used here is highly asymmetric with a block length ratio ($D_p\text{-PS}/D_p\text{-PAA}$) of 0.1 ~ 0.15. The vesicle wall, which especially consists of PS only, can be altered by varying the content of PS in the BCP.²⁹ In our experiment, two PS-*b*-PAA polymers: PS₄₀₃-*b*-PAA₆₂ and PS₁₃₉-*b*-PAA₁₇ with different chain lengths were used to prepare vesicles under exactly the same conditions. TEM imaging was then carried out to inspect the vesicular morphology of the vesicles, as shown in Figure 3.7.

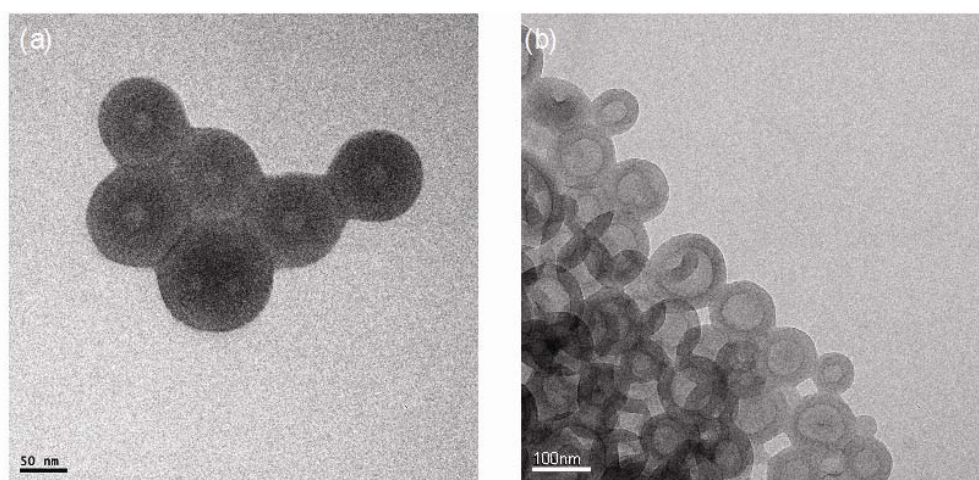


Figure 3.7 TEM images of BCP vesicles made from (a) PS₄₀₃-*b*-PAA₆₂ and (b) PS₁₃₉-*b*-PAA₁₇. Note that the scale bar is 50 nm in (a) and 100 nm in (b).

The vesicular structure of the particles can be clearly resolved in the images due to the electron density contrast between the polymer membrane and the interior of the vesicles. A dramatic difference in membrane thickness was observed for the two vesicles made from polymers with different chain lengths. In the case of PS₄₀₃-*b*-PAA₆₂, the average (outer) diameter estimated from TEM images of 50 individual vesicles was 100 ± 15 nm with a wall thickness of 40 ± 2 nm. For

PS₁₃₉-*b*-PAA₁₇ vesicles the average size was 110 ± 12 nm and the wall thickness was 25 ± 2 nm. The observed wall thickness is closely related to the end-to-end distance of the polymer $l \cdot N^{0.5}$ under theta conditions, where l is the length of one repeating monomer unit and N is the degree of polymerization. Empirically a correlation was found between the wall thickness of vesicles and the degrees of polymerization of both blocks $N_{PS}^{0.4} N_{PAA}^{-0.15}$.³⁰

It is believed that the shape and thickness of the vesicle membrane are key parameters for the mechanical stability of the vesicles and for their use in the field of encapsulation. A detailed study regarding the mechanical properties of vesicle membranes with different thicknesses prepared using BCPs with different chain lengths will be presented in Chapter 4.

3.4 Preparing PS-*b*-PAA vesicles at different temperatures

Temperature has been used for the control of the phase-separated self assembly of block copolymers for many years.^{31, 32} Several investigations have been carried out to study the effect of temperature on the phase behavior of BCPs in solution and it was found that the size as well as the morphology of the BCP aggregates in solution changes from vesicles to micelles when temperature is raised above some critical value.³³⁻³⁵ In our experiment 40 vol% of water was added into PS₁₃₉-*b*-PAA₁₇ solution in THF at different temperatures. After equilibrating for 1 hour, an excess amount of water was added into the solution mixture to “freeze” the aggregates. Subsequently, light scattering and electron microscopy were applied to study the size and morphology of the aggregates. The sizes of the aggregates prepared at different temperatures obtained by DLS are presented in Figure 3.8.

A clear trend of decreasing in the size of the aggregates as a function of temperature is observed in Figure 3.8a. The average size of the aggregates prepared at room temperature ($\sim 25^\circ\text{C}$) is 95 nm, while when the aggregates were prepared at 60°C their average size is decreased to 24 nm, corresponding to the size of micelles. The presence of micelles is confirmed from the corresponding size distribution of the aggregates. As can be seen in Figure 3.8b, bimodal distributions, instead of monomodal distributions are observed when the preparation temperature is above 40°C . The first peak at 24 nm (solid line) corresponds to the size of the micelles and the bilayer thickness of the vesicles obtained from TEM measurement. The second

peak shifts towards small values as temperature increases (dash arrow), indicating the conversion of large vesicles to small vesicles via membrane fission rather than the disintegration of vesicles.

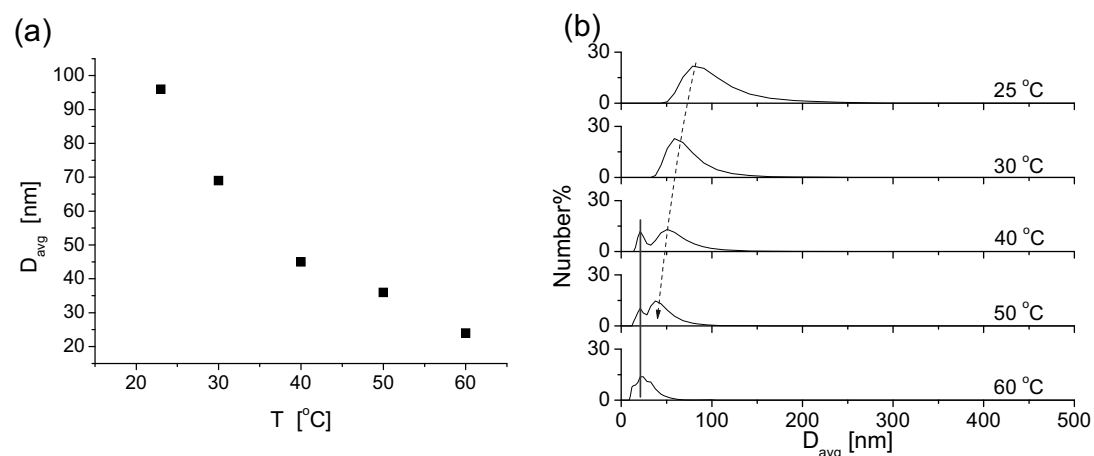


Figure 3.8 (a) Average size and (b) size distribution of PS_{139} - b - PAA_{17} vesicles (2 wt% in THF, water content 40 vol%) prepared at different temperatures, determined by DLS.

To obtain a better understanding on the morphology of the aggregates, TEM imaging was carried out on the aggregates prepared at different temperatures. Typical TEM images of the PS_{139} - b - PAA_{17} aggregates at different temperatures are presented in Figure 3.9.

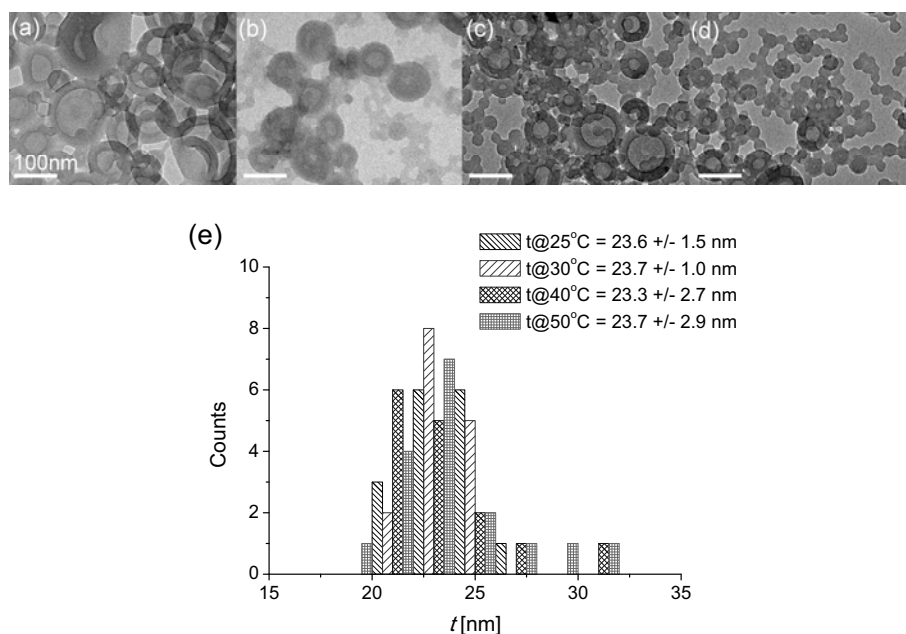


Figure 3.9 TEM images of PS_{139} - b - PAA_{17} vesicles (2 wt% in THF, water content 40 vol%) prepared at (a) 25 °C, (b) 30 °C (c) 40 °C and (d) 50 °C. Scale bar in all images is 100 nm as in (a). (e) Histogram of wall thicknesses of the vesicles as determined from the TEM images shown in (a)-(d).

A mixed morphology of vesicles and micelles, as indicated in the size distribution of the aggregates, was confirmed at elevated temperatures. However, the wall thickness of the vesicles prepared at different temperatures was effectively the same as shown in Figure 3.9e. This can be reasonably explained by the fact that the interaction between PS itself does not change in the experimental temperature range.

A temperature change can be used as a trigger since it disrupts the equilibrium of the aggregates, and causes a morphological change; in the case of PS₁₃₉-*b*-PAA₁₇ from vesicles to micelles. This can potentially be used as a release/encapsulation strategy: At temperatures above the critical temperature the morphology of the vesicles changes and the encapsulated compounds in the interior of the vesicles are released. In Chapter 7 a detailed study on the morphological changes induced by temperature will be presented and possible utilization of this morphological change in the release and encapsulation of functional molecules will be investigated.

3.5 Thermal stability of PS-*b*-PAA vesicles

BCP vesicles are known for their better stability as compared to liposomes.⁸ The stability of BCP vesicles at different temperatures is crucial for their applicability in sensor and delivery applications. Here AFM is used to characterize and inspect the integrity of PS₄₀₃-*b*-PAA₆₂ vesicles deposited on a silicon surface at different temperatures. To carry out AFM imaging, a droplet of PS₄₀₃-*b*-PAA₆₂ vesicles solution was deposited onto a silicon surface and the solvent was evaporated under a gentle nitrogen flow. A heating/cooling stage was coupled onto the sample stage to allow imaging to be carried out at different temperatures. Typical tapping mode (TM)-AFM images of PS₄₀₃-*b*-PAA₆₂ vesicles at room temperature as well as at elevated temperatures are shown in Figure 3.10.

As can be seen in Figure 3.10a, the size of vesicles did not change upon heating and their shape remained spherical till 80°C. At 100°C vesicles started to diffuse and sinter. From section analysis of height (*h*) and width (*w*) of individual vesicles at 80 and 100°C (Figure 3.10b), it is evident that the vesicles were flattened at 100°C. The boundary of the vesicles was still visible. The vesicles completely lost their shape and diffused into clusters upon heating to 120°C, which is well above the T_g of PS (100°C).³⁶ At this temperature the frozen polymer chains have regained their mobility and may aggregate with each other similar to the bulk behaviour of PS above T_g .

Cooling down the sample to room temperature does not recover the original morphology.

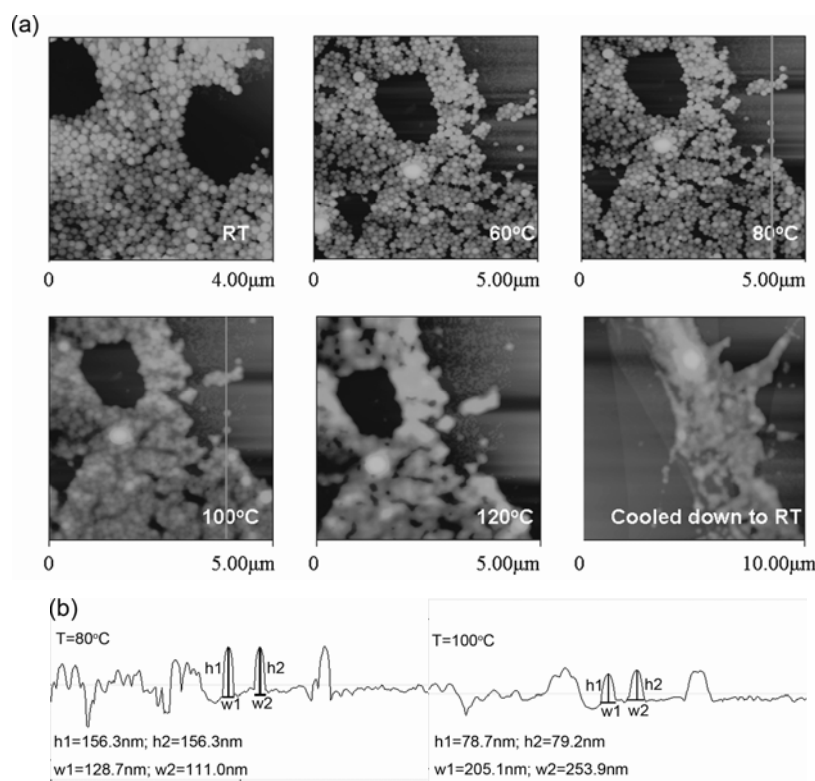


Figure 3.10 (a) TM-AFM images of PS₄₀₃-b-PAA₆₂ vesicles (2 wt% in THF, water content 50 vol%) deposited on silicon. Images were taken using tapping mode under ambient conditions. Samples were heated to different temperatures (indicated in the images) using a heating/cooling stage mounted on the sample holder. The Z range in all images is 0 - 500 nm. (b) Cross-section of the vesicles at 80 and 100 °C as indicated in the AFM images (vertical lines).

3.6 Encapsulation of fluorescent molecules in PS-*b*-PAA vesicles

For the envisioned encapsulation of functional molecules such as enzymes inside the vesicles, fluorophores with different hydrophobicities were first incorporated into the vesicles during the preparation process. The hydrophobic dye 1,1',3,3',3',3'-hexamethyl indodicarbocyanine iodide (DiIC₁(5), $\lambda_{\text{ex}} = 638 \text{ nm}$, $\lambda_{\text{em}}(\text{max}) = 658 \text{ nm}$) is expected to partition into the hydrophobic wall of the vesicles, while the hydrophilic dye 5-(6-)carboxyfluorescein (CF, $\lambda_{\text{ex}} = 490 \text{ nm}$, $\lambda_{\text{em}}(\text{max}) = 520 \text{ nm}$) is expected to reside in the aqueous vesicle interior. The absorption of CF to the vesicle wall is prevented due to the electrostatic repulsion between the negatively charged wall and CF. PS₁₃₉-b-PAA₁₇ vesicles were thus formed by adding CF solution into the

solution of PS₁₃₉-*b*-PAA₁₇ and DiIC₁(5) in THF. For analysis, a droplet of the vesicle solution was placed on a glass cover slide and imaged by confocal laser scanning microscopy (CLSM). PS₁₃₉-*b*-PAA₁₇ vesicles with an average size of 260 ± 100 nm were studied. Samples were excited by lasers with two distinctive wavelengths, namely an Ar-ion laser with a $\lambda = 488$ nm and a He-Ne laser with a $\lambda = 633$ nm to excite CF and DiIC₁(5), respectively. A typical CLSM micrograph of the sample is shown in Figure 3.11.

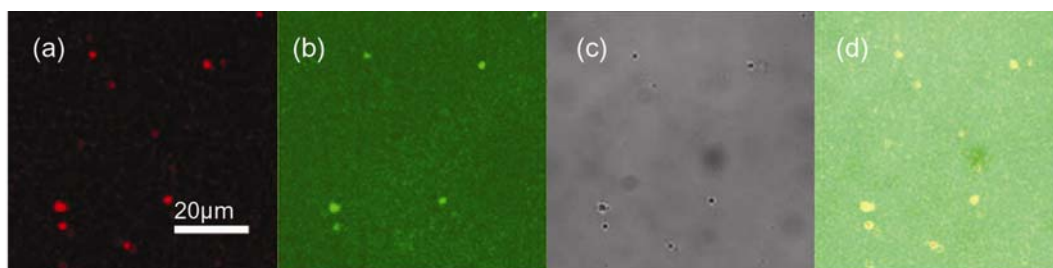


Figure 3.11 CLSM images of PS₁₃₉-*b*-PAA₁₇ vesicles prepared using an initial concentration of 5 wt% in THF with a water content of 50 wt%. The images show the fluorescence emission intensities (excitation at 488 nm and 633 nm) collected in different channels: (a) Emission wavelengths larger than 650 nm; (b) Emission wavelengths between 500 nm and 550 nm; (c) Bright-field image; and (d) Combined image of above channels. The scale bar is 20 μ m.

The red fluorescence emission in Figure 3.11a originates from the hydrophobic DiIC₁(5), which is partitioned into the hydrophobic PS wall of the vesicles. Due to the diffraction limited resolution of CLSM the partitioning of the dye in the wall cannot be directly resolved, only vesicles with sizes on the order of microns can be visualized. The green fluorescence emission in Figure 3.11b is attributed to CF, which resides in the aqueous environment of the vesicle interior. The higher background intensity present in this latter image is the result of incomplete removal of non-encapsulated CF by dialysis. Figure 3.11c shows the corresponding bright field image and Figure 3.11d displays the superimposed image of both fluorescence channels and the bright field image. From this superimposed image we can see that both fluorescent probes and the vesicles are co-localized with each other. This observation indicates that small molecules can be encapsulated inside the BCP vesicles.

3.7 Conclusion

Vesicles made from PS-*b*-PAA were prepared using the selective solvent method. Solution composition, including the water content, initial polymer concentration, added ions and the nature of the common solvent, were varied to control the size of the vesicles. The influence of the chain length of the BCPs on the wall thickness of the vesicles was explored. Preparation of vesicles at different temperatures was carried out and the morphological change from vesicles to micelles at elevated temperature was observed. Thermal stability of the vesicles was studied using AFM and it was found that vesicles were stable in air up to 80°C. Finally, small fluorescent molecules with different hydrophobicities were encapsulated in both the wall and interior of the vesicles as a first attempt to utilize these vesicles as nanocontainers for future study of biochemical reactions in confined environment.

3.8 Experimental

PS_m-*b*-PAA_n (the subscripts m, n denote the number of repeat units for respective blocks, in our experiments, m = 139, 403 while n = 17, 62 correspondingly) were purchased from Polymer Source Inc. (Dorval, Canada). THF and DMF (AR grade) was purchased from Biosolve B. V. (Valkenswaard, The Netherlands). The fluorophores DiIC₁(5) and CF were purchased from Molecular Probes/Invitrogen Co. (Carlsbad, CA, USA). Milli-Q water was produced by a Millipore Synergy system (Billerica, MA, USA). All chemicals were used as received.

PS-*b*-PAA vesicles were prepared by first dissolving the polymer in THF with initial concentrations ranging from 1 to 5 wt %, then adding Milli-Q water as a precipitant into the polymer solution until a given water percentage (50 vol%) was reached, while the entire system was under vigorous stirring using a magnetic stirring bar at ~ 600 rpm. To encapsulate small fluorescent molecules into the vesicles, DiIC₁(5) (initial concentration 10 μM) was dissolved together with the polymer in THF and CF was dissolved in water (initial concentration 10 μM) prior to the preparation. After stirring for overnight, the solution mixture was subjected to dialysis for 72 hours to remove organic solvent residue and low molecular weight impurities. Dialysis was carried out using Spectra/Por 7 dialysis tubing from Spectrum Europe B.V. (Breda, The Netherlands) with a molecular weight cut off of 50 kD.

The size of PS-*b*-PAA vesicles was determined with a Malvern Zeta-sizer 4000 (Malvern Corp., Malvern, UK) at 25°C using a laser wavelength of 633 nm and a scattering angle of 90°. The CONTIN method³⁷ was applied for data processing. The size, count rate and poly-dispersity index (PDI) of the vesicles were determined.

SEM images were obtained using a LEO 1550 high resolution SEM instrument (LEO, Cambridge, England). Vesicle solution was directly deposited on a silicon substrate and dried under nitrogen before mounting onto the sample holder. Typically an electron beam with 10 keV energy was used to scan through the sample surface.

TEM images were acquired using a Philips CM30 analytical TEM instrument (FEI, Hillsboro, OR, USA) equipped with a post-column GIF Tridiem energy filter system (Gatan, Inc., Pleasanton, CA, USA). Samples for TEM were prepared by directly depositing one droplet of vesicle dispersion onto carbon-coated TEM grids. After evaporation of the solvent, the grid was fixed onto the specimen holder and mounted into the vacuum chamber.

AFM images were obtained under ambient conditions in tapping mode with a NanoScope IIIa multimode atomic force microscope (Digital Instruments/Veeco, Santa Barbara, CA, USA) using silicon cantilevers with resonance frequencies of 200-500 kHz (type PPP-NCH-W, Nanosensors, Wetzlar, Germany) and a J-scanner (Digital Instruments/Veeco). Samples were mounted onto a cooling / heating stage and sample temperature was set using a thermal applications controller at 60, 80, 100, 120°C.

CLSM imaging was performed using a Carl-Zeiss LSM510 confocal laser scanning microscope (Carl Zeiss MicroImaging GmbH, Göttingen, Germany). In order to excite the fluorescent molecules encapsulated in the vesicles, an argon-ion laser with a wavelength of 488 nm and a HeNe laser with a wavelength of 633 nm were used for CF and DiIC₁ (5), respectively.

3.9 References

- 1 J. C. M. van Hest, D. A. P. Delnoye, M. W. P. L. Baars, M. H. P. van Genderen, E. W. Meijer, *Science* 1995, **268**, 1592.
- 2 L. Zhang, A. Eisenberg, *Science* 1995, **268**, 1728.
- 3 V. Percec, C. H. Ahn, G. Ungar, D. J. P. Yearley, M. Moller, S. S. Sheiko, *Nature* 1998, **391**, 161.
- 4 S. A. Jenekhe, X. L. Chen, *Science* 1998, **279**, 1903.
- 5 J. J. L. M. Cornelissen, M. Fischer, N. A. J. M. Sommerdijk, R. J. M. Nolte, *Science* 1998,

- 280, 1427.
- 6 A. Harada, K. Kataoka, *Science* 1999, **283**, 65.
 - 7 B. M. Discher, Y.-Y. Won, D. S. Ege, J. C. M. Lee, F. S. Bates, D. E. Discher, D. A. Hammer, *Science* 1999, **284**, 1143.
 - 8 D. E. Discher, A. Eisenberg, *Science* 2002, **297**, 967.
 - 9 C. Nardin, T. Hirt, J. Leukel, W. Meier, *Langmuir* 2000, **16**, 1035.
 - 10 S. Jain, F. S. Bates, *Science* 2003, **300**, 460.
 - 11 M. Rosoff, *Vesicles*, Marcel Dekker, New York, 1996.
 - 12 J. N. Israelachvili, *Intermolecular and Surface Forces*, Academic, San Diego, 1992.
 - 13 K. Holmberg, B. Jonsson, B. Kronberg, B. Lindman, *Surfactants and Polymers in Aqueous Solution*, Wiley, West Sussex, England, 2003.
 - 14 D. F. Evans, H. Wennerstrom, *The Colloidal Domain: Where Physics, Chemistry, Biology, and Technology Meet* Wiley-VCH, New York, 1998.
 - 15 E. Helfand, Z. R. Wasserman, *Microdomain Structure and the Interface in Block Copolymers*, Applied Science, Essex, England, 1982.
 - 16 F. S. Bates, G. H. Fredrickson, *Annu. Rev. Phys. Chem.* 1990, **41**, 525.
 - 17 I. Hamley, *The Physics of Block Copolymers*, Oxford University Press, New York, 1998.
 - 18 K. Yu, A. Eisenberg, *Macromolecules* 1996, **29**, 6359.
 - 19 L. Zhang, A. Eisenberg, *Polym. Adv. Technol.* 1998, **9**, 677.
 - 20 K. A. Davis, K. Matyjaszewski, *Macromolecules* 2000, **33**, 4039.
 - 21 L. Luo, A. Eisenberg, *Langmuir* 2001, **17**, 6804.
 - 22 L. Zhang, K. Yu, A. Eisenberg, *Science* 1996, **272**, 1777.
 - 23 L. Zhang, A. Eisenberg, *Macromolecules* 1996, **29**, 8805.
 - 24 B. Svensson, U. Olsson, P. Alexandridis, *Langmuir* 2000, **16**, 6839.
 - 25 Y. Yu, A. Eisenberg, *J. Am. Chem. Soc.* 1997, **119**, 8383.
 - 26 A. Choucair, A. Eisenberg, *Eur. Phys. J. E* 2003, **10**, 37.
 - 27 J. Brandrup, E. H. Immergut, *Polymer Handbook*, John Wiley and Sons, New York, 1989.
 - 28 R. C. Weast, *Handbook of Chemistry and Physics*, CRC Press, Florida, 1979-1980.
 - 29 T. Azzam, A. Eisenberg, *Angew. Chem. Int. Ed.* 2006, **45**, 7443.
 - 30 L. Zhang, A. Eisenberg, *J. Am. Chem. Soc.* 1996, **118**, 3168.
 - 31 K. Iyama, T. Nose, *Polymer* 1998, **39**, 651.
 - 32 S. V. Aathimanikandan, E. N. Savariar, S. Thayumanavan, *J. Am. Chem. Soc.* 2005, **127**, 14922.
 - 33 I. LaRue, M. Adam, M. Pitsikalis, N. Hadjichristidis, M. Rubinstein, S. S. Sheiko, *Macromolecules* 2006, **39**, 309.
 - 34 E. Chen, Y. Xia, M. J. Graham, M. D. Foster, Y. Mi, W. Wu, S. Z. D. Cheng, *Chem. Mater.* 2003, **15**, 2129.
 - 35 S. Pispas, N. Hadjichristidis, *Langmuir* 2003, **19**, 48.
 - 36 J. E. Mark, *Physical Properties of Polymers Handbook*, AIP Press, New York, 1996.
 - 37 S. W. Provencher, *Biophys. J.* 1976, **16**, 27.

Chapter 4

Mechanical Properties of Block Copolymer Vesicles by Atomic Force Microscopy

In this chapter the mechanical properties of polystyrene-*block*-poly(acrylic acid) (PS-*b*-PAA) vesicles prepared with different block copolymer chain lengths and block length ratios were studied in ambient conditions using atomic force microscopy (AFM). The membrane thicknesses of the vesicles were varied systematically between 22 nm and 40 nm while their external diameters were kept at ~ 150 nm. Subsequently the deformation δ , as well as the spring constant k_{mem} of the membranes were calculated from the captured AFM force displacement data. The application of the shell deformation model provided estimates of the apparent Young's moduli E of the vesicle membranes. While the values of k_{mem} increased with increasing membrane thickness, the values of E were found to decrease. This observed decrease in E with increasing shell thickness was tentatively interpreted as a result of a reduced degree of chain stretching reported in the literature for longer polymer chains in the membrane.

4.1 Introduction

Block copolymer (BCP) vesicles possess a similar structure as natural lipid bilayer vesicles (liposomes), as discussed in Chapter 2 and Chapter 3.¹ BCP vesicles are usually formed from amphiphilic block copolymers, for instance PS-*b*-PAA or polybutadiene-*block*-poly(ethylene oxide) (PBD-*b*-PEO). BCP vesicles are promising candidates in the fields of drug delivery, catalysis and ultra-small reaction vessels since they can be prepared conveniently with controlled sizes and since they combine two different local environments in one type of particle.² In these potential applications the shape and stability of the membrane constitute key parameters.³ The mechanical properties of BCP vesicle membranes cannot be studied by conventional experimental techniques that rely on optical microscopy due to the diffraction limited resolution of optics. This limitation hampers the applicability of for instance micropipette aspiration, which is widely used in the study of giant unilamellar vesicle

* Parts of this chapter were published in the following article: Q. Chen, H. Schönherr; G. J. Vancso, "Mechanical Properties of Block Copolymer Vesicle Membranes by Atomic Force Microscopy", *Soft Matter* 2009, DOI: 10.1039/b903110c.

(GUV) membranes, for the analysis of sub-wavelength sized vesicles.⁴ Therefore it is essential to assess the rigidity of the membranes of vesicles with diameters on the order of 100 nm by alternative methods. In our study the assessment of mechanical properties of BCP vesicles is crucial as they will be used later on as nanocontainers for the study of enzymatic reactions. The stability and robustness of the vesicles ensure that enzymes and substrates are encapsulated inside the containers.

Conventional indentation tests, in which a probe of well defined geometry is indented into a flat surface or a test sample by a force applied in the surface-normal direction, are well-established for the characterization of surfaces that undergo elastic-plastic deformation.⁵ It is generally accepted that methods developed for macroscopic indentation can be faithfully transferred to micron- and submicron-length scales.⁶ In recent years nano-indentation has been widely applied as an important tool in the study of soft materials. The introduction of AFM and depth-sensing nano-indentation in the 1980s⁷ made it possible to measure the local hardness and the elastic properties of nano-scaled samples. The sensitivity and resolution of the instruments have increased continuously during the past years with the advances in miniaturization-enabling technologies, such as micro-fabrication.⁸ Nowadays AFM is a versatile tool for applications like atomic-resolution imaging and force spectroscopy of inter- or intramolecular interactions.⁹ For instance, AFM's capability of combining topographical imaging and mechanical probing has been utilized to generate high resolution elasticity maps of tissues and cells, and even to assess the evolution of stiffness during cellular processes.¹⁰

In previous studies of vesicles using AFM, different mechanical models were applied to determine the rigidity of the vesicle membrane. The classical Hertz model was modified to take an elastic sphere-inelastic sphere contact into account.¹¹ Based on this modified model, the Young's moduli of unilamellar egg yolk phosphatidylcholine (eggPC) vesicles, as well as cholesterol containing eggPC vesicles, were calculated by Ng *et al.*¹² However, the use of the Hertz model leads to an underestimation of the Young's modulus of the membrane, as well as the bending modulus, since the model does not account for the unique hollow shell structure of the vesicles. Instead, Fery *et al.* utilized the shell deformation theory, which was first developed by Reissner,¹³ to analyze the elastic behavior of hollow micro-capsules fabricated by the layer-by-layer deposition of polyelectrolytes onto sacrificial colloidal particle templates.¹⁴ These authors also extended the use of this model to other shell systems, including dipalmitoylphosphatidylcholine (DPPC) vesicles. Here the value of the bending

modulus of the vesicles was in agreement with results from previous studies on GUV's using other techniques. As mentioned, estimates of the bending modulus based on the Hertz model did lead to an underestimate.¹⁵

Despite the widespread use of BCP vesicles in many applications, only few studies have been carried out to systematically investigate the mechanical properties of individual BCP vesicles. The stability of giant (radius >10 μm) PBD-*b*-PEO vesicle membranes was investigated by Discher *et al.* using micropipette manipulation and an area elasticity (K_A) independent of molecular weight (M_n) was observed.¹⁶ Later the bending rigidity of vesicle membranes of the same BCP was determined using the same technique and a near-quadratic scaling of the bending rigidity with thickness was observed.¹⁷ Finally, the structure and mechanical response of PBD-*b*-PEO colloids, with sizes on the order of a few hundreds of nanometers, were studied by Palmer *et al.* using AFM. These authors reported different force-indentation behavior among micelles, vesicles and bilayers.¹⁸

Compared to liposomes with a limited range of membrane thicknesses,¹⁹ it is well established that the thickness of BCP vesicle membranes can be controlled via the copolymer block lengths over a broad range.²⁰ However, the impact of this variation in membrane thickness on the mechanical properties of nano-sized BCP vesicles has not been addressed before using AFM.

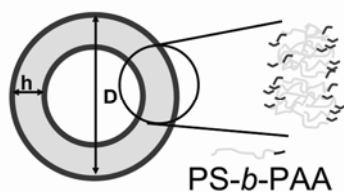
In this chapter the applicability of AFM in the study of the rigidity of the membranes of PS-*b*-PAA vesicles with different chain lengths was explored. The values of the elastic constants and apparent Young's moduli of membranes with systematically varied thicknesses were estimated and the relation between the rigidity and the thickness of the membranes was elucidated.

4.2 PS-*b*-PAA vesicles with different wall thicknesses

The self-organization of PS-*b*-PAA BCPs in selective solvent systems (*e.g.* tetrahydrofuran (THF) - water), as has been extensively studied by Eisenberg *et al.*,²¹ results in vesicles with a membrane consisting of a PS core, an inner and outer PAA corona and an aqueous interior (Scheme 4.1).²² The vesicle size strongly depends on the preparation conditions as shown in Chapter 3. By contrast, the wall thickness depends to a first approximation only on the chain length (degree of polymerization) of the corresponding blocks of the BCP. Empirically the wall thickness of a PS-*b*-PAA

vesicle is correlated with $N_{PS}^{0.4} N_{PAA}^{-0.15}$, where N_{PS} and N_{PAA} represent the degree of polymerization of the PS and the PAA block, respectively.²⁰

In our study PS-*b*-PAA vesicles with different wall thicknesses were prepared according to the literature²¹ by assembling various PS-*b*-PAA BCPs with different block lengths in a THF/H₂O mixed solvent system. The vesicle diameter D_{avg} , as well as the wall thickness h , were estimated based on dynamic light scattering (DLS) and transmission electron microscopy (TEM) data, respectively (Table 4.1). Typical TEM images of vesicles with different wall thicknesses are shown in Figure 4.1.



Scheme 4.1 Illustration of an individual PS-*b*-PAA vesicle with diameter D and thickness h depicted. The zoom-in section shows the bilayer membrane consisting of a PS core and PAA corona.

Table 4.1 Dimensions of PS-*b*-PAA vesicles with different chain lengths and block length ratios.

BCPs	Vesicle diameter D_{avg} [nm] obtained from DLS	Radius of the spherical cap R [nm] obtained from AFM	Vesicle wall thickness h [nm] obtained from TEM
PS ₁₁₅ - <i>b</i> -PAA ₁₅	150 ± 28	120 ± 12	22 ± 1
PS ₁₃₉ - <i>b</i> -PAA ₁₇	142 ± 26	114 ± 18	25 ± 2
PS ₁₈₂ - <i>b</i> -PAA ₁₉	160 ± 24	128 ± 15	29 ± 2
PS ₄₀₃ - <i>b</i> -PAA ₆₂	156 ± 26	125 ± 10	40 ± 2

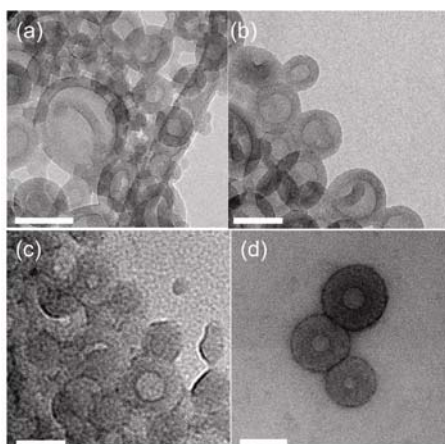


Figure 4.1 TEM images of BCP vesicles made from (a) PS₁₁₅-*b*-PAA₁₅; (b) PS₁₃₉-*b*-PAA₁₇; (c) PS₁₈₂-*b*-PAA₁₉ and (d) PS₄₀₃-*b*-PAA₆₂. The scale bars in all images are 100 nm.

The vesicular structure of the vesicles can be clearly discerned because of the electron density contrast between the membrane and the vesicle interior. The wall thickness of each BCP (at otherwise constant preparation conditions) was determined as the mean value of 50 individual vesicles. The corresponding data was plotted vs. $N_{PS}^{0.4}N_{PAA}^{-0.15}$, as shown in Figure 4.2. The data can be fitted with a straight line, which confirms the empirically determined scaling of the wall thickness with the degrees of polymerization of the PS and PAA blocks reported in the literature.²⁰

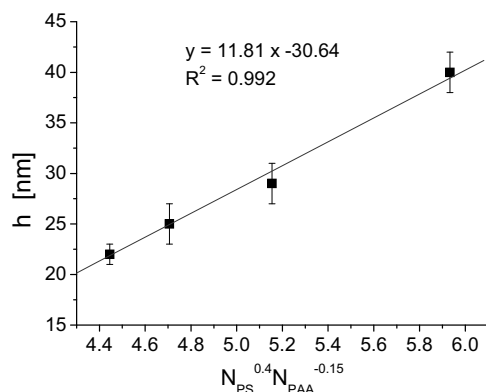


Figure 4.2 Average wall thickness of the above vesicles plotted as a function of $N_{PS}^{0.4}N_{PAA}^{-0.15}$. The solid line represents a linear least-square fit to the data.

4.3 AFM force measurement on PS-*b*-PAA vesicles

For the initial characterization, vesicles that were deposited from H₂O/THF solution onto freshly cleaved mica were imaged using AFM in intermittent contact mode in ambient conditions. A typical tapping mode (TM) AFM height image is shown in Figure 4.3a.

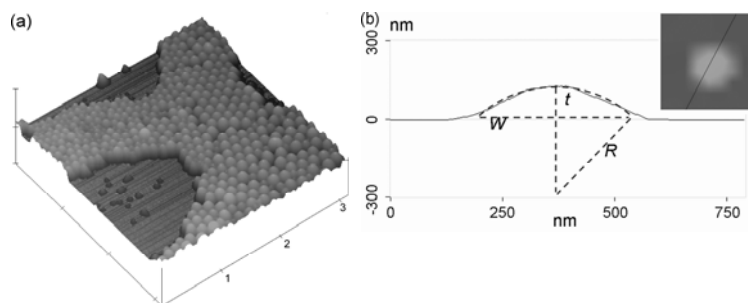


Figure 4.3 (a) A 3D perspective TM-AFM image ($3 \mu\text{m} \times 3 \mu\text{m}$) of BCP vesicles made from $PS_{139}\text{-}b\text{-}PAA_{17}$ deposited on mica acquired under ambient conditions (the z scale is 300 nm). (b) Cross section view of an individual vesicle (black line as indicated in the corresponding AFM image) and overlay of a spherical cap on the vesicle. The width (W), height (t) and the radius of the spherical cap (R) are depicted in the figure.

According to the cross section analysis of individual vesicles (Figure 4.3b), the vesicles can be represented as spherical caps and do not deform to bilayers on the surface. The radius of the spherical cap R (Table 4.1) was estimated for a large number of vesicles from the width W and height t of the features observed in AFM height images (Figure 4.3b) according to equation (4.1). (It should be noted that R differs from D_{avg} obtained from DLS as the latter is the hydrodynamic diameter of the vesicle in solution). These values were later used in the analysis of the mechanical properties.

$$R = \frac{0.25W^2 + t^2}{2t} \quad (4.1)$$

AFM force measurements were performed in the force volume (FV) mode. In the FV mode force-displacement data are acquired for an array of pixels using a triggered z-piezo extension (e.g. a pre-set trigger value of 50 nm deflection). From these data the deflection of the AFM cantilever during contact between the tip and the vesicle, as well as the topography of the sample were obtained. Typical illustrative data acquired with an increased trigger value of 300 nm are shown in Figure 4.4.

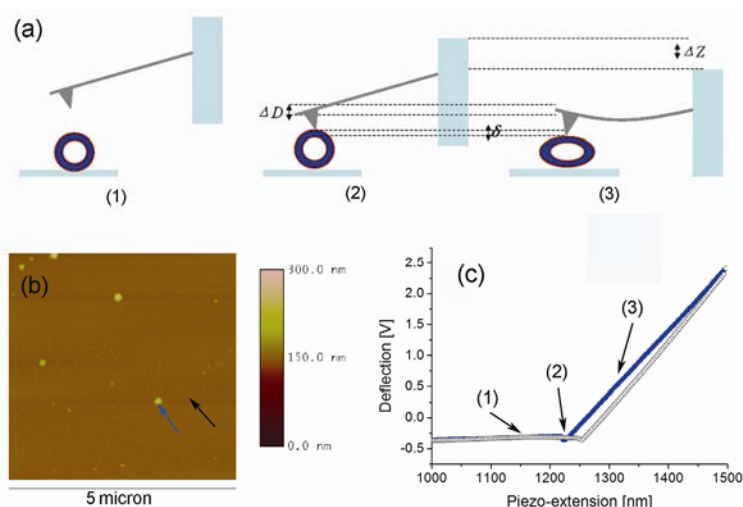


Figure 4.4 (a) Schematic of the AFM force displacement experiment: the cantilever is brought into contact with an individual vesicle and subsequently deforms the vesicle (not to scale): (1) the AFM tip and the vesicle are out of contact; (2) the tip and the vesicle are in contact but the vesicle is not deformed yet; and (3) the vesicle is deformed by the tip. (b) A typical height image ($5 \mu\text{m} \times 5 \mu\text{m}$) recorded in the force volume mode (z scale 300 nm, deflection trigger 300 nm). (c) Two typical deflection-extension curves (Blue: vesicle; Black: mica) recorded in the same experiment, the positions of the contact are highlighted by arrows in (b): Blue arrow: vesicle; Black arrow: mica. The corresponding tip-vesicle interactions (1), (2) and (3) in (a) are also indicated in the curves.

The recorded deflection of the AFM cantilever was then plotted as a function of

piezo-extension to obtain the deformation of the vesicle (Figure 4.4c). The deformation δ of the vesicle can be calculated from:

$$\delta = |Z - Z_0| - (D - D_0) \quad (4.2)$$

where Z denotes the piezo-extension, Z_0 is the piezo-extension at which tip-vesicle contact occurs, D and D_0 are the values of deflection of the cantilever and deflection of the cantilever at which tip-vesicle contact occurs, respectively. The deformation of the vesicle is then plotted against the load (F), which is calculated from $F = k \cdot (D - D_0)$, where k represents the cantilever spring constant (Figure 4.5a).

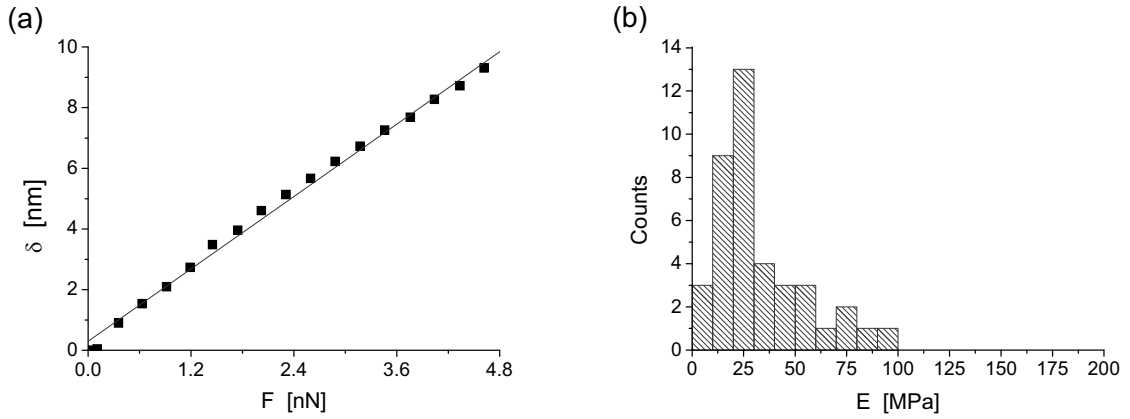


Figure 4.5 (a) Deformation of an individual PS_{403} - b - PAA_{62} vesicle plotted as a function of load. The slope of the curve yields the spring constant of the vesicle membrane. (b) Histogram of the Young's moduli of PS_{403} - b - PAA_{62} vesicle membranes.

For typical shells, an initial elastic response is observed for deformations that are on the order of the wall thickness, followed by buckling instabilities at larger deformations.²³ In our work, an almost linear deformation-load characteristic was found for deformations smaller than 25% of the wall thickness ($h = 40 \pm 2$ nm), which is fully in line with the findings for other shell systems.²⁴ In this deformation range the membrane can be treated as a spring, and the relation between the load and the deformation can be expressed as $F = k_{mem} \cdot \delta$, where k_{mem} is the spring constant of the vesicle membrane.²⁵

The shell deformation model developed by Fery *et al.*¹⁴ was utilized to quantify the mechanical properties of these membranes. Based on this model, the stiffness of the vesicle membrane (k_{mem}), can be expressed as:

$$k_{mem} = \frac{4Eh^2}{R\sqrt{3(1-\nu^2)}}, \quad (4.3)$$

where E denotes the apparent Young's modulus of the membrane, h is the wall

thickness of the membrane, R is the radius of curvature of the spherical cap and ν is the Poisson ratio.

Since k_{mem} can be determined from the deformation-load curve (*vide supra*) and all other parameters are known (we assume a Poisson's ratio of 0.5 as a typical value for soft matter, however, the result does not depend markedly on the choice of ν), we can easily calculate E . In addition to the estimation of E , the apparent bending modulus k_{bend} can be calculated from the following equation according to Landau²⁶:

$$k_{bend} = \frac{Eh^3}{12(1-\nu^2)} \quad (4.4)$$

For the applicability of the shell deformation theory a number of assumptions must be fulfilled. The validity of the theory is restricted to deformations that are on the order of the shell thickness.²⁵ Small deformations are also required to accurately predict the elastic behaviour of a relatively thick shell ($h/R > 0.1$) using the shell deformation theory.^{24, 27} In our calculation only deformations less than 25% of the membrane thickness were used to evaluate the apparent Young's moduli. However, it should be noted that this simple approach neglects the anisotropy of the Young's modulus, which is anticipated not only for BCP vesicles, as studied here, but also for lipid vesicles.¹⁵

It is also important to consider that the interior of the vesicle may not be empty, but may be filled with water. The incompressibility of the liquid inside the vesicle would require volume conservation at all times during deformation. Experimentally the filling of a racquetball was reported not to cause any difference in deformations limited to up to 20% of the radius.²⁴ In our case, residual water inside the vesicles was found to be reduced to negligible amounts after storage of the vesicles for 8 hours in ambient.²⁸ Therefore an empty interior of the vesicle was assumed in our analysis.

Figure 4.5b shows the distribution of the apparent Young's moduli of the membrane ($h = 40$ nm) of 50 individual PS₄₀₃-*b*-PAA₆₂ vesicles. The broad distribution can be explained by the fact that the contact point may not be completely identical for each vesicle though attempts were made to choose only vesicles that were deformed axi-symmetrically by the AFM tip. Secondly the local membrane structure may differ from vesicle to vesicle due to the polydisperse nature of the formation process.⁷ From the distribution histogram the arithmetic mean value of the apparent Young's modulus of the membrane of a PS₄₀₃-*b*-PAA₆₂ vesicle was calculated: $E = 43 \pm 6$ MPa.

4.4 Determination of the apparent Young's modulus of the membrane with different thicknesses

The values of the spring constants (k_{mem}) and the apparent Young's moduli (E) of the membranes of PS-*b*-PAA vesicles with different wall thicknesses were determined using the same approach as described above and are shown in Figure 4.6.

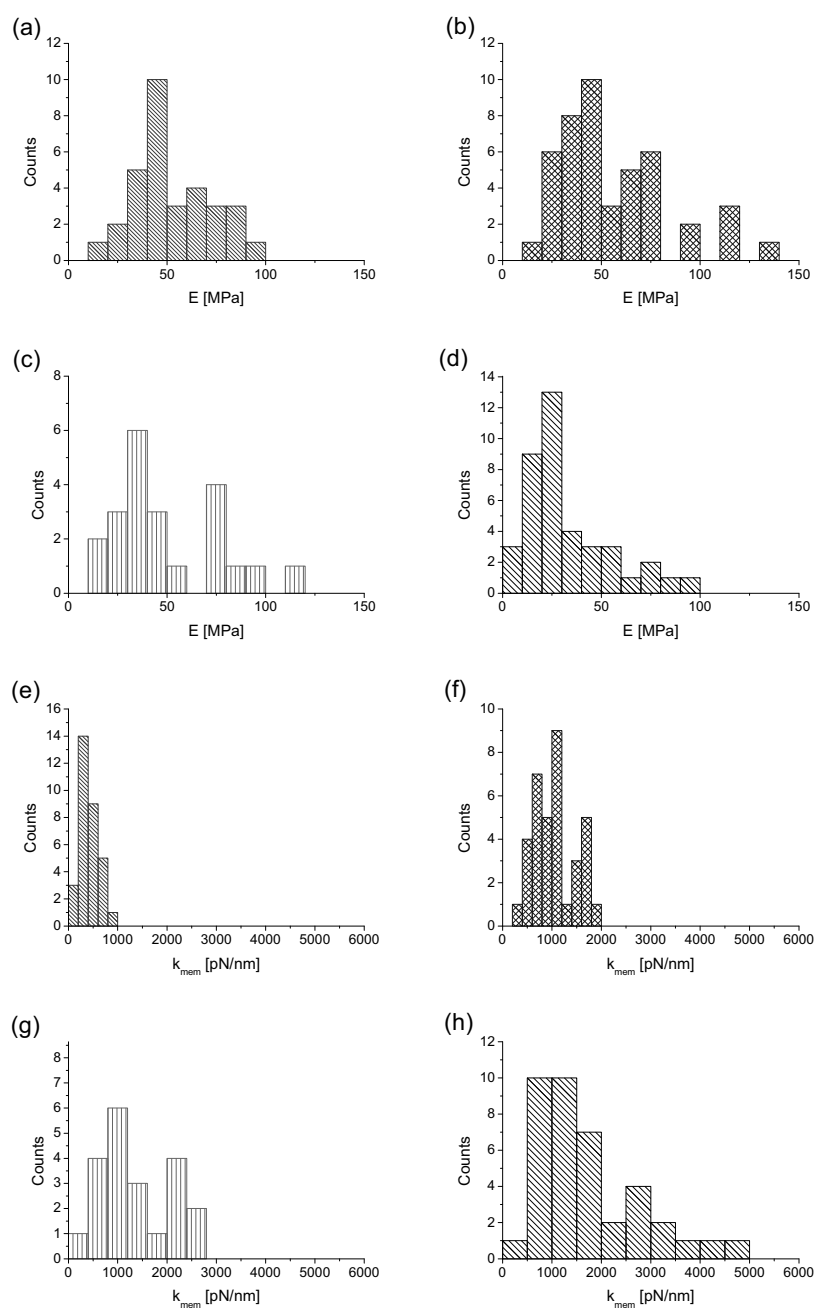


Figure 4.6 Histograms of the calculated apparent Young's moduli of the membranes for (a) $PS_{115}\text{-}b\text{-}PAA_{15}$; (b) $PS_{139}\text{-}b\text{-}PAA_{17}$; (c) $PS_{182}\text{-}b\text{-}PAA_{19}$ and (d) $PS_{403}\text{-}b\text{-}PAA_{62}$ and histograms of the spring constants of the membranes for (e) $PS_{115}\text{-}b\text{-}PAA_{15}$; (f) $PS_{139}\text{-}b\text{-}PAA_{17}$; (g) $PS_{182}\text{-}b\text{-}PAA_{19}$ and (h) $PS_{403}\text{-}b\text{-}PAA_{62}$.

A plot of the mean k_{mem} as a function of the square of the membrane thickness shows clearly that the value of k_{mem} increases with increasing membrane thickness (Figure 4.7a). However, k_{mem} and h^2 are not proportional with each other, as would be expected based on equation (4.3), when constant E and R are assumed. Since the radii of the spherical caps for all vesicles were almost identical (the slight variations cannot account for the observed deviation), it is plausible to conclude that the apparent Young's modulus of the membrane is not constant. Figure 4.7b shows that indeed the value of the apparent Young's modulus of the membrane, determined according to equation (4.3), decreases with increasing membrane thickness. No correlation was found between E and R as shown in Figure 4.7c, ruling out a possible size effect in the size range of the vesicles we have studied.

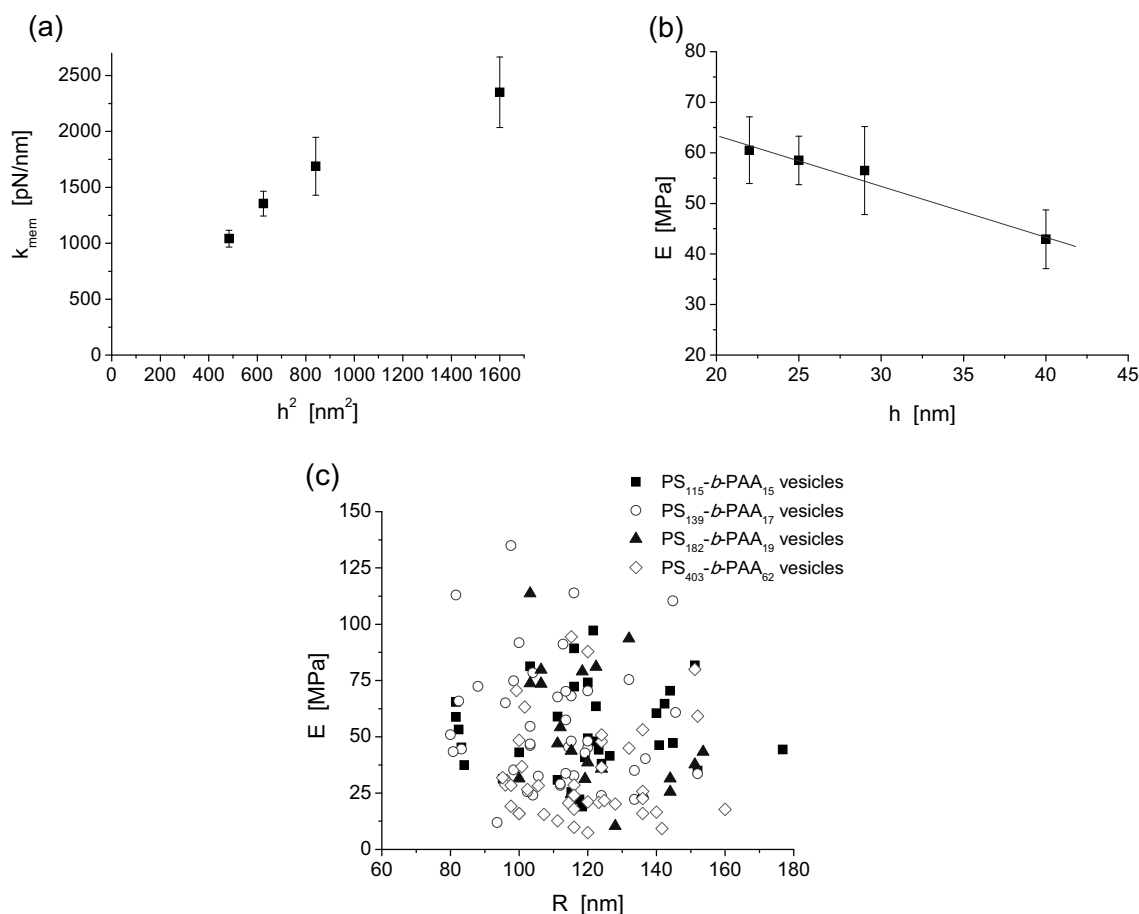


Figure 4.7 (a) Spring constants of the BCP vesicle membranes vs. the square of the membrane thickness. (b) Apparent Young's moduli of the membranes plotted as a function of the membrane thickness. (c) Apparent Young's moduli of various PS-*b*-PAA vesicle membranes vs. radius of the spherical caps.

The observed decrease in E with increasing membrane thickness coincides with an altered degree of chain stretching in the PS block, as reported in the literature.²⁹ In a

PS-*b*-PAA aggregate system, the degree of PS stretching (S_c), defined as the ratio between the micellar core radius (in the case of vesicles, half the bilayer thickness is used) to the PS chain end-to-end distance in the unperturbed state, was found to be dependent on the composition of the copolymers, as shown in equation (4.5).²⁹

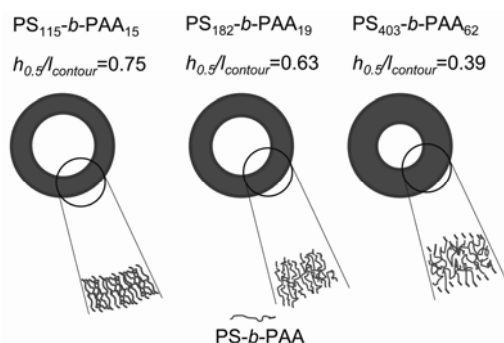
$$S_c \propto N_{PS}^{-0.1} N_{PAA}^{-0.15} \quad (4.5)$$

In addition, the degree of stretching can also be assessed from the ratio of the half wall thickness ($h_{0.5}$), which represents the length of a PS-*b*-PAA molecule in the bilayer membrane, and the contour length of the molecule ($l_{contour}$). It is evident that the degree of chain stretching of PS is different for the various BCPs investigated in this study (Table 4.2).

Table 4.2 Comparison of membrane rigidity of PS-*b*-PAA vesicles with different membrane thicknesses.

BCPs	PS ₁₁₅ - <i>b</i> -PAA ₁₅	PS ₁₃₉ - <i>b</i> -PAA ₁₇	PS ₁₈₂ - <i>b</i> -PAA ₁₉	PS ₄₀₃ - <i>b</i> -PAA ₆₂
k_{mem} (pN/nm)	1040 ± 80	1350 ± 110	1690 ± 260	2350 ± 320
E (MPa)	61 ± 7	59 ± 5	57 ± 9	43 ± 6
k_{bend} (10 ⁻¹⁸ Pa)	72 ± 10	102 ± 8	153 ± 24	306 ± 41
$N_{PS}^{-0.1} N_{PAA}^{-0.15}$	0.414	0.399	0.382	0.296
$h_{0.5}/l_{contour}$	0.75	0.71	0.63	0.39

In the case of PS₁₁₅-*b*-PAA₁₅ vesicles, the copolymers are stretched to 3/4 of their contour length and are expected to display anisotropy to the direction perpendicular to the membrane. By contrast, in PS₄₀₃-*b*-PAA₆₂ vesicles the molecules are only extended to 40% of their contour length thus showing a more isotropic elastic behaviour (Scheme 4.2). This monotonic decrease in the degree of chain stretching coincides with a decrease in the apparent Young's modulus.



Scheme 4.2 Schematic of the cross-section of vesicle membranes made from PS-*b*-PAAs with different degrees of polymerization.

The apparent Young's moduli of the PS-*b*-PAA membranes studied here possess values that are comparable to the value of the (apparent) Young's modulus of DPPC vesicles ($E = 110$ MPa at room temperature).¹⁵ The k_{bend} of our BCP vesicle membranes exhibit a value that is two orders of magnitude higher compared to that of the lipid bilayer vesicles ($\sim 1.3 \times 10^{-18}$ Pa) at room temperature. This shows that vesicles made of block copolymers possess better mechanical stability compared to lipid bilayer vesicles, since the molar masses of the molecules that comprise the membrane is much higher than that of lipid molecules, which resulted in the formation of membranes with larger thickness.¹ The increase in k_{bend} as a function of the increase of membrane thickness is in line with the findings of giant PBD-*b*-PEO vesicles.¹⁷ The increase in thickness does not necessarily lead to an increase in elasticity, as shown by Discher *et al.*¹⁶ These authors observed that the area elasticity of the vesicle membrane is independent on the molecular weight of the block copolymer.¹⁶ In our current study, the use of molecules with a higher molar mass leads to a higher k_{bend} (Table 4.2). However, it also results in a decrease in the apparent Young's modulus of the membrane with increasing polymer molar masses. This effect can be related to the change in the chain stretching of the macromolecules. However, a more definite conclusion requires the extension of the thin shell theory to anisotropic materials, which is currently unavailable.

4.5 Conclusion

The mechanical properties of PS-*b*-PAA vesicles assembled from polymers with different chain lengths and hence different membrane thicknesses were assessed using AFM. The BCP membrane thickness was shown by TEM to scale in accordance with literature data with the degree of polymerization of both blocks. Based on AFM force data and the application of the shell deformation theory, the apparent isotropic Young's moduli of the membranes were estimated. While the values of the spring constant of the membrane were found to be directly proportional to the membrane thickness for vesicles with the same diameter, the apparent Young's moduli were found to decrease with increasing wall thickness. This effect coincides with the decreasing degree of PS stretching that has been previously reported in the literature for membranes with increasing thickness.²⁹

4.6 Experimental

PS_m-*b*-PAA_n (the subscripts *m*, *n* denote the number of repeat units for respective blocks, in our experiments, *m* = 115, 139, 182, 403 while *n* = 15, 17, 19, 62 correspondingly) were purchased from Polymer Source Inc. (Dorval, Canada). THF (AR grade) was purchased from Biosolve B. V. (Valkenswaard, The Netherlands). Milli-Q water was produced by a Millipore Synergy system (Billerica, MA, USA). All chemicals were used as received.

PS-*b*-PAA vesicles were prepared by first dissolving the polymer in THF with initial concentrations ranging from 1 to 5 wt %, then adding Milli-Q water as a precipitant into the polymer solution until a given water percentage (50 vol%) was reached, while the entire system was under vigorous stirring using a magnetic stirring bar with ~ 600 rpm. After stirring for overnight, the solution mixture was subjected to dialysis for 72 hours to remove organic solvent residue and low molecular weight impurities.

The size of PS-*b*-PAA vesicles was determined with a Malvern Zeta-sizer 4000 (Malvern Corp., Malvern, UK) at 25°C using a laser wavelength of 633 nm and a scattering angle of 90°. The CONTIN method³⁰ was applied for data processing. The size, count rate and poly-dispersity index (PDI) of the vesicles were determined.

TEM images were acquired using a Philips CM30 analytical TEM instrument (FEI, Hillsboro, OR, USA) equipped with a post-column GIF Tridiem energy filter system (Gatan, Inc., Pleasanton, CA, USA). Samples for TEM were prepared by directly depositing one droplet of vesicle dispersion onto carbon-coated TEM grids.

AFM images were obtained under ambient conditions in tapping mode with a NanoScope IIIa multimode atomic force microscope (Digital Instruments/Veeco, Santa Barbara, CA, USA) using silicon cantilevers with resonance frequencies of 200-500 kHz (type PPP-NCH-W, Nanosensors, Wetzlar, Germany). For evaluation of the mechanical properties softer silicon nitride cantilevers (type NP, Veeco Instruments Inc., Plainview, NY, USA) were employed (the spring constant was determined using the thermal tune method, $k = 0.12 \pm 0.04$ N/m). Force Volume imaging with a z-scan rate of 5 Hz, a ramp size of 1 μm, a deflection trigger of 50 nm and a scan area of 5 μm × 5 μm was carried. Individual vesicles were identified and force curves in which the contact took place between the AFM tip and the center of the vesicle were chosen for the assessment of the Young's modulus of the vesicle membranes.

4.7 References and notes

- 1 D. E. Discher, A. Eisenberg, *Science* 2002, **297**, 967.
- 2 J. L. Chávez, J. L. Wong, A. V. Jovanovic, E. K. Sinner, R. S. Duran, *IEE Proc. – nanobiotechnol.* 2005, **152**, 73.
- 3 R. Lipowsky, E. Sackmann, *Structure and Dynamics of Membranes*, Elsevier Science, Amsterdam, 1995.
- 4 J. R. Henriksen, J. H. Ipsen, *Eur. Phys. J. E* 2004, **14**, 149.
- 5 B. Bhushan, H. Fuchs, *Applied Scanning Probe Methods*, Springer, Berlin, 2008.
- 6 (a) G. Pelled, K. Tai, D. Sheyn, Y. Zilberman, S. Kumbar, L. S. Nair, C. T. Laurencin, D. Gazit, C. Ortiz, *J. Biomech.* 2007, **40**, 399; (b) Z. Peng, J. Gong, H. Miao, *J. Eur. Ceram. Soc.* 2004, **24**, 2193.
- 7 G. Binnig, C. F. Quate, C. Gerber, *Phys. Rev. Lett.* 1986, **56**, 930.
- 8 D. C. Lin, F. Horkay, *Soft Matter* 2008, **4**, 669.
- 9 (a) F. J. Giessibl, *Rev. Mod. Phys.* 2003, **75**, 949; (b) F. Kienberger, A. Ebner, H. J. Gruber, P. Hinterdorfer, *Acc. Chem. Res.* 2006, **39**, 29.
- 10 (a) N. Almqvist, R. Bhatia, G. Primbs, N. Desai, S. Banerjee, R. Lal, *Biophys. J.* 2004, **86**, 1753; (b) C. Rotsch, F. Braet, E. Wisse, M. Radmacher, *Cell Bio. Int.* 1997, **21**, 685.
- 11 D. E. Laney, R. A. Garcia, S. M. Parsons, H. G. Hansma, *Biophys. J.* 1997, **72**, 806.
- 12 (a) X. Liang, G. Mao, K. Y. S. Ng, *Colloids Surf. B* 2004, **34**, 41; (b) X. Liang, G. Mao, K. Y. S. Ng, *J. Colloid Interface Sci.* 2004, **278**, 53.
- 13 (a) E. Reissner, *J. Math. Phys.* 1946, **25**, 80; (b) E. Reissner, *J. Math. Phys.* 1946, **25**, 279.
- 14 N. Elsner, F. Dubreuil, R. Weinkamer, M. Wasicek, F. D. Fischer, A. Fery, *Progr. Colloid Polym. Sci.* 2006, **132**, 117.
- 15 N. Delorme, A. Fery, *Phys. Rev. E* 2006, **74**, 030901-1.
- 16 H. Bermúdez, A. K. Brannan, D. A. Hammer, F. S. Bates, D. E. Discher, *Macromolecules* 2002, **35**, 8203.
- 17 H. Bermúdez, D. A. Hammer, D. E. Discher, *Langmuir* 2004, **20**, 540.
- 18 S. Li, A. F. Palmer, *Macromolecules* 2005, **38**, 5686.
- 19 D. Marsh, *CRC Handbook of Lipid Bilayers*, CRC Press, Boca Raton, 1990.
- 20 T. Azzam, A. Eisenberg, *Angew. Chem. Int. Ed.* 2006, **45**, 7443.
- 21 P. L. Soo, A. Eisenberg, *J. Polym. Sci. Part B: Polym. Phys.* 2004, **42**, 923.
- 22 L. Luo, A. Eisenberg, *Langmuir* 2001, **17**, 6804.
- 23 R. R. Maccarini, A. Saetta, R. Vitaliani, *Comput. Meth. Appl. Mech. Eng.* 2001, **190**, 4967.
- 24 L. A. Taber, *J. Appl. Mech.-Trans. ASME* 1982, **49**, 121.
- 25 A. Fery, R. Weinkamer, *Polymer* 2007, **48**, 7221.
- 26 L. D. Landau, E. M. Lifshitz, *Theory of Elasticity*, Pergamon Press, New York, 1986.
- 27 R. D. Gregory, T. I. Milac, F. Y. M. Wan, *SIAM J. Appl. Math.* 1999, **59**, 1080.
- 28 ft-IR, NMR and DSC measurements were carried out on vesicle samples dried under ambient conditions for different time intervals. All results pointed to the conclusion that water amount decreased substantially to a negligible amount after 8 hours.
- 29 L. Zhang, A. Eisenberg, *J. Am. Chem. Soc.* 1996, **118**, 3168.
- 30 S. W. Provencher, *Biophys. J.* 1976, **16**, 27.

Chapter 5

Block Copolymer Vesicles as Nanosized Reactors for

Trypsin Catalysis

In this chapter the impact of spatial confinement of polystyrene-*block*-poly(acrylic acid) (PS-*b*-PAA) vesicles on the reactivity of encapsulated bovine pancreas trypsin was studied. Enzyme trypsin and substrate R110 bisamide were encapsulated with loading efficiencies up to 30% in block copolymer (BCP) vesicles with variable internal volumes between 0.05 aL (internal vesicle diameter, $d_{in} = 45$ nm) and 4.6 aL ($d_{in} = 200$ nm), obtained by manipulating the vesicle preparation conditions as described in Chapter 3. The kinetics of the trypsin-catalyzed reaction of a fluorogenic substrate inside and outside the vesicles was quantitatively estimated using fluorescence spectroscopic analyses in combination with the use of NaNO₂ as a selective quencher for non-encapsulated fluorophores. The values of the catalytic turnover number obtained for reactions in nanoscale reactors with different sizes showed a significant increase (up to $\sim 5\times$) with decreasing BCP vesicle volume (to 0.05 aL), while the values of the Michaelis-Menten constant decreased, respectively. The observed increase in enzyme efficiency by 2 orders of magnitude compared to in bulk solutions is attributed to an enhanced rate of enzyme - substrate and molecule - wall collisions inside the nanosized reactors, in agreement with simulations in the literature using a Monte Carlo approach.

5.1 Introduction

The mimicry of chemical transformations in living systems, in particular in cells or cell compartments has recently triggered considerable interest.¹ Due to their diversity and complexity enzymatic reactions have become and remain a key issue also in this context.² Most enzyme studies to date were based on ensemble level experiments, employing enzymes either in aqueous buffered solutions or enzymes that were immobilized on surfaces. In contrast, in many natural systems enzymes may be confined in ultra-small compartments or containers at dilutions down to the single-molecule level. At these length scales the local environment preserved by the

** Parts of this chapter were published in the following article: Q. Chen, H. Schönherr, G. J. Vancso, "Block Copolymer Vesicles as Nanosized Reactors for Enzymatic Reactions", Small 2009, 5, 1436–1445.*

boundaries of the containers and volume confinement may play an important role in the reaction kinetics and mechanisms.³ Therefore, to elucidate the nature of enzymatic reactions in confinement and to study possible effects of enzyme-environment interactions, it is essential to encapsulate enzymes into ultra-small containers and to follow the enzymatic reactions in real-time.

As discussed in detail in Chapter 2, previous studies on single enzyme reaction kinetics already pointed at a deviation of the behavior of single enzymes compared to conventionally studied ensembles of enzymes.⁴ The observation of fluctuation in enzyme reactivity was explained by assuming conformational changes of the enzyme that manifest themselves in different activity.⁵ The Michaelis-Menten theory is commonly used in the analysis of enzymatic reactions on the ensemble (bulk) level and was shown to provide a description of single enzyme kinetics as discussed in Chapter 2. On the other hand confining the enzyme in a nanometer-scale container, similar to digestive enzymes being encapsulated in lysosomes, may cause a change in the enzymatic reaction kinetics compared to solution or compared to the reactions of enzymes immobilized on planar surfaces. In fact, surface immobilized enzymes often exhibit retarded reaction kinetics compared to unrestricted enzymes in solution.⁶ Fluorescence quenching and photo-induced electron transfer taking place in lipid bilayer vesicles were investigated in several studies and it was found that the finite space of the system caused unusual kinetic behavior compared to infinite systems.⁷

The encapsulation of enzymes or functional molecules is also an area of considerable interest for (bio)technological applications. Reaction vessels, drug delivery and catalysis are three examples of the many potential applications for encapsulated systems.⁸ Different methodologies for the realization of such systems have been presented in the literature in the last few years. Dendrimers, layer-by-layer microcapsules, micro-emulsions and phase-separated BCP aggregates have all been reported as being potential candidate materials and approaches for encapsulation.⁹ Especially important in this field is the study of phase-separated BCP vesicles. These BCP systems offer (i) the possibility to combine two different environments in one individual particle, (ii) close similarity to natural counterparts, *i.e.* lipid vesicles and, (iii) ease of synthesis with control over size and chemical composition (see Chapter 3).

As discussed already in Chapter 3, BCPs will phase separate into different morphologies such as micelles and vesicles in selected solvents due to the balance of entropy loss and interaction enthalpy increase.¹⁰ As a result of the different

hydrophobicities of the environment (both interior and exterior) and the membrane of the vesicles, molecules with different hydrophobicities can be enriched either in the interior or in the membrane. Despite the molecularly thin nature of the membrane, vesicles can effectively entrap dissolved molecules and may retard or even prevent diffusion of small species across the membrane, which is a very important characteristic for application in the field of encapsulation.¹¹ Work done by Meier *et al.* on the reconstitution of membrane channel proteins in synthetic BCP vesicle membranes showed how natural, functional molecules and synthetic polymers can be integrated together and how selective diffusion of molecules across the BCP membrane is achieved.¹²

PS-*b*-PAA, a typical amphiphilic BCP, has been extensively studied by Eisenberg *et al.* using a selective solvent method.¹¹ The morphologies of the BCP aggregates are governed primarily by a balance of contributions to the free energy.¹³ Therefore, by changing thermodynamical parameters as discussed in Chapter 3, it is possible to control the aggregate morphology and size.¹⁴

In this chapter PS₁₃₉-*b*-PAA₁₇ vesicles were utilized as size-tunable atto-liter reactors for the study of enzymatic reactions of encapsulated trypsin.¹⁵ Using a fluorogenic substrate the relation of vesicle diameter (internal volume) and enzyme reactivity was unraveled (Figure 5.1).¹⁶

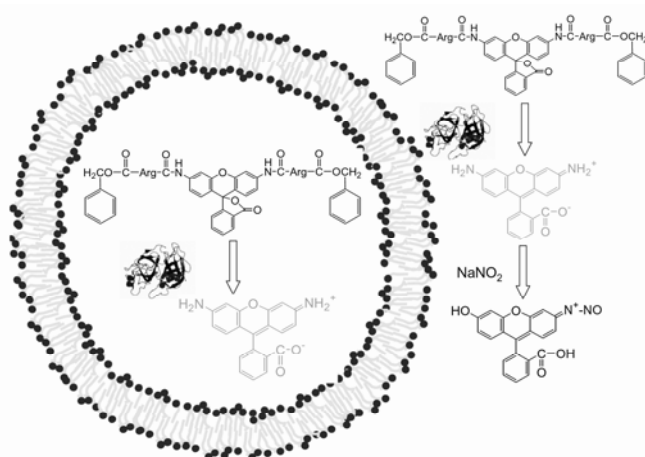


Figure 5.1 Schematic of a PS-*b*-PAA vesicle (filled circles represent the PAA block, while the lines denote the PS block of the BCP), in which the enzymatic reaction of trypsin with the fluorogenic substrate rhodamine 110 bis-(benzyloxycarbonyl(CBZ))-L-arginine amide) dihydrochloride (R110-Arg₂) liberates the fluorescent dye rhodamine 110 (R110) in the enclosed aqueous interior. Upon reaction with sodium nitrite, the R110 generated in the solution outside the vesicles is converted into a non-fluorescent nitroso compound.¹⁷ This quenching reaction does not occur inside the vesicles, since the wall is impermeable to the quencher. Hence the reaction inside and outside of the vesicles can be experimentally differentiated.

5.2 Preparation of PS-*b*-PAA vesicles using different conditions

Studies on PS-*b*-PAA vesicles carried out by Eisenberg *et al.* showed that the size of the vesicles depends strongly on several preparation parameters.¹³ These parameters include the amount of water present in the mixture, the chemical composition of the BCP, the concentration of BCP in the organic solution, the nature of the solvent, etc. The control over the size of the vesicles via preparation conditions has been established in Chapter 3 as a pre-requisite for the study of confinement effect of the vesicle size (internal volume) on the reactivity of encapsulated enzymes.

Vesicle dispersions with different water content (volume percentage) in the mixed water- tetrahydrofuran (THF) solvent were prepared and the hydrodynamic radius (as a measure for the external diameter D) of these vesicles was determined by dynamic light scattering (DLS) (Table 5.1).

Table 5.1 Sizes and preparation conditions of PS₁₃₉-*b*-PAA₁₇ nanocontainers.

Vesicle diameter (external) [nm]	Internal volume [aL]	Initial polymer concentration [wt%]	Water percentage [vol%]
95.0 ± 8	0.05	2	40
126 ± 22	0.23	2	50
209 ± 29	2.10	4	50
257 ± 32	4.64	4	60

Vesicles form spontaneously in the mixture when the concentration of BCP exceeds that of the micelle-to-vesicle transition, thereby creating an aqueous interior environment in which active compounds, for instance enzymes and substrates can be encapsulated.¹⁸ By modifying the initial concentration of the polymer or the water percentage in the system, the average external diameter of PS-*b*-PAA vesicles could be manipulated between 100 and 250 nm. The combined experimental results lead to the conclusion that the size of PS-*b*-PAA vesicles can be controlled over a broad range, which is in agreement with previous findings on similar systems.¹⁹ We note that practically identical size distributions were observed in the presence of the enzyme and substrate molecules studied here (Figure 5.2).

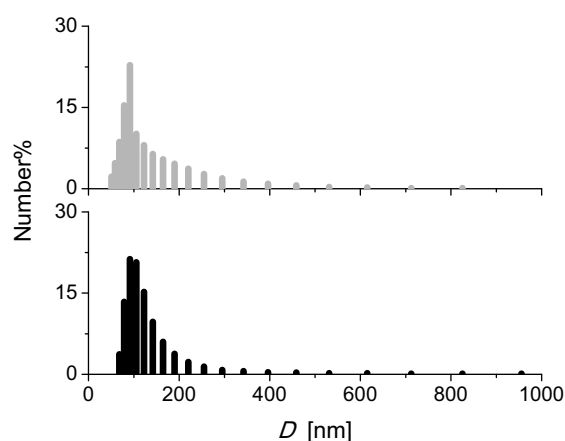


Figure 5.2 Size distribution histogram of trypsin and R110-Arg₂ containing PS-*b*-PAA vesicles (light, $D_{avg} = 123.4$ nm) and empty vesicles (dark, $D_{avg} = 124.2$ nm). Preparation conditions for two vesicle samples are the same. In the case of enzyme and substrate containing vesicles, trypsin ($C = 0.05$ μ M) and R110-Arg₂ ($C = 12.8$ μ M) solution instead of pure water is added into the polymer solution.

Transmission electron microscopy (TEM) data confirmed the vesicular structure of the vesicles. Samples for TEM were prepared by depositing ~ 10 μ L of the vesicle dispersion on a carbon-coated copper grid followed by drying. No staining was used. Figure 5.3a shows an image of PS-*b*-PAA vesicles prepared using an initial polymer concentration of 2 wt% in THF with a water content of 50 vol%. The hydrophobic wall of the vesicles comprised of PS is clearly differentiated from the interior due to the electron density contrast between the membrane and the center part of the vesicles.

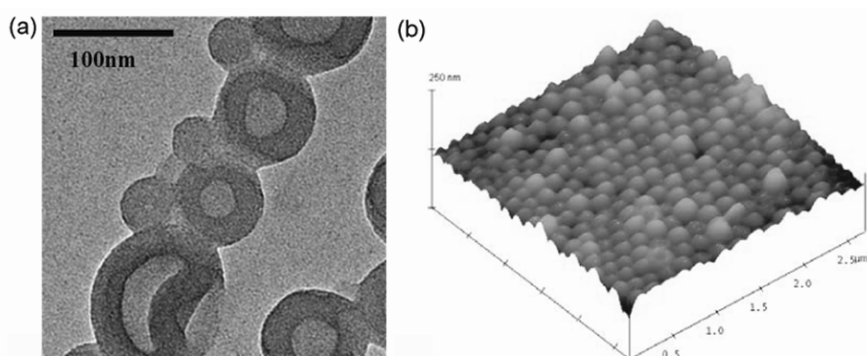


Figure 5.3 (a) Transmission electron micrograph of PS₁₃₉-*b*-PAA₁₇ vesicles; (b) 3D perspective AFM micrograph (2.5 μ m \times 2.5 μ m) of PS₁₃₉-*b*-PAA₁₇ vesicles deposited on mica. The z scale is 250 nm.

The average outer diameter of the vesicles estimated from TEM images of 50 individual vesicles was 107 ± 12 nm with a wall thickness of 25 ± 2 nm. The wall

thickness of PS-*b*-PAA vesicles was found to be independent on the different preparation conditions utilized, in full agreement with reports in the literature.¹⁴ For comparison, the diameter (calculated from the hydrodynamic radius) of the same batch of vesicles determined by DLS was 126 ± 22 nm.

PS-*b*-PAA vesicles were also deposited onto freshly cleaved mica and imaged by atomic force microscopy (AFM) in intermittent contact mode in ambient conditions. A 3D perspective AFM image of the vesicles prepared using the same conditions as the vesicles imaged with TEM is shown in Figure 5.3b. The shape of the vesicles can be described as a spherical cap. Here the vesicles are arranged in a close-packed manner on the mica surface. Cross-sectional analyses of 50 individual vesicles showed that the vesicles were 138 ± 25 nm in width and 72 ± 8 nm in height. From a comparison of height of the vesicles (72 nm) with twice the wall thickness obtained from TEM (50 nm) it can be concluded that the vesicles remained intact and did not collapse to form a bilayer on the surface when exposed to air, in agreement with the data presented in Chapter 4.

5.3 Encapsulation of enzyme and substrate in PS-*b*-PAA vesicles

In order to carry out enzymatic reactions inside the nanocontainers made from PS-*b*-PAA, enzyme bovine pancreas trypsin and the fluorogenic substrate R110-Arg₂ were incorporated into the BCP vesicles. The cleavage of the bond between the rhodamine moiety and the short peptide chain will release the fluorescent product R110, which possesses $\lambda_{em} = 525$ nm.¹⁶ Since the reaction takes place on a much faster time scale than any applicable separation method (*e.g.* dialysis), it is difficult to remove the non-encapsulated trypsin and R110-Arg₂. Experiments with the fluorescence quencher sodium nitrite helped to prove that trypsin does react with R110-Arg₂ inside the vesicles. NaNO₂ reacts with the product of the enzymatic reaction, R110, to form a non-fluorescent molecule (Figure 5.1), which results in a decrease of the fluorescence emission intensity attributed to the product.¹⁷ The negatively charged vesicle wall, on the other hand, will protect R110 formed inside the vesicles from reacting with sodium nitrite, since the negatively charged nitrite ion cannot penetrate through the wall. Hence all remaining fluorescence signal will originate from the fluorescent product formed in the vesicle interior.

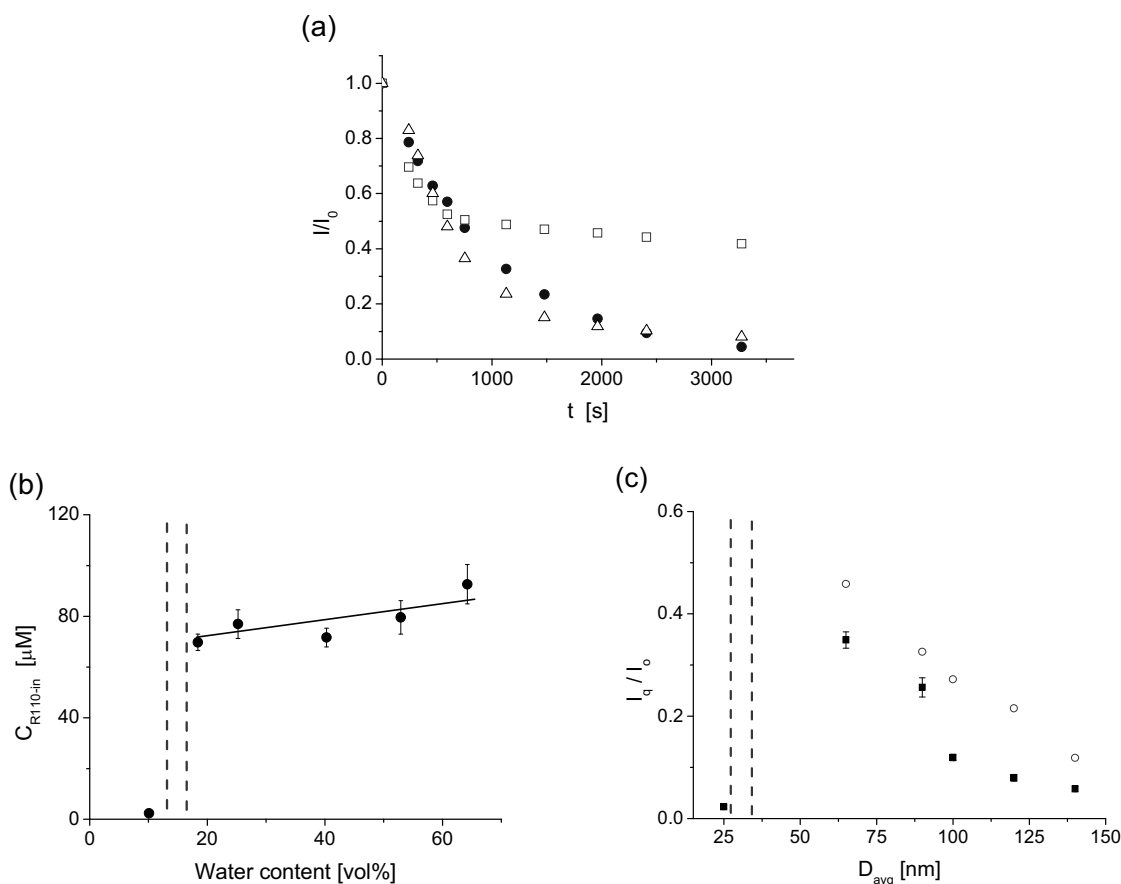


Figure 5.4 (a) Fluorescence emission intensity ratio before and after the quencher was added plotted as a function of reaction time. Quenching experiments were carried out in solutions of pure enzyme and substrate (dots); in solutions of enzyme and substrate together with empty PS-*b*-PAA vesicles (triangles, $d_{ext} = 126$ nm) and in solutions of enzyme and substrate partly incorporated in PS-*b*-PAA vesicles (squares, $d_{ext} = 126$ nm) with the same polymer concentration as the solution with empty vesicles. (b) Dynamic study on the encapsulation percentage of substrates during vesicle formation, as a function of water content. The total substrate concentration increases with increasing water content from 0 to 1.5 μ M while the encapsulated substrate concentration remains almost constant after the micelle to vesicle transition indicated by the vertical dash lines. (c) Emission intensity ratio plotted as a function of the actual vesicle size in (b). The squares represent the experimental data and the circles are the calculated values of volume ratio between the total volume of the vesicle interior and the total volume of the aqueous solution.

The result of the experiment is shown in Figure 5.4a. Trypsin and R110-Arg₂ were mixed and after 15 minutes of reaction time, sodium nitrite was added to the mixture. The observed overall fluorescence intensity of the solution decreased immediately. After ~ 1 hour the residual fluorescence intensity was less than 10% of the original intensity before the quencher was added (dots). Performing the same experiment by mixing the trypsin and R110-Arg₂ with pre-formed *empty* vesicles led to the same

observation. The total fluorescence intensity dropped down to values less than 10% of the initial intensity (triangles). These results prove that the presence of PS-*b*-PAA vesicles did not have any measurable effect on the enzymatic as well as the quenching reaction.

However, if trypsin and R110-Arg₂ were *both* incorporated during the formation of the vesicles and the quencher was added after 15 minutes, the total intensity decreased to nearly ~ 50% of the original level within 1 hour. (The high residual intensity does not account for a high residual product concentration since the enzymatic reaction did not reach steady-state). This significant level of residual fluorescence emission intensity must originate from the fluorescent product R110 of the enzymatic reaction that is located *inside* the vesicles (squares). Thus, a significant fraction of trypsin and R110-Arg₂ added during the vesicle preparation was indeed encapsulated and subsequently reacted *inside* the vesicles.

The ratio of encapsulated to total substrates was determined analogously by quenching the emission of the non-encapsulated fluorescent product R110 by the addition of sodium nitrite. Since the vesicle wall is impermeable to the quencher, R110 generated inside the vesicles is not affected. The loading percentage is defined as the residual fluorescence emission intensity after complete quenching (I_q) divided by the total fluorescence emission intensity before quenching (I_o).

In the experiment solution of trypsin and R110-Arg₂ was added drop-wise to the polymer solution in THF. Initially micelles were formed, at water contents in excess of 10 - 15 vol% vesicle formation is expected based on reports of Eisenberg *et al.*²⁰ After a specific water content was reached, an aliquot of the solution was removed and mixed with an excess of aqueous sodium nitrite solution. The fluorescence emission intensity of the solution with and without quencher was then measured to determine the encapsulation percentage as the intensity ratio between the encapsulated and all substrates in the solution.

Figure 5.4b shows the encapsulated R110-Arg₂ concentration plotted as a function of water content of the system during the formation of vesicles. The concentration of substrate inside the vesicles remained almost zero, when no vesicles were formed in the solution. After the micelle-to-vesicle transition took place (at a water percentage of 10% to 15%, as indicated by the dash vertical lines in Figure 5.4b and c), a sharp increase in the concentration of the substrate as well as the ratio between the quenched solution to the original solution, *i.e.* the encapsulation percentage was observed. Further increasing the total concentration of substrate in the solution only

caused a slight increase of the concentration of substrate inside the vesicles, which indicates that more substrate molecules were situated outside of the vesicles. This trend continued and eventually led to a decrease of the encapsulation percentage to 10% as the water percentage of the system reached 50% (vesicle size \sim 100 nm), shown in Figure 5.4c (squares). The volume ratio between the volume of vesicle interior and the total volume of the aqueous solution was also calculated and plotted in Figure 5.4c (circles) and it is seen that the ratio decreases as the vesicle size increases, displaying the same trend as the experimental results. However, the actual loading percentage is lower than the volume ratio at all vesicles.

This observation indicates that during the formation of the vesicles, most encapsulated substrate molecules are confined into the vesicles during the micelle-to-vesicle transition. After the transition takes place, the addition of substrate solution increases the size of the vesicles due to the balance of entropy loss and increase of interfacial energy, as discussed in Chapter 3. However, the size increase of the vesicles only marginally increases the concentration of substrate molecules inside the vesicles. The result of this experiment can also provide some insight into the formation mechanism of the vesicles. It is documented that vesicle fusion and fission are responsible for the size equilibration of the vesicles, since the critical micelle concentration of the polymers is very low and single chain incorporation can be neglected.¹⁴ Therefore, after the original vesicle formation at the micelle-to-vesicle transition, substrate molecules are not encapsulated to a significant extent into the vesicles with further increasing the total concentration of substrate solution since the fusion of the vesicles did not incur a significant exchange of materials across the membrane. In addition to an estimate of the loading percentage, the determination of the ratio of encapsulated and free molecules in different stages of the vesicle formation process thus also provided insight into the mechanism of the formation process.

5.4 Study of kinetics of trypsin catalysis

Prior to the study of the kinetics of the enzymatic reaction confined inside the BCP vesicles, the reaction kinetics was first studied in solution. The utilization of the fluorogenic substrate R110-Arg₂ allowed us to directly follow the reaction kinetics by monitoring the increase in the fluorescence emission intensity of the reaction product R110. In order to prevent the influence of salt from affecting the reaction kinetics, no

buffer was used in the experiments. A typical set of fluorescence emission spectra recorded in a kinetics measurement is shown in Figure 5.5a.

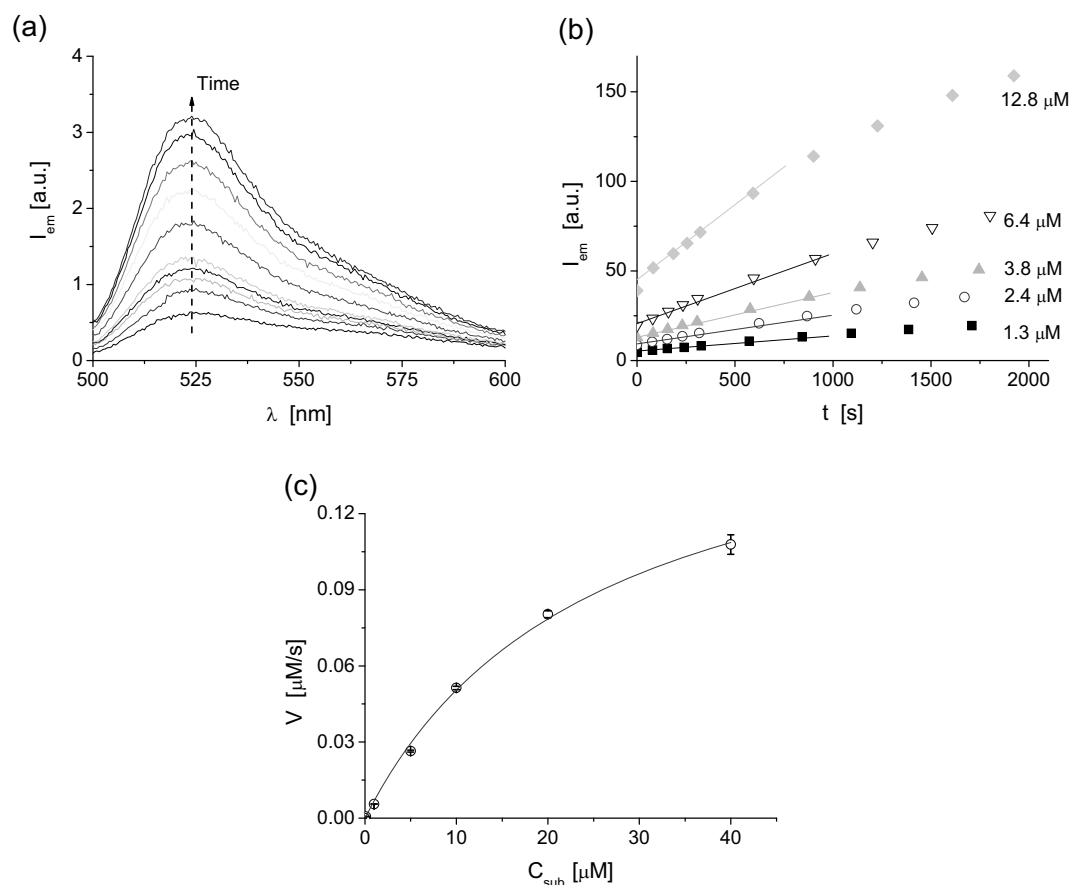


Figure 5.5 (a) Fluorescence emission spectra of enzymatic reaction product R110 at different reaction time intervals. ($C_{sub} = 12.8 \mu\text{M}$, $C_{enzyme} = 0.05 \mu\text{M}$) (b) Integrated fluorescence emission intensity of R110 as a function of time for different substrate concentrations (reaction in solution). From the plot the rate of the reaction was obtained (The lines are linear fits to the corresponding data sets). (c) Michaelis-Menten plot of trypsin ($c = 5 \times 10^{-8} \text{ M}$) in solution. The solid line represents a fit to the hyperbolic function.

As the reaction progresses, R110-Arg₂ is converted to R110, resulting in the increase of emission intensity at 525 nm, which is the peak emission of the fluorescent product. Figure 5.5b shows the fluorescence intensity (integrated over the whole spectrum as shown in Figure 5.5a) as a function of reaction time. The concentration of trypsin was kept constant ($c = 5 \times 10^{-8} \text{ M}$), while the concentration of R110-Arg₂ was varied between 1.28 μM and 12.8 μM in a THF/H₂O solvent mixture. As can be seen in Figure 5.5b, increased reaction rates were observed for increasing substrate concentrations. The initial rate of the reaction was obtained from the slope of the initial linear part of the plot. After the determination of the rate of the reaction with

different substrate concentrations, the rates were plotted against the substrate concentrations, as shown in Figure 5.5c.

The plot was fitted to a hyperbolic function (red line) according to the Michaelis-Menten equation:²¹

$$V = \frac{V_{\max} [S]}{K_M + [S]} \quad (5.1)$$

where V is the rate of the reaction, $[S]$ is the substrate concentration, K_M is the Michaelis-Menten constant and V_{\max} is the maximum rate of the reaction, from which the k_{cat} , catalytic turnover number of the enzyme can be calculated:

$$k_{cat} = \frac{V_{\max}}{[E]_t} \quad (5.2)$$

Fitting the data for different trypsin concentrations according to the Michaelis-Menten equation yields the catalytic turnover number of trypsin proteolysis of R110-Arg₂ as $3.17 \pm 0.14 \text{ s}^{-1}$ and the Michaelis-Menten constant as $26.6 \pm 2.5 \text{ }\mu\text{M}$. These data are in agreement with published literature values.¹⁶

Finally, trypsin and R110-Arg₂ were incorporated into the PS-*b*-PAA vesicles during the formation process. The vesicle preparation conditions were manipulated to encapsulate trypsin and R110-Arg₂ into vesicles with different diameters. The progress of the enzymatic reaction was monitored and the kinetic parameters were determined in the same way as for reactions in solution. The Michaelis-Menten plots of trypsin partly encapsulated in vesicles with different diameters are shown in Figure 5.6.

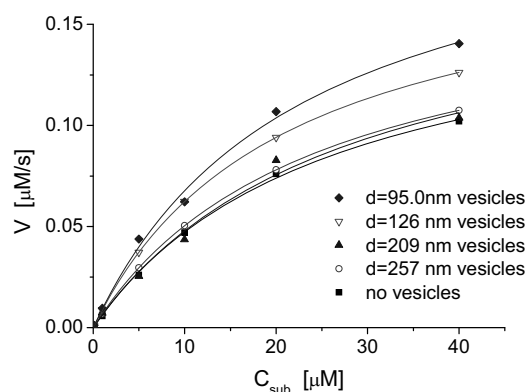


Figure 5.6 Michaelis-Menten plots of enzymatic reactions catalyzed by trypsin ($c = 5 \times 10^{-8} \text{ M}$) partly encapsulated in vesicles with different external diameters (as indicated in the legend), as well as in the absence of vesicles. The solid lines are hyperbolic fits to the corresponding data sets.

The catalytic turnover number (k_{cat}) was found to possess a higher value than the value obtained in solution (3.17 s^{-1}), if trypsin and R110-Arg₂ were incorporated in the vesicles. These values also showed a clear dependence on the size of the vesicles. As the size of the vesicles decreased, the observed k_{cat} possessed a more elevated value compared with the value of k_{cat} in solution. The Michaelis-Menten constant (K_M), which is a measure of the enzyme-substrate affinity, showed the opposite tendency. All K_M values obtained for partially encapsulated trypsin and R110-Arg₂ were lower than the value found in solution and the smaller the vesicle, the lower the value of K_M .

Since also a large amount of the trypsin and R110-Arg₂ resided outside the vesicles during the experiments, we observed the overall kinetics of the reaction both inside and outside the vesicles. Based on three assumptions, the kinetic parameters of the *encapsulated* trypsin can be calculated. (1) The reaction of trypsin both outside and inside the vesicles follows the Michaelis-Menten kinetics, (2) the encapsulation efficiencies for R110-Arg₂ and trypsin are identical, and (3) the photophysics are not changed for encapsulated fluorophores. Measurements of the same quantum yield of both encapsulated and free fluorophores support the validity of the later assumption.

The apparent rate of the reaction (V_{total}) can be expressed as follows:

$$V_{total} = -\frac{d[S]_{total}}{dt} = -\frac{d[S]_{out}}{dt} - \frac{d[S]_{in}}{dt} = V_{out} + V_{in} \quad (5.3)$$

The kinetic parameters of the encapsulated trypsin, $k_{cat,in}$ and $K_{M,in}$, can be calculated by using the Michaelis-Menten equation and equation (5.3):

$$V_{in} = \frac{V_{max,in} [S]_{in}}{K_{M,in} + [S]_{in}} = \frac{V_{max,total} [S]_{total}}{K_{M,total} + [S]_{total}} - \frac{V_{max,out} [S]_{out}}{K_{M,out} + [S]_{out}} \quad (5.4)$$

Since the encapsulation percentage was determined using fluorescence quenching, the percentage of encapsulated and non-encapsulated molecules is known. Therefore the rate of the reaction of encapsulated trypsin can be calculated and plotted as a function of the concentration of encapsulated R110-Arg₂. The kinetic parameters of encapsulated trypsin obtained by fitting the plot according to the Michaelis-Menten equation are summarized in Table 5.2.

The values of k_{cat} of the encapsulated trypsin were found to be as high as five times the value observed in solution and the values of K_M are one order of magnitude lower than the bulk value. In addition, a significant difference in values of k_{cat} among trypsin encapsulated in vesicles with different sizes was observed. The value of k_{cat} of trypsin encapsulated in $d_{ext} = 95 \text{ nm}$ vesicles (internal volume of 0.05 aL) is twice the

value of k_{cat} of trypsin encapsulated in $d_{ext} = 257$ nm vesicles (internal volume of 4.6 aL). In Figure 5.7 the kinetic parameters of trypsin in vesicles with different sizes are plotted against the reaction volume. The parameters of trypsin in solution are also shown in the graph (data point at $V = 2$ mL).

Table 5.2 Kinetic parameters of enzymatic reaction under different conditions.^[a]

	Average k_{cat} (s^{-1})	Average K_M (μM)
Free enzyme	3.17 ± 0.14	26.6 ± 2.5
Enzyme with $d_{ext} \sim 257$ nm vesicles	3.45 ± 0.13	24.2 ± 2.5
Enzyme with $d_{ext} \sim 209$ nm vesicles	3.64 ± 0.10	24.0 ± 2.6
Enzyme with $d_{ext} \sim 126$ nm vesicles	3.83 ± 0.13	20.7 ± 5.1
Enzyme with $d_{ext} \sim 95$ nm vesicles	4.10 ± 0.11	18.4 ± 1.3
Encapsulated enzyme in $d_{ext} \sim 257$ nm vesicles ^[b]	6.84 ± 2.9	1.36 ± 0.30
Encapsulated enzyme in $d_{ext} \sim 209$ nm vesicles ^[b]	8.70 ± 3.0	1.28 ± 0.20
Encapsulated enzyme in $d_{ext} \sim 126$ nm vesicles ^[b]	11.4 ± 3.5	1.16 ± 0.18
Encapsulated enzyme in $d_{ext} \sim 95$ nm vesicles ^[b]	14.7 ± 3.6	1.12 ± 0.15

[a] The errors of the kinetic parameters are the standard errors of the mean of n measurements (for experiments in solution $n = 15$, for experiments with the presence of vesicles $n = 3$). [b] Calculated values.

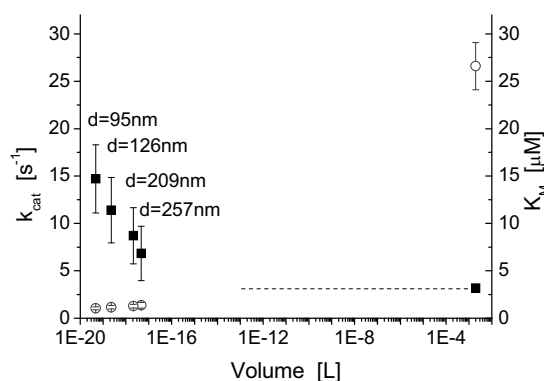


Figure 5.7 Kinetic parameters of trypsin proteolysis in confinement plotted against internal volume of the PS_{139} - b - PAA_{17} vesicles. Squares: catalytic turnover numbers (k_{cat}). Circles: Michaelis-Menten constants (K_M).

In these experiments the average number of substrate molecules in a single vesicle of $d_{ext} = 95$ nm (internal volume of 0.05 aL) ranged from ~ 800 to $\sim 40,000$, depending on the concentration utilized. The average number of encapsulated enzymes was estimated to be ~ 3 . By contrast, the number of molecules in a vesicle of $d_{ext} = 257$ nm (internal volume of 4.6 aL) ranges from $\sim 80,000$ to $\sim 4,000,000$ substrate and ~ 300 enzyme molecules. Under these conditions (for vesicles with a volume of 0.05 aL),

which approach the single enzyme level, the reactivity of trypsin depends markedly on the size of the nanocontainer. Compared to the reported enzyme efficiency ($k_{cat} / K_M = 1.7 \times 10^5 \text{ s}^{-1}\text{M}^{-1}$) of trypsin and R110-Arg₂,¹⁶ we observed a similar efficiency of free trypsin ($1.2 \times 10^5 \text{ s}^{-1}\text{M}^{-1}$) and a significantly increased efficiency of $k_{cat} / K_M = 1.6 \times 10^7 \text{ s}^{-1}\text{M}^{-1}$ when trypsin was encapsulated in vesicles ($d_{ext} = 95 \text{ nm}$).

This apparent enhancement of the reactivity of trypsin can be attributed to several reasons. Chiu *et al.* utilized a simple diffusion model to estimate the collision frequency of a single substrate and a single enzyme inside a vesicle.²² The vesicle was treated as a spherical container with a hard wall. The authors did not account for any charge or hydrophobic interactions between the wall and the encapsulated molecules. The simulation results showed that the collision frequency between the substrate and the enzyme, as well as the collision frequency between the two encapsulated molecules and the wall, increased dramatically as the size of the vesicle decreased. Moreover, collisions between the two encapsulated molecules and the wall were more than 2 orders of magnitude more frequent than collisions between the substrate and the enzyme. This implies that interactions between the surface and encapsulated molecules (also the enzyme-substrate complex) may result, in our case, in a significant effect on the rate and possibly also the mechanism of the reaction, since the probability of collisions between the enzyme and substrate will occur at or near the wall is increased. As both k_{cat} and K_M were found to be altered, it is reasonable to conclude that the rate constants of the three processes involved in enzyme-substrate complex formation and reaction to the product are affected to a different extent.

Furthermore, interactions between the encapsulated molecules and the wall cannot be ignored in our case because of the presence of carboxylic acid groups in PS-*b*-PAA vesicle system. According to zeta-potential measurements of PS-*b*-PAA vesicles, the outer surface of the vesicles has a negative potential of $\sim -50 \text{ mV}$, thus the carboxylic acid groups on the BCP chain are (partly) deprotonated. During the experiments carried out under pH 6 - 7, trypsin, which has an isoelectric point of 8.2,²³ is positively charged and attracted to the vesicle wall.

Both the increased collision frequency and the enzyme-vesicle wall interactions may affect the rate of the conformational transitions and folding of the enzyme, as reported by Nolte and co-workers for CALB on the basis of single molecule studies.⁵ Hence catalytically active states may become more populated. In conclusion, the volume confinement of the ultra-small containers is likely responsible for the observed enhancement of trypsin reactivity.

However, we must emphasize that the structure of BCP vesicles is more complicated than that of *e.g.* micelles and a systematic analysis of the reaction kinetics in vesicles that takes their small sizes into account is yet absent. In the literature, as also applied here, a simplified kinetic analysis was performed with the help of suitable equations for infinite space. To truly unravel the nature of the kinetics of (bio)chemical reactions in small volumes, single molecule studies should be carried out to avoid possible ensemble averaging. Single molecule studies on the kinetics of enzymatic reactions have been reported by different groups (see Chapter 2),⁴ yet none of them were performed with enzymes confined in 3D containers.

A difficulty in these studies lies in the initiation and control of the reactions, since either the reagents had to diffuse through the barrier of the container, which rendered the entire reaction diffusion-controlled, or the finite amount of encapsulated reagents limited the time scale of the process. Therefore it is also essential to control and initiate the reactions at the single molecule level. With all these tools at hand, we believe it is possible to monitor reactions of single enzymes inside an ultra-small container in real time, as in its natural state, and to unravel the relation of vesicle size and single enzyme reactivity.

5.5 Conclusion

Atto-liter volume PS-*b*-PAA vesicles with controlled external (internal) diameters ranging from 95 (45) nm to 257 (207) nm were successfully prepared and enzyme trypsin and fluorogenic substrate R110-Arg₂ were loaded into the vesicles. The catalytic turnover number (k_{cat}) and the Michaelis-Menten constant (K_M) for the unrestricted reaction of trypsin in solution and the reaction confined in the vesicles were found to differ significantly. While the values of k_{cat} of trypsin encapsulated in vesicles with different diameters were always higher than that of trypsin in solution, the values of K_M were decreased. Compared to the reaction in solution, the enzyme efficiency (k_{cat} / K_M) increased by two orders of magnitude. This observed higher reactivity of encapsulated trypsin is attributed to the molecular confinement inside the vesicles, which causes higher collision frequencies between the reagents as well as higher collision frequencies between the encapsulated molecules and the container wall.

5.6 Experimental

PS₁₃₉-*b*-PAA₁₇ (the subscripts denote the number of repeat units for each block; $M_n = 15.7$ kg/mol, polydispersity index = 1.07) was purchased from Polymer Source Inc. (Dorval, Canada). Enzyme bovine pancreas trypsin and the fluorescence quencher sodium nitrite were purchased from Sigma-Aldrich Co. (St. Louis, MO, USA). The fluorogenic substrate R110-Arg₂ was purchased from Molecular Probes/Invitrogen Co. (Carlsbad, CA, USA). THF (AR grade) was purchased from Biosolve B. V. (Valkenswaard, the Netherlands). Milli-Q water was produced by a Millipore Synergy system (Billerica, MA, USA). All chemicals were used as received.

PS-*b*-PAA vesicles were prepared by first dissolving the polymer in THF with various initial concentrations, then adding Milli-Q water as a precipitant into the polymer solution until a given water percentage was reached, while the entire system was under vigorous stirring using a magnetic stirring bar at ~ 600 rpm. After stirring for overnight, the solution mixture was subjected to dialysis for 72 hours to remove organic solvent residue and low molecular weight impurities. Dialysis was carried out using Spectra/Por 7 dialysis tubing from Spectrum Europe B.V. (Breda, the Netherlands) with a molecular weight cut off of 50 kD. Enzymes and substrates were encapsulated in the vesicles by dissolving both enzymes and substrates in water followed by immediate mixing. To compare the kinetics of the enzymatic reaction in solution (temperature = 25°C) and in PS-*b*-PAA vesicles, a series of substrate concentrations of 0.1, 1, 5, 10, 20, 40 μM and different enzyme concentrations were used in both cases. To determine the influence of water percentage on the size of vesicles or the encapsulation percentage of the fluorogenic substrates, an aliquot of the mixture was withdrawn from the system to allow further characterization, after a certain amount of water or enzyme/substrate solution was added into the system.

The size of PS-*b*-PAA vesicles was determined with a Malvern Zeta-sizer 4000 (Malvern Corp., Malvern, UK) at 25°C using a laser wavelength of 633 nm and a scattering angle of 90°. The CONTIN method²⁴ was applied for data processing. The size, count rate and poly-dispersity index (PDI) were determined. The zeta-potential of the vesicles was measured using Laser Doppler Velocimetry with a Malvern Zeta-sizer 2000 (Malvern Corp., Malvern, UK), in which the velocity of the vesicles moving in a fluid medium that is exposed to an electric field is measured. Measurements were carried out at 25°C using 1 kHz modulator frequency and 120V cell drive voltage.

AFM images were obtained under ambient conditions in tapping mode with a NanoScope IIIa multimode atomic force microscope (Digital Instruments/Veeco, Santa Barbara, CA, USA) using silicon cantilevers with resonance frequencies of 200-500 kHz (type PPP-NCH-W, Nanosensors, Wetzlar, Germany) and a J-scanner (Digital Instruments/Veeco).

TEM images were acquired using an analytical TEM instrument Philips CM30 (FEI, Hillsboro, OR, USA) equipped with a post-column GIF Tridiem energy filter system (Gatan, Inc., Pleasanton, CA, USA). Samples for TEM were prepared by directly depositing a droplet of vesicle dispersion onto a carbon-coated TEM grid. After evaporation of the solvent the grid was fixed onto the specimen holder and mounted into the vacuum chamber.

To follow the enzymatic reactions, fluorescence emission spectra were recorded using an Edinburgh F900 analytical instrument (Edinburgh Instruments Ltd., Livingston, UK). A Xe lamp was used as the light source and the excitation and emission slits were set to constant value (0.5 mm) in order to be able to compare the intensities from different samples. The spectra were recorded with 0.5 nm intervals and 0.2 s dwell time for the entire spectral range from 500 nm to 600 nm. A baseline correction of the spectra was carried out by subtracting the recorded emission spectrum of the pure solvent from the spectra of the samples. To ensure that the photophysical properties of R110 are independent of the local environment, we measured the integrated emission intensity I and the absorption at the excitation wavelength A for the sample (*sam*; R110 encapsulated in BCP vesicles) and the reference (*ref*; free R110 in solution), respectively, and compared the quantum yield of the sample to that of the reference:

$$\phi_{sam} = \frac{n_{sam}^2 I_{sam} A_{ref}}{n_{ref}^2 I_{ref} A_{sam}} \phi_{ref}. \text{ Here } n \text{ is the refractive index of the solution and } \phi \text{ denotes}$$

the quantum yield. ϕ_{sam} and ϕ_{ref} were found to possess identical values to within the experimental error (5%).

5.7 References and notes

- 1 A. Pohorille, D. Deamer, *TRENDS in Biotech.* 2002, **20**, 123.
- 2 V. W. Rodwell, P. J. Kennelly, in *Harper's Illustrated Biochemistry 26th ed*, Lange Medical Books/McGraw-Hill, New York, 2003.

- 3 D. T. Chiu, C. F. Wilson, F. Ryttsén, A. Strömberg, C. Farre, A. Karlsson, S. Nordholm, A. Gaggar, B. P. Modi, A. Moscho, R. A. Garza-López, O. Orwar, R. N. Zare, *Science* 1999, **283**, 1892.
- 4 (a) H. Lu, L. Xun, X. S. Xie, *Science* 1998, **282**, 1877; (b) L. Edman, Z. Földes-Papp, S. Wennmalm, R. Rigler, *Chem. Phys.* 1999, **247**, 11; (c) L. Edman, R. Rigler, *Proc. Natl. Acad. Sci. USA* 2000, **97**, 8266.
- 5 (a) K. Velonia, O. Flomenbom, D. Loos, S. Masuo, M. Cotlet, Y. Engelborghs, J. Hofkens, A. E. Rowan, J. Klafter, R. J. M. Nolte, F. C. de Schryver, *Angew. Chem. Int. Ed.* 2005, **44**, 560; (b) O. Flomenbom, K. Velonia, D. Loos, S. Masuo, M. Cotlet, Y. Engelborghs, J. Hofkens, A. E. Rowan, R. J. M. Nolte, M. van der Auweraer, F. C. de Schryver, J. Klafter, *Proc. Natl. Acad. Sci. USA* 2005, **102**, 2368.
- 6 R. F. Khairutdinov, N. Serpone, *Prog. Reaction Kinetics* 1996, **21**, 1.
- 7 (a) T. Nomura, J. R. Escabi-Perez, J. Sunamoto, J. H. Fendler, *J. Am. Chem. Soc.* 1980, **102**, 1484; (b) K. Kano, H. Kawazumi, T. Ogawa, *J. Phys. Chem.* 1981, **85**, 2998; (c) D. J. Barbar, D. A. Morris, J. K. Thomas, *Chem. Phys. Lett.* 1976, **37**, 481; (d) P. Herve, F. Nome, J. H. Fendler, *J. Am. Chem. Soc.* 1984, **106**, 8291; (e) P. Walde, S. Ichikawa, *Biomol. Engin.* 2001, **18**, 143.
- 8 J. L. Chávez, J. L. Wong, A. V. Jovanovic, E. K. Sinner, R. S. Duran, *IEE Proc. – nanobiotechnol.* 2005, **152**, 73.
- 9 W. Meier, *Chem. Soc. Rev.* 2000, **29**, 295.
- 10 D. G. Bucknall, H. L. Anderson, *Science* 2003, **302**, 1904.
- 11 D. E. Discher, A. Eisenberg, *Science* 2002, **297**, 967.
- 12 A. Graff, M. Sauer, P. van Gelder, M. Meier, *Proc. Natl. Acad. Sci. USA* 2002, **99**, 5064.
- 13 P. L. Soo, A. Eisenberg, *J. Polym. Sci. Part B: Polym. Phys.* 2004, **42**, 923.
- 14 L. Luo, A. Eisenberg, *Langmuir* 2001, **17**, 6804.
- 15 Trypsin, a serine protease found in the digestive system, was used as the model enzyme. Trypsin predominantly cleaves peptide chains at the carboxyl side of lysine or arginine, which can be easily monitored by applying a fluorogenic substrate R110-Arg₂.¹⁶ The cleavage of the peptide chains catalyzed by trypsin will liberate the fluorescent product R110, which will cause an increase in the emission intensity.
- 16 S. P. Leytus, L. L. Melhado, W. F. Mangel, *Biochem. J.* 1983, **209**, 299.
- 17 X. Zhang, H. Wang, N. Fu, H. S. Zhang, *Spectrochimica Acta Part A* 2003, **59**, 1667.
- 18 L. Zhang, A. Eisenberg, *Science* 1995, **268**, 1728.
- 19 L. Zhang, A. Eisenberg, *J. Am. Chem. Soc.* 1996, **118**, 3168.
- 20 A. A. Choucair, A. H. Kycia, A. Eisenberg, *Langmuir* 2003, **19**, 1001.
- 21 L. Michaelis, M. Menten, *Biochem. Z.* 1913, **49**, 333.
- 22 D. T. Chiu, C. F. Wilson, A. Karlsson, A. Danielsson, A. Lundqvist, A. Strömberg, F. Ryttsén, M. Davidson, S. Nordholm, O. Orwar, R. N. Zare, *Chem. Phys.* 1999, **247**, 133.
- 23 R. A. Anderson, S. A. Beyler, S. R. Mack, L. J. Zaneveld, *Biochem. J.* 1981, **199**, 307.
- 24 S. W. Provencher, *Biophys. J.* 1976, **16**, 27.

Chapter 6

Study of α -Chymotrypsin Catalysis under Confinement using Block Copolymer Vesicles

In this chapter the catalytic reactivity of enzyme α -chymotrypsin under the confinement of polystyrene-*block*-poly(acrylic acid) (PS-*b*-PAA) vesicles was investigated in order to test confinement effects on the kinetics of the reaction. Enzyme and substrate molecules were encapsulated into PS-*b*-PAA vesicles with diameters from 100 nm up to 250 nm during the formation of vesicles. The encapsulation percentages of the enzymes and substrates were determined based on the ratio of specific absorption of respective molecules before and after dialysis. The encapsulation percentages of enzymes and substrates in vesicles with identical size were practically the same. Interestingly, the loading efficiency increased with decreasing vesicle size. The kinetics of the α -chymotrypsin catalyzed hydrolysis of *N*-succinyl-Ala-Ala-Phe-7-amido-4-methylcoumarin (AMC) was evaluated following the increase of the specific absorption of the product 7-amino-4-methylcoumarin by UV-Vis spectroscopy. The catalytic turnover numbers and Michaelis-Menten constants of the enzymatic reactions inside the vesicles were obtained by subtracting the kinetics of unencapsulated reagents ($k_{cat} = 0.122 \pm 0.006 \text{ s}^{-1}$; $K_M = 27.3 \pm 2.1 \text{ }\mu\text{M}$) from the overall kinetics. The values of the catalytic turnover number obtained for reactions in vesicles with different sizes showed a significant increase (up to ~ 15 times compared to bulk value) with decreasing vesicle volume, while the values of the Michaelis-Menten constant decreased, respectively. This increase in reactivity of α -chymotrypsin is attributed to the effect of the vesicle walls, which included two aspects: (1) the finite space (confinement) where the reagents were allowed to diffuse and (2) a strong vesicle-wall interaction which further localized the spot where the reagents can interact.

6.1 Introduction

Recently, considerable efforts are focused on engineering molecular systems that mimic functional aspects of cells.¹ A common feature of many cell function mimics is the containment of a small, aqueous volume. Small volume containers obviate the need for mixing and establish local conditions that are favorable for *e.g.* enzyme function. Furthermore small volumes reduce the number of molecules needed for

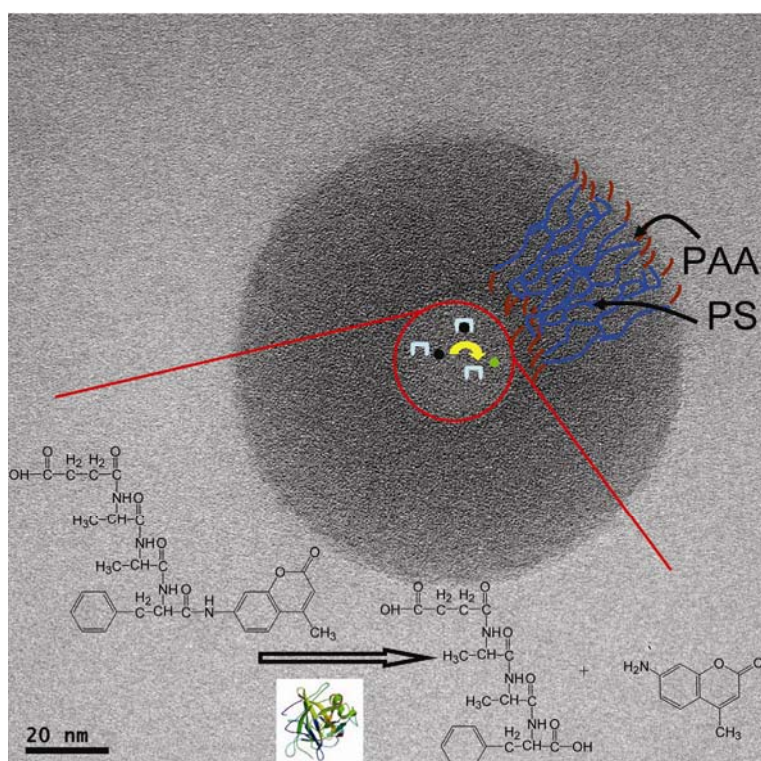
carrying out a function. The ability to contain small volumes of liquid (zepto- to atto-liter) is hence a critical aspect of biological cells, enables the creation of synthetic cell-like systems² and can be used for understanding molecular reaction systems and self organization at the cellular scale.³⁻⁸ In addition, such enclosed volumes are ideal for studying reactions that involve single molecules. On the application side, miniaturization of reactor volumes may result in the creation of massively parallel analytical systems.⁹⁻¹¹

Studies of the reaction kinetics in restricted or confined spaces are not only essential for a better understanding of the (bio) chemical reactions in nanostructures, they also help to design new nanosystems to carry out efficient catalytic processes.¹² A confined chemical reaction refers to the situation when the volume of the system is too small to allow the use of conventional infinite space theories of chemical kinetics. In such cases, a reaction cannot be modeled by an infinite volume with a constant density, *i.e.* constant concentration of enclosed molecules.¹² Examples are micellar and vesicular systems,¹³⁻¹⁵ polymer coils in solution,¹⁶ zeolite structures,¹⁷ porous materials,¹⁸ silica gels¹⁹ and nanoparticles^{20, 21}. Common to these systems is that reactant molecules occupy space in restricted geometries. The reaction kinetics in such systems may differ from the kinetic behavior in infinite space. A study of the kinetic peculiarities of chemical processes in restricted systems may thus provide important information on their structures and dynamics.¹²

A previous study carried out on trypsin catalysis (Chapter 5) already showed an enhanced reactivity of the enzymes when they were encapsulated in PS-*b*-PAA vesicles.²² The values of the catalytic turnover number of trypsin encapsulated in vesicles with different diameters were always higher than that of free, non-encapsulated trypsin in solution. Compared to the reaction in solution, the enzyme efficiency (k_{cat} / K_M) increased by two orders of magnitude. The observed higher reactivity of encapsulated trypsin was attributed to a confinement effect caused by the vesicles, which resulted in higher collision frequencies between the reagents and between the encapsulated molecules and the container wall.²²

In order to further study the enzymatic reaction in nanocontainers and to extend our understanding on the volume confinement effect on the catalytic activity of different enzymes, PS₄₀₃-*b*-PAA₆₂ vesicles were utilized in this chapter as small volume containers to investigate catalytic reactivity of encapsulated α -chymotrypsin. Using the fluorogenic substrate AMC the kinetic parameters were obtained for the

unrestricted reaction in solution as well as for the reaction confined to the interior of polymeric vesicles with different sizes. (Scheme 6.1).



Scheme 6.1 Illustration of structural details overlaid on an individual PS_{403} - b - PAA_{62} vesicle (TEM image) and the encapsulated reagents enzyme α -chymotrypsin and substrate AMC (not to scale). The thick (40 nm) vesicle membrane consisted of PS, as visualized by TEM, provides the confinement of the reagents inside the nanocontainers. The hydrolysis of the substrate catalyzed by chymotrypsin results in the formation of the fluorescent product 7-amino-4-methylcoumarin, as shown in the scheme.

6.2 Results and discussion

6.2.1 Preparation of PS- b -PAA vesicles with different sizes

In order to carry out enzymatic reactions inside of PS- b -PAA vesicles and study possible size effects on the reactivity of the encapsulated enzymes, vesicles with different sizes were prepared by varying the initial polymer concentration (wt%) and water percentage in the solution (vol%) as discussed in Chapter 3. The diameter of the vesicles obtained was measured using dynamic light scattering (DLS) (Table 6.1). The membrane thickness (40 ± 2 nm), as determined from transmission electron

microscopy (TEM) images (Scheme 6.1), was found to be independent on the preparation conditions. Based on the parameters obtained, the internal volume of the vesicles was calculated assuming that the vesicles adapt an ideal hollow spherical structure. The volume of the containers was thus between zepto-liter (10^{-21} L) and atto-liter (10^{-18} L), which is on the same volumetric scale as observed for natural liposomes. The encapsulation of enzyme and substrate molecules was carried out using the same procedure as described in Chapter 5. No differences of vesicle size were observed among the empty vesicles and reagent-containing vesicles, in agreement with previous results.²²

Table 6.1 Vesicle size and preparation conditions.

Vesicle diameter (external)	Vesicle diameter (internal)	Internal volume	Initial polymer concentration	Water percentage
106 ± 8 nm	26 ± 9 nm	0.009 aL	1wt%	30vol%
123 ± 10 nm	43 ± 11 nm	0.042 aL	1wt%	50vol%
169 ± 26 nm	89 ± 26 nm	0.369 aL	2wt%	50vol%
180 ± 36 nm	100 ± 36 nm	0.523 aL	1wt%	70vol%
190 ± 54 nm	110 ± 54 nm	0.697 aL	2wt%	70vol%
245 ± 70 nm	165 ± 70 nm	2.351 aL	5wt%	50vol%

6.2.2 α -chymotrypsin catalysis in solution

The enzymatic reaction studied here is the hydrolysis of AMC catalyzed by α -chymotrypsin. This enzyme is a well known serine protease that selectively cleaves the hydroxyl side of tyrosine, tryptophan and phenylalanine due to the presence of aromatic rings in these amino acids. It is a globular protein with a molecular mass of 24,800 g/mol and dimensions of 4.0 nm × 4.0 nm × 5.1 nm.²³ The reaction of the hydrolysis is shown in Scheme 6.1.

Upon hydrolysis, the peptide sequence containing phenylalanine (Phe) is cleaved off from the substrate. Thereby the fluorescent product 7-amino-4-methylcoumarin is liberated, which has an absorption maximum at 345 nm. In our experiments the absorption of products after mixing of the enzyme and substrate was followed using UV-Vis spectroscopy. A series of typical spectra recorded during the enzymatic reaction is shown in Figure 6.1a.

During ten minutes of reaction time the absorption at 345 nm increased in an almost linear fashion, as shown in the inset of Figure 6.1a. After ~ 30 minutes the increase

slowed down before the absorption reached a constant level, indicating a near complete conversion of the substrates. It should be noted that in the spectra the decrease of the substrate absorption was also observed at 325 nm (downward arrow in Figure 6.1), in addition to the increase of the product absorption at 345 nm (upward arrow in Figure 6.1). At ~ 330 nm an isosbestic point can be distinguished, as at this wavelength the product and the substrate possess the same molar absorptivity. In order to separate the two peaks, a Lorentzian two peak fit was carried out on the data. The result of the fit on the spectrum recorded after 1 minute reaction time (bold curve) is shown in Figure 6.1b. From the fitting an absorption peak at 325.5 ± 2.0 nm and another peak at 346.8 ± 1.5 nm were found, which are in agreement with the literature values of the peak absorption of the substrate and product, respectively.²⁴

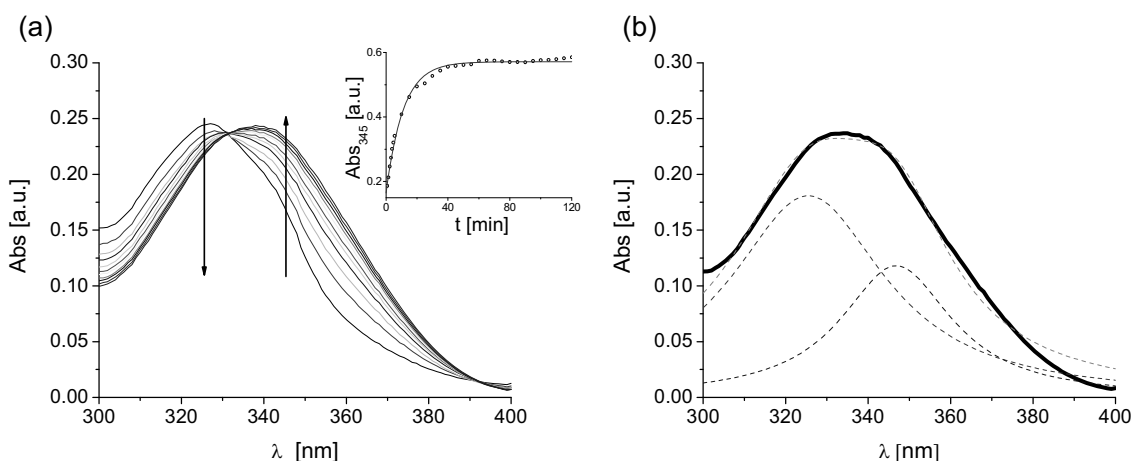


Figure 6.1 (a) Absorption spectra showing the progress of the enzymatic reaction. The specific absorption of the product at 345 nm increases, while the absorption of the substrate at 325 nm decreases, as indicated in the graph by the arrows. The inset shows the increase of product absorbance as a function of time. The initial linear part of the trace is used to calculate the rate of the reaction. (b) Lorentz two-peak fit on the spectrum with substrate concentration of $8.85 \mu\text{M}$ and enzyme concentration of $2 \mu\text{M}$ after a 1-minute reaction.

To evaluate the reaction kinetics, the initial reaction rate (V) was obtained from the slope of the increase of the product absorption for a reaction time of ≤ 10 minutes. The actual concentration of the product was calculated from the measured absorption of the product (extinction coefficient of 7-amino-4-methylcoumarin: $\epsilon = 16000 \text{ cm}^{-1}\text{M}^{-1}$). Different initial reaction rates were then calculated for experiments in which the substrate concentration was varied and the enzyme concentration was kept constant ($0.02 \mu\text{M}$). A plot between the initial reaction rates and the substrate concentrations according to the Michaelis-Menten kinetics theory was constructed (Figure 6.2).

The catalysis of α -chymotrypsin is known to follow Michaelis-Menten kinetics. In our analysis the plot was fitted to a hyperbolic function (solid line, $R^2 = 0.99$) according to the Michaelis-Menten equation:²⁵

$$V = \frac{V_{\max}[S]}{K_M + [S]} \quad (6.1)$$

where V is the rate of the reaction, $[S]$ is the substrate concentration, K_M is the Michaelis-Menten constant and V_{\max} is the maximum rate of the reaction, from which the k_{cat} , catalytic turnover number of the enzymatic reaction can be calculated:

$$k_{cat} = \frac{V_{\max}}{[E]_t} \quad (6.2)$$

In our study multiple experiments ($n = 10$) were carried out with the same enzyme concentration. The obtained average catalytic turnover number of the enzymatic reaction is $0.122 \pm 0.006 \text{ s}^{-1}$ and the Michaelis-Menten constant is $27.3 \pm 2.1 \text{ }\mu\text{M}$. The efficiency (k_{cat} / K_M) of the enzyme determined in our experiments is $4.5 \times 10^3 \text{ s}^{-1}\text{M}^{-1}$. The value of the enzyme efficiency using the same substrates reported in the literature is $1.9 \times 10^3 \text{ s}^{-1}\text{M}^{-1}$,²⁴ which is within the same order of magnitude with the value we obtained.

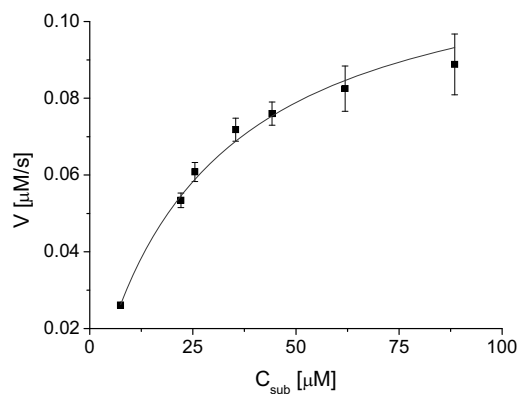


Figure 6.2 Michaelis-Menten plot of α -chymotrypsin catalyzed AMC hydrolysis in solution.

6.2.3 Encapsulation efficiency of enzymes and substrates inside PS-*b*-PAA vesicles

As it is difficult to remove the unencapsulated reagents before the reaction starts, our strategy was to first observe the overall enzymatic reaction, which comprises two contributions: the reaction that occurred outside the vesicles and the reaction that took place inside the vesicles. The kinetics of the latter process was obtained by subtracting

the kinetics of the unrestricted reaction, which follows the bulk reaction kinetics determined previously. In order to carry out this subtraction the exact percentage of the encapsulated and non-encapsulated reagents must be known. In our experiments, enzymes and substrates were mixed and encapsulated into PS-*b*-PAA vesicles with different sizes. After the reaction was completed, the solution was dialyzed against pure water using membranes with molecular weight cut off of 50 kDalton to remove the unencapsulated molecules. The specific absorption of the enzyme ($\lambda = 280$ nm) and the product ($\lambda = 345$ nm) before (Abs_o) and after the dialysis (Abs_d) were recorded using UV-Vis spectrophotometry and the ratio between Abs_d and Abs_o , *i.e.* the encapsulation percentage was calculated. A plot of the obtained encapsulation percentages of enzymes and substrates as a function of vesicle sizes is shown in Figure 6.3.

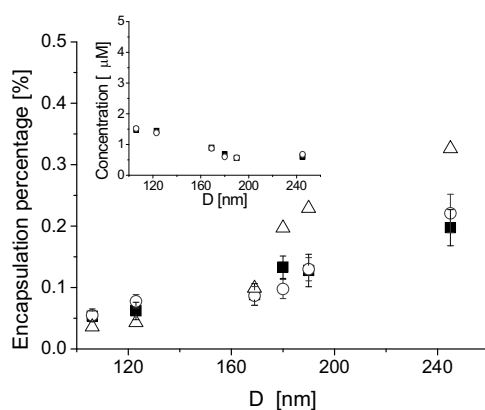


Figure 6.3 Encapsulation percentage of substrates (squares) and enzymes (circles) for different vesicle outer diameters. Triangles: Calculated ratio between the internal volume of the vesicles and the total volume of the aqueous solution. The inset shows the concentration of the encapsulated substrates (squares) and enzymes (circles) as a function of vesicle size.

As can be seen from the graph, the encapsulation percentages increased when the size of the vesicles was increased, as the total internal volume of the vesicles with respect to the total volume of the aqueous solution increased (triangles shown in Figure 6.3). There was no obvious difference in the encapsulation percentage of the enzymes (circles in Figure 6.3) and substrates (squares in Figure 6.3) when they were encapsulated into vesicles with the same sizes. An interesting observation was that molecules were more “efficiently” encapsulated into vesicles with smaller sizes (~123 nm) as the actual percentage of the encapsulated molecules was higher than the volume ratio between the interior volume and the total volume, which can be treated as the theoretical encapsulation percentage. When the molecules were encapsulated

into larger vesicles (> 180 nm), the obtained percentage was lower than the theoretical value. This is also seen as the concentration of the encapsulated substrates (squares) and enzymes (circles) decreases as the size of the vesicles increases, shown in the inset of Figure 6.3. Similar results were found in the literature²⁶: Stamou *et al.* used fluorescence microscopy to quantitatively determine the encapsulation efficiency (EE) of fluorescent molecules C₁₈-DiD and CoroNa Green in single lipid vesicles and they observed an *inverse* relation between EE and vesicle diameter. The mechanism behind this observation was not clear and the authors speculated it was related to the vesicle formation process.²⁶

6.2.4 α -chymotrypsin catalysis in PS-*b*-PAA vesicles

To analyze the reaction kinetics enzymes and substrates were encapsulated into vesicles with different sizes during the vesicle formation process. The progress of the enzymatic reaction was monitored the same way as described in the previous sections. The reaction rate was then calculated from the slope of the plot between the specific product absorption and reaction time. In Figure 6.4 the absorption of products formed in enzymatic reactions occurred in solution (filled symbols, different symbols represent different data sets) and partly encapsulated in vesicles (open symbols, $d = 123$ nm) with the same substrate concentration and enzyme concentration ($C_{sub} = 8.85$ μ M, $C_{enz} = 0.02$ μ M) were plotted as a function of time with their respective linear least squares fits.

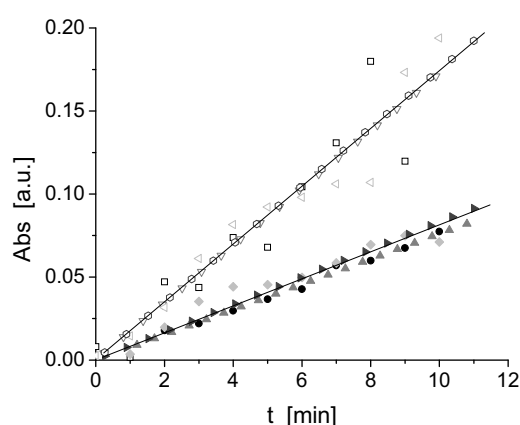


Figure 6.4 Kinetics plots of the enzymatic reaction in solution (filled symbols, different symbols indicate different experiments) and partly encapsulated in vesicles (open symbols) with the same total enzyme and substrate concentrations. The rate of the reaction is calculated from the slope of the linear fit (solid lines).

A clear difference was observed in the slope between the partly encapsulated enzymatic reaction and the reaction in solution. As the total concentration of the reagents were the same in both experiments, it is plausible that the reaction rate in the encapsulated system was higher, *i.e.* the reaction is faster compared to the system in solution. As will be shown below, this enhancement of the reaction rate cannot be explained by the increase in concentration observed for small vesicles (Figure 6.3).

Subsequently the reaction rates in the encapsulated system as well as the bulk system with different substrate concentrations were determined and the resulting Michaelis-Menten plots of enzymes partly encapsulated in vesicles with different diameters are shown in Figure 6.5.

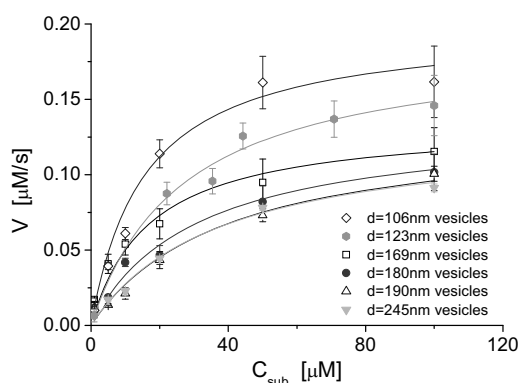


Figure 6.5 Michaelis-Menten plots of enzymatic reactions occurring partly inside of vesicles with different sizes as indicated in the legend. The substrate concentration refers to the nominal concentration. The solid lines represent hyperbolic fits to the data.

As can be seen in the graph, the overall reaction rates possessed a higher value for the same substrate concentration when the enzymes and substrates were encapsulated into vesicles with smaller sizes. Fitting the data to the Michaelis-Menten equation provided the apparent kinetic parameters of the enzymatic reactions in vesicles with different sizes, listed in the first two columns of Table 6.2.

Finally the kinetic parameters of the encapsulated enzymatic reactions were calculated based on the same procedure as described in Chapter 5. The apparent rate of the reaction (V_{total}) is expressed as follows²²:

$$V_{total} = -\frac{d[S]_{total}}{dt} = -\frac{d[S]_{out}}{dt} - \frac{d[S]_{in}}{dt} = V_{out} + V_{in} \quad (6.3)$$

Assuming the encapsulated enzymatic reaction follows Michaelis-Menten kinetics, the kinetic parameters of the encapsulated α -chymotrypsin, $k_{cat,in}$ and $K_{M,in}$, can be calculated by using equation (6.1) and (6.3):

$$V_{in} = \frac{V_{\max in} [S]_{in}}{K_{Min} + [S]_{in}} = \frac{V_{\max total} [S]_{total}}{K_{Mtotal} + [S]_{total}} - \frac{V_{\max out} [S]_{out}}{K_{Mout} + [S]_{out}} \quad (6.4)$$

As the encapsulation percentage (EP) was determined both for enzymes and substrates, the reaction rates of encapsulated enzymes (V_{in}) were calculated and plotted as a function of encapsulated substrate concentration ($[S]_{in}$). The kinetic parameters of encapsulated enzymatic reactions obtained by fitting the plot according to the Michaelis-Menten equation are summarized in Table 6.2.

Table 6.2 Kinetic parameters of the enzymatic reactions in solution as well as in vesicles with different sizes.

D_{avg} (external)	Apparent k_{cat}	Apparent K_M	Encapsulated k_{cat}	Encapsulated K_M
Bulk	$0.122 \pm 0.006 \text{ s}^{-1}$	$27.3 \pm 2.1 \text{ }\mu\text{M}$	-	-
106 nm	$0.219 \pm 0.028 \text{ s}^{-1}$	$23.0 \pm 4.1 \text{ }\mu\text{M}$	$1.71 \pm 0.21 \text{ s}^{-1}$	$1.07 \pm 0.13 \text{ }\mu\text{M}$
123 nm	$0.189 \pm 0.024 \text{ s}^{-1}$	$27.1 \pm 2.8 \text{ }\mu\text{M}$	$0.99 \pm 0.13 \text{ s}^{-1}$	$1.64 \pm 0.18 \text{ }\mu\text{M}$
169 nm	$0.139 \pm 0.007 \text{ s}^{-1}$	$29.6 \pm 0.9 \text{ }\mu\text{M}$	$0.33 \pm 0.03 \text{ s}^{-1}$	$2.25 \pm 0.13 \text{ }\mu\text{M}$
180 nm	$0.135 \pm 0.011 \text{ s}^{-1}$	$30.3 \pm 3.0 \text{ }\mu\text{M}$	$0.26 \pm 0.05 \text{ s}^{-1}$	$2.78 \pm 0.32 \text{ }\mu\text{M}$
190 nm	$0.133 \pm 0.012 \text{ s}^{-1}$	$28.9 \pm 5.0 \text{ }\mu\text{M}$	$0.21 \pm 0.04 \text{ s}^{-1}$	$3.24 \pm 0.30 \text{ }\mu\text{M}$
245 nm	$0.130 \pm 0.007 \text{ s}^{-1}$	$27.3 \pm 3.8 \text{ }\mu\text{M}$	$0.17 \pm 0.02 \text{ s}^{-1}$	$3.87 \pm 0.26 \text{ }\mu\text{M}$

The errors of the kinetic parameters are the standard errors of the mean of n measurements (for experiments in solution $n = 10$, for experiments with the presence of vesicles $n = 4$)

The average number of molecules in a single vesicle ($d = 106 \text{ nm}$) was estimated to be close to 1 for enzymes and from tens to thousands for substrates. Under these conditions which are on the single molecule level, it is expected that the behavior of the molecules depends strongly on the size of the container. The efficiency (k_{cat} / K_M) of the enzyme encapsulated in vesicles with $d = 106 \text{ nm}$ was calculated to be $1.6 \times 10^6 \text{ s}^{-1}\text{M}^{-1}$, three orders of magnitude higher than that of the enzyme in solution ($4.5 \times 10^3 \text{ s}^{-1}\text{M}^{-1}$).

A significantly higher value of k_{cat} of the encapsulated enzyme (14 times higher in the case of enzymes and substrates encapsulated in vesicles with $d = 106 \text{ nm}$) was found compared to the value observed in solution. The values of K_M are one order of magnitude lower than the bulk value. The values of k_{cat} and K_M were plotted as a function of diameter of the vesicles in Figure 6.6a.

A pronounced dependence of the kinetic parameters on the size of the vesicle is observed in the figure.^a The data was fitted to a power-law function $y = ax^b$, shown in Figure 6.6a as a solid line. The exponent (b) obtained from the fit is -3 with a coefficient of determination (R^2) of 0.993. The collision frequency between the enzyme and substrate inside a spherical container, which is closely related to the reaction rate, obeys the same size dependency ($\omega_{ES} = AR^{-3}$) as reported by Chiu *et al.*²⁸ (see section 2.5.2 and Figure 2.24 in Chapter 2).

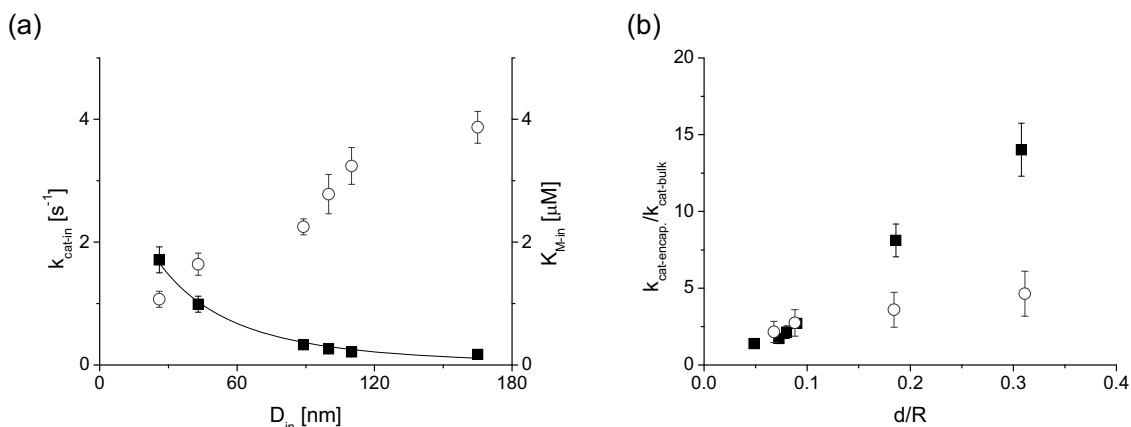


Figure 6.6 (a) Kinetic parameters of the enzymatic reactions (squares: k_{cat} ; circles: K_M) occurred inside the vesicles with different sizes subtracted from the apparent kinetic parameters plotted as a function of vesicle diameter. The solid line is a fit to the data according to $y = ax^b$, with $b = -3$ and $R^2 = 0.993$. (b) The ratio $k_{cat-encap}/k_{cat-bulk}$ plotted as a function of the ratio between the size of α -chymotrypsin ($d = 4$ nm) and the inner radius of the container (R) (squares). The data set obtained from the study of trypsin catalysis (Chapter 5) is also plotted (circles).

The confinement of reagents inside a spherical volume was studied before by Khairutdinov *et al.*¹² (see section 2.5.1 in Chapter 2) The problem of bimolecular reaction kinetics inside the sphere volume was solved using the solution of a similar problem, 3D heat flow survival probability, obtained by Carslaw and Jaeger.²⁹ It was found that the rate constant in confined space k_q , depended on the relative size of the reagent molecules and of the sphere.

The dependence for the current enzyme-catalyzed reaction is illustrated in Figure 6.6b, which presents $k_{cat-encap}/k_{cat-bulk}$ as a function of d/R , where d is the approximate

^a The enhancement of k_{cat} cannot be attributed to merely concentration deviation, as a 14 times enhancement would lead to an encapsulation percentage of more than 80%, which is physically impossible according to the internal volume of the vesicles and the size of the enzyme. Previous study showed that ionic strength (I) has an effect on the reactivity of surface-bounded chymotrypsin. However, the value of k_{cat} elevated only ~ 1.5 times when I was increased from 0.01 to 2.00 M, and the enzyme efficiency remained in the same order of magnitude.²⁷

diameter of α -chymotrypsin (4 nm) and R represents the radius of the aqueous interior of the vesicle. The experimental data obtained for trypsin (Chapter 5) is plotted in the same graph as well.

It can be clearly seen that the data for α -chymotrypsin and the data for trypsin show different slopes. This difference may be explained by the interaction between the enzymes and the surface of the vesicle. In our experimental conditions (pH 6 - 7), the carboxylic acid groups presented at the surface of PS-*b*-PAA vesicles were partly deprotonated (pK_A (acrylic acid) = 4.25) as determined from the zeta-potential experiments (~ -50 mV) and were thus negatively charged. α -chymotrypsin, which possess an isoelectric point (pI) of 10.5,³⁰ has a higher degree of ionization as compared to trypsin ($pI = 8.2$).³¹ Therefore, α -chymotrypsin was significantly biased to reside near the vesicle wall during the reaction, which further hindered the movement of the enzyme in the confined space and increased the probabilities of enzyme-substrate interaction near the wall. The reactions thus might occur at or near the wall because of collisions between the two-dimensionally diffusing molecules rather than three-dimensionally. This behavior can be understood as a “higher local concentration” of enzymes and substrates near the vesicle wall. This is reflected in the increase of rate constants, as vesicles with smaller sizes have a higher surface-to-volume ratio, thus a more profound enzyme-wall interaction. In the case of vesicles with larger sizes, the enhancement of α -chymotrypsin reactivity is comparable with the results from the study of trypsin catalysis.

Although ensemble studies, as carried out in our study described here, already led to interesting results that were not observed before, we believe it will be highly desirable to perform enzymatic reactions on a single enzyme level and to observe the reaction occurring inside individual containers in real-time. It should be noted that the number of encapsulated molecules in a single vesicle in our study is an average value and the actual number of enzymes encapsulated per container would fluctuate around this number. Empty vesicles are expected to present among the enzyme-containing vesicles. To have a precise evaluation on the kinetics, a mathematical approach of stochastic modeling (instead of deterministic modeling), which is absent in the literature, should be developed to allow the fluctuation of the concentration (number) of the encapsulated species. Also it is well known that the catalytic activity of individual enzymes can differ from each other when they possess different conformational states.³² Under the conditions in our study, the strong enzyme-wall interaction may alter the conformational states and state transitions of the enzymes as

these will affect the corresponding elementary processes to a different extent and subsequently alter the kinetics. The change in conformation as well as the catalytic activity of the enzyme can only be observed by single molecule detection as it will otherwise be averaged out by ensemble measurements. A single enzyme was loaded into liposomes and large deviation in the enzyme activities, which was concealed by ensemble averaging, was observed.³³

We believe that single molecule studies carried out in nanocontainers would allow us to unravel the nature of the kinetics of (bio)chemical reactions in finite/confined space and that the future research will in part focus on the study of single enzyme reactions in nanocontainers. By systematically altering the physics of the confined environment, additional insight into single enzyme kinetics may be obtained.

6.3 Conclusion

α -chymotrypsin and its fluorogenic substrate AMC were encapsulated into PS₄₀₃-*b*-PAA₆₂ vesicles with different sizes. The encapsulation percentages of the enzymes and substrates were found to be the same when loaded into vesicles with the same size. The efficiency of the encapsulation increased as the size of the vesicles decreased. The values of catalytic turnover number (k_{cat}) of the enzymatic reactions encapsulated in vesicles with different diameters were always higher (15 times for the most pronounced enhancement) than that of the enzymatic reactions in solution, the values of Michaelis-Menten constant (K_M) were decreased. Size dependence of the k_{cat} of encapsulated enzymatic reactions was observed for vesicles with an inner diameter ranging from 30 nm to 170 nm. This observed higher reactivity of encapsulated α -chymotrypsin is attributed to the molecular confinement inside the vesicles, which is a combined effect of high collision frequencies between the reagents and a strong interaction between the enzymes and the vesicle wall.

6.4 Experimental

PS₄₀₃-*b*-PAA₆₂ (the subscripts denote the number of repeat units for each block; $M_n = 46.5$ kg/mol, polydispersity index = 1.18) was purchased from Polymer Source Inc. (Dorval, Canada). Enzyme α -chymotrypsin and substrate AMC were purchased from

Sigma-Aldrich Co. (St. Louis, MO, USA). All chemicals were used as received. THF (AR grade) was purchased from Biosolve B. V. (Valkenswaard, the Netherlands). Milli-Q water was produced by a Millipore Synergy system (Billerica, MA, USA).

PS-*b*-PAA vesicles were prepared by first dissolving the polymer in THF with various initial concentrations, then by adding Milli-Q water as a precipitant into the polymer solution until a given water percentage was reached, while the entire system was under vigorous stirring using a magnetic stirring bar at ~ 600 rpm. Enzymes and substrates were encapsulated in the vesicles by dissolving both enzymes and substrates in water followed by immediate mixing. To compare the kinetics of the enzymatic reaction in solution (temperature = 25°C) and in PS-*b*-PAA vesicles, a series of substrate concentrations of 1, 5, 10, 20, 50, 100 μM and a constant enzyme concentration of 0.02 μM were used in both cases.

The size of PS-*b*-PAA vesicles was determined with a Malvern Zeta-sizer 4000 (Malvern Corp., Malvern, UK) at 25°C using a laser wavelength of 633 nm and a scattering angle of 90°. The CONTIN method³⁴ was applied for data processing. The size, count rate and poly-dispersity index (PDI) were determined. The zeta-potential of the vesicles was measured using Laser Doppler Velocimetry with a Malvern Zeta-sizer 2000 (Malvern Corp., Malvern, UK), in which the velocity of the vesicles moving in a fluid medium that is exposed to an electric field is measured. Measurements were carried out at 25°C using a 1 kHz modulator frequency and a 120V cell drive voltage.

TEM images were acquired using an analytical TEM instrument Philips CM30 (FEI, Hillsboro, OR, USA) equipped with a post-column GIF Tridiem energy filter system (Gatan, Inc., Pleasanton, CA, USA). Samples for TEM were prepared by directly depositing a droplet of vesicle dispersion onto a carbon-coated TEM grid. After evaporation of the solvent the grid was fixed onto the specimen holder and mounted into the vacuum chamber. The membrane of the vesicles was resolved due to the electron density contrast between the polymer and the interior of the vesicles. The thickness (t) was determined based on 50 individual vesicles and the interior volume was then calculated: $V_{in} = 4/3\pi(R_{out} - t)^3$, where R_{out} is the outer radius of the vesicle, obtained from the zeta-sizer.

UV/Vis spectra were recorded using a Varian Cary 300 Bio UV/Visible spectrophotometer (Varian, Inc. Palo Alto, CA, USA). To follow the enzymatic reaction, a scanning kinetics mode was used to record spectra ranging from 300 nm to 400 nm. A baseline correction of the spectra was carried out by subtracting the

recorded spectrum of the pure solvent from the spectra of the samples. The absorption value of enzymes and products with and without partly encapsulation into the vesicles were compared and found to possess identical values within the experimental errors (5%).

To determine the encapsulation efficiency of the vesicles, dialysis was used to remove the unencapsulated substances. Dialysis was carried out using Spectra/Por 7 dialysis tubing from Spectrum Europe B.V. (Breda, the Netherlands) with a molecular weight cut off of 50 kD.

6.5 References

- 1 A. Pohorille, D. Deamer, *TRENDS in Biotech.* 2002, **20**, 123.
- 2 M. J. Doktycz, M. L. Simpson, *Mol. Syst. Biol.* 2007, **3**, 125.
- 3 B. Hess, A. Mikhailov, *J. Theor. Biol.* 1995, **176**, 181.
- 4 D. T. Chiu, C. F. Wilson, F. Ryttsén, A. Strömberg, C. Farre, A. Karlsson, S. Nordholm, A. Gaggar, B. P. Modi, A. Moscho, R. A. Garza-López, O. Orwar, R. N. Zare, *Science* 1999, **283**, 1892.
- 5 T. Misteli, *J. Cell Biol.* 2001, **155**, 181.
- 6 P. C. Marijuan, *Biosystems* 1995, **35**, 167.
- 7 M. S. Long, C. D. Jones, M. R. Helfrich, L. K. Mangeney-Slavin, C. D. Keating, *Proc. Natl. Acad. Sci. USA* 2005, **102**, 5920.
- 8 G. J. Pielak, *Proc. Natl. Acad. Sci. USA* 2005, **102**, 5901.
- 9 J. Wolcke, D. Ullmann, *Drug Discov. Today* 2001, **6**, 637.
- 10 M. J. Heller, *Annu. Rev. Biomed. Eng.* 2002, **4**, 129.
- 11 J. Khandurina, A. Guttman, *Curr. Opin. Chem. Biol.* 2002, **6**, 359.
- 12 R. F. Khairutdinov, *Prog. Reaction Kinetics*, 1996, **21**, 1.
- 13 V. Ramamurthy, *Photochemistry in organized and constrained media*, VCH Publishers, Inc. New York, 1991.
- 14 M. Almgren, *Kinetics and catalysis in microheterogeneous systems*, Marcel Dekker, New York, 1991.
- 15 M. Tachiya, *Kinetics of non homogeneous processes*, Wiley, New York, 1987.
- 16 M. D. Ediger, M. D. Fayer, *Macromolecules* 1983, **68**, 13.
- 17 D. Mobius, *Kinetics of non homogeneous processes*, Wiley, New York, 1987.
- 18 J. Klafter, J. M. Drake, *Molecular dynamics in restricted geometries*, Wiley, New York, 1989
- 19 J. M. Drake, P. Levitz, N. J. Turro, K. S. Nitsche, K. F. Cassidy, *J. Phys. Chem.* 1988, **92**, 4680.
- 20 R. F. Khairutdinov, P. P. Levin, S. M. B. Costa, *Langmuir* 1996, **12**, 714.
- 21 R. F. Khairutdinov, N. A. Rubtsova, S. M. B. Costa, *J. Lumin.* 1996, **68**, 299.
- 22 Q. Chen, H. Schönherr, G. J. Vancso, *Small* 2009, **5**, 1436.
- 23 A. L. Creagh, J. M. Prausnitz, H. W. Blanch, *Enzyme Microb. Technol.* 1993, **15**, 383.

- 24 R. Biswas, S. K. Pal, *Chem. Phys. Lett.* 2004, **387**, 221.
- 25 L. Michaelis, M. Menten, *Biochem. Z.* 1913, **49**, 333.
- 26 B. Lohse, P. -Y. Bolinger, D. Stamou, *J. Am. Chem. Soc.* 2008, **130**, 14372.
- 27 L. Goldstein, *Biochemistry* 1972, **11**, 4072.
- 28 D. T. Chiu, C. F. Wilson, A. Karlsson, A. Danielsson, A. Lundqvist, A. Strömberg, F. Ryttsén, M. Davidson, S. Nordholm, O. Orwar, R. N. Zare, *Chem. Phys.* 1999, **247**, 133.
- 29 H. S. Carslaw, J. C. Jaeger, *Proc. London Math. Soc.* 1940, **46**, 36.
- 30 G. Tubio, B. Nerli, G. Picó, *J. Chromatogr. B* 2007, **852**, 244.
- 31 R. A. Anderson, S. A. Beyler, S. R. Mack, L. J. Zaneveld, *Biochem. J.* 1981, **199**, 307.
- 32 Q. Chen, R. Groote, H. Schönherr, G. J. Vancso, *Chem. Soc. Rev.* 2009, **38**, 2671.
- 33 T. -M. Hsin, E. S. Yeung, *Angew. Chem. Int. Ed.* 2007, **46**, 8032.
- 34 S. W. Provencher, *Biophys. J.* 1976, **16**, 27.

Chapter 7

Temperature Induced Vesicle-to-Micelle Transition of Block Copolymer Aggregates in Solution and Encapsulation / Release of Molecular Cargos

In this chapter the temperature induced vesicle-to-micelle transition behaviour of polystyrene-block-poly acrylic acid (PS-*b*-PAA) aggregates in THF/H₂O solvent mixtures was studied. For a typical system with 2 wt% initial PS₁₃₉-*b*-PAA₁₇ concentration and 50 vol% of H₂O the morphology of the aggregates changed from vesicles at room temperature to micelles at elevated temperature (~ 45°C). The transition temperature was found to depend on the polymer concentration as well as solvent composition. A higher polymer concentration, as well as a lower THF concentration, *i.e.* plasticizer content, led to a higher transition temperature. The driving force of the transition was attributed to the change in the solvent-polymer interactions, which resulted in a reduction in interfacial energy. The change in free energy of the aggregate formation was estimated to be -29 kJ/mol at 45°C. The corresponding temperature induced morphological change was employed as a strategy for the release and encapsulation of small molecules. The release of Rhodamine 110 bisamide above the transition temperature was observed as a result of the trypsin-catalyzed hydrolysis of the bisamide into Rhodamine 110. Likewise, the successful encapsulation of Rhodamine 110 after heating /cooling cycles of PS-*b*-PAA aggregates was proven using sodium nitrite as a chemical quencher.

7.1 Introduction

Self-assembly of amphiphilic block copolymers (BCPs) in aqueous media and in organic solvents has received considerable attention in the past several decades. One of the reasons of this interest is the possibility to create microenvironments as a result of the formation of ordered structures such as vesicles and micelles.¹ The internal volume of vesicles, on the order of atto-liter and zepto-liter, can be used to entrap hydrophilic molecules in the interior or hydrophobic molecules in the membrane. Because of the high molar mass of the BCPs, polymer vesicles have superior stability and great toughness and stiffness when compared to their low molecular weight

and great toughness and stiffness when compared to their low molecular weight analogues, the liposomes.² More interestingly, the structures of the vesicles can be tailored by varying the chemical structure³⁻⁶ and the length of each of the polymer blocks,⁷ etc. Therefore the development of vesicle systems attracted broad interest for applications from drug delivery to cosmetics.

One crucial question in these applications is how to release active substances that are encapsulated inside the vesicles in a controlled manner. The continuous loss of encapsulated compounds via diffusion is very slow as a result of the high molecular weight of the BCPs and the considerable thickness of the membrane.⁸ In some studies, selective permeability was achieved through the use of special chemical structures for BCPs⁹ or by incorporating biological membrane proteins that regulate permeability of selective substances into the polymer vesicle membranes.^{10, 11} In most applications it is highly desirable to be able to control the release of encapsulated substances by triggering a change in the structure or membrane permeability of the vesicles via an external stimulus. In the literatures reported stimuli include hydrolysis,^{12, 13} oxidation¹⁴ and reduction,¹⁵ pH^{5, 16-18} and light.¹⁹

Temperature has been used to control BCP self assembly in solution for years.²⁰⁻²³

The nature of polymer-solvent interactions is an important parameter in the studies involved. Poly (N-isopropylacrylamide) (PNIPAM) is known to display a lower critical solution temperature (LCST) behaviour, that is, above a critical temperature, the solubility of the polymer changes dramatically and micellization takes place.²⁴ Because of this phenomenon several PNIPAM-based BCPs have been investigated by different research groups,²⁴⁻²⁷ and indeed temperature dependent micellization of the BCP aggregates in aqueous solution was observed. Upon cooling down below the LCST those thermo-sensitive vesicles dissociated and released the encapsulated cargos that were loaded previously during the assembly of the BCPs.²⁴

The temperature dependent morphology and size of the aggregates made from polystyrene-*block*-poly dimethylsiloxane (PS-*b*-PDMS) was reported in the literature.²⁸ Distinct phases of spherical micelles and cylindrical micelles with different temperatures and polymer concentrations were estimated based on the results from static and dynamic light scattering experiments and a temperature-concentration phase diagram was mapped. Subsequently different morphologies induced by temperature changes were directly observed by atomic force microscopy for polystyrene-*block*- polyisoprene (PS-*b*-PI) in a selective solvent for the PI block.²⁹ A rod to sphere change and a vesicle to cylinder change were observed for two different

BCP compositions. The phase change was found to be reversible. However, no encapsulation experiments were made possible in these studies since pure organic solvents were used.

The morphology of polystyrene-*block*-poly acrylic acid (PS-*b*-PAA) was studied by Eisenberg *et al* under different temperatures using alcohols as solvents.³⁰ Different morphologies of the aggregates ranging from vesicles to cylindrical micelles and spherical micelles were observed as the system was cooled down from $\sim 160^{\circ}\text{C}$ to room temperature. The authors argued that it was the change of solvent-polymer interaction parameters with temperature that caused the formation of aggregates with different morphologies. Unfortunately the extreme high temperature during the formation of aggregates prevented the use of this system in any release or encapsulation applications.

In another study carried out by Cheng *et al.*, reversible phase changes of polystyrene-*block*-poly ethyleneoxide (PS-*b*-PEO) aggregates in a water and dimethylformamide (DMF) mixed solvent system induced by temperature were observed using transmission electron microscopy (TEM) and dynamic light scattering (DLS).³¹ The morphology of the aggregates changed from vesicles at room temperature to cylindrical micelles at $\sim 50^{\circ}\text{C}$ and to spherical micelles at 70°C . According to the authors the main driving force for the changes was the reduction of the free energy of the corona. However, as the water concentration presented in the system was very low (~ 5 wt%) no release or encapsulation experiments were carried out.

In this chapter, the morphology and size of PS₁₃₉-*b*-PAA₁₇ aggregates prepared at different temperatures with a mixed water/THF solvent were investigated. The existence of a vesicle-to-micelle transition from vesicles to micelles as a result of temperature change was confirmed by experimental techniques including TEM, DLS, and UV-Vis spectroscopy. Finally, the relative high concentration of water in the mixed solvent ($\sim 50\%$) allowed us to utilize temperature as an external stimulus to study the release and encapsulation of small molecules.

7.2 Observation of temperature induced morphological changes of PS-*b*-PAA aggregates

In order to study the morphologies of PS-*b*-PAA aggregates at different temperatures, vesicle samples prepared by first adding water into PS₁₃₉-*b*-PAA₁₇ solution in THF were subsequently heated up to higher temperatures. An aliquot of the solution was taken out at a desired temperature and added into an excess amount of water to “freeze” the morphology. Typical transmission electron microscopy images of the aggregate samples taken at different temperatures are shown in Figure 7.1.

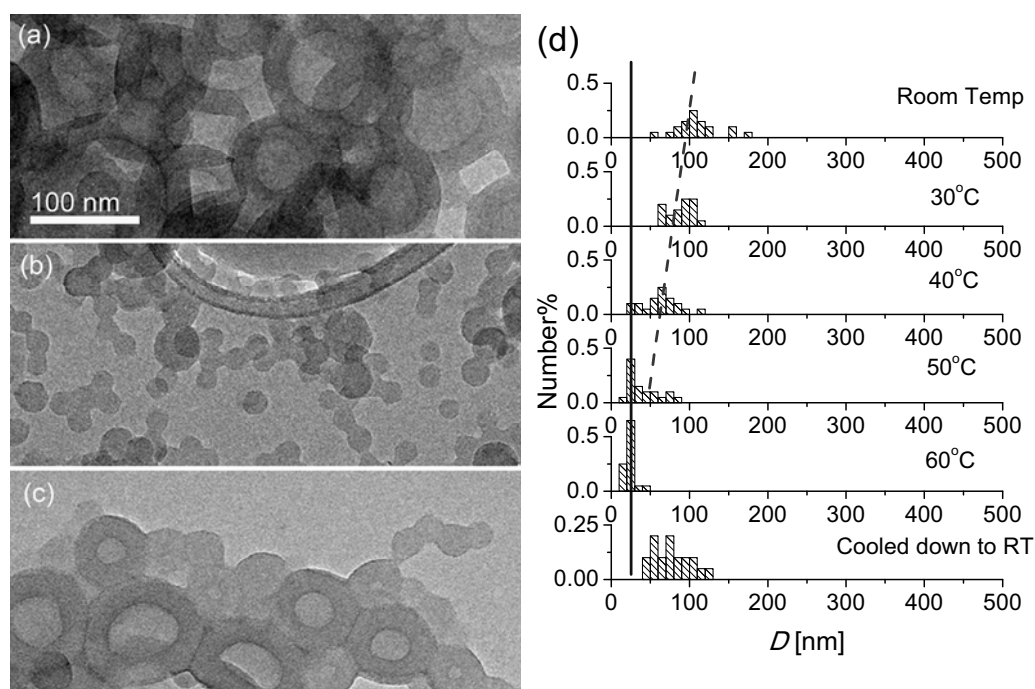


Figure 7.1 TEM images of PS₁₃₉-*b*-PAA₁₇ vesicles (2 wt% in THF, water content 50 vol%) prepared at (a) room temperature, (b) 60 °C and (c) reformed at room temperature. Scale bar in all images are 100 nm as in (a). (d) Size distribution of the vesicles at different temperatures as indicated in the legend, determined from TEM images. The vertical solid line represents the micellar peak at 25 nm. The dash line indicates the decrease of vesicle size (to guide the eye).

As can be seen in Figure 7.1a, the morphology of the aggregates with a PS₁₃₉-*b*-PAA₁₇ concentration of 2 wt% in THF and water content of 50 vol% is vesicular at room temperature, which is in agreement with the morphology of the system as determined in Chapter 3. By contrast, at 60°C the morphology of the aggregates is micellar (spherical micelles), as shown in Figure 7.1b. Aggregates prepared at temperatures lower than 60°C possess a mixed morphology of vesicles and micelles as also shown in Chapter 3. When the aggregates were first heated up and then cooled down to room temperature, the vesicular morphology of the

aggregates was regenerated. (Figure 7.1c) This was clearly seen in the size distribution of vesicles obtained from TEM images as well. (Figure 7.1d)

To obtain a better statistics dynamic light scattering was used to determine the size of the aggregates obtained at different temperatures. Samples were prepared the same way as those for TEM imaging and the results are shown in Figure 7.2.

DLS results show that the average size of the PS₁₃₉-*b*-PAA₁₇ vesicles decreases from ~ 100 nm at room temperature to ~ 25 nm at 60°C, as can be seen in Figure 7.2a. The size of the aggregates at 60°C corresponds to the bilayer thickness of the vesicles determined from TEM, indicating the primary morphology being spherical micelles, conform with the TEM images. Upon cooling back to room temperature (Figure 7.2a, circles), the size of the aggregates increases, albeit to a lower value than the original size at the same temperature, indicating the process is reversible to a certain extent. The apparent hysteresis is likely due to the inefficient mixing between water and THF after cool-down as a result of previous heating.

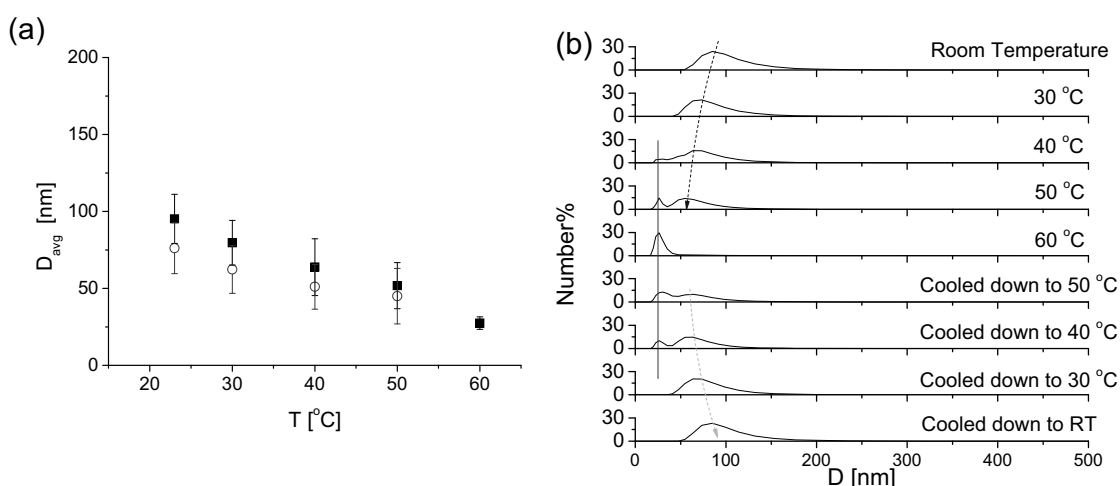


Figure 7.2 (a) Average size of PS₁₃₉-*b*-PAA₁₇ vesicles (2 wt% in THF, water content 50 vol%) as a function of temperature, determined by DLS. Squares: heating; Circles: cooling. (b) Size distribution of PS₁₃₉-PAA₁₇ aggregates (2 wt% in THF, water content 50 vol%) in (a).

Based on the DLS data size distribution histograms of the PS₁₃₉-*b*-PAA₁₇ aggregates at different temperatures were constructed and shown in Figure 7.2b. A bimodal distribution is clearly visible for the aggregates prepared at 50°C. The peak at smaller size (~ 25 nm) corresponds to the micelles, while the peak at ~ 60 nm corresponds to the vesicles. At 60°C the vesicle peak disappears and the distribution can be faithfully represented by a single peak model with a peak centred at 25 nm. The transition from a monomodal to a bimodal distribution proves that the transition of the aggregates

from vesicles to micelles indeed takes place when the temperature of the aggregates is elevated.

The driving force for the morphological changes of similar block copolymer systems was studied and reported in the literature.^{30, 31} It is believed that the morphological changes are based on the free energy of the aggregates, which consists of the free energy of the hydrophobic phase, the free energy of the hydrophilic phase and the free energy of the interface.³² To understand these changes, the interactions between the solvent and the polymer and how they are affected by temperature changes should be estimated. The interaction parameter χ is the key parameter to represent the interaction between the polymer and the solvent. If the entropy contribution is neglected, χ can be calculated based on the van Laar-Hildebrand equation³³:

$$\chi_{P-S} = \frac{V_S}{RT} (\delta_P - \delta_S)^2 \quad (7.1)$$

where V_S is the molar volume of the solvent and δ_P and δ_S are the solubility parameters for the polymer and solvent, respectively. The temperature dependence of these parameters is neglected for the sake of simplicity in calculations, and indeed they are only slightly temperature-dependent.³³ By definition the equation shows a decrease in χ as the temperature increases. Substituting the values in ($\delta_{PS} \sim 19 \text{ MPa}^{0.5}$, $\delta_{PAA} \sim 24.5 \text{ MPa}^{0.5}$, $\delta_{H_2O} = 47.9 \text{ MPa}^{0.5}$, $\delta_{THF} = 18.6 \text{ MPa}^{0.5}$)³⁴, it is seen that χ_{PS-H_2O} decreases ($\Delta\chi = 0.8$) more significantly than χ_{PS-THF} ($\Delta\chi = 0.0007$), χ_{PAA-H_2O} ($\Delta\chi = 0.25$) and $\chi_{PAA-THF}$ ($\Delta\chi = 0.1$) in the same temperature range. Also, assuming the system obeys the ideal solution behaviour (the solubility parameters in the mixture follows a linear addition), for a system containing 50 vol% of H₂O and 50 vol% of THF, the change in $\chi_{PS-solvent}$ and $\chi_{PAA-solvent}$ with temperature change from 25 to 60°C calculated reveals that the value of $\chi_{PS-solvent}$ at 25°C (4.0) is much higher than that of $\chi_{PAA-solvent}$ (1.5), indicating the solvent mixture is a much poorer solvent for PS than for PAA at room temperature. As the temperature increases to 60 °C, the value of $\chi_{PS-solvent}$ decreases to 3.1 as the mixed solvent becomes less poor for PS, while $\chi_{PAA-solvent}$ is essentially the same (1.4). This change in solvent quality for PS will subsequently cause a reduction of total interfacial energy. As discussed in Chapter 3, a change in the total interfacial energy will sensitively change the size and morphology of the aggregates obtained, *e. g.* the addition of water into the solution mixture will cause an increase in the total interfacial energy and as a result the aggregates will form bigger vesicles, reducing the total interfacial area to counteract the total interfacial energy increase.

7.3 Turbidity change with temperature for PS-*b*-PAA aggregates

The morphological change of the PS₁₃₉-*b*-PAA₁₇ aggregates was also observed by following the change in turbidity using UV-Vis spectroscopy. The absorbance at 400 nm of a system with 2 wt% initial polymer concentration and 50 vol% of water was monitored by an UV-Vis spectrophotometer as the turbidity of the solution when the sample was heated from room temperature to 60°C as shown in Figure 7.3. Turbidity of the system is mainly caused by the scattering of incoming light through the sample, with the PS₁₃₉-*b*-PAA₁₇ aggregates as the scatterer. The intensity of the scattered light is largely dependent on the size of the scatterer, therefore the change in turbidity corresponds to the change in the size of the aggregates and by detecting the onset of the vesicle-to-micelle transition during a temperature ramp, the transition temperature is determined.

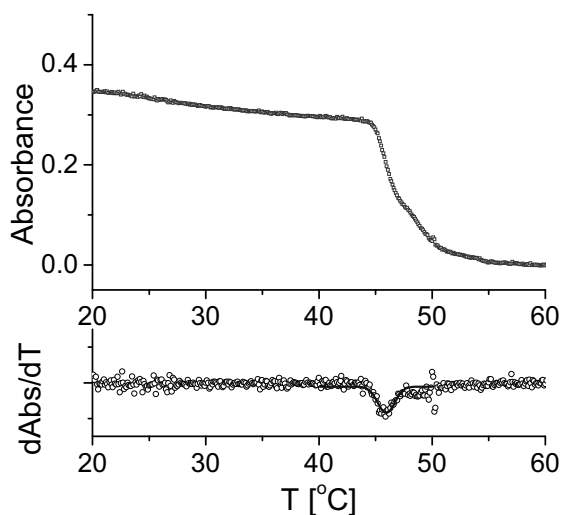


Figure 7.3 Turbidity of the solution recorded as a function of temperature. The sudden decrease of turbidity represents the vesicle-to-micelle transition of the aggregates. The transition temperature is determined from the inflection point of the curve.

As shown in Figure 7.3, the absorbance of the sample decreased slightly in the initial part of the trace, followed by a sudden decrease when the temperature of the sample was raised to above 40°C. This is caused by the transition of the aggregates from vesicles to micelles, as determined from the TEM and DLS measurements in the previous session. After the transition the absorbance of the system dropped to almost zero. To precisely determine the transition temperature, the first derivative of the trace was calculated and plotted in Figure 7.3. The minimum of the curve occurs at 45.3°C and that temperature is defined as the transition temperature.

The effect of the heating rate on the transition temperature of the aggregates was studied for PS₁₃₉-*b*-PAA₁₇ vesicles with 1 wt% initial polymer concentration and 50 vol% H₂O. Samples with the same composition were heated from room temperature to 60°C using different heating rates and their corresponding turbidity traces were shown in Figure 7.4a. Transition temperatures (T_c) were determined based on the traces and plotted as a function of heating rate in Figure 7.4b.

The transition temperature was found to be dependent on the heating rate of the experiments. T_c increased from 34.7°C to 53.3°C as the heating rate changed from 0.1°C/min to 30°C/min. The value of T_c remained constant when the heating rate was below 5°C/min as can be seen in the inset of Figure 7.4b and increased in a linear fashion when the heating rate was above 5°C/min. In a similar study on the transition temperature of dioctadecyldimethyl ammonium bromide vesicles using differential scanning calorimetry (DSC) a roughly sigmoidal way of T_c increase as a function of heating rate was observed for heating rate ranging from 20 to 80°C/min.³⁵ In our case restrictions on the instrument do not allow us to apply a high heating rate in the experiments, therefore the T_c was not determined at high heating rates. Unless otherwise mentioned, all turbidity measurements were scanned at a heating rate of 0.5°C/min.

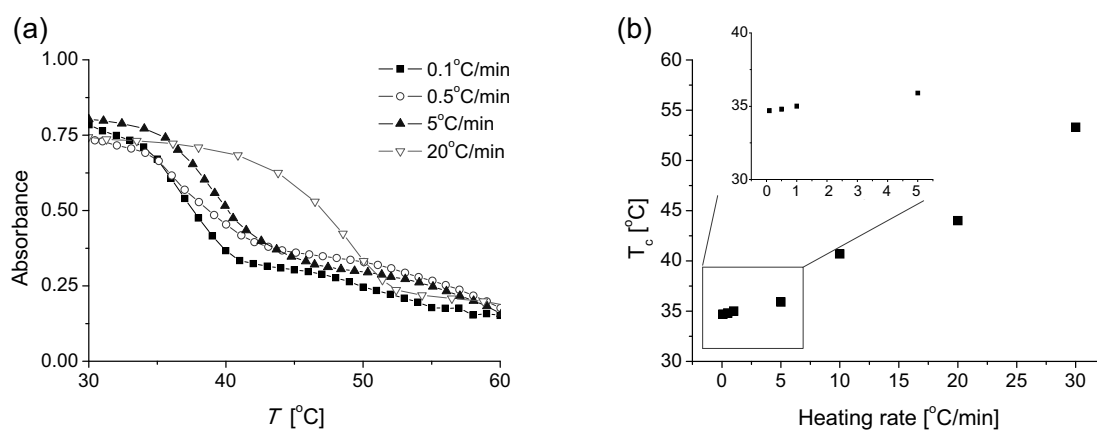


Figure 7.4 (a) Turbidity diagram as a function of temperature for different heating rates as indicated in the legend. (b) Transition temperature plotted as a function of scanning rate. The inset is the zoom-in of the selected box region.

Assuming PS₁₃₉-*b*-PAA₁₇ vesicles are thermodynamically equilibrium structures that respond to changes, *e. g.* temperature and solvent composition in the system by changing their sizes and morphology, it becomes interesting to study how fast these changes occur. Here PS₁₃₉-*b*-PAA₁₇ vesicles with 2 wt% initial polymer concentration and 50 vol% H₂O were first prepared at room temperature, and then added into the

sample chamber at different temperatures. The equilibrium state of the system was perturbed and the system adjusted itself to new equilibrium conditions accompanied by a change in the size or morphology of the aggregates, represented by the change in turbidity as observed above. By monitoring the change in turbidity as a function of time the kinetics of the change in the size of the aggregates as a result from temperature change was resolved. Turbidity traces recorded at different temperatures are shown in Figure 7.5.

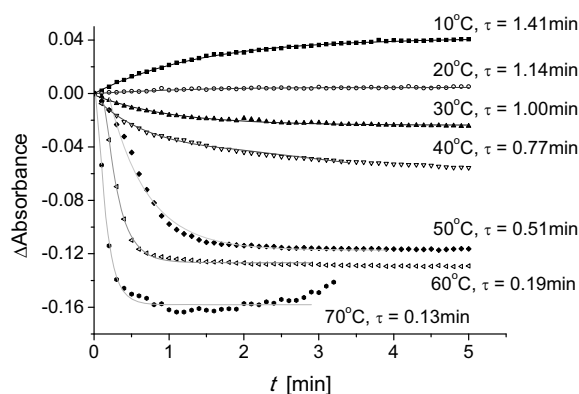


Figure 7.5 Measurement of kinetics of vesicle size increase / decrease at different temperatures. The change in absorbance was plotted as a function of time and the solid lines are the exponential decay fits to the data points, with τ as the characteristic relaxation time.

The turbidity of the system decreased to a constant value when the temperature was higher than room temperature, while the turbidity increased as the system was cooled down to 10°C as shown in Figure 7.5. All turbidity traces were fitted to a single exponential function:

$$\Delta Absorbance = Abs_0 \exp(-t / \tau) \quad (7.2)$$

where τ is the relaxation time for the process and Abs_0 is an adjustable constant. Figure 7.5 shows that the change of aggregate size occurs over shorter time periods at higher temperature, as the value of relaxation time decreases from 85 s at 10°C to 11 s at 60°C. The characteristic timescale for vesicle fusion was studied by Eisenberg *et al* and a typical timescale of 60 s was observed when 2% water was added into the solution causing the change in vesicle size, which is similar to what was observed here.³⁶

7.4 The influence of solution composition on the transition temperature

7.4.1 The effect of initial polymer concentration

The morphological changes of the PS-*b*-PAA aggregates with temperature for different initial polymer concentrations were followed by monitoring the turbidity change as a function of temperature. The water content of all systems was kept at constant (50 vol%). The results are shown in Figure 7.6a.

The critical transition temperature (T_c) of the system, as indicated in Figure 7.6a by vertical arrows, was found to increase as the initial polymer concentration of the system increased. The values of T_c for 1, 2 and 5 wt% of polymers are 35.5, 45.3 and 69.5°C, respectively. The observation can be explained again on the basis of the polymer-solvent interaction parameter χ . It is known that χ is related to the polymer concentration ϕ by the following equation³³:

$$\chi_{P-S} = \chi_0 + \chi_1\phi + \chi_2\phi^2 + \dots \quad (7.3)$$

where χ_0 , χ_1 , χ_2 are empirical constants. At low polymer concentrations, the higher order terms are negligible, but at higher concentrations they become important and contribute to the increase of χ_{P-S} . As a result the system needs to be heated to a higher temperature to cause a sufficient decrease in χ_{P-S} for the morphological change to take place.

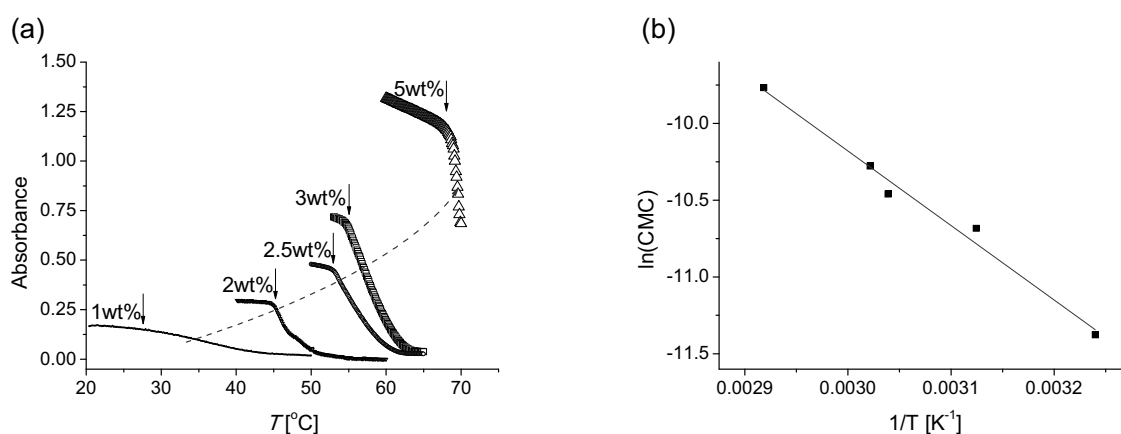


Figure 7.6 (a) Changes in turbidity with temperature for PS₁₃₉-*b*-PAA₁₇ vesicles with different initial polymer concentrations as indicated in the graph and a constant THF percentage of 50 vol%. (b) Plot of the logarithmic critical micelle concentration as a function of the reciprocal temperature. The solid line represents the least square fit to the data.

The standard free energy and standard enthalpy of aggregate formation are sensitively (ΔG° and ΔH° per mole of solute) related to the critical micelle concentration (CMC) and temperature according to the following equations³⁷:

$$\Delta G^\circ = RT \ln(\text{CMC}) \quad (7.4)$$

$$\Delta H^\circ = R \frac{d \ln(\text{CMC})}{d(1/T)} \quad (7.5)$$

where CMC is in molar concentration. The two standard thermodynamic states in our experiments are the vesicles and micelles. Equation 7.5 can be integrated to yield:

$$\ln(\text{CMC}) = \Delta H^\circ / RT + A \quad (7.6)$$

where A is a constant. The initial polymer concentration at critical transition temperature, in our case, can be treated as the critical micelle concentration at temperature T_c . Based on the experimental results from the turbidity measurements, a plot between the logarithm of CMC and the reciprocal temperature was constructed and shown in Figure 7.6b. The slope of the linear least square fit to the data was used to calculate ΔH° in the temperature range investigated. The value of ΔH° is -40.3 ± 2.8 kJ/mol. The value of ΔG° at 45°C is -29 kJ/mol and the corresponding $T\Delta S^\circ = -11.3$ kJ/mol. The large negative standard enthalpy of aggregate formation, which is related to the interactions between the polymer themselves as well as the polymer solvent interactions, outweighs the entropic factors that tend to distribute the polymer chains into the solvent rather than aggregate them to form vesicles or micelles.

7.4.2 The effect of solvent composition

Turbidity diagrams of systems with a constant 2 wt% initial polymer concentration and different water contents were recorded to study the effect of solvent composition on the critical transition temperature and are shown in Figure 7.7a.

The decrease of interaction parameter χ_{P-S} is related to the concentration of solvent with different solubility parameters presented in the system, according to equation 7.1. However, for a system with PS₁₃₉-*b*-PAA₁₇ vesicles in pure water (THF removed by dialysis), the absorbance remained constant in the duration of heating from room temperature to 60°C as can be seen from Figure 7.7a. With the presence of up to 40 vol% THF, absorbance decreased to a certain extent but no clear transition was observed. At water concentration lower than 60 vol%, *i.e.* THF content higher than 40 vol%, a sudden decrease in absorbance, indicating the transition from vesicles to

micelles occurred during heating-up of the samples. The transition temperature was found to be dependent on the THF content, with higher THF content a lower T_c was observed. A plot between T_c and THF concentration was constructed in Figure 7.7b.

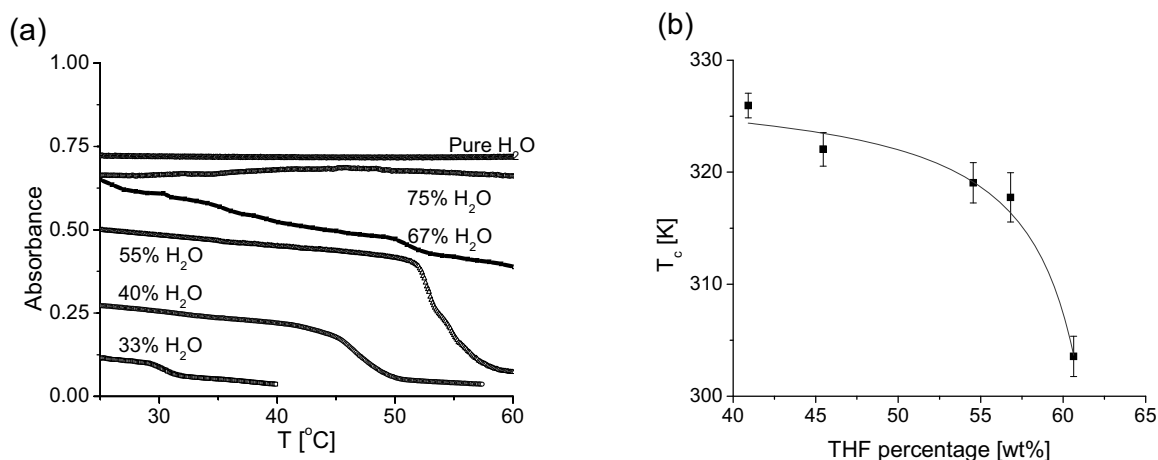


Figure 7.7 (a) Change in turbidity with temperature for PS_{139} - b - PAA_{17} vesicles with different THF percentages and a constant initial polymer concentration of 2 wt%. (b) The transition temperature plotted as a function of THF percentage (vol%). The curve corresponds to the fit to the Wood equation.

The reason that no vesicle-to-micelle transition occurred at higher water concentrations cannot be contributed to thermodynamical considerations since the decrease of χ is equally significant for pure water and water/THF mixtures. (see section 7.2) A possible explanation is that the mobility of PS could be severely hindered in the presence of water, due to the strong hydrophobic nature of the polymer chain. THF, which is a good solvent for PS, acts as a plasticizer in the system to lower the glass transition temperature (T_g) of PS and provides enough mobility in the chain to allow them reorganize and aggregate in a different fashion.

The T_g of a mixed system can be described by the Wood equation:³⁸

$$T_g = \frac{w_1 T_{g1} + k w_2 T_{g2}}{w_1 + k w_2} \quad (7.7)$$

where w_1 , w_2 , T_{g1} and T_{g2} are the weight fraction and glass transition temperatures of the components, respectively. k is an empirical constant which is related to the heat capacity increments of the components. In our case, the trend of T_c decrease as a function of THF percentage increase was fitted by equation 7.7 using the literature values of PS and THF ($T_{g-PS} = 373$ K, $T_{g-THF} = 165$ K).³⁴ The fit afforded a value of $k = 0.7 \pm 0.03$. (Figure 7.7b, solid line). This concludes that THF plays a crucial part in the vesicle-to-micelle transition investigated here as it enhances the mobility of PS

blocks by decreasing the T_g of PS, and the occurrence of vesicle-to-micelle transition is sensitively linked to the mobility of PS. Similar results were reported in the literature.³¹

7.5 Release and encapsulation of molecular cargos employing the temperature induced vesicle-to-micelle transition

Vesicle-to-micelle transition of the BCP aggregates in solution induced by temperature is potentially a means to encapsulate functional molecules into the aqueous interior of the vesicles and to subsequently release those cargos. In our experiments, hydrolysis of rhodamine 110 bis-(benzyloxycarbonyl-L-arginine amide) dihydrochloride (R110-Arg₂) catalyzed by enzyme bovine pancreas trypsin,³⁹ as described in Chapter 5, was used to investigate the feasibility of such strategy. Substrates R110-Arg₂ were first encapsulated into PS₁₃₉-*b*-PAA₁₇ vesicles during the preparation. The substrate-containing vesicles were then mixed with enzymes and the sample was heated from room temperature to 65°C. The absorbance at 495 nm, which is the specific peak absorption of the enzymatic reaction product rhodamine 110 (R110), was monitored with a reference of empty vesicles. The result of the experiment is shown in Figure 7.8.

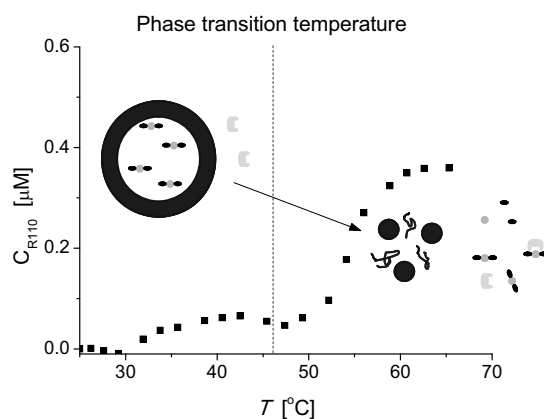


Figure 7.8 Concentration of R110 for a mixture of R110-Arg₂ containing PS₁₃₉-*b*-PAA₁₇ vesicles (2 wt% in THF, water content 50 vol%) and trypsin as a function of temperature. Release of the encapsulated R110 bisamide as a result from the transition of PS₁₃₉-*b*-PAA₁₇ aggregates from vesicle to micelle and single chains and the subsequent hydrolysis of R110 bisamide to R110 (peak absorption at 495 nm) catalyzed by trypsin is shown in the scheme.

At room temperature, R110-Arg₂ was confined into the aqueous interior of the vesicles and was inaccessible to trypsin. As can be seen in Figure 7.8, the absorbance

of the sample changed slightly before the transition, possibly due to incomplete removal of the un-encapsulated substrates by dialysis and morphological change of fractions of small vesicles. Upon heating above the transition temperature at 45°C as determined from section 7.3 (indicated by a dash line), the vesicles underwent transition to micelles, losing the membrane-enclosed volume. The substrates were allowed to be released and react with the enzymes. The absorbance increased dramatically, indicating the substrates were converted into the products. (see Scheme 7.1 for the enzymatic reaction equation) Provided that the value of extinction coefficient of R110 is known ($\epsilon = 92000 \text{ cm}^{-1}\text{M}^{-1}$),⁴⁰ the actual concentration of the product was calculated from the absorbance in Figure 7.8. The concentration of the converted substrates (0.36 μM), is roughly 14% of the original concentration of the substrates (2.5 μM). Assuming a complete reaction of the substrates, this indicates the encapsulation efficiency of the substrates into vesicles is 14%, which is in agreement with the results obtained from Chapter 5. A control experiment with the same vesicles without the presence of enzymes was carried out and no increase of absorbance was observed, indicating the formation of product is indeed a result from enzyme catalysis.

Utilizing the same principle, molecules were encapsulated into the vesicles during the transition. In the experiment empty PS₁₃₉-*b*-PAA₁₇ vesicles were mixed with R110 at room temperature. The mixture was then heated up to 60°C and divided into two portions. In the first portion a chemical quencher sodium nitrite (NaNO₂) was added directly into the solution (see Scheme 7.1 for the quenching reaction equation), while in the second portion NaNO₂ was added into the solution when it was cooled down to room temperature, as can be seen from Figure 7.9a.

The fluorescence emission spectra of the original vesicles and R110 mixture (1), as well as the quenched solution when NaNO₂ was added at 60 °C (2) and the quenched solution when NaNO₂ was added at room temperature (3) were recorded using spectrofluorometry (see Figure 7.9b). The peak emission wavelength of R110 was 525 nm in the spectrum of the original solution, which is in agreement with the literature reported on the fluorescent probes. In the spectrum of the solution when NaNO₂ was added at 60°C, the emission intensity decreased to almost zero, indicating a complete quenching of R110 due to the formation of a non-fluorescent nitroso compound.³⁹ In the spectrum of the solution when NaNO₂ was added at room temperature, a residual fluorescence with intensity roughly 13% of the original solution was measured. This can only be explained by the re-formation of the vesicles when the solution mixture

was cooled down from above the transition temperature, as depicted in Figure 7.9a. During vesicle formation R110 was encapsulated partly into the aqueous interior of the vesicles and the ion impermeable membrane protected them from reacting with NaNO_2 as shown previously in Chapter 5. The ratio between the quenched solution intensity and the original solution intensity yields the encapsulation percentage of R110. In the example shown in Figure 7.9b, the encapsulation percentage is 13%, which is in agreement with the results from the release experiments, as well as the results from Chapter 5.

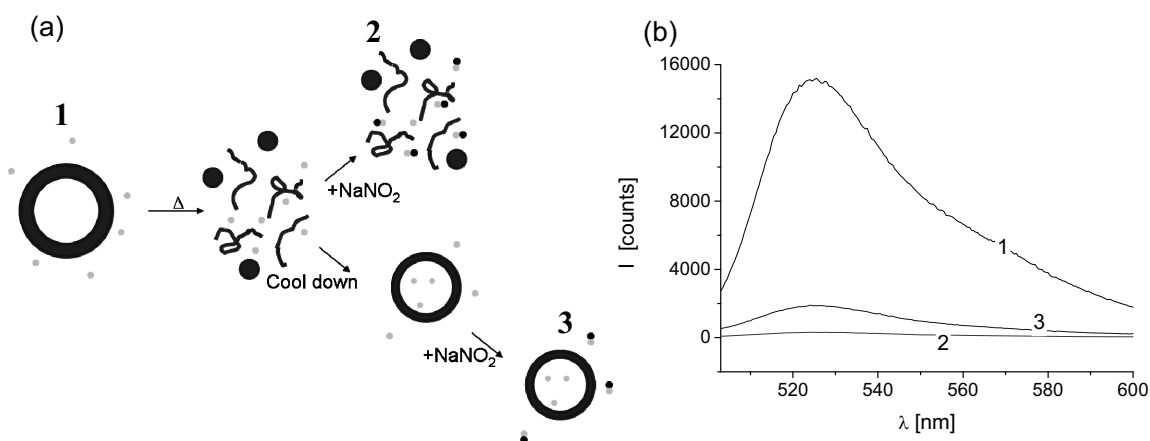


Figure 7.9 (a) Schematic representation of the encapsulation of R110 by cooling down the $\text{PS}_{139}\text{-}b\text{-PAA}_{17}$ solution and (b) Fluorescence emission spectra of R110 (1) after mixing with empty $\text{PS}_{139}\text{-}b\text{-PAA}_{17}$ vesicles (2 wt% in THF, water content 50 vol%) at room temperature; (2) after the quencher NaNO_2 was added at 60°C and (3) after NaNO_2 was added at room temperature when the vesicle solution was cooled down.

Finally, $\text{PS-}b\text{-PAA}$ vesicles with partly encapsulated substrates R110-Arg₂ were mixed with trypsin ($c = 0.01 \mu\text{M}$) at 20°C . The solution mixture was heated up to 50°C after placing it in dark for overnight. After 5 hours of heating the solution was brought back to 20°C , followed by the addition of NaNO_2 into the solution. The specific absorbance of the fluorescent product R110 was monitored using UV-Vis spectrophotometer during the process and plotted as a function of time in Figure 7.10a (red curve). A control experiment with pure substrates and enzymes of the same concentration (*i.e.* without the presence of vesicles) was carried out and the absorbance of R110 was also shown in the same graph (black curve). The spectra displaying the actual progression of absorption peak of the products in the enzymatic reaction, as well as the diminishing of the product in the quenching reaction, were shown in Figure 7.10b and c.

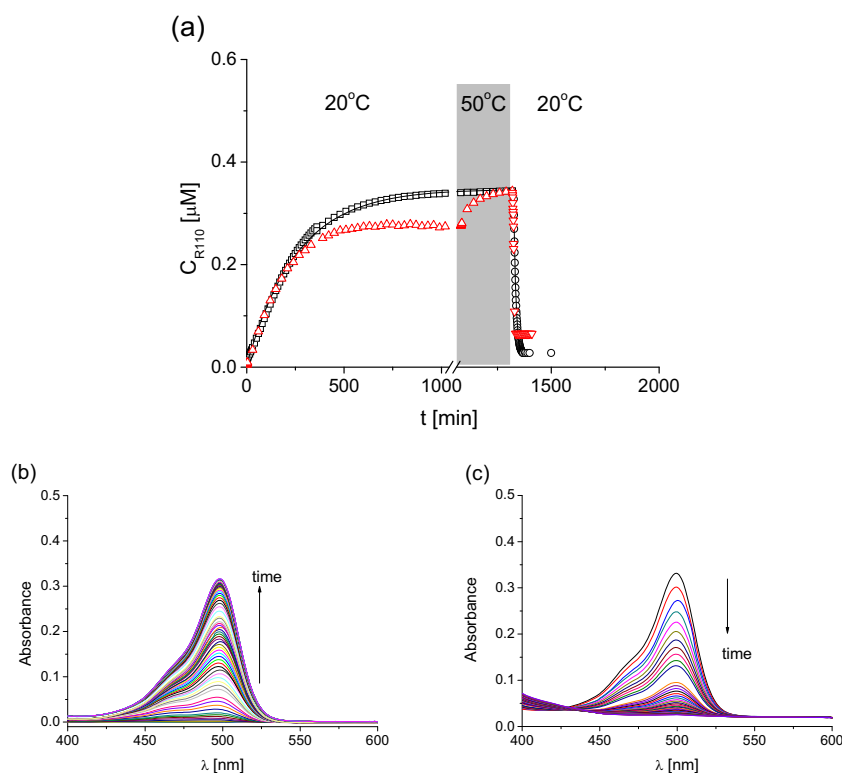
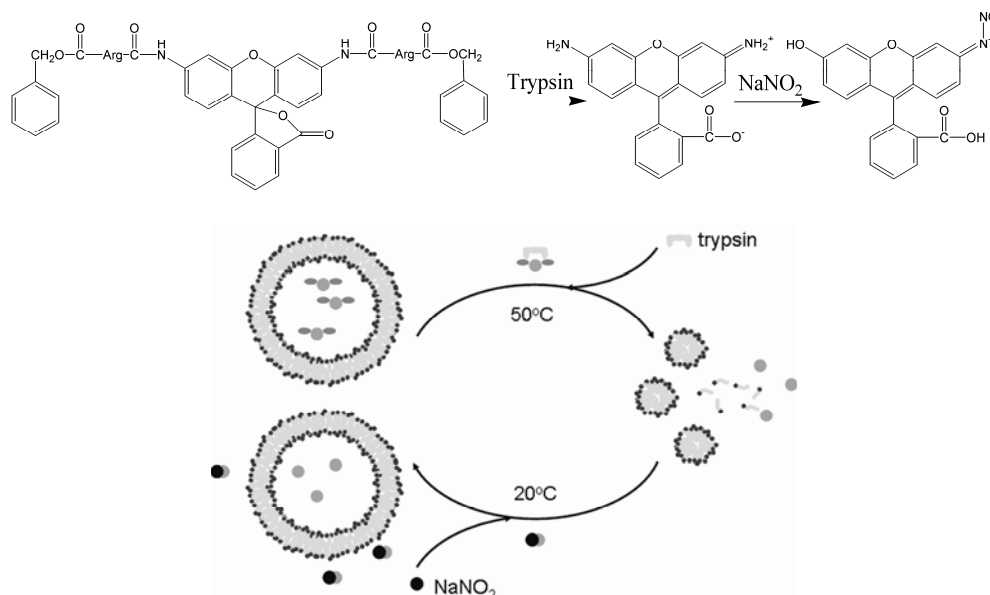


Figure 7.10 (a) Kinetic plots of hydrolysis of rhodamine 110 bisamide catalyzed by trypsin, with (red) and without (black) the presence of $\text{PS}_{139}\text{-}b\text{-PAA}_{17}$ vesicles. After the reaction reached steady state the temperature was raised to and kept at 50 °C to allow the release of encapsulated substrates and the full conversion to the products. When the solution was cooled down sodium nitrite was added to quench the product. The progress of the enzymatic reaction (b) as well as the quenching reaction (c) is also shown.

In both curves the absorbance of R110 increased linearly in the first four hours of reaction time before it gradually reached a steady state, indicating the complete conversion of the accessible substrates. In the case when part of the substrates was encapsulated into the vesicles, the absorbance at steady state was about 83% of the value of absorbance when no vesicles were present. This is due to the encapsulation of the substrates into $\text{PS-}b\text{-PAA}$ vesicles, thus preventing them from reacting with trypsin. The encapsulation percentage calculated according to the absorbance ratio was 17%, well in agreement with previous results.

The samples were then heated to 50°C, indicated by the grey bar in Figure 7.10a. The absorbance of the product did not change in the control sample (black squares), while in the sample with substrate-containing vesicles the absorbance increased to the same level as the control sample. This indicates the conversion of the encapsulated substrates to products, as a result of the transition of vesicles to micelles when the temperature was above the transition temperature of the system. When both samples were cooled down to 20°C NaNO_2 was added into the solution. The absorbance

decreased to zero within 30 minutes in the case of the control sample, while in the sample containing vesicles the absorbance remained 11% of its original value, which was thought to be the result from encapsulated R110 during vesicle reformation as discussed earlier. The encapsulation and release of reagents utilizing heating / cooling across the transition temperature of the vesicles was schematically depicted in Scheme 7.1.



Scheme 7.1 The reaction equation showing the hydrolysis of Rhodamine 110 arginine bisamide catalyzed by enzyme bovine pancreas trypsin, and the subsequent quenching of the fluorescent product Rhodamine 110 using sodium nitrite. The temperature induced release and encapsulation of the reactants are shown in the scheme.

The above discussed strategy utilized temperature induced vesicle-to-micelle transition of BCP aggregates in solution to encapsulate and release small molecules. Temperature was used as an external stimulus to regulate the release of a reagent to allow the reaction to take place, as well as the encapsulation of a product to protect it from unwanted interaction with other substances. We believe the study of assembly and disassembly of BCP vesicles across the transition temperature will provide a new pathway for temperature controlled release of drugs or nutrients and should find potential applications in the fields such as therapeutics and medicine. The advantages of this system lie in the simplicity of synthesis, easy tuning of transition temperature by solution composition and the complementarities to the existing systems containing polymers with low critical solution temperature (LCST) behaviour. However, the necessity to use organic solvents in the system limits the choice of reagents that can be encapsulated. An alternative is the exploration of organic solvent-free vesicle

systems, where polymer chains in the membrane are mobile in the aqueous environment.

7.6 Conclusion

The size and morphology of PS-*b*-PAA aggregates in THF/H₂O mixed solvent system was studied under different temperatures using TEM and light scattering. PS-*b*-PAA vesicles underwent a transition to micelles as the temperature was raised. The vesicle-to-micelle transition was a result from the change in polymer solvent interaction at different temperatures, which was confirmed by varying the polymer concentration, as a higher polymer concentration would result in a larger value of the interaction parameter. Thus the system must be heated to a higher temperature to cause a sufficient decrease in interaction parameter for the vesicle-to-micelle transition. The free energy change of the aggregate formation was determined to be – 29 kJ/mol at 45°C. In addition, the presence of the common solvent THF was found to be crucial for the vesicle-to-micelle transition, as this lowered the T_g of PS in the vesicle membrane to allow the polymer chains to reorganize. A higher THF content lowers the transition temperature, as polymer chains gained mobility at lower temperature. Successful encapsulation and release of small molecules was achieved utilizing the assembly and disassembly of PS-*b*-PAA aggregates cross the transition temperature. R110-Arg₂, whose hydrolysis reaction was studied in Chapter 5, was preloaded into the vesicles and released when the system was heated above the transition temperature to react with enzyme trypsin to form fluorescent product R110. The product was then encapsulated into reformed vesicles when the system was cooled down below transition temperature, proven by the use of sodium nitrite.

7.7 Experimental

PS₁₃₉-*b*-PAA₁₇ (the subscripts denote the number of repeat units for each block; M_n = 15.7 kg/mol, polydispersity index = 1.07) was purchased from Polymer Source Inc. (Dorval, Canada). Trypsin and sodium nitrite were purchased from Sigma-Aldrich Co. (St. Louis, MO, USA). R110-Arg₂ were purchased from Molecular Probes/Invitrogen Co. (Carlsbad, CA, USA). All chemicals were used as received. THF (AR grade) was

purchased from Biosolve B. V. (Valkenswaard, the Netherlands). Milli-Q water was produced by a Millipore Synergy system (Billerica, MA, USA).

PS-*b*-PAA vesicles were prepared by first dissolving the polymer in THF with various initial concentrations, then adding Milli-Q water as a precipitant into the polymer solution until a given water percentage was reached, while the entire system was under vigorous stirring using a magnetic stirring bar at ~ 600 rpm in a water bath of designated temperature. Enzymes and substrates were encapsulated in the vesicles by dissolving both enzymes and substrates in water followed by immediate mixing.

TEM images were acquired using an analytical TEM instrument Philips CM30 (FEI, Hillsboro, OR, USA) equipped with a post-column GIF Tridiem energy filter system (Gatan, Inc., Pleasanton, CA, USA). Samples for TEM were prepared by directly depositing a droplet of vesicle dispersion onto a carbon-coated TEM grid.

The size of PS-*b*-PAA vesicles was determined with a Malvern Zeta-sizer 4000 (Malvern Corp., Malvern, UK) at 25°C using a laser wavelength of 633 nm and a scattering angle of 90°. CONTIN method⁴¹ was applied for data processing. The size, count rate and poly-dispersity index (PDI) were determined.

UV/Vis spectra were recorded using a Varian Cary 300 Bio UV/Visible spectrophotometer (Varian, Inc. Palo Alto, CA, USA). A designated thermal mode was used to monitor the absorbance of the samples at 400 nm as a function of temperature. To follow the enzymatic reaction, a scanning kinetics mode was used to record spectra ranging from 400 nm to 600 nm.

Fluorescence emission spectra were recorded using an Edinburgh F900 analytical instrument (Edinburgh Instruments Ltd., Livingston, UK). A Xe lamp was used as the light source and the excitation and emission slits were set to constant value (0.5 mm) in order to be able to compare the intensities from different samples.

7.8 References

- 1 Z. Tuzar, P. Kratochvil, *Adv. Colloid Interface Sci.* 1976, **6**, 201.
- 2 M.-H. Li, P. Keller, *Soft matter* 2009, **5**, 927.
- 3 B. M. Discher, Y. -Y. Won, D. S. Ege, J. C.-M. Lee, F. S. Bates, D. E. Discher, D. A. Hammer, *Science* 1999, **284**, 1143.
- 4 J. C. M. van Hest, D. A. P. Delnoye, M. W. P. L. Baars, M. H. P. Genderen, E. W. Meijer, *Science* 1995, **268**, 1592.
- 5 L. Zhang, K. Yu, A. Eisenberg, *Science* 1996, **272**, 1777.
- 6 J. J. L. M. Cornelissen, M. Fischer, N. A. J. M. Sommerdijk, R. J. M. Nolte, *Science* 1998,

- 280, 1427.
- 7 T. Azzam, A. Eisenberg, *Angew. Chem. Int. Ed.* 2006, **45**, 7443.
 - 8 D. E. Discher, A. Eisenberg, *Science* 2002, **297**, 967.
 - 9 D. M. Vriezema, P. M. L. Garcia, N. S. Oltra, N. S. Hatzakis, S. M. Kuiper, R. J. M. Nolte, A. E. Rowan, J. C. M. van Hest, *Angew. Chem. Int. Ed.* 2007, **46**, 7378.
 - 10 W. Meier, C. Nardin, M. Winterhalter, *Angew. Chem. Int. Ed.* 2000, **39**, 4599.
 - 11 H.-J. Choi, C. D. Montemagno, *Nano Lett.* 2005, **5**, 2538.
 - 12 F. Ahmed, D. E. Discher, *J. Control.Release* 2004, **96**, 37.
 - 13 F. Meng, C. Hiemstra, G. H. Engbers, J. Feijen, *Macromolecules* 2003, **36**, 3004.
 - 14 A. Napoli, M. Valentini, N. Tirelli, M. Muller, J. A. Hubbell, *Nature Mater.* 2004, **3**, 183.
 - 15 S. Cerritelli, D. Velluto, J. A. Hubbell, *Biomacromolecules* 2007, **8**, 1966.
 - 16 F. Liu, A. Eisenberg, *J. Am. Chem. Soc.* 2003, **125**, 15059.
 - 17 Y. Geng, F. Ahmed, N. Bhasin, D. E. Discher, *J. Phys. Chem. B* 2005, **109**, 3772.
 - 18 H. -C. Chiu, Y. -W. Lin, Y. -F. Huang, C.- K. Chuang, C.-S. Chern, *Angew. Chem. Int. Ed.* 2008, **47**, 1875.
 - 19 T. Ikeda, J. -I. Mamiya, Y. Yu, *Angew. Chem. Int. Ed.* 2007, **46**, 506.
 - 20 Z. Zhou, B. Chu, D. G. Peiffer, *Macromolecules* 1993, **26**, 1876.
 - 21 Y. Fukumine, K. Inomata, A. Takano, T. Nose, *Polymer* 2000, **41**, 5367.
 - 22 S. V. Solomatin, T. K. Bronich, A. Eisenberg, V. A. Kabanov, A. V. Kabanov, *Langmuir* 2004, **20**, 2066.
 - 23 S. V. Aathimanikandan, E. N. Savariar, S. Thayumanavan, *J. Am. Chem. Soc.* 2005, **127**, 14922.
 - 24 S. Qin, Y. Geng, D. E. Discher, S. Yang, *Adv. Mater.* 2006, **18**, 2905.
 - 25 X. M. Liu, L. Wang, J. Huang, C. He, *Biomaterials* 2004, **25**, 5659.
 - 26 X. Andre, M. Zhang, A. H. E. Mueller, *Macromol. Rapid Commun.* 2005, **26**, 558.
 - 27 H. Wei, X. Z. Zhang, Y. Zhou, S. X. Cheng, R. X. Zhuo, *Biomaterials* 2006, **27**, 2028.
 - 28 K. Iyama, T. Nose, *Polymer* 1998, **39**, 651.
 - 29 I. LaRue, M. Adam, M. Pitsikalis, N. Hadjichristidis, M. Rubinstein, S. S. Sheiko, *Macromolecules* 2006, **39**, 309.
 - 30 L. Desbaumes, A. Eisenberg, *Langmuir* 1999, **15**, 36.
 - 31 P. Bhargava, Y. Tu, J. X. Zheng, H. Xiong, R. P. Quirk, S. Z. D. Cheng, *J. Am. Chem. Soc.* 2007, **129**, 1113.
 - 32 L. Zhang, A. Eisenberg, *Polym. Adv. Technol.* 1998, **9**, 677.
 - 33 A. F. M. Barton, *Handbook of Polymer-Liquid Interaction Parameters and Solubility Parameters*, CRC Press, Boca Raton, 1990.
 - 34 J. Brandrup, E. H. Immergut, *Polymer Handbook*, John Wiley and Sons, New York, 1989.
 - 35 E. Feitosa, P. C. A. Barreleiro, G. Olofsson, *Chem. Phys. Lipids* 2000, **105**, 201.
 - 36 A. A. Choucair, A. H. Kycia, A. Eisenberg, *Langmuir* 2003, **19**, 1001.
 - 37 B. Lindman, H. Wennerstrom, *Top. Curr. Chem.* 1980, **87**, 1.
 - 38 (a) J. M. Bardin, D. Patterson, *Polymer* 1969, **10**, 247; (b) L. A. Wood, *J. Polym. Sci.* 1958, **28**, 319.
 - 39 Q. Chen, H. Schönherr, G. J. Vancso, *Small* 2009, **5**, 1436.
 - 40 S. P. Leytus, L. L. Melhado, W. F. Mangel, *Biochem. J.* 1983, **209**, 299.
 - 41 S. W. Provencher, *Biophys. J.* 1976, **16**, 27.

Chapter 8

Immobilization and Patterning of Block Copolymer

Vesicles onto Surfaces

The immobilization and positioning of nanoparticles on solid supports open new ways in applications such as lab-on-a-chip, sensors, microanalyses and microreactors such as the examples described in Chapter 5 and 6. In this chapter polymeric vesicles made from polystyrene-*block*-polyacrylic acid (PS-*b*-PAA) were immobilized onto amino-functionalized silicon or silicon oxide surfaces via electrostatic interactions between the positively charged amino groups on the surface of the substrates and the negatively charged carboxylic acid groups presented at the surface of the vesicles. Fourier transform infrared (FTIR) spectroscopy, as well as fluorescence optical microscopy and atomic force microscopy (AFM) were used to investigate the immobilization of the vesicles onto the surface. Different parameters, such as pH and ionic strength were used to control the amount of vesicles deposited on the surface. Finally micro-molding in capillaries was utilized to create line patterns of the vesicles containing the enzyme trypsin and the fluorogenic substrate rhodamine 110 bisamide. The formation of the fluorescent product rhodamine 110 inside the vesicles allowed the direct observation of the patterns using fluorescence microscopy. The selective positioning of vesicles in conjunction with electrostatic immobilization serves as a proof of principle for potential applications in real-time observation of confined chemical reaction inside vesicles as nanocontainers and fabrication of integrated microarray system.

8.1 Introduction

A miniature integrated system that contains thousands to millions of individual subjects which can act as isolated or inter-connected functional units is always an interesting topic for scientists, due to their promising applications in fields such as bio-analysis and biosensing.^{1,2} Polymersomes or block polymer (BCP) vesicles, with a diameter of hundreds of nanometers and a corresponding volume of atto-liters, are ideal candidates as ultra-small individual units in an integrated microarray system, owing to their unique structure. The closed membrane of the vesicles isolates the interior from outside space and can provide a microenvironment different from the

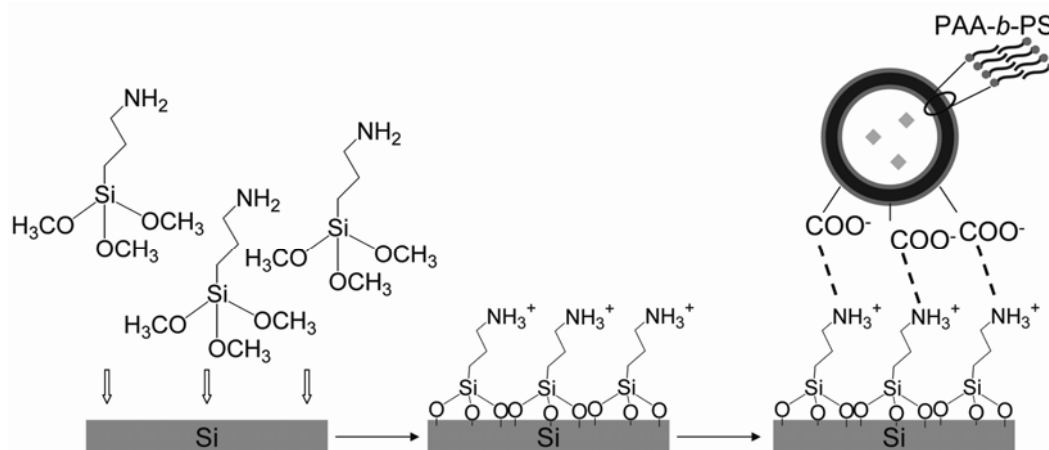
bulk.³ The architectures of these vesicles, including overall dimensions, membrane thicknesses and structures, can be precisely tuned as shown in previous chapters. Various substances, such as biomolecules, fluorescent probes can be encapsulated in the vesicle interior. Binding of such a vessel onto surfaces is of scientific interest as it may provide a confined environment for studying the kinetics of biochemical reactions and dynamic behavior of biomolecules such as enzymes and DNA.⁴ Accordingly, integrating these vessels into a microarray system can also find applications in protein chips,^{5,6} sensors,^{7,8} microanalysis⁹ and micro-reactors.^{10,11}

Different methodologies have been applied to immobilize BCP vesicles or lipid vesicles on solid supports, utilizing interactions such as electrostatic interactions, receptor-ligand binding and covalent linkage.⁴ In a study carried out by Li *et al.*¹² vesicles formed by Pluronic L121 (PEO₅-PPO₆₈-PEO₅) triblock copolymers were immobilized to a negatively charged surface via negatively charged polyelectrolytes in combination with Mg²⁺ ions. Pluronic L121 was mixed with a few weight percent of high molecular weight poly(acrylic acid) (PAA), which was negatively charged at neutral pH. The vesicles were then stabilized with an interpenetrating polymer network.¹³ These vesicles were immobilized onto a glass or a mica surface by Mg²⁺-mediated electrostatic interactions and hence could be studied by AFM. In another example, Stamou *et al.*¹⁴ defined specific regions on substrates for the immobilization of lipid bilayer vesicles through a streptavidin-biotin ligand-receptor pair. Vesicles with exposed biotin ligands on their surface locked exclusively onto the parts of the substrate where the active complementary receptor was immobilized. Later on a nanoreactor system was designed for controlled biological chemistries.¹⁵ With the help of the immobilization technique, it was possible to monitor reactions that occur inside the vesicles using fluorescence microscopy.

Soft lithography techniques, *e.g.* micro-contact printing (μ CP) and micro-molding in capillaries (MIMIC)¹⁶ greatly enhance the development for arraying or patterning vesicles onto surfaces under common laboratory conditions. The interaction between the vesicles and the substrates is of course the key issue in the process.⁴ Mahajan *et al.*¹⁷ patterned 1,2-bis(tricosyl-10,12-diynoyl)-sn-glycero-3-phosphocholine (DC_{8,9}PC) lipid vesicles with soft lithography. After preparation the vesicles were polymerized with UV light to avoid the formation of planar bilayers through fusion and rupture processes. The vesicles were patterned on glass substrates by both μ CP and MIMIC. AFM studies showed that the patterned vesicle structures were stable on glass substrates due to the electrostatic interaction between the anionic glass surface and the

cationic head groups of the lipid. MIMIC was also used by Baek *et al.*¹⁸ to pattern poly (diacetylene) vesicles for future uses in sensor and optical applications. Vesicles made from monomers such as 10,12-pentacosadiynoic acid (PCDA), PCDA-2,2'-(ethylenedioxy)bis-(ethylamine) (EDEA) displayed interesting optical properties upon UV irradiation. These vesicles were covalently immobilized on the substrate due to the reactions between the amino groups outside the vesicles and the aldehyde groups on the substrate surface.¹⁹

In this chapter a simple approach to immobilize PS₁₃₉-*b*-PAA₁₇ vesicles onto amino-terminated silicon/silicon oxide surfaces based on electrostatic interaction was explored (Scheme 8.1). Combining electrostatic interactions and soft lithography line patterns containing the vesicles were created, which serve as a pre-requisite for preparing future microarray systems utilizing these vesicles as functional elements.



Scheme 8.1 Schematic of the vesicle immobilization strategy. Silicon (or glass) substrates were treated with 3-aminopropyl trimethoxysilane. The amino-terminated substrates were then used to immobilize polymeric vesicles of polystyrene-block-poly(acrylic acid) (PS-*b*-PAA) via electrostatic interactions between the positively charged amino groups of the surface and the negatively charged carboxylic acid groups of the polymer.

8.2 Investigation on the electrostatic immobilization of PS-*b*-PAA vesicles on NH₂-terminated surfaces

In order to facilitate the electrostatic interaction between the PS-*b*-PAA vesicles and the substrates, surface silanization was carried out to introduce amino groups onto the silicon surface (see Scheme 8.1). The amino-terminated substrates were then immersed into PS-*b*-PAA vesicles solution (pH = 7.4, $C_{buffer} = 50$ mM) for 2 hours,

followed by immersion into pure water and extensive rinsing to remove physisorbed vesicles. A control experiment with normal silicon substrate was carried out and the samples were characterized with FTIR. Selected regions of FTIR spectra that PS-*b*-PAA absorbed are shown in Figure 8.1 for the amino-terminated substrates as well as the control sample.

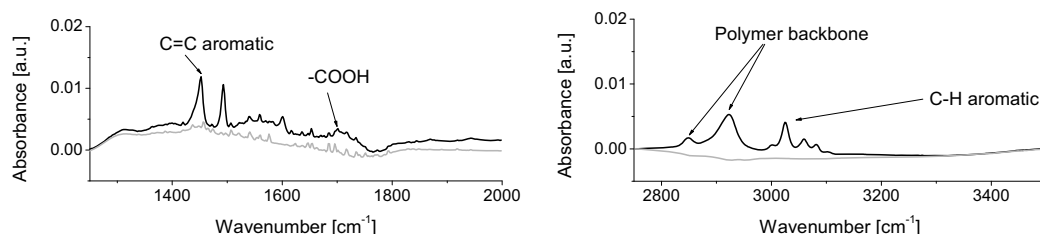


Figure 8.1 FTIR spectra of PS-*b*-PAA vesicles deposited onto silicon substrates with (black) and without (grey) surface silanization. The characteristic vibration bands of PS-*b*-PAA are assigned to the spectra as indicated in the graph.

The vibrational assignments as well as the peak wavenumbers of the major absorption bands in the spectra of PS-*b*-PAA are indicated in Figure 8.1 and listed in Table 8.1.

Table 8.1 Peak assignments and wavenumbers for infrared spectra of PS-*b*-PAA vesicles on silicon substrates.^{20, 21}

Vibration	PS (cm ⁻¹)	PAA (cm ⁻¹)
ν(CH) _{aromatic}	3083	
	3060	
	3026	
ν _{as} (CH ₂)	2924	2926
ν _s (CH ₂)	2860	2852
ν(C=O)		1710
ν(C-C) _{aromatic}	1493	
	1453	

Clear differences were observed in the FTIR spectra of the two samples. In the spectrum of samples prepared on NH₂-terminated substrates the major absorption bands of PS-*b*-PAA were clearly visible. By contrast, for the control sample all absorption peaks were missing, indicating that the presumably only loosely physisorbed vesicles were effectively removed by the rinsing step.

In order to determine the amount of polymer adsorbed on the surfaces, PS-*b*-PAA thin films were prepared by spin-coating the polymer from THF solution onto Si surfaces with different spinning speeds and polymer concentrations. The thickness of the

obtained polymer thin films was determined using ellipsometry. The films were then characterized using FTIR. The characteristic absorption of PS-*b*-PAA at 3026 cm^{-1} (assigned to the vibration of the aromatic ring of PS) is shown in Figure 8.2 for films with different thicknesses. The absorbance of this band was integrated and plotted against the film thickness as shown in the inset. A linear relationship was observed as shown in the inset. The scaling of film thickness (t) with respect to the absorbance (Abs) determined using FTIR can be described as: $t = 1014 \cdot Abs + 5.3$ ($R^2 = 0.95$).

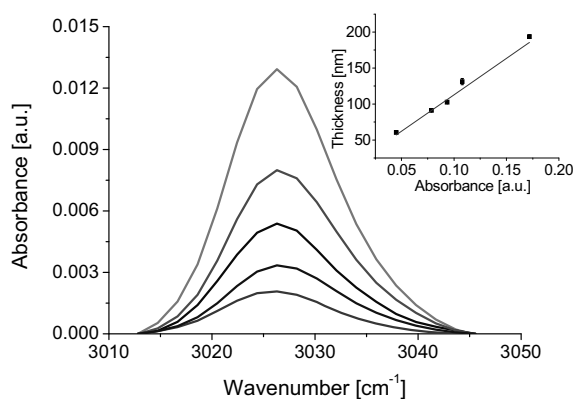


Figure 8.2 FTIR spectra showing the characteristic absorption peak of PS-*b*-PAA at 3026 cm^{-1} for different polymer film thicknesses. The inset shows a plot of the film thickness vs. the integrated absorption at 3026 cm^{-1} with a linear least squares fit (represented by the solid line) to the data.

Microscopy techniques were also used to investigate the immobilization of PS-*b*-PAA vesicles on surfaces with and without amino groups. Samples were prepared under the same conditions as described earlier. For fluorescence imaging glass substrates were used to immobilize PS-*b*-PAA vesicles with encapsulated fluorescent probes rhodamine 110, while silicon surfaces were used to prepare samples for atomic force microscopy (AFM) imaging. The micrographs obtained are shown in Figure 8.3. Samples prepared using surfaces with amino groups are displayed in the left column and the control samples without amino-terminated surfaces are displayed in the right. Fluorescence microscopic images are shown in Figure 8.3a and b. Appropriate light source and filter set were used to specifically excite the fluorescent probe rhodamine 110 (excitation peak at 490 nm) and to detect the emission ($\lambda > 515\text{ nm}$). There was a clear difference in the overall intensity of the image between the surface with and without amino functional groups. The intensity histograms based on the fluorescent images are shown in Figure 8.3c and d, respectively. The peak intensity of the image from the active sample is three times higher than the control sample. The high intensity of the sample with NH_2 terminated surface is the result from the

immobilization of rhodamine 110 containing vesicles. In the case of the control sample physisorbed vesicles were rinsed off the surface, yielding a much lower intensity.

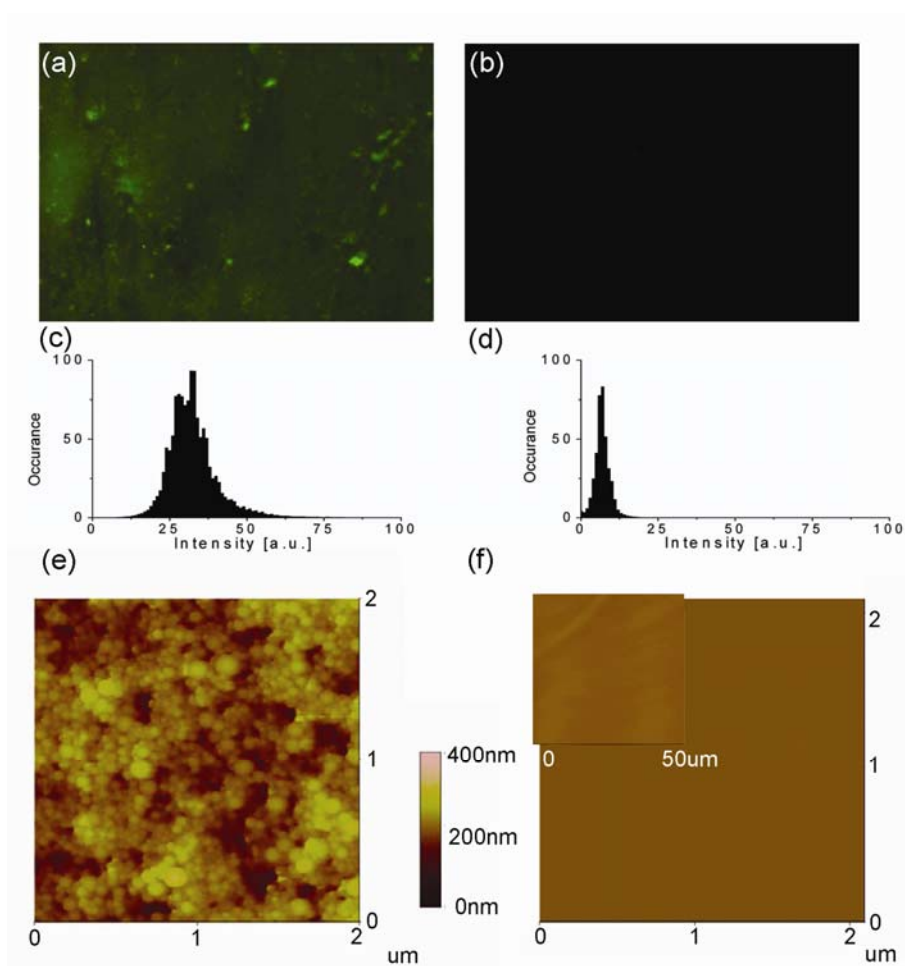


Figure 8.3 Top: Fluorescence microscopy images of PS-*b*-PAA vesicles preloaded with rhodamine 110 on (a) NH_2 -terminated and (b) normal glass substrates. (c), (d) the corresponding intensity histogram of the fluorescence images. Bottom: TM-AFM images of PS-*b*-PAA vesicles deposited on (e) NH_2 -terminated and (f) normal silicon substrates. The inset shows a zoom-out image with a scan size of $50 \times 50 \mu\text{m}^2$.

This was confirmed by AFM results. PS-*b*-PAA vesicles deposited on NH_2 terminated silicon surface were imaged by tapping mode AFM in air, as shown in Figure 8.3e. Vesicles retained their spherical shapes and arranged in a close-packed manner on the NH_2 surface. In a large scan area ($50 \mu\text{m} \times 50 \mu\text{m}$) no vesicles were found on the surface of the control sample (Figure 8.3f inset). All microscopic measurements, as well as the FTIR results, pointed to the conclusion that a much stronger affinity exists between PS-*b*-PAA vesicles and NH_2 terminated surfaces as compared to vesicles and

surfaces absent of NH₂ groups. This is attributed to the electrostatic interaction between the negatively charged carboxylic acid groups present on the vesicles and the positively charged amino groups on the surface.

8.3 Influence of pH and ionic strength on the electrostatic immobilization

8.3.1 Influence of pH

In order to prove that the PS-*b*-PAA vesicles are immobilized at the NH₂-terminated surface by electrostatic interactions, immobilization experiments were carried out at different pH values. The ionization of the vesicle surface and the substrate surface is sensitively related to the pH of the environment. By varying the pH, it is possible to change the degree of ionization of one or both of the opposite charges, thus enhancing or weakening the electrostatic interaction between the vesicles and the surfaces. In our experiments standard sodium hydroxide (or hydrochloric acid) solution (0.1 M) was added to the vesicle solution to modify the pH. Sodium chloride was added to keep the ionic strength of the solution constant ($I = 14$ mM). NH₂ terminated silicon substrates were then immersed into the vesicle solutions, followed by rinsing with water of the corresponding pH. The samples were subsequently characterized with FTIR. The absorption peaks at 3026 cm⁻¹ of different samples are shown in Figure 8.4a.

The IR spectra for samples prepared at different pH showed different values for the integrated absorption, indicating that different amount of polymer (vesicles) was adsorbed onto the surfaces under different pH. The spectra were integrated and the absorption was converted to thickness according to the calibration curve obtained from the inset of Figure 8.2. The converted film thicknesses were plotted as a function of pH in Figure 8.4b. Assuming the coverage of the vesicles is homogenous on the surface, the number of vesicles per unit area is estimated based on the amount of polymer (thickness per unit area) on the surface, which is also shown in the figure.²²

As can be seen in the graph, the amount of polymer adsorbed onto the surfaces was low at both low and high pH and reached a maximum at around pH 7.5. The fact that the high amount of vesicles immobilized onto surfaces at neutral pH again indicates the interaction between the vesicles and the surfaces is of electrostatic nature. At a pH below the pK_a of both acrylic acid (4.25)²³ and primary amine (10.64),²⁴ the

carboxylic acid groups presented on the surface of the vesicles are protonated, thus are not negatively charged while the amine groups on the substrates are positively charged; at pH above the pK_a of both primary amine and acrylic acid, the amine groups on the substrates are de-protonated, therefore losing their positive charges, yet the carboxylic acid groups on the polymer chains are negatively charged. In both cases, the electrostatic interaction is less pronounced since one of the opposite charges is absent. At neutral pH, as acrylic acid is above its pK_a and the amine is below its pK_a, both functional groups are charged and these facilitate the interaction between the opposite charges. All three scenarios are also schematically shown in Figure 8.4b.

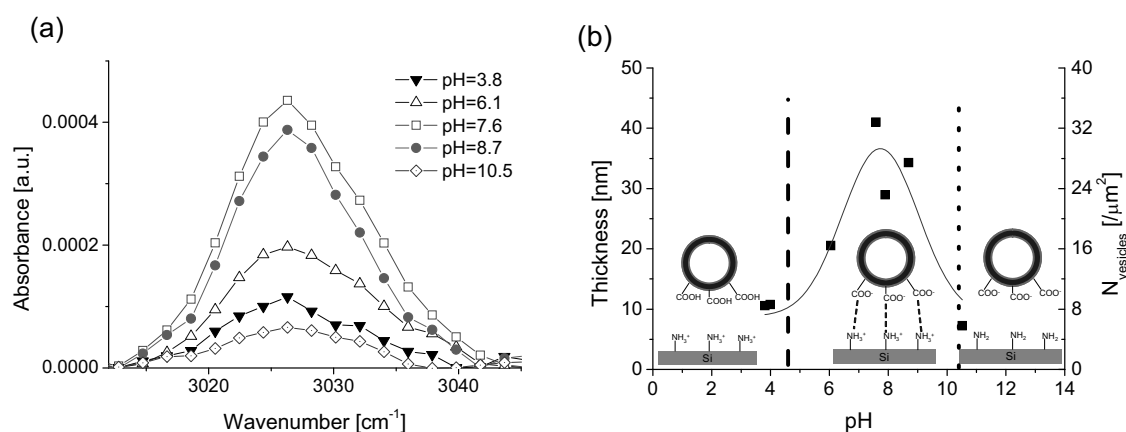


Figure 8.4 Influence of pH on the immobilization of PS-*b*-PAA vesicles on NH₂-terminated silicon substrates. Absorbance at 3026 cm⁻¹ in the FTIR spectra of PS-*b*-PAA vesicle deposited on NH₂-terminated silicon substrates from solutions with different pH values are shown in (a), integrated and plotted in (b) as a function of pH. The pK_a value of acrylic acid and primary amine are highlighted by a dash line and a dotted line, respectively.

Further AFM was used to obtain the morphology of the vesicles immobilized onto NH₂-terminated silicon under different pH and typical AFM images are shown in Figure 8.5.

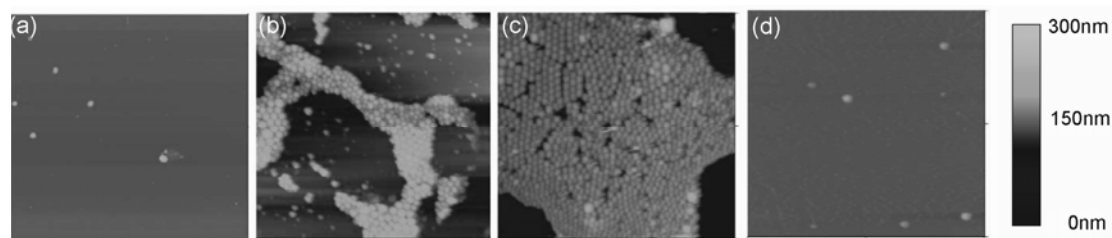


Figure 8.5 TM-AFM images of PS-*b*-PAA vesicles immobilized onto NH₂-terminated silicon surfaces at pH (a) 3.8, (b) 6.0, (c) 7.6, (d) 10.5 in ambient conditions. Scan size is 5 μm × 5 μm and z range is 300 nm in all images.

It is clearly seen that at low (3.8) and high (10.5) pH only a few vesicles were immobilized onto the substrates in a $5 \mu\text{m} \times 5 \mu\text{m}$ scan area. The same area was covered with vesicles in Figure 8.5c, under the optimal pH condition (7.6). The coverage was less when the pH (6.0) was lower than the neutral pH as in Figure 8.5b. Based on the conversion mentioned above, a full coverage of a single layer of vesicles corresponds to ~ 50 vesicles per μm^2 or a 62 nm film thickness. According to AFM bearing analysis ($n = 5$ images) the surface coverage of vesicles in Figure 8.5b and c is $46 \pm 1\%$ and $86 \pm 3\%$, respectively. This is in good agreement with the results from the FTIR measurements, as the corresponding coverage obtained from the conversion is 41% for the sample in Figure 8.5b and 82% for the sample in Figure 8.5c. The coverage in Figure 8.5a and d, however, does not correspond to the FTIR results, which is due to the low amount of vesicles adsorbed on the surface and a less constant surface density of the vesicles. A larger area should be mapped to obtain a reliable surface coverage of the samples.

8.3.2 Influence of ionic strength

Besides the electrostatic attraction between the opposite charges presented on the surface of the vesicles and the substrates, interaction between the vesicles due to the repulsion between the same charges should also be considered. For this purpose, vesicles were prepared by adding sodium chloride (NaCl) solution with different concentrations into PS-*b*-PAA solution in THF. Immobilization experiments were then carried out using the same condition as described above with constant pH 7.4. FTIR was used to characterize the samples and spectra displaying the absorption peak at 3026 cm^{-1} are shown in Figure 8.6a.

The absorbance increased as the concentration of NaCl in the solution increased as can be seen in the figure, indicating an increased number of vesicles immobilized onto the surfaces when the salt concentration was higher. This is primarily the result of the screening of surface charges. The Debye screening length (κ^{-1}), which is the scale over which mobile charge carriers screen out electric fields in an electrolyte or in a colloid system, is described by the following equation²⁵:

$$\kappa^{-1} = \sqrt{\frac{\epsilon_0 \epsilon_r kT}{2N_A e^2 I}} \quad (8.1)$$

where I is the ionic strength of the electrolyte solution with the unit in mole/m^3 , ϵ_0 and ϵ_r are the dielectric constants of vacuum and the medium, k is the Boltzmann constant,

T is temperature in Kelvin, N_A is the Avogadro's number and e is the elementary charge. Since NaCl is a symmetric mono-valent electrolyte, the ionic strength equals to the concentration of the electrolyte. In short, the Debye length obeys an inverse square-root dependence of concentration of the salt. With increasing salt concentration, the Debye length decreases, reducing the repulsion between the vesicles. This would result in larger number of vesicles immobilized onto the surfaces.

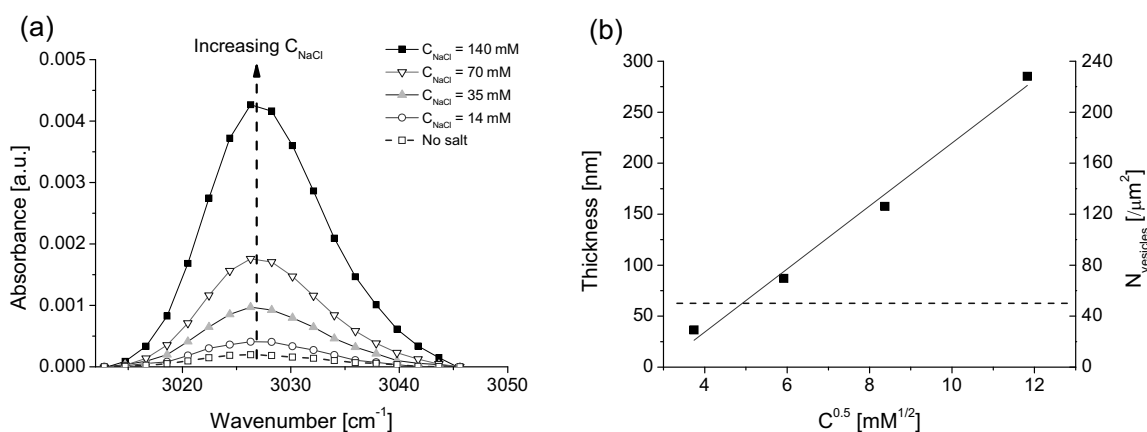


Figure 8.6 Influence of ionic strength on the immobilization of PS-*b*-PAA vesicles on NH₂-terminated silicon substrate. Absorbance at 3026 cm⁻¹ in the FTIR spectra of PS-*b*-PAA vesicle solutions with different salt concentrations deposited on NH₂-terminated silicon substrates are shown in (a), integrated and plotted in (b) as a function of the square root of the ionic strength. The solid line is a least square fit to the data. The horizontal line indicates the thickness (and the corresponding N_{vesicles}), which corresponds to a monolayer coverage of vesicles.

Furthermore, the IR spectra were integrated, converted to PS-*b*-PAA film thickness and plotted as a function of the square root of concentration ($C^{0.5}$), shown in Figure 8.6b. An almost linear relationship was observed between the two parameters, which follows the same trend as the square root dependence of Debye length with respect to the ionic strength of the electrolytes. The thickness and number of vesicles per μm² corresponding a full coverage of a single layer of vesicles are also shown in the figure. The thickness / N_{vesicles} for samples with salt concentration higher than 35 mM is higher than the value of a single layer, which indicates that vesicles are stacking on the surface, as a result of the reduction in electrostatic repulsion between the vesicles.

8.4 Patterning of PS-*b*-PAA vesicles on surfaces using MIMIC

MIMIC is remarkable for its simplicity and fidelity in transferring patterns from the mold to the structures that it forms.¹⁶ Since the vesicles are dispersed in the solution with a rather low concentration and MIMIC has the unique advantage of creating line patterns from liquid phase, we chose MIMIC in our experiments to immobilize PS-*b*-PAA vesicles in a patterned way. In the experiment a polydimethylsiloxane (PDMS) mold with 16 μm wide line patterns, separation of 16 μm between the lines and depth of 20 μm was first treated with oxygen plasma to render the surface hydrophilic, it was then placed on the surface of a substrate and a conformal contact with that surface was established. The relief structure in the mold formed an array of empty channels. Then a droplet of vesicle solution was placed at the open ends of the network channels, the liquid spontaneously filled the channels by capillary action. Snapshots of the process observed under optical microscopy are shown in Figure 8.7 for vesicle solution with and without the presence of salt.

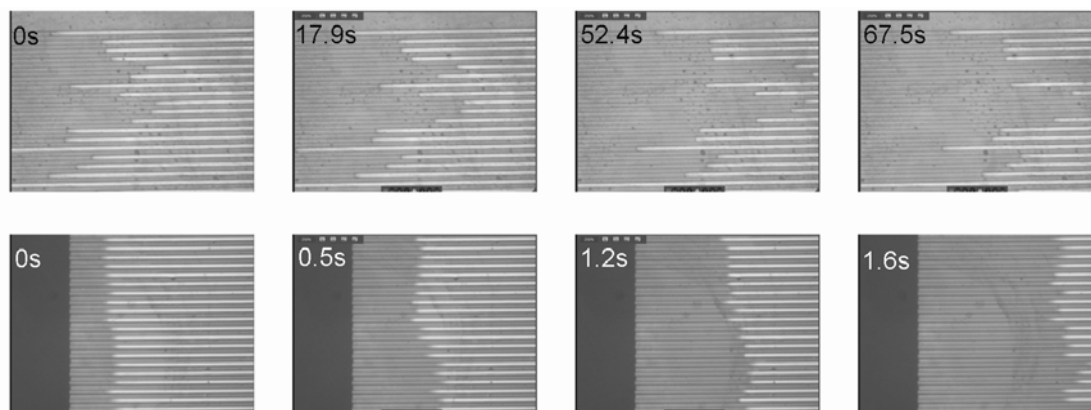


Figure 8.7 Snapshots of the filling of the PDMS channel using PS-*b*-PAA vesicles with or without the presence of salt. Upper row: No salt, filling speed $8.1 \pm 0.8 \mu\text{m/s}$. Lower row: NaCl concentration 35 mM, filling speed $478 \pm 29 \mu\text{m/s}$.

Advancement of the solution meniscus is clearly seen from the snapshots shown in Figure 8.7. It should be noted that the time interval between the snapshots was different and the solution with different salt concentration filled the channel with substantially different speeds. The filling speed for vesicle solution containing 35 mM NaCl ($478 \mu\text{m/s}$) was almost 60 times higher than vesicle solution without any salt ($8 \mu\text{m/s}$). The reason for this difference is explained by the fact that the filling speed is closely related to the surface tension and viscosity of the liquid by the following

equation¹⁶:

$$\frac{dz}{dt} = \frac{R\gamma_{LV} \cos \theta}{4\eta z} = \frac{R(\gamma_{SV} - \gamma_{SL})}{4\eta z} \quad (8.2)$$

where z is the length of the filled section of the capillary, R is the radius of the capillary, η is the viscosity of the liquid, γ_{LV} , γ_{SV} , γ_{SL} are the liquid-vapor, solid-vapor, solid-liquid interfacial free energies. It has been long known that the presence of salt in water generally increases the surface tension of the solution.²⁶ Therefore, a higher filling speed was achieved when salt was added into the solution, as demonstrated here.

Subsequently PS-*b*-PAA vesicles encapsulated with substrates rhodamine 110 arginine bisamide and enzymes trypsin were used to fill the channels. The enzymes and substrates are known to be able to react inside the vesicles and form a highly fluorescent product rhodamine 110.²⁷ Filling experiments were carried out as described above. After the solution was dried out, the stamp was removed from the surface and the glass substrate was rinsed extensively with pure water. Fluorescence microscopy was used to inspect the patterns created before and after the rinsing. (Figure 8.8a and b)

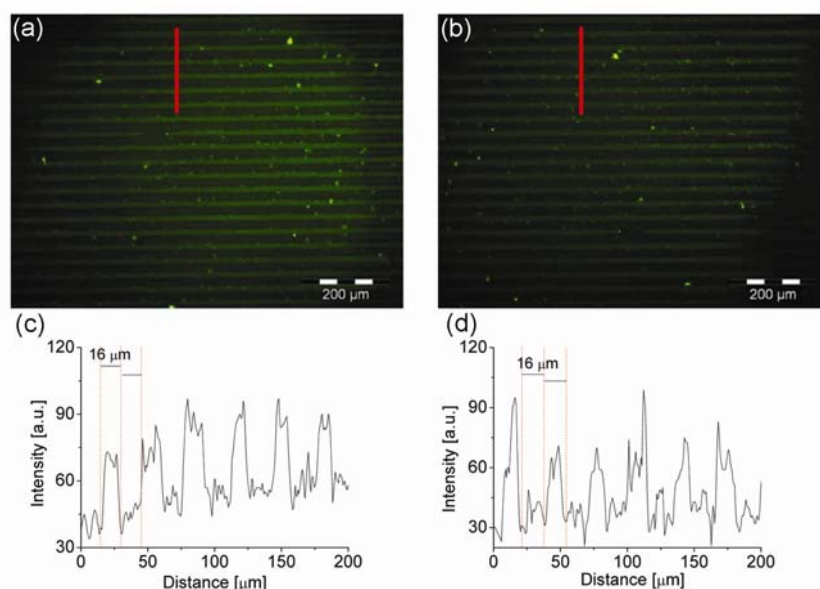


Figure 8.8 Fluorescence images of line patterns of PS-*b*-PAA vesicles preloaded with rhodamine 110 bisamide and trypsin deposited on NH_2 -terminated glass substrate using MIMIC technique (a) after the solvent was evaporated and (b) after rinsing extensively with Milli-Q water. (c) and (d) are the cross-sectional intensity profiles of the fluorescence image as indicated by the red lines in (a) and (b).

As shown in the images line patterns were created using MIMIC. The fluorescent signals were originated from rhodamine 110 as the product of trypsin catalyzed hydrolysis reaction inside the vesicles. No substantial loss of fluorescence intensity was observed when comparing the images before (Figure 8.8a) and after (Figure 8.8b) extensive rinsing, indicating that the vesicles were firmly immobilized onto the surfaces via the electrostatic interaction discussed in previous sections. Cross-section analysis of the image (Figure 8.8c and d) showed that the dimensions of the patterns faithfully obeyed the dimensions of the channels fabricated with PDMS mold used (channel width 16 μm , separation 16 μm). The successful filling of PS-*b*-PAA vesicles containing functional molecules using MIMIC and creation of line patterns of these vesicles provide us a pathway to selectively immobilize functional miniature vessels onto surfaces which may find future applications in real-time observation of reaction kinetics and dynamic behavior of biomolecules of interest. Future studies could be focused on optimization and further miniaturization of the patterns, introduction of multiple functional vessels and integration of different functional subunits for the realization of a microarray system.

8.5 Conclusion

PS-*b*-PAA vesicles were immobilized onto solid surfaces functionalized with amino groups by means of electrostatic interaction. This was further confirmed by varying the pH of the solution during the immobilization experiments. Vesicles were found to have a higher affinity to the surface at neutral pH as electrostatic interaction was minimized at both low and high pH. Ionic strength was also used to control the amount of vesicles immobilized on the surface. A higher salt concentration resulted in a higher number of vesicles deposited due to the screening of the electrostatic repulsion. Soft lithography, namely MIMIC was used in combination with the electrostatic immobilization to create line patterns of PS-*b*-PAA vesicles containing functional molecules enzyme trypsin and substrate rhodamine 110 arginine bisamide, which can serve as a potential means in the fabrication of a microarray system.

8.6 Experimental

PS₁₃₉-*b*-PAA₁₇ (the subscripts denote the number of repeat units for respective blocks) were purchased from Polymer Source Inc. (Dorval, Canada). 3-aminopropyl trimethoxysilane, sodium hydroxide (0.1M), hydrochloric acid (0.1M) and enzyme bovine pancreas trypsin was purchased from Sigma-Aldrich, Inc. (St. Louis, MO, USA). The fluorogenic substrate rhodamine 110-arginine bisamide was purchased from Molecular Probes/Invitrogen Co. (Carlsbad, CA, USA). Buffer solution containing sodium chloride and sodium hydrogen phosphate and sodium dihydrogen phosphate was purchased from B. Braun Melsungen AG (Melsungen, Germany). THF (AR grade) was purchased from Biosolve B. V. (Valkenswaard, the Netherlands). Milli-Q water was produced by a Millipore Synergy system (Billerica, MA, USA). All chemicals were used as received.

PS-*b*-PAA vesicles were prepared by first dissolving the polymer in THF with initial concentrations of 2 wt%, then adding Milli-Q water (or aqueous solution containing the active substances) as a precipitant into the polymer solution until a given water percentage (50 vol%) was reached, while the entire system was under vigorous stirring using a magnetic stirring bar at ~ 600 rpm. After stirring for overnight, the solution mixture was subjected to dialysis for 72 hours to remove organic solvent residue and low molecular weight impurities. Dialysis was carried out using Spectra/Por 7 dialysis tubing from Spectrum Europe B.V. (Breda, the Netherlands) with a molecular weight cut off of 50 kD.

The size of PS-*b*-PAA vesicles was determined with a Malvern Zeta-sizer 4000 (Malvern Corp., Malvern, UK) at 25°C using a laser wavelength of 633 nm and a scattering angle of 90°. The CONTIN method²⁸ was applied for data processing. The size, count rate and poly-dispersity index (PDI) of the vesicles were determined.

Silicon and glass substrates of approximately 1 by 1 cm were used in the immobilization experiments. Substrates were first cleaned with piranha solution (3:1 (v:v) mixture of sulfuric acid and 30% hydrogen peroxide) to remove organic impurities, subsequently silanized by immersing into 3-aminopropyltrimethoxysilane solution in toluene (10 mM) for 8 hours. The NH₂-silane coated substrates were subsequently rinsed with toluene and dried under nitrogen. Immobilization of the vesicles was carried out by immersing the substrates into various vesicle solutions for 2 hours. Afterwards the samples were taken out and rinsed extensively with MilliQ water and dried under nitrogen flow.

AFM images were obtained under ambient conditions in tapping mode with a NanoScope IIIa multimode atomic force microscope (Digital Instruments/Veeco, Santa Barbara, CA, USA) using silicon cantilevers with resonance frequencies of 200 - 500 kHz (type PPP-NCH-W, Nanosensors, Wetzlar, Germany) and a J-scanner (Digital Instruments/Veeco).

Transmission mode FTIR spectra were obtained using a BIO-RAD model FTS575C FTIR spectrometer (Bio-rad Laboratories, Inc., Hercules, CA, USA) equipped with a liquid nitrogen cooled cryogenic mercury cadmium telluride (MCT) detector. Background spectra were obtained using cleaned silicon substrates.

Fluorescence microscopy images were obtained by an Olympus inverted microscope IX71 (Olympus corporation, Tokyo, Japan) equipped with a mercury burner U-RFL-T as the light source and a digital camera for image acquisition. Blue excitation (450 nm < λ < 480 nm) and green emission light (λ > 515 nm) were properly filtered using a U-MWG Olympus filter tube (Olympus corporation, Tokyo, Japan).

Patterning of PS-*b*-PAA vesicles was carried out using PDMS stamps with channels of 16 μ m and a height of 20 μ m. The PDMS stamps were made hydrophilic with O₂ plasma treatment and were brought in contact with glass substrates cleaned with piranha solution. Vesicle solutions of 2 wt% PS-*b*-PAA in THF with 50% water content with trypsin and rhodamine 110 bisamide inside the vesicles were added to the edge of the stamp where the opening of the channels located. Filling of the channels immediately took place as a result of capillary force. The process was recorded using optical microscopy. After drying at room temperature the stamps were removed and the samples were rinsed extensively with Milli-Q water.

8.7 References and notes

- 1 M. Bally, M. Halter, J. Vörös, H. M. Grandin, *Surf. Interface Anal.* 2006, **38**, 1442.
- 2 D. N. Howbrook, A. M. van der Valk, M. C. O'Shaughnessy, D. K. Sarker, S. C. Barker, A. W. Lloyd, *Drug Discov. Today* 2003, **8**, 642.
- 3 D. E. Discher, A. Eisenberg, *Science* 2002, **297**, 967.
- 4 J. E. Yang, C. Y. Gao, *Chin. Sci. Bull.* 2008, **53**, 3477.
- 5 T. Kodadek, *Chem. Biol.* 2001, **8**, 105.
- 6 H. Zhu, M. Snyder, *Curr. Opin. Chem. Bio.* 2003, **7**, 55.
- 7 R. Jelinek, S. Kolusheva, *Biotech. Adv.* 2001, **19**, 109.
- 8 M. A. Cooper, *J. Mol. Recognit.* 2004, **17**, 286.
- 9 G. Tresset, S. Takeuchi, *Anal. Chem.* 2005, **77**, 2795.
- 10 A. Antipov, D. Shchukin, Y. Fedutik, I. Zhanavskina, V. Klechkovskaya, G. Sukhorukov, H.

- Möhwald, *Macromol. Rapid Commun.* 2003, **24**, 274.
- 11 P. Y. Bolinger, D. Stamou, H. Vogel, *J. Am. Chem. Soc.* 2004, **126**, 8594.
- 12 F. Li, T. Ketelaar, M. A. C. Stuart, E. J. R. Sudholter, F. A. M. Leermakers, A. T. M. Marcelis, *Langmuir* 2008, **24**, 76.
- 13 F. Li, T. Ketelaar, A. T. M. Marcelis, F. A. M. Leermakers, M. A. C. Stuart, E. J. R. Sudholter, *Macromolecules* 2007, **40**, 329.
- 14 D. Stamou, C. Duschl, E. Delamarche, H. Vogel, *Angew. Chem. Int. Ed.* 2003, **42**, 5580.
- 15 P. Y. Bolinger, D. Stamou, H. Vogel, *Angew. Chem. Int. Ed.* 2008, **47**, 5544.
- 16 Y. N. Xia, G. M. Whitesides, *Angew. Chem. Int. Ed.* 1998, **37**, 551.
- 17 N. Mahajan, R. B. Lu, S. T. Wu, J. Y. Fang, *Langmuir* 2005, **21**, 3132.
- 18 J. H. Baek, H. Ahn, J. Yoon, J. M. Kim, *Macromol. Rapid Commun.* 2008, **29**, 117.
- 19 D. J. Ahn, J. M. Kim, *Acc. Chem. Res.* 2008, **41**, 805.
- 20 A. Gopferich, *Biomaterials* 1996, **17**, 103.
- 21 Z. H. Lu, G. Liu, S. Duncan, *Macromolecules* 2004, **37**, 174.
- 22 The conversion of PS-*b*-PAA film thickness (d) to the number of vesicles ($N_{vesicles}$) per μm^2 was done assuming the coverage of vesicles is homogeneous on the surface and the vesicles have a monomodal size distribution with a radius of $R = 75$ nm and a membrane thickness of $t = 25$ nm. The PS volume (V_{PS}) for an individual vesicle is expressed by the following equation: $V_{PS} = 4/3\pi R^3 - 4/3\pi(R-t)^3$. The total volume of PS is kept constant, which equals the PS volume for an individual vesicle multiplied by the number of vesicles per unit area ($A = 1 \mu\text{m}^2$ is used for the simplicity of calculation), as well as the thickness of the film multiplied by the area of the film: $V_{totalPS} = N_{vesicles} \cdot V_{PS} = d \cdot A$.
- 23 J. Brandrup, E. H. Immergut, *Polymer Handbook*, John Wiley and Sons, New York, 1989.
- 24 D. R. Corbin, S. Schwarz, G. C. Sonnichsen, *Catalysis Today* 1997, **37**, 71.
- 25 W. B. Russel, D. A. Saville, W. R. Schowalter, *Colloidal Dispersions*, Cambridge University Press, Cambridge, 1989.
- 26 L. Onsager, N. N. T. Samaras, *J. Chem. Phys.* 1934, **2**, 528.
- 27 Q. Chen, H. Schönherr, G. J. Vancso, *Small* 2009, **5**, 1436.
- 28 S. W. Provencher, *Biophys. J.* 1976, **16**, 27.

Summary

This Thesis describes thoroughly the preparation and characterization of vesicles made from amphiphilic block copolymers and subsequently their use as nanocontainers for the study of enzymatic reactions in atto-liter confined space. The confinement caused by the membrane boundaries of the vesicles was found to enhance the catalytic activity of the encapsulated enzymes. This enhancement was attributed to a combined effect of high collision frequencies between the reagents and a strong interaction between the enzymes and the vesicle wall, which was predicted in previous theoretical studies yet not observed experimentally. In addition to kinetic investigation of enzymatic catalysis, the “polymersome” nanocontainers were characterized and their thermodynamics in mixed solvents was studied.

A short introduction to the topics treated in this Thesis and the motivation of the research is presented in *Chapter 1*.

In *Chapter 2* a literature overview is given on different types of synthetic nanocontainers. The general background of enzyme kinetics, as well as recent developments in the field of single enzymology are introduced, followed by a discussion of theoretical studies on reactions occurring in finite space, *i.e.* inside nanocontainers.

In *Chapter 3* the preparation of vesicles made from polystyrene-*block*-poly (acrylic acid) (PS-*b*-PAA) using the selective solvent method is described. Solution composition, including the water content, initial polymer concentration, added ions and the nature of the common solvent were varied to control the size of the vesicles. The effect of the chain length of the block copolymers on the wall thickness of the vesicles was explored. Preparation of vesicles at different temperatures was carried out and the morphological change from vesicles to micelles at elevated temperature was observed. The thermal stability of the vesicles was studied using atomic force microscopy (AFM) and it was found that substrate supported vesicles were stable in air up to 80°C. Finally small fluorescent molecules with different hydrophobicities were encapsulated both in the wall and in the interior of the vesicles as a first attempt to utilize these vesicles as nanocontainers for future study of biochemical reactions in confined environment.

Chapter 4 describes the assessment of the mechanical properties of PS-*b*-PAA vesicles assembled from polymers with different chain lengths, *i.e.* different

membrane thickness, using AFM. The vesicle membrane thickness was shown by transmission electron microscopy (TEM) to scale in accordance with literature data with the degree of polymerization of both blocks. Based on AFM force data and the application of the shell deformation theory, the apparent isotropic Young's moduli of the membranes were estimated. While the values of the spring constant of the membrane were found to be directly proportional to the membrane thickness for vesicles with the same diameter, the apparent Young's moduli were found to decrease with increasing wall thickness. This effect coincides with the decreasing degree of polystyrene stretching that was reported in the literature for membranes with increasing thickness.

As described in Chapter 3 atto-liter volume PS-*b*-PAA vesicles with controlled internal diameters ranging from 45 nm to 210 nm were successfully prepared. In **Chapter 5** the study of loading enzyme trypsin and its fluorogenic substrate R110-Arg₂ into the vesicles is discussed. The catalytic turnover number (k_{cat}) and the Michaelis-Menten constant (K_M) for the unrestricted reaction of trypsin in solution and for the reaction confined in the vesicles were found to differ significantly. While the values of k_{cat} of trypsin encapsulated in vesicles with different diameters were always higher than those of trypsin in solution, the values of K_M were lower. Compared to the reaction in solution, the enzyme efficiency (k_{cat} / K_M) increased by two orders of magnitude. This observed higher reactivity of encapsulated trypsin is attributed to the molecular confinement inside the vesicles, which causes higher collision frequencies between the reagents as well as higher collision frequencies between the encapsulated molecules and the container wall.

The study of enzymatic reactions in nanocontainers and the investigation of confinement effects on the catalytic activity of enzymes are extended and present in **Chapter 6**. α -Chymotrypsin and its fluorogenic substrate *N*-succinyl-Ala-Ala-Phe-7-amido-4-methylcoumarin were encapsulated into PS-*b*-PAA vesicles with different sizes. The encapsulation percentages of the enzymes and substrates were found to be the same when loaded into vesicles with the same size. The efficiency of the encapsulation increased as the size of the vesicles decreased. The values of k_{cat} of the enzymatic reactions encapsulated in vesicles with different diameters were always higher (15 times for the most pronounced enhancement) than those of the enzymatic reactions in solution. A clear size dependence of the k_{cat} of enzymatic reactions inside the capsules was observed for vesicles with an inner diameter ranging from 30 nm to 170 nm. The observed higher reactivity of encapsulated α -chymotrypsin is attributed

to the molecular confinement inside the vesicles, which is a combined effect of high collision frequencies between the reagents and a significant interaction between the enzymes and the vesicle wall.

The study on the size and morphology of PS-*b*-PAA aggregates in a tetrahydrofuran (THF)/H₂O mixed solvent system at different temperatures is presented in **Chapter 7**. It was found that PS-*b*-PAA aggregates underwent a vesicle-to-micelle transition as the temperature of the system was raised above a critical value. The transition was a result of the change in polymer solvent interaction at different temperatures. In addition, the presence of the common solvent THF was found to be crucial for the transition, as this lowered the glass transition temperature of polystyrene in the vesicle membrane to allow the polymer chains to reorganize. Successful encapsulation and release of small molecules was achieved utilizing the assembly and disassembly of PS-*b*-PAA aggregates cross the transition temperature. Rhodamine 110 bisamide, whose hydrolysis reaction was discussed in Chapter 5, was preloaded into the vesicles and released when the system was heated to above the transition temperature to react with enzyme trypsin to form fluorescent product rhodamine 110. The product was then encapsulated into reformed vesicles when the system was cooled down to below transition temperature, proven using sodium nitrite.

Finally, the results of a study on the immobilization and patterning of PS-*b*-PAA vesicles onto amino-functionalized solid supports via electrostatic interactions is discussed in **Chapter 8**. The electrostatic nature of the immobilization of the vesicles on surfaces was confirmed by varying the pH of the solution during the immobilization experiments. Vesicles were found to have a higher affinity to the surface at neutral pH as electrostatic attraction was minimized at both low and high pH. The ionic strength was also used to control the amount of vesicles immobilized on the surface. A higher salt concentration resulted in an increased number of vesicles deposited due to the screening of the electrostatic repulsion. Micromolding in capillaries (MIMIC) was used in combination with the electrostatic immobilization to create line patterns of PS-*b*-PAA vesicles containing trypsin and a fluorogenic substrate. This approach may serve as a potential means to fabricate microarray systems and may find future applications in real-time observations of reaction kinetics and dynamic behavior of biomolecules of interest inside the vesicles.

Samenvatting

Dit proefschrift beschijft in detail de vorming en karakterisering van “vesicles” bestaande uit amfifiele blokcopolymeren en het gebruik van deze “vesicles” als nanocontainers om enzymatische reacties te bestuderen in atto-liter volumes. De begrenzend aanwezigheid van de membraanwanden in de “vesicles” liet een verhoogde catalytische activiteit van de geencapsuleerde enzymen zien. Deze verhoogde activiteit werd toegeschreven aan een gecombineerd effect van hogere botsingsfrequenties tussen de aanwezige reactanten en de sterke interactie tussen de enzymen en de wanden van de “vesicles”. Dit effect was in eerdere theoretische studies wel voorspeld, maar nog niet eerder experimenteel waargenomen. Naast de kinetiek van de enzymatische katalyse werden de “polymerosome” nanocontainers gekarakteriseerd en werd de thermodynamica in gemengde oplosmiddelen bestudeerd. Een korte introductie van de onderwerpen beschreven in dit proefschrift en de motivatie voor dit onderzoek wordt gegeven in *Hoofdstuk 1*.

In *Hoofdstuk 2* wordt een overzicht gegeven van verschillende typen synthetische nanocontainers bekend uit de literatuur. Algemene achtergrondinformatie met betrekking tot enzymkinetiek en recente ontwikkelingen in het onderzoeksveld van “single enzymology” wordt geven, alsmede een discussie over theoretische studies naar reacties in beperkt volume, ofwel in nanocontainers.

In *Hoofdstuk 3* wordt de productie van polystyrene-*block*-poly(acrylic acid) (PS-*b*-PAA) “vesicles” met de “selective solvent” methode beschreven. Oplossingsamenstelling, inclusief het watergehalte, initiële polymeerconcentratie, toegevoegde ionen en het soort gemeenschappelijk oplosmiddel werden gevarieerd om de grootte van de “vesicles” te controleren. De invloed van de ketenlengte van de blokcopolymeren op de wanddikte van de “vesicles” werd onderzocht. Productie van de “vesicles” werd uitgevoerd bij verschillende temperaturen en de morfologieovergang van “vesicles” naar micellen werd waargenomen bij hogere temperaturen. De thermische stabiliteit van de “vesicles” werd onderzocht met Atomic Force Microscopy (AFM) en het bleek dat substraat ondersteunde vesicles stabiel waren bij temperaturen tot 80°C in lucht. Tot slot werden kleine fluorescerende moleculen met verschillende mate van hydrofobiciteit geencapsuleerd in zowel de wand als in het interieur van de “vesicles” in een eerste poging de “vesicles” als nanocontainers te gebruiken voor toekomstig onderzoek naar biochemische reacties in

een omgeving met beperkt volume.

Hoofdstuk 4 beschrijft de bepaling van de mechanische eigenschappen van PS-*b*-PAA “vesicles” bestaande uit polymeren met verschillende ketenlengte, ofwel verschillende wanddiktes, door middel van AFM. De vesicle membraandikte als gemeten met transmission electron microscopy (TEM) kwam overeen met literatuurdata voor de polymerisatiegraad van beide blokken. Gebaseerd op AFM kracht data en de toepassing van de “shell deformation” theorie werd de schijnbare isotrope Young’s modulus van de membranen geschat. De bepaalde waarden voor de veerconstante van het membraan namen linear toe met de membraan dikte voor “vesicles” van dezelfde grootte, terwijl de schijnbare Young’s modulus afnam met toenemende wanddikte. Dit effect komt overeen met een afname van de polystyreen strekking zoals bekend in de literatuur voor membranen met toenemende dikte.

Zoals beschreven in Hoofdstuk 3 werden atto-liter volume PS-*b*-PAA “vesicles” met gecontroleerde interne diameters variërend van 45 nm tot 210 nm succesvol gemaakt. In **Hoofdstuk 5** wordt de studie naar het beladen van de “vesicles” met het enzym trypsin en zijn “fluorogenic” substraat R110-Arg₂ besproken. Het “catalytic turnover number” (k_{cat}) en de Michaelis-Menten konstante (K_M) bleken voor de vrije reactie van trypsin in oplossing en de in volume beperkte reactie in de “vesicles” significant te verschillen. Terwijl de waarden voor k_{cat} van trypsin geencapsuleerd in de “vesicles” met verschillende diameters altijd hoger waren vergeleken met die van trypsin in de vrije oplossing, bleken de K_M waarden lager te zijn. Vergeleken met de reactie in oplossing nam de enzymatische efficiëntie (k_{cat} / K_M) met twee ordes van grootte toe. Deze waargenomen hogere activiteit van geencapsuleerd trypsin wordt toegeschreven aan de moleculaire beperking binnenin de “vesicles”, met als gevolg hogere botsings frequenties tussen de reagenten en daarnaast een toename in botsings frequenties tussen de geencapsuleerde moleculen en de containerwand.

Het bestuderen van enzymatische reacties in nanocontainers en het onderzoek naar het effect van het beperkte volume op de katalytische activiteit van de enzymen wordt voortgezet en besproken in **Hoofdstuk 6**. α -Chymotrypsin en zijn “fluorogenic” substraat *N*-succinyl-Ala-Ala-Phe-7-amido-4-methylcoumarin werden geencapsuleerd in PS-*b*-PAA “vesicles” van verschillende grootte. Het encapsuleringspercentage van zowel enzymen en substraten was gelijk voor encapsulering in “vesicles” met dezelfde grootte. De encapsulerings-efficiëntie was hoger voor kleinere “vesicles”. De k_{cat} waarden voor de enzymatische reacties in de “vesicles” waren in alle gevallen hoger (tot maximaal 15 keer) vergeleken met de enzymatische reacties in oplossing.

Een duidelijke grootte afhankelijkheid van k_{cat} voor de enzymatische reacties in de capsules werd waargenomen voor “vesicles” met een binnendiameter variërend van 30 nm tot 170 nm. De waargenomen hogere reactiviteit van de geencapsuleerde α -chymotrypsin is het gevolg van het beperkte volume binnen in de vesicles, wat een gecombineerd effect is van hoge botsings frequenties tussen de reagenten en een significante interactie tussen de enzymen en de “vesicle” wand.

Het bestuderen van de grootte en morfologie van PS-*b*-PAA aggregaten in tetrahydrofuran (THF)/H₂O mengsels bij verschillende temperaturen wordt beschreven in **Hoofdstuk 7**. De PS-*b*-PAA aggregaten ondergingen een overgang van “vesicle” naar micel bij temperaturen boven een kritische temperatuur. Deze overgang is het gevolg van de verandering in polymeer-oplosmiddel interacties bij verschillende temperaturen. Daarnaast bleek de aanwezigheid van het gezamenlijke oplosmiddel THF van essentieel belang voor de overgang, omdat zo de glasovergangstemperatuur van polystyreen in de “vesicle” wand verlaagd wordt zodat de polymeerketens kunnen reorganiseren. Succesvolle encapsulering en afgifte van kleine moleculen was mogelijk via de “assembly” en “dissassembly” van PS-*b*-PAA aggregaten door verwarmen tot boven of afkoelen tot onder de overgangstemperatuur. Vooraf in de “vesicles” geencapsuleerd Rhodamine 110 bisamide, waarvan de hydrolyse reactie is besproken in Hoofdstuk 5, werd afgegeven door de “vesicles” te verwarmen boven de transitie temperatuur om daarna te reageren met het enzym trypsin tot het fluorescente product rhodamine 110. Het ontstane product werd vervolgens geencapsuleerd in de hervormde “vesicles”, zoals bewezen met natrium nitriet, tijdens het afkoelen tot onder de overgangstemperatuur.

Tot slot worden de resultaten van een studie naar de immobilisatie en patroonvorming van PS-*b*-PAA “vesicles” op amino-gefunctionaliseerde harde substraten via elektrostatistische interacties besproken in **Hoofdstuk 8**. De elektrostatistische aard van de binding van de “vesicles” op deze oppervlakken werd bevestigd door de pH van de oplossing te variëren voor de immobilisatie experimenten. “Vesicles” vertoonden een hogere affiniteit met het oppervlak bij neutrale pH, doordat de elektrostatistische aantrekkingskracht geminimaliseerd was bij zowel lage als hoge pH. De ionsterkte werd ook gebruikt om de hoeveelheid geïmmobiliseerde “vesicles” op het oppervlak te beïnvloeden. Een hogere zoutconcentratie resulteerde in een toename van het aantal gedeponeerde “vesicles” op het oppervlak door de screening van de elektrostatistische afstoting. “Micromolding in capillaries” (MIMIC) gecombineerd met de elektrostatistische immobilisatie werd gebruikt om lijnpatronen van PS-*b*-PAA

“vesicles” beladen met trypsin en een “fluorogenic” substraat te creëren. Deze immobilisatiemethode kan potentieel gebruikt worden voor de fabricage van “microarray” systemen met toekomstige toepassingen in de “real-time” observatie van reactiekinetiek en dynamisch gedrag van interessante biomoleculen in de “vesicles”.

Acknowledgements

The research work presented in the Thesis can not be achieved without the help of many people, to whom I would like to show my gratitude. Thanks to their help, the project can be carried out smoothly and grow beyond my original imagination. I feel from time to time appreciated that I am surrounded by such a group of nice and motivating people.

The first person I would like to acknowledge is my promoter, Prof. Julius Vancso, who offered me the opportunity to start as a master student in the program of Nanotechnology, and later on as a PhD student in his group. Thanks to this Master program, to which he was a coordinator, I got to know what Nanotechnology is and had the chance to touch the different perspectives of this multidisciplinary field. Julius, during the four years of PhD study, you allowed me to define and carry out my own research. On the other hand, when it comes to discussions, your attitude towards fundamental science, your passion on pursuing emerging applications on nanotechnology and nanoscience, set up a nice example for me to follow. I really hope that I can still work with you and learn from you.

I sincerely thank my assistant promoter, Prof. Holger Schönherr. As a daily supervisor you helped me a lot in shaping up the project. Discussions with you on the project always lead to fruitful results. Your critical view helped me to improve the quality of many experiments and analysis. I could not succeed without your patience and support. Dear Holger, thank you once more.

I am grateful to Dr. Mark Hempenius, who taught me a lot of things in the chemical lab. You are the master of synthesis and I wish I had the honor to do synthesis with you. Also thank you for correcting the Dutch translation of the summary. Many thanks to the master of the instruments Clemens Padberg! Without you I think the whole group will be down. Another person who is indispensable for the group is Geneviève Rietveld. Gen, thank you for all the paperwork, and your professional opinions on the cover design of my Thesis.

I also feel lucky to have a few students helping me with some of the work described in the Thesis. Kristin Rausch, a Socrates exchange student from the University of Mainz, spent five months working on the kinetics of chymotrypsin catalysis within the boundary of vesicles. Her devoted contribution constituted a substantial part of Chapter 6. Master student Wilma de Groot did her master project with me and her

master research was the main part of Chapter 8. Ramon Groote is acknowledged for his contribution on part of Chapter 2, which resulted in a very nice review article. I thank you all for your help.

I wish to express my special thanks to my paranimfen and officemates: Edit Kutnyanszky and Joost Duvigneau. Edit is always there to share the daily highs-and-lows, also the “top” story from the “top-team”. Joost is my favorite and only matching AIO. We spend together a lot of “useful” time in the user-committee meetings. Joost is also acknowledged for translating my English summary into Dutch. Edit and Joost, thank you for accepting to be my paranimfen, you are the best!

I did not and could not work alone in the lab. A nice working environment is sometimes the most critical factor to get the work done. For that I want to thank all members from the MTP group. Also I would like to extend my gratitude to the help from members of other research groups: SMCT, PBM and BPE, where I frequently visited for experiments. Mark Smithers is acknowledged for his help (SEM and TEM) in the CMAL.

I truly appreciate the support and company of many friends here in Enschede, you make my life easier and happier: The small Chinese community: Shan and Yuguo, Jing, Weiqing, Hui, Xiaofeng, Xiao and Zheng, Rui, Hongmei, Ai-Ling and Boon-Hua, Lanti and Hao, Rong and Chao, Xuexin, Huaping, Weihua, Xin and Tian; My fellow countrymen: Wei (Wuhanese), Jiajie (Cantonese); and The first generation of Master students Nanotechnology: Antonella, Maryana, Ivan, Lorand and Ramon. Thank you so much for the wonderful times we had together.

Finally, I would like to dedicate this Thesis to my family: my mother Mrs. Tianmei Jing, my father Mr. Zhaoji Chen, my mother and father-in law, Mrs. Fuli Wang and Mr. Can Ma, my wife Yujie, and little Walter Zihe. You are the most important part of my life. And I will cherish you for the time to come.

Qi Chen

陈奇

Enschede 2009

Curriculum Vitae

Qi Chen was born on October 27th, 1978 in Guangdong (Canton), China. After graduating from Zhi Xin Middle School in Guangzhou, he continued his study at the Jiao Tong University in Shanghai. In 2001, he obtained his BE degree in Polymer Materials and Engineering. During 2001-2002, he worked at Shanghai Weicon Optics, Co. Ltd. as a researcher, focusing on developing contact lens materials made from methacrylates and hyaluronate-containing contact lens solution (Chinese patent, ZL02112141.9, 2006). In 2003 he joined the Master program of Nanotechnology at the University of Twente in Enschede, The Netherlands. In the program he worked as a research assistant in three different research groups: Biophysical Engineering group headed by Prof. Vinod Subramaniam, Optical Techniques group headed by Prof. Niek van Hulst, and Transducer Science and Technology group headed by Prof. Miko Elwenspoek, before finishing his Master research in the group of Materials Science and Technology of Polymers (MTP), headed by Prof. Julius Vancso. With a Master Thesis entitled “*Ordering of Poly(isoprene-block-ferrocenylsilane) Block Copolymer Thin Films: Bulk Structure Properties and Thin Film Wetting Properties*”, he obtained his MSc degree in Nanotechnology from the University of Twente in 2005. From September 2005, he started his PhD project in MTP group at the University of Twente, focusing on the self-assembly of block copolymers in solution and the utilization of these ordered structures as nanocontainers for enzymatic reactions. The results of this four year research are presented in this Thesis.